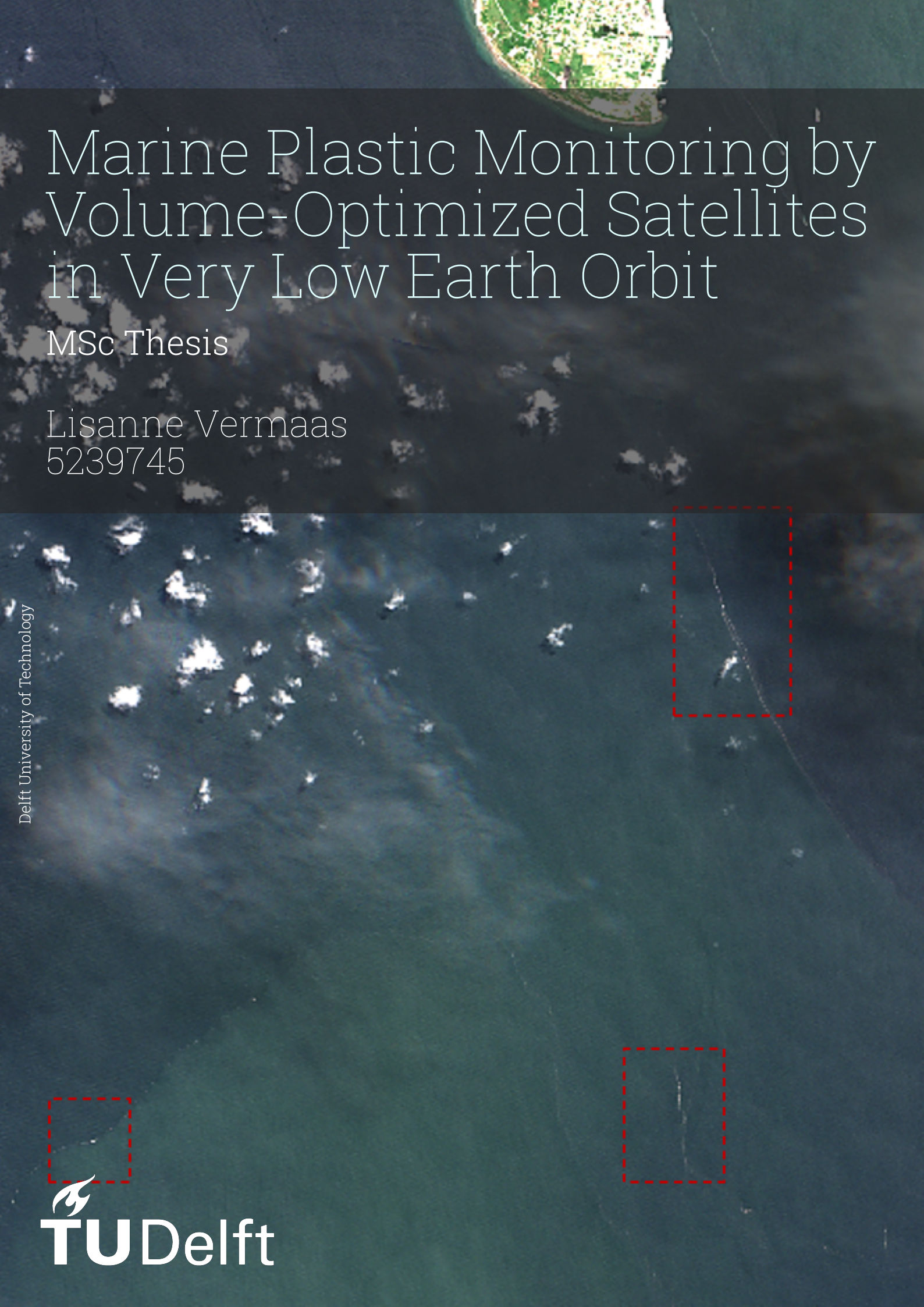

Marine Plastic Monitoring by Volume-Optimized Satellites in Very Low Earth Orbit

MSc Thesis

Lisanne Vermaas
5239745

Delft University of Technology

TU Delft

Marine Plastic Monitoring by Volume-Optimized Satellites in Very Low Earth Orbit

MSc Thesis

by

Lisanne Vermaas
5239745

to obtain the degree of Master of Science
at the Delft University of Technology,
to be defended publicly on Thursday July 3, 2025 at 14:00 PM.

Student number:	5239745
Project duration:	November 11, 2024 – July 3, 2025

Thesis committee:

Daily supervisor	Dr. ir. J. Bouwmeester,	TU Delft, SSE
Chair	Prof. dr. E.K.A. Gill,	TU Delft, SSE
External	Dr. ir. W. van der Wal,	TU Delft, PE

Cover: Dense plastic patches identified by Copernicus Sentinel-2 [1]

An electronic version of this thesis is available at http://repository.tudelft.nl/.

TU Delft

Preface

Deze scriptie sluit een bijzondere periode af. Met ongekende fascinatie voor het universum liep ik voor het eerst de faculteit Aerospace Engineering binnen. Met een rugzak vol kennis en een enorme liefde voor engineering loop ik straks naar buiten. Ik heb genoten van mijn tijd als student, ontzettend veel geleerd over het vak en mijzelf, en een hoop inspirerende mensen ontmoet. Ik heb dan ook met veel plezier en overgave aan deze scriptie gewerkt.

Ik zou graag van de gelegenheid gebruikmaken om een aantal prominente personen te bedanken. Allemaal hebben zij op hun eigen manier een significante bijdrage geleverd aan de totstandkoming van deze scriptie.

Allereerst spreek ik graag mijn grote waardering uit voor mijn supervisor in dit proces, professor J. Bouwmeester. U hebt niet alleen gezorgd voor een vlekkeloos verloop, maar ook voor een kritische blik en betrouwbare adviezen. Ik heb veel geleerd van de constructieve discussies en uw ervaren visie, en zal hier veel profijt van hebben in mijn verdere professionele carrière.

Daarnaast bedank ik graag mijn ouders voor hun onvoorwaardelijke steun in dit proces. Dankzij jullie heb ik de afgelopen jaren zorgeloos mogen studeren en kon ik mij volledig focussen op mijn studie. Ook in deze laatste fase heeft dat erin geresulteerd dat ik het optimale uit mijzelf heb kunnen halen.

Tot slot heb ik enorm genoten van alle vriendschappen die zijn ontstaan en blijven bestaan op, naast en tijdens de universiteit. Samen hebben we gelachen, gesport, gekampeerd, gekookt en gestreden. Dankzij jullie kijk ik met het allergrootste plezier terug op vijf mooie jaren.

Lisanne Vermaas
May 28, 2025

Summary

This thesis investigates the effects of deployable optics and Very Low Earth Orbit (VLEO) on satellite volume with the aim of improving spatial and temporal data on marine plastic debris. Even though satellites such as Sentinel-2 have proven the value of remote data on this matter, the lack of a dedicated mission limits current capabilities to detection of large scale plastic accumulations and fails to capture its dynamic behavior.

The Delft University of Technology is developing a Deployable Space Telescope (DST), featuring an instrumentation box and baffle segment that contains the Primary and Secondary Mirror (M1 and M2), a foldable suspension in between and a telescopic baffle. This deployable instrument optimizes stowed-to-deployed volume, enhancing volume optimization and spatial resolution. VLEO also promises to improve spatial resolution while reducing the required aperture diameter. This together with deployable optics supports a volume optimized design, which in turn reduces launch cost. By reduction of this recurring cost, constellation deployment is encouraged, leading to a higher temporal resolution as well. A key challenge in VLEO is the drag induced by the residual atmosphere, which drives the design of the propulsion and Attitude and Orbit Control Subsystem (AOCS). Designing to minimize drag inevitably brings the focus back to volume optimization. Therefore, an analysis of the net effect of deployable optics and VLEO on the satellite volume is required to assess the feasibility of this novel concept as compared to a traditional, non-deployable space telescope in Low Earth Orbit (LEO).

For this, volumes of the (non-)deployable payload and all satellite subsystems were modeled. Smart integration of the Command and Data Handling (CDH) unit, Electric Power Subsystem (EPS) control and distribution unit, AOCS computations and communication electronics was applied to minimize bus volume. The models include uncertainties in the input parameters by the use of probability distributions and compute the subsystem volume for a set of input samples as a function of orbital altitude, which was uniformly distributed from $150\,\mathrm{km}$ to $600\,\mathrm{km}$ to include both VLEO and LEO. The models were combined in a system model, which was verified by four manually computed reference cases. The number of solar panel segments was found to be a point of attention, just like the discrepancy between the computed body dimensions and the ones assumed in the model development.

The model was then integrated in a Monte Carlo simulation that computes satellite volume for various sampled input parameter sets to produce the satellite volume envelope as seen in Figure 1a. Data was refined by removal of outliers using a z-score of 3. Indeed, an average optimal volume of $0.0341\,\mathrm{m}^3$ was found at an altitude of $295\,\mathrm{km}$ with a standard deviation of $0.0128\,\mathrm{m}^3$. The optimum is constructed by the dominant propulsion power and thus the EPS at low altitudes and a driving payload (primarily baffle) volume at high altitudes as seen in Figure 1b. The former is a direct result of the advantageous volume of Electric Propulsion (EP) over chemical propulsion at this altitude, though a transition is observed around $350\,\mathrm{km}$ to $550\,\mathrm{km}$. The feasibility of Atmosphere Breathing Electric Propulsion (ABEP) was also investigated but found to be currently very low due to excessive power consumption and intake volume.

The effects of mission parameters were explored: mission lifetime has a limited effect on satellite volume and hence, a longer mission duration is recommended to maximize data. The number of segments that compose the instrument's deployable baffle on the other hand, was found to be very influential. The optimal amount exceeds practical feasibility and thus, it must be traded off against complexity and the resulting number of solar panels. The reason for the latter relationship lies in the geometry of the satellite: beyond $260\,\mathrm{km}$, the majority of the satellite geometries is driven by the outer dimensions of the baffle, leading to a flatter body and a direct relation between stowed baffle height and body dimensions (and thus the area available for solar panels). Due to this dependency, the sensitivity analysis also found that the effective stowed volume is very sensitive to a change in aperture dimensions.

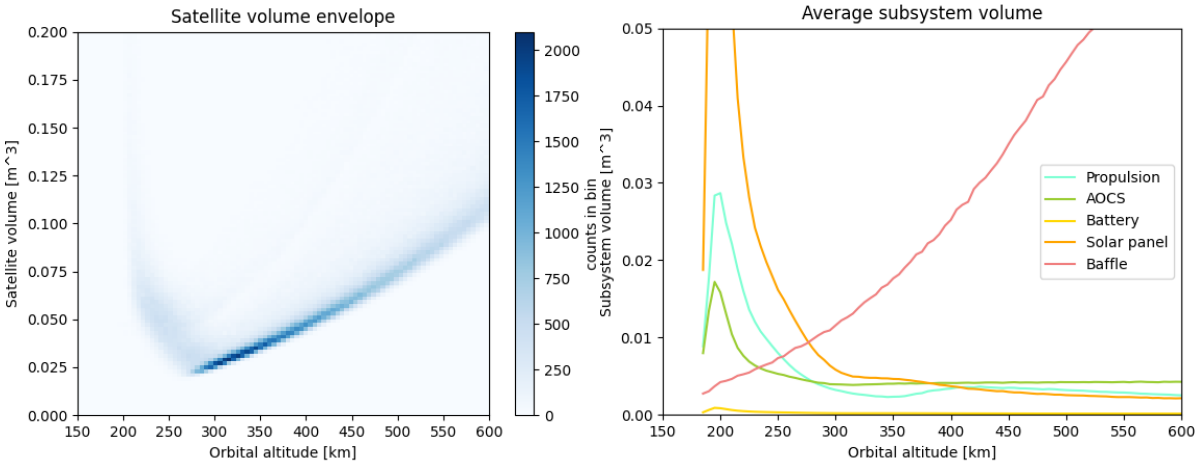

(a) The Monte Carlo simulation result of the satellite volume envelope as a function of orbital altitude without outliers (bin size=$(5\,\mathrm{km}, 0.002\,\mathrm{m}^3)$)

(b) The Monte Carlo simulation result of the average subsystem volume as a function of orbital altitude without outliers

Figure 1: The Monte Carlo simulation results of the volume envelope and average subsystem volume

The four possible combinations of orbital altitude and instrument deployability along with their average effective stowed volume resulting from the Monte Carlo simulation are summarized in Table 1 and depicted in Figure 2. With a volume reduction of $89.1\,\%$ compared to a traditional, non-deployable LEO approach, the combination of VLEO and deployable optics was found to be most promising. Ranging between $2-9$, the number of solar panel for these designs segments is not directly problematic.

Table 1: The average effective stowed volume of the four competing configurations

Orbital altitude	Deployability	Effective stowed volume
VLEO $(295\,\mathrm{km})$	No	$0.0598\,\mathrm{m}^3$
VLEO $(295\,\mathrm{km})$	Yes ($n_{segments} = 3$)	$0.0361\,\mathrm{m}^3$
LEO $(600\,\mathrm{km})$	No	$0.332\,\mathrm{m}^3$
LEO $(600\,\mathrm{km})$	Yes ($n_{segments} = 3$)	$0.183\,\mathrm{m}^3$

However, it is recommended to re-evaluate the design of the thermal control subsystem, as it does not fit the body of the current design optimum. Moreover, the discrepancy between the computed body dimensions and the ones assumed in the model development has led to extrapolation of the AOCS model on the low-end. This likely resulted in an over-estimation of its power consumption. Therefore, iterations on this design should use smaller AOCS reference systems as a basis for the model. This could snowball to a reduction in power consumption so that the number of solar panel segments is of no concern anymore.

Furthermore, the optical requirements should be consolidated to fix the aperture dimensions as the sensitivity analysis revealed a strong dependency of the design optimum on this parameter. Finally, even though structure and material trade-offs were not performed in this work, they deserve careful consideration in future design phases as they strongly interact with the VLEO environment. Not only could they enable aerodynamic attitude control and drag optimization, they are also important when evaluating the possibility of stacking the flatter geometry satellites in the launcher to further reduce cost.

With the feasibility of deployable optics in VLEO proven, this thesis opens the doors for a new approach to Earth Observation missions.

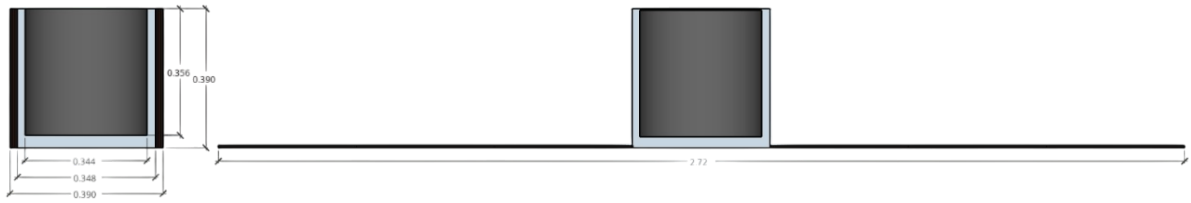

(a) Non-deployable space telescope in VLEO

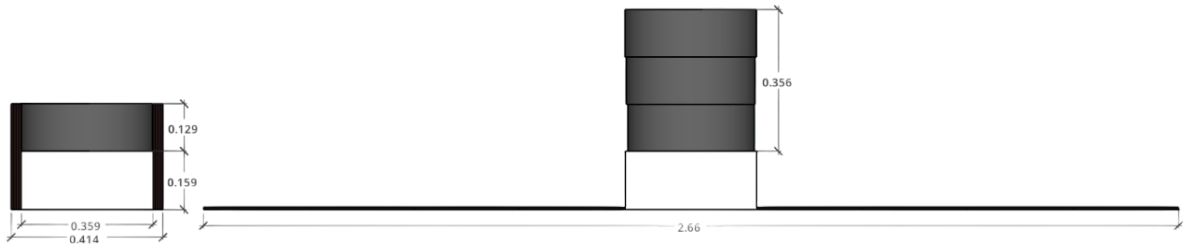

(b) DST in VLEO

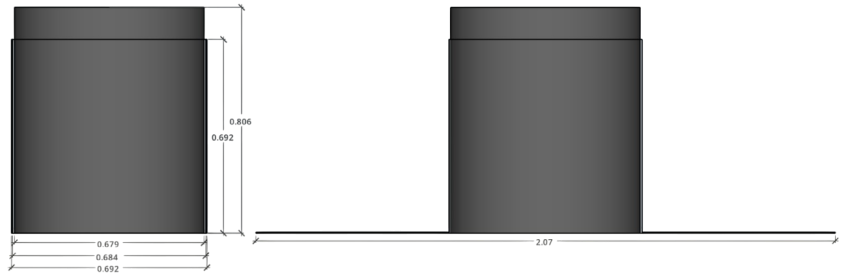

(c) Non-deployable space telescope in LEO

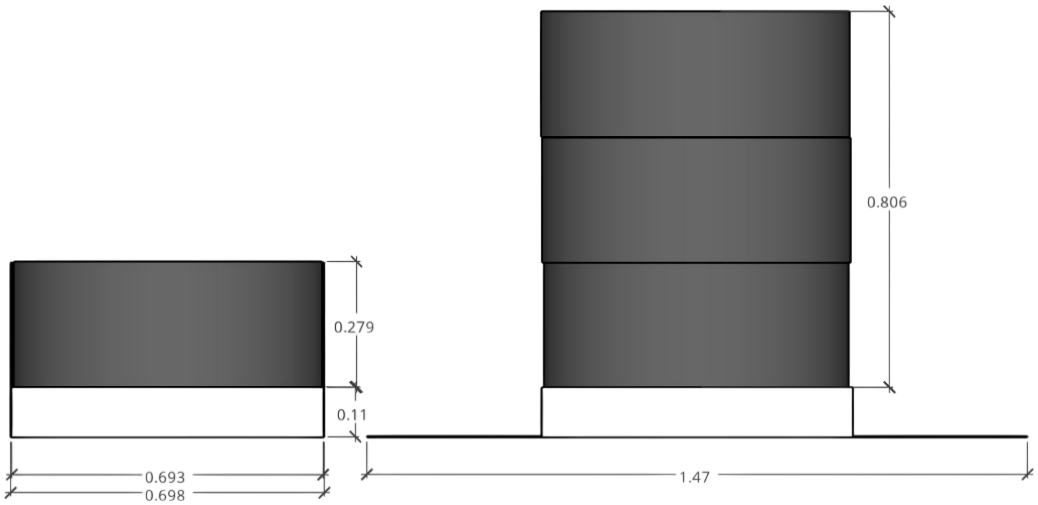

(d) DST in LEO

Figure 2: The four combinations of payload deployability and orbital altitude

Contents

List of Figures

List of Tables

List of Symbols and Abbreviations

Abbreviations

Abbreviation	Definition
ABEP	Atmosphere-Breathing Electric Propulsion
ADCS	Attitude Determination and Control Subsystem
AETHER	Air-breathing Electric THrustER
AO	Atomic Oxygen
AOCS	Attitude and Orbit Control Subsystem
AOFT	Acoustic Optical Tunable Filter
ASC	Artificial Stem Cells
ASIM	Applique Sensor Interface Modules
BER	Bit Error Rate
CDH	Command and Data Handling
CMG	Control Moment Gyro's
CONOPS	CONcept Of OPerationS
COTS	Commercial-Off-The-Shelf
DFAC	Drag-Free and Attitude Control
DoD	Depth of Discharge
DST	Deployable Space Telescope
DVB-S2	Digital Video Broadcasting - Second Generation
EM	Electro-Magnetic
EP	Electric Propulsion
EPS	Electric Power Subsystem
ESA	European Space Agency
ESD	Electro Static Discharge
ESD	Equivalent Solar Day
eXCITe	eXperiment for Cellular Integration Technologies
FDI	Floating Debris Index
FMF	Free Molecular Flow
FoV	Field of View
GOCE	Gravity field and steady-state Ocean Circulation Explorer
GSD	Ground Sampling Distance
GSI	Gas-Surface Interactions
GPS	Global Positioning System
HET	Hall-Effect Thruster
HISat	Hyper Integrated Satellite
IMU	Inertial Measurement Unit
ISS	International Space Station
JAXA	Japan Aerospace eXploration Agency
LEO	Low Earth Orbit
MDM	Material Degradation Monitor
MEMS	Micro-ElectroMechanical System
MISSE	Materials International Space Station Experiment
MLI	Multi-Layer Insulation
MPPT	Maximum Power Point Tracking
MSI	Multi-Spectral Instrument
M1	Primary Mirror

Abbreviation	Definition
M2	Secondary Mirror
NDVI	Normalized Difference Vegetation Index
NMF	Nano-Modular Format
OBC	On-Board Computer
OSR	Optical Solar Reflectors
PCB	Printed Circuit Board
PEACE	Polymers Erosion And Contamination Experiment
PRISMA	PRecursore IperSpettraledella Missione Applicativa
QPSK	Quadrature Phase-Shift Keying
RF	Radio Frequency
RW	Reaction Wheel
SAR	Synthetic Aperture Radar
SHAPE	Stable and Highly Accurate Pointing Earth-imager
SIMPL	Satlet Initial-Mission Proofs and Lessons
SLATS	Super Low-Altitude Test Satellite
SNR	Signal-to-Noise Ratio
SOAR	Satellite for Orbital Aerodynamics Research
SPA	Space Plug-and-play Avionics
SPARC-1	Space Plug-and-play Architecture Research Cubesat-1
QPSK	Quadrature Phase Shift Keying
SSO	Sun-Synchronous Orbit
SWAP	Size, Weight and Power
TBD	To Be Determined
TRL	Technical Readiness Level
UAV	Unmanned Aerial Vehicle
UHF	Ultra-High Frequency
UV	Ultra Violet
VHR	Very High Resolution

Symbols

Symbol	Definition	Unit
A	Frontal area	m^2
A_{baffle}	Frontal area of the deployed baffle	m^2
A_c	Intake area	m^2
A_{ref}	Reference surface area	m^2
A_{sp}	Solar panel area	m^2
A_{tc}	Thermal control side cover area	m^2
a_{drag}	Drag acceleration	$m \cdot s^{-2}$
C/N_0	Carrier to noise power	dB
C_{bat}	Battery capacity	J
C_D	Drag coefficient	$-$
c	Speed of light	$m \cdot s^{-1}$
cm	Center of mass	m
cp_a	Aerodynamic center of pressure	m
D	Diameter of the primary mirror	m
D_{max}	Baffle outer diameter	m
DoD	Depth of Discharge	$-$
DP	Dipole moment	$A \cdot m^2$
DP_{sat}	Residual dipole moment of the satellite	$A \cdot m^2$
DR_{avg}	Average data rate	$Mbps$
DR_{down}	Downlink data rate	$Mbps$

d_{M1-M2}	M1-M2 distance	m
E	Young's modulus	$N \cdot m^{-2}$
E_b/N_0	Bit Energy to Noise Ratio	dB
$EIRP$	Equivalent Isotropic Radiated Power	$dB \cdot W$
F_{drag}	Drag force	N
F_{thrust}	Thrust force	N
f	Frequency	Hz
$\bar{f}$	Average eclipse fraction	$-$
$f_{Solstice}$	Eclipse fraction at Solstice	$-$
G	Gravitational constant	$m^3 \cdot kg^{-1} \cdot s^{-2}$
G/T	Receiving-antenna Gain to noise Temperature	$dB \cdot K^{-1}$
G_{Tx}	Transmission antenna gain	dB
GSD	Ground sampling distance	m
g_0	Earth standard acceleration of gravity	$m \cdot s^{-2}$
h	Orbital altitude	km
$h_{segment}$	Baffle segment height	m
h_x	Additional baffle height to shade from the Sun	m
h_{min}	Height of the stowed baffle	m
I_{sp}	Specific impulse	s
$I_{sp,ABEP}$	ABEP specific impulse	s
$I_{sp,EP}$	Regular EP specific impulse	s
$L/\sqrt{A}$	Inlet aspect ratio	$-$
L_A	Atmospheric loss	dB
L_P	Pointing loss	dB
L_S	Free space loss	dB
L_{Rl}	Line loss on receiving side	dB
L_{Tl}	Line loss on transmitting side	dB
l_{baffle}	Baffle length in deployed conditions	m
l_{sp}	Total solar panel length	m
$l_{sp,max}$	Solar panel length of longest array	m
M	Earth's mass	kg
M_{mag}	Magnetic moment of Earth	$T \cdot m^3$
m	Mean	$-$
$m_{ch,prop}$	Chemical propulsion propellant mass	kg
$m_{EP,prop}$	Regular EP propellant mass	kg
m_{prop}	Propellant mass	kg
$M_{accumulated}$	Accumulated momentum	$N \cdot ms$
M_{mag}	Magnetic moment of Earth	$T \cdot m^3$
N	Sample size	$-$
$n_{segments}$	Number of baffle segments	$-$
$n_{segments,Max}$	Maximum feasible number of baffle segments	$-$
P_{ABEP}	ABEP power	W
P_{AOCS}	AOCS power	W
P_{avg}	Relative average generated power excluding eclipse	W
$P_{avg,e}$	Relative average generated power including eclipse	W
P_{basis}	Base power consumption of the communications subsystem	W
P_{CMG}	CMG power	W
P_{com}	Communication power	W
P_{EP}	Regular EP power	W
P_{in}	Transmitter input power	W
P_{MTQ}	Magnetorquer power	W
P_{OBC}	OBC power	W
P_{PL}	Payload power	W
P_{prop}	Propulsion power	W
P_{Tx}	Transmission power	W

$P_{Tx,dB}$	Transmission power	dB
P_{tot}	Total average power consumption	W
q_{refl}	Unitless reflectance factor	$-$
q	Distributed load	$N \cdot m^{-2}$
R_{boom}	Radius of the suspension boom	m
R_b	Data rate	$dB - Hz$
R_e	Earth's radius	km
R_x	Width added due to segments	m
r	Distance between two antennas	km
SR	Slew rate	$rad \cdot s^{-1}$
T	Orbital period	s
T_a	Aerodynamic torque	$N \cdot m$
T_{desat}	Desaturation torque	$N \cdot m$
T_g	Gravity gradient torque	$N \cdot m$
T_{MTQ}	Torque from magnetorquer	$N \cdot m$
T_m	Magnetic dipole torque	$N \cdot m$
T_s	Solar radiation pressure torque	$N \cdot m$
t	Time	s
t_{com}	Communication window	s
$t_{eclipse}$	Eclipse time	s
t_{life}	Satellite lifetime	s
t_{prop}	Propulsion time	s
t_{sp}	Solar panel thickness	m
$V_{ABEP,dry}$	ABEP dry volume	m^3
V_{baffle}	Baffle volume in stowed conditions	m^3
V_{bat}	Battery volume	m^3
V_{bus}	Total subsystem volume	m^3
$V_{ch,dry}$	Chemical propulsion dry volume	m^3
$V_{ch,prop}$	Chemical propulsion propellant volume	m^3
V_{dry}	Dry volume	m^3
$V_{EP,dry}$	Regular EP dry volume	m^3
$V_{EP,prop}$	Regular EP propellant volume	m^3
$V_{eff,stowed}$	Effective stowed volume	m
V_{ICU}	Integrated core unit volume	m^3
$V_{instumentbox}$	Instrumentation box volume	m^3
V_{intake}	Intake volume	m^3
V_{prop}	Propellant volume	m^3
V_{sp}	Solar panel volume	m^3
v_{sat}	Satellite orbital velocity	$m \cdot s^{-1}$
v	Variance	$-$
V	Volume	m^3
x_{body}	Body dimension along the local x-axis	m
x_{cm}	X-coordinate of the center of mass	m
x_{cp_a}	X-coordinate of the center of pressure	m
y_{body}	Body dimension along the local y-axis	m
z	Statistic related to confidence interval	$-$
z_{body}	Body dimension along the local z-axis	m

Symbol	Definition	Unit
α	Elevation angle of the satellite $+90$ °	rad
β_{bc}	Ballistic coefficient	$kg \cdot m^{-2}$
β	Half power beamwidth angle	rad
γ_{max}	Maximum angle between the solar rays and M2	rad
ΔV	Delta V	$m \cdot s^{-1}$

Symbol	Definition	Unit
δ	Tip deflection	m
ϵ	Precision	U
η_c	Collection efficiency	$-$
η_{DC-RF}	DC-to-RF efficiency	$-$
η_{spec}	Spectral efficiency	$bps \cdot Hz^{-1}$
θ	Angle between ground station and satellite from Earth's center	rad
θ_{point}	Pointing knowledge	rad
θ_{res}	Angular resolution	rad
ι	Attitude pointing angle	$^\circ$
λ	Celestial longitude of the Sun	$^\circ$
λ_{mag}	Unitless function of magnetic latitude	$-$
$\lambda_{mag,avg}$	Average unitless function of magnetic latitude	$-$
λ_{wave}	Wavelength	m
$\mu*$	Location parameter	$-$
ν	Poisson's ratio	$-$
Φ	Solar constant	$W \cdot m^{-2}$
ρ	Material density	$kg \cdot m^{-3}$
ρ_{atm}	Atmospheric density	$kg \cdot m^{-3}$
σ	Standard deviation	$-$
$\sigma*$	Scale parameter	$-$
ϕ_{min}	Minimum angle between nadir direction and incoming sunlight	rad
$\Omega - \lambda$	Longitude of the ascending node	$^\circ$

1 Introduction

This thesis details a study on the feasibility of volume optimized satellites in Very Low Earth Orbit (VLEO). Designed for marine plastic debris monitoring, a constellation of such satellites carrying a Deployable Space Telescope (DST) promises to deliver higher spatial and temporal resolution data compared to single satellites at greater altitudes. This concept thereby improves localization and tracking of marine plastics. Volume optimization of the satellites not only improves VLEO feasibility by reducing the amount of drag, which enhances spatial resolution, it aids constellation deployment in terms of cost and thus improves temporal resolution as well.

Due to the critical influence of system volume on mission feasibility, it is the main focus of this thesis. This introduction outlines the relevance of addressing the challenge of marine debris now and elaborates on the overall thesis objective. Moreover, an outline of the document is provided.

1.1. Background

With the increasing amount of plastic debris in Earth's aquatic environments, worries about its effect on the flora and fauna become more and more prominent. The technological advancements in spaceflight, especially with the rise of the New Space era, present a unique opportunity to address this problem efficiently.

Combining a novel instrument with an optimized satellite platform in a low orbit enhances imaging capabilities in terms of spatial resolution and reveals great potential [2]. Therefore, the Delft University of Technology is developing a deployable optical telescope with the aim to reduce payload size and suppress total mission cost. This, in turn, supports constellation deployment, leading to enhanced revisit times and better temporal resolutions. The envisioned mission is composed of 50-100 satellites with a lifetime of $5\,\mathrm{years}$.

The current baseline design foresees a deployable telescope with an aperture size of $20\,\mathrm{cm}$ to $40\,\mathrm{cm}$ and observes the visible, near-infrared and short-wave infrared wavelengths along with the linear polarization to enable differentiation of plastics in the image [3]. The instrument makes use of an Acoustic Optical Tunable Filter (AOTF) to select a part of the spectrum, allowing for hyperspectral observation. Preliminary estimations state a power consumption of $5\,\mathrm{W}$ to $10\,\mathrm{W}$ and a mass of $0.5\,\mathrm{kg}$ for the filter with an angular aperture of $20\,°$. A primary (M1) and secondary (M2) mirror are used respectively to focus the light and are shielded from the Sun by a deployable baffle consisting of cylindrical shell segments. M2 is mounted on a foldable suspension via a spider so that it can deploy to a defined distance from M1. The goal of this DST design is to optimize the payload's stowed-to-deployed volume.

A VLEO orbit in combination with deployment of the optical telescope realizes sufficient spatial resolution while minimizing launch volume and thus suppressing launch cost. Active mechanical alignment is foreseen to allow the use of lightweight materials and reduce the on-ground alignment effort. Further launch cost reduction is achieved by smart integration of the satellite subsystems resulting in further volume optimization.

Efforts in volume optimization of the payload only make sense when the instrument is integrated into a volume-optimized satellite platform. So, this work focuses on this aspect of the mission design and explores the characteristics of the envisioned concept. Moreover, key challenges associated with the novelties of this concept are studied, in particular the increased drag in VLEO in combination with the relatively large surface area of the deployable telescope. This namely, is expected to translate into more stringent requirements on the propulsion and Attitude and Orbit Control Subsystem (AOCS) and might negatively impact their volume budgets. Combining volume optimization measures with the negative effects of the key challenges allows for an analysis of the net volume gain. This budget is fundamental to the concept's feasibility as it directly relates to drag and mission (launch) cost. Feasibility is also affected by design decisions on the Technological Readiness Level (TRL) of technologies used in the concept. TRL is thus carefully considered if the design converges to the use of low TRL technologies.

1.2. Thesis Objective

This thesis compares the volume of a smartly integrated spacecraft carrying a deployable optical telescope in VLEO to a traditional Earth observation satellite that achieves the same spatial resolution. By considering the net volume gain resulting from the budget-optimization strategies (DST and VLEO) as well as their negative effects, it aims at determining concept feasibility. Moreover, the optimal combination of the aforementioned strategies for the envisioned mission along with their TRL is studied. In doing so, this work contributes to the development and improvement of Earth observation missions and more specifically, to marine plastic debris monitoring. By advancing data on plastic location and motion, the higher-level goal is to develop effective and efficient solutions to this global challenge.

1.3. Thesis Outline

In Chapter 2, an elaborate literature review is presented. Three main aspects are focused on: marine plastic monitoring, VLEO and satellite bus volume optimization. From the information gathered, a clear research gap was identified and is described in Chapter 3. Chapter 4 outlines the approach to fill this gap and summarizes how the feasibility of the proposed concept is assessed. In Chapter 5, the model used for evaluation of the satellite volume is detailed. The following chapter focuses on verification and validation of this model, as well as how it is used in a Monte Carlo simulation. Chapter 7 covers the outcome of the simulation, along with a sensitivity analysis and description of the design optimum so that Chapter 8 can answer the research question. This chapter also discusses recommendations for future work in this research area.

2

Literature Review

The literature review presented in this chapter gives an elaborate summary of the research done in the field of marine plastic debris detection and monitoring. It focuses on satellite imagery, which leaves a clear research gap to be filled by the conceptual satellite design proposed in this thesis. Moreover, critical mission aspects of this proposed spacecraft such as orbit definition and satellite miniaturization are explored to obtain an extensive overview of the state-of-the-art knowledge and the technologies available to enhance a cost-effective yet capable design.

2.1. Marine Plastic Monitoring

Even though large-scale plastic production only dates back to after World War II, over 8300 million metric tons have been produced as of 2017 [4]. The majority of this plastic had a lifetime of less than $10\,\mathrm{years}$, resulting in a significant amount of waste (220 million tonnes in 2024 alone [5]), 79% of which accumulated in landfills or the natural environment [4]. It was calculated that just in 2016, 19 to 23 million metric tons of plastic debris entered the marine environment [6]. This, combined with the fact that one can eliminate plastic only permanently by thermal destruction raises concerns about plastic accumulation in Earth's waters [7].

Addressing the aforementioned issue requires identifying sources, tracking the movement and pinpointing the accumulation locations of marine plastic debris [8]. This, however, has proven to be challenging. In-situ measurements are costly and lack temporal resolution and coverage, while numerical methods such as particle tracing models require sufficient data for validation purposes in the first place [9][10]. This section explores past efforts to detect and monitor marine plastic debris.

2.1.1. Remote Sensing by Sentinel-2

In order to enhance temporal resolution and coverage of data on marine plastic debris, the use of satellites has been studied. Multi-spectral images taken by ESA's (European Space Agency) Sentinel-2 spacecraft have been used to explore the possibilities of remote sensing for marine plastic debris detection and monitoring. The Multi-Spectral Instrument (MSI) onboard the spacecraft has detection bands in the infrared region. With these, it can detect the spectral radiation fingerprint of plastic, although the band wavelengths are not optimal for plastic detection and only high density plastic patches can be observed due to water absorption interference [11][12]. Sentinel-2 has the advantage of a relatively high spatial resolution up to $10\,\mathrm{m}$ (compared to for example Landsat 8 with $30\,\mathrm{m}$ [13]) and revisit times of five days, albeit only coastal waters are covered [8]. Moreover, the data is publicly available, making it a suitable candidate to explore marine plastic debris using remote sensing.

Sentinel-2 data was successfully used to map the hot-spots and motion trends of marine debris in the Mediterranean Sea [11]. Meter-sized debris aggregations (limited to a minimum length of $70\,\mathrm{m}$ against false positives) called litter-windrows were used as proxy for monitoring. They allowed for characterizing the complex and seasonal dynamics driving marine debris movement. An optimal instrument is expected to reduce the detection sensitivity by an entire order of magnitude compared to Sentinel-2,

with a minimum surface plastic coverage of 1% within a pixel (compared to 20% in the sub-optimal MSI of Sentinel-2). In this way, the study proved the capabilities of remote sensing in tracking the movement of marine debris aggregations, while noting that Sentinel-2 lacks sufficient spatial and temporal resolution, coverage and optimal detection bands for effective global marine plastic debris detection.

2.1.2. Machine Learning Applications

Several studies have explored machine learning algorithms to detect marine plastic debris in spacecraft imagery. These methods heavily rely on the amount of in-situ data to validate the machine learning models, especially in presence of spectral distortions due to the use of multiple detection bands [14][15][16][17][18]. On top of that, spectral similarity between marine debris and sea snot requires additional analysis for reliable discrimination [19].

Sentinel-2 data was also used to detect and classify marine plastic debris in Brazilian coastal areas by the use of a machine learning algorithm in combination with the Floating Debris Index (FDI) [20]. Such index is meant to enhance discrimination of plastic from other materials. FDI is based on four out of twelve Sentinel-2's MSI bands and was found to be the most important variable for detection of floating debris among several indices tested in an earlier study [16]. FDI is combined with the Normalized Difference Vegetation Index (NDVI) to distinguish vegetation from other floating debris [20]. This method allowed sub-pixel scale detection and material classification with 87.25% accuracy, slightly improving on the 86% accuracy achieved using a similar approach [21]. Insufficient pixel coverage led to misclassification, suggesting the need for higher spatial resolution [20]. Another source of faulty detection is rooted in spectral similarities between classes, which could be improved by the use of hyperspectral rather than multi-spectral imaging [14].

2.1.3. Other Spacecraft

WorldView-2/3, PRISMA (PRecursore IperSpettraledella Missione Applicativa) hyperspectral satellite and LandSat-8 have also been used to detect and track marine plastic debris. Worldview-2 and 3 achieve a high spatial resolution of $2\,\mathrm{m}$ and $4\,\mathrm{m}$ respectively [22]. However, the lack of information in the short-wave infrared region makes plastic indistinguishable from other floating materials. Moreover, its hyperspectral imaging capability shows significantly reduced response for wet plastic compared to dry conditions [23]. Efforts to combine the information from WorldView's Very High Resolution (VHR) images with Sentinel-2's favorable spectral, but lower spatial resolution data allowed for detection of plastic targets as small as $0.6\,\mathrm{m}$ x $0.6\,\mathrm{m}$, only covering 3% of Sentinel-2's pixel, proving the value of combining satellite data [22]. This approach, however, is limited by the need for near 'simultaneous' imaging due to the quick appearance, movement and disappearance of litter accumulations [22].

Data from PRISMA and LandSat-8, on the other hand, suffered from poor spatial and spatial-temporal resolution respectively [24]. By the use of pansharpening techniques, which combine the hyperspectral image with PRISMA's high-resolution but noisy panchromatic data, PRISMA data could be used to detect plastic targets as small as $2.4\,\mathrm{m}$ x $2.4\,\mathrm{m}$, about 8% of a hyperspectral image pixel's coverage [25]. Limitations of this technique are found in the fact that, due to seawater abundance within a lower-resolution hyperspectral pixel, the smoothening effect on the observed spectrum in that pixel is not enhanced by the pansharpening technique and thus, the smoothening effect persists in the pansharpened image.

2.1.4. Overcoming Limitations

Combining satellite data with that of UAV's (Unmanned Aerial Vehicles) has been attempted to overcome Sentinel-2's limited spatial and temporal resolution as well as its weather and atmospheric dependency which introduces uncertainty [8][26]. Even though UAV data does not suffer these limitations, it poses major deficiencies in coverage and automation.

In another attempt to circumvent weather dependency, SAR (Synthetic Aperture Radar) data from Sentinel-1 was used in to detect plastic islands in rivers [27]. It was hypothesized that water without plastic shows a specular reflection of the signal, whereas in presence of plastic, scattering is observed. Indeed, SAR was capable of detecting marine plastics. However, it was also found that sources such as wind and riverbanks introduce false positives. Moreover, this study could not distinguish between plastic and other marine debris including natural objects.

In conclusion, recent studies have proven satellites' value and capabilities in detecting and monitoring marine plastic debris. However, in the absence of a dedicated mission, current methods lack spatial resolution, optimal detection instruments and global coverage. These deficiencies hinder detection and monitoring of smaller-sized plastics and restrict global surveillance. Thus, there is a clear need for global data on marine plastic debris with improved spatial resolution in order to optimize detection and monitoring and finally, effectively address the issue of plastic in the marine environment [9]. The proposed mission shall thus provide a high spatial ($1\,\mathrm{m}$ to $5\,\mathrm{m}$) and radiometric resolution (information depth, possibly hyperspectral) [12]. A sensor with bands in the visible and short-infrared range is required to distinguish plastic from other types of litter. As a result, the swath width would be about $10\,\mathrm{km}$. Revisit times should be minimized in order to capture the dynamic existence of marine plastic debris.

2.2. Very Low Earth Orbit (VLEO)

One method to address the need for improved spatial resolution is flying at lower altitudes compared to current missions such as Sentinel-2. The possibility of flying in Very Low Earth Orbit (VLEO) with an altitude below $400\,\mathrm{km}$ is very promising for this purpose [28]. This section starts with a summary of the advantages of flying in VLEO. Then, several atmospheric aspects critical to a mission in VLEO are elaborated on, followed by a literature study on possible propulsion methods in this orbit. The section closes with the analysis of VLEO concepts and missions and some concluding remarks that relate to the proposed mission.

2.2.1. Advantages

The primary advantage of VLEO for the proposed mission is the improved diffraction limited spatial resolution due to the fact that the satellite is flying closer to its target [29]. As concluded form Section 2.1, current Earth observation satellites lack sufficient spatial resolution for efficient marine plastic debris monitoring. Rather than improving instrument performance in these orbits, a lower orbit can enhance spatial resolution using the same instrument. Moreover, it could be even possible to reduce sensor aperture dimensions, which is advantageous for the mission lifetime. Reason for this is the reduction in drag which causes orbital decay, as discussed in Subsection 2.2.2. An implicit disadvantage of the increased spatial resolution is a reduction in coverage with decreasing altitude [28].

Also, the radiometric resolution could be improved in a lower orbit if desired [28]. The signal power remains higher due to the reduced free space loss and therefore allows for more information to be transmitted, resulting in a higher Signal-to-Noise Ratio (SNR) for the same spatial resolution or a higher spatial resolution for the same signal-to-noise ratio. This effect is only slightly compensated by the increased ground speed at lower altitudes, which in turn reduces the integration of signal power over time. Like the payload SNR, the communication link budget is also improved. The low orbit, however, limits the elevation angle as this affects the signal absorption through the atmosphere. Also, the time for communication with a ground station is reduced due to the higher ground speed. Therefore, the link budget must be considered in the orbit selection.

Another advantage of VLEO is the reduction of errors resulting from attitude determination and pointing accuracy, leading to improved geospatial position accuracy [29][28]. This then reduces requirements on the attitude determination and control of the spacecraft. Contrastingly, position knowledge requirements increase as a result of altitude reduction [28]. Also, the presence of atmospheric particles challenges attitude control, as discussed in Subsection 2.2.2.

VLEO also supports natural decay. Not only does this mean that low orbits house less debris, thus reducing the possibility of collision, but it also eliminates the necessity for a dedicated deorbit subsystem as most objects decay within weeks [30]. Absence of such system reduces satellite mass and complexity.

Temporal resolution in VLEO is worse than in higher orbits [28]. The main reason for this is the reduced swath size for the same instrument in a lower orbit. For reference, an instrument with a view angle of $\pm\ 10\,°$ in VLEO at $300\,\mathrm{km}$ altitude achieves a swath width of $106\,\mathrm{km}$, while in $600\,\mathrm{km}$ LEO, this is $212\,\mathrm{km}$. This means that the VLEO spacecraft needs more revolutions to cover the same area as a LEO spacecraft and thus, has a worse temporal resolution. Next to swath width, also revisit time plays a

role in temporal resolution. Typically, the altitude range of $600\,\mathrm{km}$ to $800\,\mathrm{km}$, far beyond VLEO, is optimal for Earth observation missions in terms of revisit time. For certain altitude ranges in VLEO, revisit time peaks, which is the result of resonance between Earth's rotation period and the orbital period. Orbital altitude and precession must thus be carefully chosen to avoid these regions. As temporal resolution was identified critical to marine plastic monitoring, the deployment of a constellation in VLEO is preferred to reduce revisit time and increase temporal resolution accordingly.

Finally, space radiation, composed of energetic particles in the Earth's magnetic field, solar flares, and galactic cosmic rays is less prominent in VLEO [28]. The main reason for this is the shielding provided by Earth's magnetic field and the presence of atmospheric particles. Therefore, COTS (Commercial-Off-The-Shelf) components which are not necessarily radiation-hardened, shielded or fault-resilient, can be used onboard VLEO satellites. This significantly reduces the cost of the mission. On the other hand, VLEO contains atmospheric particles such as Atomic Oxygen (AO), which impose different challenges on the design as described in the next subsection.

2.2.2. Atmosphere

Next to the aforementioned advantages, VLEO also brings some challenges to the design due to its environmental conditions. Firstly, the presence of atmospheric particles induces drag and decelerates the spacecraft. This, in turn, causes orbital decay and limits mission lifetime. The addition of a propulsion system is common practice to counteract atmospheric drag and is further discussed in Subsection 2.2.3. Moreover, the VLEO atmosphere contains Atomic Oxygen (AO) that affects the exterior materials and leads to material degradation. Another concern is interaction of the spacecraft with plasma, possibly leading to power loss and unreliable communication. This subsection expands on these challenges.

Atmospheric Drag

Drag is the result of gas-surface collisions between the atmospheric particles and the satellite body. Due to the relative velocity of the satellite with respect to the atmosphere, the total force exerted by such collisions results in a deceleration experienced as drag. As the concentration of particles in VLEO is low, the flow encountered by a spacecraft is generally considered to be a free molecular flow [31]. This means that the gas-surface interactions are dominant and inter-particle collisions are neglected. This then also implies that the incoming flow is not affected by the presence of the spacecraft. Two types of gas-surface interactions can be distinguished: specular and diffuse, depending on how the material reflects the particles. In VLEO, reflections are generally considered to be diffuse due to surface material erosion by AO (which is further discussed below) [32].

Another aspect to consider in the light of drag is the energy transfer in such collisions. The accommodation coefficient characterizes this energy transfer and takes values between 0-1 [31]. It depends on the kinetic energy of the particle, the wall temperature of the spacecraft and the surface material properties. For VLEO spacecraft, the accommodation coefficient is generally speaking considered to be 1, due to adsorption and material degradation by AO.

Drag is typically calculated with Equation 2.1.

$$a_{drag} = \frac{1}{2}\rho v^2 C_D \frac{A_{ref}}{m} \tag{2.1}$$

Important to note is that large uncertainties exist in determining the value for the atmospheric density ρ and relative spacecraft velocity v_{rel} in VLEO due to solar activity and thermospheric winds [31]. Moreover, the density greatly varies with latitude/longitude and day/night [33]. These effects disturb the satellite's attitude and should be carefully evaluated in the design of the propulsion and Attitude and Orbit Control Subsystem (AOCS).

Isolating all design parameters in Equation 2.1 leads to the definition of the ballistic coefficient β_{bc}:

$$\beta_{bc} = \frac{m}{C_D A_{ref}} \tag{2.2}$$

From a study conducted in 2023, it was found that the drag coefficient C_D decreases as the orbital altitude decreases, while the drag itself increases due to an increasing atmospheric density [34]. This

again highlights the importance of considering drag in low orbits and challenges the validity of a free molecular flow below $130\,\mathrm{km}$. The study considered both frontal drag as well as lateral side drag to find an optimal drag minimization strategy and concluded that this required a combination of shape optimization and lateral side smoothing. The shape optimization primarily affects the frontal drag by optimizing the spacecraft's aspect ratio, while lateral side smoothing addresses the accommodation coefficient, which in turn affects the drag coefficient and thus the drag. For the frontal face, a large accommodation coefficient is preferred while for the lateral side faces, this should be minimized [34]. Generally speaking, a low accommodation coefficient is achieved by using smooth surface materials. The reason for the difference in drag minimization strategy is the fact that, as the accommodation coefficient increases, the drag coefficient increases at small angles of attack (lateral side faces), while it decreases for large angles of attack (frontal face). In conclusion, drag minimization is most efficiently achieved by a combination of geometry optimization and material choice.

Optimized satellite geometries were found to extend the lifetime of the spacecraft by an additional 13% compared to a slender body geometry [31][35]. The proposed geometry includes a tail that occupies 25% of the satellite's total length. Longer tail lengths were found to negatively affect the drag due to increased frontal area to keep the same volume.

Aerodynamic Attitude Control

Atmospheric particle impacts not only result in orbital decay, but can also be used to the advantage of spacecraft stabilization as well as attitude and formation flight control [36][37][38]. Aerodynamic stabilization is acquired by the positioning of aerodynamic surfaces behind the spacecraft's center of gravity [39]. Pointing maneuvers by aerodynamic control surfaces are proven feasible, though they are limited by settling time and range [40]. This method was also found to be insufficient in the case of chaotic motion, which is caused by a combination of aerodynamic, gravitational and magnetic torques [36]. Therefore, 3-axis active attitude control is still required for controlled operations [40]. Another study proposed the use of deployable solar arrays as aerodynamic actuators to support the internal momentum devices [37]. The study numerically validated the use of four control surfaces complementing reaction wheels, which saturate quickly due to aerodynamic torques, for course attitude pointing in presence of inaccurate environmental modeling [39][40]. This method could greatly benefit spacecraft operations in VLEO, especially in case of actuator failure, volume limitations or large aerodynamic torques. To date, aerodynamic attitude control has been demonstrated by means of differential drag for collision avoidance [39]. Also, the HIBARI satellite has demonstrated attitude control by means of shape variations in LEO, performing a $15\,^\circ$ attitude change in $10\,\mathrm{s}$ [41]. Moreover, aerodynamic attitude control for trimming and momentum dumping has been demonstrated by MagSat [39].

The use of differential drag for formation deployment and maintenance has been demonstrated by two AeroCube-4 satellites as early as 2013 [42]. For such formations, it was shown that, even though orbital decay cannot remain completely unaffected by maneuvers, geometry optimization could improve lifetime by 12% compared to a reference satellite, GOCE (Gravity field and Ocean Circulation Explorer), while generating differential drag (in-plane) and lift (out-of-plane) forces to alter the formation [38].

Research was also conducted on material properties for attitude control in VLEO. Study results show that for a diffuse reflecting material, a reduction in accommodation coefficient is the most effective way to increase the available lift forces [38]. Though, these forces remain an order of magnitude lower than the drag and thus do not yet provide an efficient means of attitude control [39]. Specular reflection, however, is more powerful. This namely allows for selective optimization of lift and drag, thereby enhancing lifetime extension and aerodynamic attitude control via differential drag. For this reason, specular reflective materials are an active area of research.

Atomic Oxygen

Atomic Oxygen (AO) is formed under the influence of UV (Ultra Violet) radiation, which dissociates the covalent bond in the oxygen or ozone molecule [43]. Due to the increased mean free path with altitude, less recombination takes place, leading to the persistence of AO in VLEO. As AO forms under UV influence, AO density thus peaks in sunlit conditions with an optimum at 3 P.M. due to the heated co-rotating atmospheric buldge [44]. Depending on the altitude, inclination, mission duration, solar activity and AO thermal velocity, a satellite encounters a certain amount of AO throughout its mission lifetime.

Due to the co-rotating buldge, the anti-solar facing sides encounter 25% more AO than the sunlit faces of the spacecraft.

The presence of AO at VLEO altitudes contributes to the degradation of the satellite's exterior [29]. Such degradation is two-fold: firstly, the atomic oxygen breaks the organic bonds within polymers and either adheres or causes oxidative erosion/outgassing [43]. Secondly, AO induces oxidation in metals, which is especially destructive when the oxidation layer is porous so that oxidation can progress. Ceramics on the other hand are AO resistant. Changes in the material's surface characteristics such as roughening due to erosion affect its thermal and reflective properties, typically reducing spacecraft performance. An example was described in Subsection 2.2.2, where advantageous specular properties degrade due to AO erosion, resulting in diffuse reflections. Moreover, oxidation can lead to deposit of outgassed and eroded products on for example optical surfaces, blocking the view [44]. Deposited products can in turn also change surface characteristics such as reflectance and thermal performance. The addition of a thin film protective layer, modification of the polymer surface and alternative polymers containing metals are the three most common methods used to mitigate AO-related risks. The protective layer contains metals that form a dense oxide layer. However, damages to the film which cut through the film thickness form a starting point for undercutting oxidation. The application of leveling coatings underneath the film enhances thin film performance and comes with the additional advantage of improved specular reflectance. The second mitigation measure, polymer surface modification, is achieved by insertion of metals or silicons. The effectivity is related to the amount of inserted atom in the material. Downsides of this method include increased density and more complex procurement. The third method uses the same principle, but is not limited to the polymer surface.

MISSE (Materials International Space Station Experiment) and PEACE (Polymers Erosion And Contamination Experiment) are two examples of material experiments that started in 2001 [45]. 41 polymers were positioned on the ISS's (International Space Station) exterior and retrieved almost $4\,\mathrm{years}$ later. Important findings were that erosion can occur in underlying materials even though the surface is structurally intact. Moreover, erosion could lead to free particles that could induce contamination on other surfaces. Also, oxide ash on the eroded surface protects it from further erosion.

The MDM (Material Degradation Monitor) and MDM-2 experiments onboard SLATS (Super Low-Altitude Test Satellite) and the ISS respectively, exposed 11 different materials to the VLEO environment at different altitudes [46]. In ISS-orbit, at $400\,\mathrm{km}$ altitude, the AO fluence was calculated to be $1.3 \cdot 10^{21} \mathrm{atoms/cm^2}$ to $2.1 \cdot 10^{21} \mathrm{atoms/cm^2}$ at an UV irradiance of $98\,\mathrm{ESD}$. Under these conditions, specific MLI's (Multi-Layer Insulation) (silsesquioxane containing coated polyimide film, polysiloxane-block polyimide films, an indium tin oxide-coated polyimide film, and a Beta Cloth) and flexible ORS' (Optical Solar Reflectors) were found to have a high AO resistance (based on mass loss and thermo-optical properties). Also, the films that contained silicon (Si) (silsesquioxane containing coated polyimide and polysiloxane-block polyimide) were found to form a dense, protective silica layer, although the thickness of this layer was different but unrelated to their Si density. On the other hand, films containing a silver (Ag) coating performed not as good, due to oxidation of the Ag and formation of a porous layer. Moreover, cracks were noticed on the silsesquioxane containing coated polyimide film. The crack formation process is a result of shrinkage due to the removal of methyl groups, leading to a silicone-silica conversion [44]. Thus, attention should be given to the materials and constituents when opting for a certain coating.

Plasma

Another concern in low orbits is charge buildup, either at the spacecraft surface or internally. Spacecraft charging and Electro Static Discharge (ESD) events respectively, are a result of the interaction between the satellite and space plasma [47]. ESD imposes risks on the satellite and was even found to be the most commonly reported anomaly related to the space environment [48]. The implementation of a Faraday Cage around vulnerable systems enhances resistance against ESD [49]. Another mitigation measure is designing the power supply to be able to cope with temporary shorts and high voltage breakdowns in case of an ESD event [50]. Lastly, robust grounding of the spacecraft reduces internal electron leakage and thus charge buildup [49].

The use of Electric Propulsion (EP), discussed in Subsection 2.2.3, introduces additional risks in terms of plasma interaction [51]. The dense exhaust plasma could namely backflow to the solar arrays, thereby increasing electron flow and reducing the array's potential, which could lead to arcing between

spacecraft components. This, in turn, could damage the solar array circuitry and even lead to total loss of solar power. The solar arrays could be protected by maximizing the physical distance to the exhaust plume, adding insulation and preventing the use of high voltage solar arrays [51][49]. Moreover, the plasma plumes could scatter radio signals, leading to unreliable communication [52]. Reducing or interrupting thrust during communication windows is one obvious mitigation measure for this risk.

2.2.3. Propulsion

To increase mission lifetime, propulsion is of the essence, as was concluded in Subsection 2.2.2. Propulsion strategies can be either continuous or periodic, for example based on solar power availability or payload operations [39]. In VLEO, Electric Propulsion (EP) has been widely studied for its high specific impulse. For a $27\,\mathrm{U}$ CubeSat with a frontal area of $0.09\,\mathrm{m}^2$ and a drag coefficient of 2.2 (a typical value for satellites) in VLEO ($400\,\mathrm{km}$), continuously counteracting drag would require roughly $0.18\,\mathrm{mN}$ of thrust (this is an estimation as atmospheric density is highly variable over time) [53]:

$$F_{drag} = \frac{1}{2}\rho v^2 C_D A \tag{2.3}$$

$$F_{drag} = \frac{1}{2}\cdot 3\cdot 10^{-11}\left(\sqrt{\frac{6.7\cdot 10^{-11}\cdot 6\cdot 10^{24}}{6.8\cdot 10^{6}}}\right)^2 \cdot 2.2\cdot 0.09 = 1.8\cdot 10^{-4} N$$

For a $5\,\mathrm{year}$ mission with chemical propulsion (average specific impulse, I_{sp} of $300\,\mathrm{s}$), $9.4\,\mathrm{kg}$ of propellant would be required to counteract the drag [54]. This is almost 20% of the maximum mass for a 27U CubeSat. For an electrical propulsion system with an average I_{sp} of $3000\,\mathrm{s}$, propellant mass would only be $0.94\,\mathrm{kg}$. Thus, a higher specific impulse directly reduces propulsion subsystem mass. A study on microsatellites concluded that for a $5\,\mathrm{year}$ mission at $300\,\mathrm{km}$ during high solar activity, I_{sp} must be at least $1000\,\mathrm{s}$ for a feasible design while during solar minimum, >$230\,\mathrm{s}$ would suffice [55]. This then implies that cold gas thrusters for this application are not deemed feasible at all, and monopropellant and resistojet thrutsers only conditionally.

There are several types of EP for spacecraft applications. The most common and relevant ones are briefly elaborated on here. A novel propulsion method, Atmosphere-Breathing Electric Propulsion (ABEP), is described in more detail due to is great potential for VLEO missions specifically.

Electrostatic Thrusters

Electrostatic thrusters are characterized by an electric field in the direction of the ion acceleration that finally results in thrust [56]. In a gridded ion thruster, propellant is ionized in a discharge chamber to form a plasma, consisting of ions and electrons. The ions are then accelerated by a potential difference between two grids. A neutralizer is used to expel electrons and prevent charge buildup in the satellite. A miniaturized version of this thruster, the RIT-μX engine, delivers $500\,\mu\mathrm{N}$ of thrust with a specific impulse of $900\,\mathrm{s}$, provided a nominal power of $50\,\mathrm{W}$.

An Hall-effect thruster (HET) is also commonly integrated in space systems and uses an electric field for plasma acceleration [56]. However, this type of thruster does not use grids, as the thrust generation is controlled by electromagnetic fields. Electrons from the cathode are attracted to the anode due to the electric field, but are trapped by a radial magnetic field. The resulting spiral motion generates a Hall current at the thrusters exit. This Hall current is responsible for the propellant ionization. The ions are then accelerated by the electric field to produce thrust. Neutralization of the ion beam is provided by the cathode as well. Channel wall erosion due to impacting ions is the biggest challenge for HETs. Addressing the issue of channel wall erosion, the cusped field thruster has a modified magnetic field. This field decelerates and reverts the charged particles near the wall and thereby reduces the erosion effectively. A cylindrical Hall thruster with a diameter of $26\,\mathrm{mm}$ developed at the Space Flight Laboratory produced $6.2\,\mathrm{mN}$ of thrust with $200\,\mathrm{W}$ of power and a specific impulse of $1139\,\mathrm{s}$ [57]. Downscaling cusped field thrusters, however, revealed low ionization efficiencies and plume divergence.

Electrothermal Thrusters

Electrothermal thrusters such as arcjets, resistojets and microwave thrusters heat up the plasma [56]. The thermal energy is then converted into kinetic energy, resulting in thrust. The specific impulse of such systems is generally speaking relatively low, usually in the order of $100\,\mathrm{s}$ compared to over to $1000\,\mathrm{s}$ for other types of EP [58]. Therefore, these systems are less suitable for VLEO purposes.

Electromagnetic Thrusters

A third type of EP makes use of Electro-Magnetic (EM) fields and the Lorentz force to accelerate a propellant [56]. EM thrusters eliminate the need for a neutralizing cathode, improving system complexity and reducing system mass. Various types of EM propulsion systems exist, some of which do not use electrodes to generate an electric field. As electrode erosion is one of the main challenges for EP (especially for atmosphere-breathing propulsion, discussed below), the electrodeless alternative effectively mitigates the risk of system deficiencies [59].

Differences between the EM thruster types are based on propellant origin, geometry and Lorentz force generation. The ablative pulsed plasma thruster, for example, produces gaseous propellant by means of ablation, while other systems already carry propellant in gaseous state [60]. The thruster creates Lorentz forces by arcs between two electrodes, which generate a magnetic field. Two geometries of ablative pulsed plasma thrusters exist: parallel plates and coaxial ones. The electrodeless inductive pulsed plasma thruster generates and EM field through current pulses in an inductor [61]. This field then drives current in a plasma resulting in a Lorentz force which accelerates the plasma to produce thrust. Magnetoplasmadynamic thrusters on the other hand, accelerate propellant with the Lorentz force through a cathode-anode and a current-induced or externally applied magnetic field [62]. Combinations and variants of the aforementioned types also exist. Experimental performance characteristics of some electromagnetic thrusters are summarized in Table 2.1. One can observe a wide variety of specific impulses from about $300\,\mathrm{s}$ to far beyond $3000\,\mathrm{s}$ as well as thrust and power which range between about $3\,\mathrm{mN}$ to $850\,\mathrm{mN}$ and $0.1\,\mathrm{kW}$ to $25\,\mathrm{kW}$ respectively. Higher thrust is generally speaking associated with higher required power.

Table 2.1: The experimental performance characteristics of some electromagnetic thrusters

Thruster type	Specific impulse	Thrust	Power
Magnetic nozzle enhanced magnetoplasmadynamic thruster [63]	$2356\,\mathrm{s}$	$485\,\mathrm{mN}$	$22\,\mathrm{kW}$
Applied field magnetoplasmadynamic thruster [64]	$3840\,\mathrm{s}$	$850\,\mathrm{mN}$	$25\,\mathrm{kW}$
Electrodeless RF thruster [65]	$1350\,\mathrm{s}$	$6.2\,\mathrm{mN}$	$0.44\,\mathrm{kW}$
RF plasma thruster [66]	$303\,\mathrm{s}$	$10.8\,\mathrm{mN}$	$2\,\mathrm{kW}$
Electrodeless helicon plasma thruster [67]	$380\,\mathrm{s}$	$3.3\,\mathrm{mN}$	$0.13\,\mathrm{kW}$
Permanent magnet helicon plasma thruster [68]	$2000\,\mathrm{s}$	$15\,\mathrm{mN}$	$2\,\mathrm{kW}$

Atmosphere-Breathing Electric Propulsion

All of the aforementioned propulsion methods, however, make use of a propellant that must be carried on-board. Therefore, Atmosphere-Breathing Electric Propulsion (ABEP) is an interesting concept. ABEP uses the atmospheric particles to generate thrust and thereby counteract the drag induced by these same particles. This method thus eliminates the need for a propellant tank [69]. ABEP has great potential in VLEO, where there is significant residual atmosphere to replace the on-board propellant. This specific concept has been investigated in several studies. Some of which are discussed below.

The RF helicon-based inductive plasma thruster is a novel type of ABEP. Its schematic can be seen in Figure 2.1 [59]. This thruster was the main focus of the EU-funded DISCOVERER project and will increase TRL under the ESA RAM-CLEP project [59][69]. The intake of this thruster collects the atmospheric particles, which are then fed to the thruster. In the RF helicon-based inductive plasma thruster, the particles are ionized and accelerated using Radio Frequency (RF) waves for EM fields that are generated by a cylindrical, directive birdcage antenna. Compared to other antennae, a cylindrical, directive birdcage antenna has a low power consumption, as this antenna is operated at resonance condition. Moreover, birdcage antennas allow for EM field configuration. This capability is used to accelerate the quasi-neutral plasma plume by inducing a drift velocity for both ions and electrons in

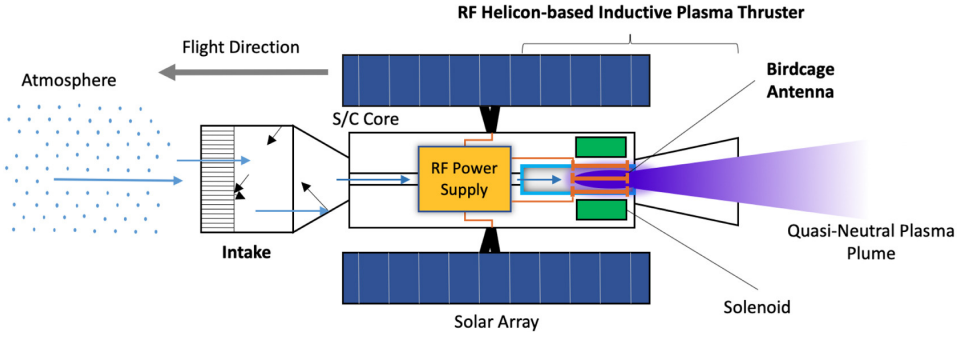

Figure 2.1: A schematic of an RF Helicon-based Inductive Plasma Thruster [59]

the same $\vec{E}$x$\vec{B}$ direction [59]. A solenoid around the discharge channel is used to generate a static field that ensures the formation of helicon waves within the plasma. These waves increase plasma density and improve power absorption of this propellant [70]. The fact that no electrodes are necessary enhances system compatibility with the residual atmospheric particles, especially AO, which induces significant erosion. Atmospheric compatibility is also enhanced by this thruster's flexibility with regard to propellant density and composition [69]. Another advantage of this concept is that the plasma exhaust is quasi-static, as both ions and electrons are present in the flow [59]. Therefore, there is no need for a neutralizer. On the downside, this thruster suffers from a lower demonstrated thrust efficiency (0.2-0.25) compared to current EP options due to immaturity. A laboratory prototype with a discharge channel diameter of $37\,\mathrm{mm}$ operated at $40.68\,\mathrm{MHz}$, requiring $50\,\mathrm{W}$ to $150\,\mathrm{W}$, and produced the expected thrust at mN-level with an estimated efficiency of 0.2 [69].

Next to the RF helicon-based inductive plasma thruster, other inductive plasma thrusters (not based on helicon waves) were studied for VLEO applications. An inlet area of $1\,\mathrm{m}^2$ and available power in the range of $2.2\,\mathrm{kW}$ to $3.5\,\mathrm{kW}$ was shown to provide complete drag-compensation at an altitude of $180\,\mathrm{km}$ to $200\,\mathrm{km}$ for a conceptual satellite [71]. Another study applied geometry optimization and could thereby reduce the intake area to $0.25\,\mathrm{m}^2$ to $0.4\,\mathrm{m}^2$. Similarly to the RF helicon-based inductive plasma thruster, this method of propulsion is electrodeless and thus avoids erosion limited lifetimes. Also, there is no need for an additional neutralizer.

Ion thrusters for ABEP were studied as early as 2003 [71]. Focus lied on the use of an electron cyclotron resonator for ionization purposes. Grids induced ion acceleration and a neutralizer was required for charge balancing. The concept was deemed promising due to the expected possibility of operation at lower pressures. $0.13\,\mathrm{mN}$ was experimentally achieved for a power of $60\,\mathrm{W}$.

Research in atmosphere-breathing Hall-effect thrusters was also conducted [72][71]. The electrodes in this concept are still present and thus limit the thruster's lifetime. A RAM-HET (RAM-EP) was developed by the aerospace company SITAEL and achieved $6\,\mathrm{mN}$ of thrust at the expense of $900\,\mathrm{W}$ of power [64]. However, the concept is not yet found feasible as mission analysis revealed the need for at least $26\,\mathrm{mN}$ of thrust to counteract the drag of the concept satellite. The AETHER (Air-breathing Electric THrustER) project will continue development of this engine. Busek Co. Inc. developed MABHET for Martain exploration specifically. Their thruster produced $70\,\mathrm{mN}$ with $2.2\,\mathrm{kW}$ of power. An HET featuring an extended channel produced $17\,\mathrm{mN}$ at $500\,\mathrm{W}$, due to the elongated ionization zone [73]. In an effort to minimize wall erosion, a cusped plasma ABEP thruster was also investigated [74]. The system allows for a large power range of $0.006\,\mathrm{W}$ to $1300\,\mathrm{W}$ with a peak performance of $13.3\,\mathrm{mN}$ at $997\,\mathrm{W}$. HET implementation on system level has also been analyzed: A 2-stage cylindrical Hall ABEP system at $200\,\mathrm{km}$ altitude on a $0.5\,\mathrm{m}^2$ spacecraft required $1\,\mathrm{kN}$ of power for operations, whereas another analysis concluded a required power of $306\,\mathrm{W}$ for a frontal area of $0.36\,\mathrm{m}^2$ and system mass of $325\,\mathrm{kg}$ [71].

Research was also focused on atmosphere-breathing magnetoplasmadynamic thrusters [75][76]. A thrust of $0.015\,\mathrm{mN}$ was gained from $1.86\,\mathrm{W}$ of power. However, significant erosion at the anode was observed due to the interaction with the high temperature plasma. Dense plasma focus is a propulsion method similar to magnetoplasmadynamic, only having reversed polarity and a slightly different geometry [64]. This thruster also efficiently functions on micro-scale and inspired the development of

an ABEP pulsed plasma thruster, which demonstrated a superior thrust density with a thrust of $4.8\,\mathrm{mN}$ with a power of $0.17\,\mathrm{kW}$. Another study that analyzed a pulsed plasma thruster estimated $4.4\,\mathrm{mN}$ for a mass flow of $1\,\mathrm{mgs}^{-1}$ and a power density of $30\,\mathrm{mNkW}^{-1}$. Though, electrode erosion, high voltage and mass combined with low specific impulse are disadvantages of this system.

Atmospheric intake is essential to the thrusting capabilities of ABEP and has been widely studied [77]. Different parameter combinations can lead to an optimal design [78][79][80]. A specular and diffuse intake were recently compared [69]. The specular intake considered had a parabolic shape. It was found that this intake is less sensitive to flow misalignment, but more to material degradation over the mission lifetime compared to the diffuse intake, which consists of an hexagonal longer straight section followed by a converging one. The diffuse intake also featured small ducts to trap particles and increase the intake efficiency. In general, a specular intake is preferred over a diffuse one, as represented by their intake efficiencies of 0.94 and 0.46 respectively [81]. The choice of material was therefore found to be essential to the intake efficiency. Moreover, a strong dependency between intake efficiency and intake length was noticed as a result of thermal velocity in the flow (the flow is hypothermal: it cannot be considered collimated (hyperthermal) and thus, also shaded parts of the spacecraft are subject to drag [31]), which significantly affected the efficiency of the specular intake. This might imply that a parabolic intake is not optimal in practice [69].

Another novel intake concept includes the combination of 'variable aspect ratio ducts' with a conical geometry for collection efficiency as well as drag reduction [82]. The collection efficiency is enhanced by the implementation of smaller ducts towards the outer perimeter, as thermal backflow from the walls is expected and this way, diffusion rather than back-scattering is supported. Furthermore, active intake designs were developed. The use of phase changes is explored to improve intake efficiency in an active cryogenic intake [83]. By condensation of the free-stream gas, the propellant is effectively compressed and thereby, the density is increased. This then improves ABEP performance.

The design of the spacecraft body in combination with the intake area determines the total drag and thus defines the required thrust for a satellite featuring ABEP. A slender body with a single thruster and subsystems surrounding it was compared to a flat body that houses multiple thrusters in line with their subsystems in the slipstream [69]. The flat body was found to excel in specific impulse as well as required power. Moreover, a study on the critical parameters for feasibility and advantage of air-breathing electric propulsion systems revealed that ABEP feasibility increases with reducing spacecraft dimensions when considering mass and volume [84].

For ABEP, there exists an optimal altitude [28]. This altitude balances the atmospheric density and thus mass flow and thrust with the drag caused by the increase in intake area. A concept study on a $200\,\mathrm{kg}$ spacecraft found an upper altitude limit of $193\,\mathrm{km}$ due to atmospheric density [85]. Analysis of this concept during medium to high solar activity led to stable long-term orbit at altitudes of $160\,\mathrm{km}$ to $183\,\mathrm{km}$ by the use of gridded-ion ABEP. Another study found that an altitude of $150\,\mathrm{km}$ would require too much power to counteract the drag and lead to excessive spacecraft heating in times of low solar activity [86]. The same study noted an upper limit of $250\,\mathrm{km}$ as a result of atmospheric density. A third study on ABEP flight envelopes found that a radio-frequency ion thruster could successfully compensate drag from $196\,\mathrm{km}$ to $248\,\mathrm{km}$ [87]. Altitude also significantly influences the intake discharge power, circling back to intake design [28].

Even though ABEP is a very promising concept, it is also still an active area of research and has not fully matured yet. With successful laboratory demonstrations of several thrusters in space-like environments, its TRL is currently at 6. A study on ABEP revealed that advancements in inlet efficiency, low drag materials, solar array efficiency and thrust-to-power will significantly boost technology maturity for VLEO missions [88].

Electrodynamic Tethers

Another disruptive propulsion concept makes use of the interaction between a conducting tether carrying a current and a planetary magnetic field [89]. The combination induces a Lorentz force that can be used for propulsion. Insulated tethers require a significant length of $40\,\mathrm{km}$ to provide sufficient propulsive forces. Bare tethers on the other hand, promise a great length reduction. This concept is planned for in-orbit demonstration by the E.T.PACK mission in 2025, where it will facilitate a passive deorbit with a tether length of $500\,\mathrm{m}$.

Power Requirements and Orbit

The power required by electric propulsion could imply the need for deployable solar panels. In order to enhance mission lifetime, these panels are preferably aligned with the spacecraft's velocity vector. Depending on the spacecraft's orbital position, however, this might contradict the preference to point the solar panels towards the Sun. A study on this subject found that a minimum drag configuration implies a reduction of the available power of at least 1-12% (Dusk-Dawn), up to 47% in the worst case (Noon-Midnight) [90]. A Dusk-Dawn Sun-Synchronous Orbit (SSO) yields the best performance in this case. However, it should be noted that this orbit does not provide the optimal temporal resolution [28] (see Subsection 2.2.1). It was also concluded that the optimum strategy would be to keep the solar panels aligned with the velocity vector due to the significant drag penalty imposed by the atmospheric particles in Sun-pointing mode [90]. This conclusion is supported by the fact that a Dusk-Dawn SSO already minimizes cosine loss of solar power [39]. However, eclipse time in this orbit increases with reducing altitude.

As touched upon in Subsection 2.2.2, the orbit also affects observation and communication time. More specifically, the higher ground velocity in VLEO challenges observations and data transmission. These effects must be considered in the satellite design, especially when aiming for a constellation where different orbital planes apply. Next to circular orbits, also the use of elliptical orbits can be considered to balance VLEO ad- and disadvantages. An elliptical orbit between $150\,\mathrm{km}$ to $250\,\mathrm{km}$ has been numerically validated for a mission concept using ABEP and on-off control [91]. In combination with constant thrust, the argument of perigee could be kept constant over time. However, optimal intake at perigee combined with optimal orbit maintenance at perigee and suboptimal thrust efficiency during intake results in contraindicating requirements. Therefore, the 'in-orbit balance' strategy was proposed [92]. Following this method, some elliptical orbits are used for intake whereas others contain a thrusting maneuver. Nevertheless, an elliptical orbit greatly affects observations which are of primary concern in the mission design and thus, a circular orbit is preferred.

To summarize, spacecraft in VLEO require propulsive thrust throughout their lifetime for orbit maintenance. Electric propulsion is the most feasible candidate for VLEO propulsion due to its high specific impulse, whereas monopropellant thrusters were found to only suffice in solar minimum conditions. Moreover, ABEP offers great potential by eliminating the need for on-board propellant, but suffers from a low TRL. Several types of EP have been successfully tested with atmospheric propellant. Their experimentally determined performance characteristics are summarized below. One must note that specific impulse and thrust heavily depend on particle density and intake efficiency and thus, these numbers only serve as an indication for in-orbit performance.

Table 2.2: The experimental performance characteristics of ABEP systems

Thruster type	Thrust	Power
RF helicon-based inductive plasma thruster	$1\,\mathrm{mN}$	$0.05\,\mathrm{kW}$ to $0.15\,\mathrm{kW}$
Inductive plasma thruster	-	$2.2\,\mathrm{kW}$ to $3.5\,\mathrm{kW}$
Ion thruster	$0.13\,\mathrm{mN}$	$0.06\,\mathrm{kW}$
Hall-effect thruster	$6\,\mathrm{mN}$	$0.9\,\mathrm{kW}$
Martian Hall-effect thruster	$70\,\mathrm{mN}$	$2.2\,\mathrm{kW}$
Cusped plasma thruster	$17\,\mathrm{mN}$	$0.5\,\mathrm{kW}$
Magnetoplasmadynamic thruster	$0.0015\,\mathrm{mN}$	$0.001\,86\,\mathrm{kW}$
Pulsed plasma thruster	$4.8\,\mathrm{mN}$	$0.17\,\mathrm{kW}$

2.2.4. Concepts and Missions

This section provides an overview of several concepts designed for VLEO and missions conducted in this region. The aim of this section is establishment of common practices and possible improvements to guide the design of the foreseen mission.

Table 2.3 provides an overview of some concept studies for VLEO, along with some mission parameters. The lifetime of the analyzed concepts ranges from $2\,\mathrm{years}$ to $7\,\mathrm{years}$, where a shorter lifetime is generally associated with lower operational altitudes. The table also presents a wide variety in spacecraft mass. Moreover, all missions make use of EP and the far majority foresees the use of ABEP.

Table 2.3: Some VLEO satellite concepts along with their mission parameters

Ref.	Lifetime	Orbital altitude	Mass	Propulsion
[93]	5 years	280 km to 300 km	300 kg	Gridded ion engines
THOR [94]	5 years	227 km		Electric propulsion
DMC-HD [94]	5 years	315 km		Electric propulsion
Skimsat [95]	2 years	160 km	75 kg	RF ion ABEP
[47]	7 years	160 km to 230 km	1138 kg	ABEP
[96]	7 years	200 km to 250 km	1000 kg	RAM-EP
[97]		200 km		Cylindrical Hall-effect ABEP
[98]	3 years	200 km	325 kg	RF plasma ABEP
[99]		90 km to 95 km		Hall-effect ABEP
[100]	2 years	170 km		Ion ABEP

The concepts in Table 2.3 also revealed several challenges. These challenges are briefly summarized below:

- Geometry is mostly driven by drag minimization and the need for propulsion.
- Imaging payloads need shielding form AO.
- Communication windows are limited due to the increased ground speed. One study found that transmission via geostationary spacecraft was more cost-effective than direct transmission to ground [94]. However, the currently available Inter-Satellite Data Relay System by Addvalue only supports data rates up to $200\,\mathrm{kbps}$ [1].
- Atmospheric particles affect the aerostability, leading to attitude change resistance, hence increased AOCS requirements.
- Forecasting space weather proves to be challenging, but is essential to predict radiation events and the subsequent damage.

Another interesting concept mission focused on ADCS (Attitude Determination and Control Subsystem) design for a 6U CubeSat (see Section 2.3) flying at an altitude of $230\,\mathrm{km}$ [101]. The 6U CubeSat, called 'Stable and Highly Accurate Pointing Earth-Imager' (SHAPE), houses a momentum bias wheel and magnetorquers. Pointing accuracy is $<1\,°$ with an instability of $<0.1\,°$. The magnetorquers achieve a detumbling rate of $35\,°\mathrm{s}^{-1}$.

Also, several missions have already flown in VLEO. One of these is SLATS, a mission conducted by JAXA (Japan Aerospace eXploration Agency) and launched in 2017 [102]. The spacecraft flew at altitudes of $180\,\mathrm{km}$ to $250\,\mathrm{km}$ to measure the atmospheric density and investigate the effects of AO in VLEO. The satellite had a wet mass of $383\,\mathrm{kg}$ and an operational lifetime of $2\,\mathrm{years}$, enabled by ion engines. The latter consumed $370\,\mathrm{W}$ of power to provide $10\,\mathrm{mN}$ of thrust. The satellite was equipped with a Next-generation Star Tracker for attitude determination with an accuracy of $<4\,\mathrm{arcsec}$ random and $<6\,\mathrm{arcsec}$ bias. This sensor has a mass of $<6.2\,\mathrm{kg}$ and consumes $<20\,\mathrm{W}$ of power.

SOAR (Satellite for Orbital Aerodynamics Research) is a 3U CubeSat (see Section 2.3) with a mass of $3.4\,\mathrm{kg}$ and was launched in 2021 [103][104]. This satellite tested the aerodynamic performance of four materials in VLEO [103]. For this, it exploited the aerodynamic attitude control strategies introduced in Subsection 2.2.2. Four steerable fins containing different materials were used to induce a torque and measure the attitude response to derive the lift and drag coefficients. Moreover, SOAR could measure atmospheric characteristics such as density and composition. For attitude determination, the system featured an IMU (Inertial Measurement Unit), fine Sun sensors and magnetometers. Attitude control was allowed by a reaction wheel assembly and magnetorquers. A GPS (Global Positioning System) was used for orbital position and velocity determination. The spacecraft reentered after $9\,\mathrm{months}$ of operation [104].

[1] `https://www.idrsspace.com/technology`

GOCE, the Gravity field and steady-state Ocean Circulation Explorer, aimed at measuring Earths gravity field and flew at an altitude of $250\,\mathrm{km}$ [105]. The mission was launched in 2009 and required very precise positioning, which was achieved with the Drag-Free and Attitude Control (DFAC). This system was composed of redundant ion thrusters (gridded ion engines) for drag compensation, three internally redundant magnetic torquers for 3-axis control and an internally redundant cold-gas thruster for calibration purposes [106]. Electric thrusters were considered but got rejected for their low TRL at the time. The sensor pack consisted of a gravity gradiometer for linear and angular acceleration measurements, redundant GPS receivers, six heads for coarse Earth and Sun sensors, two digital Sun sensors and three star tracker units for attitude determination. Successful operation of the spacecraft was confirmed and led to a mission extension until 2013, which defined the end of operations due to depletion of the propellant.

To conclude, VLEO presents several advantages over higher obits, the most important one being the improved spatial resolution. However, several aspects require careful consideration when designing for VLEO:

- Ground coverage as well as temporal resolution in VLEO is negatively affected compared to LEO. Constellation deployment could compensate for this.
- Ground speed in VLEO is increased. This affects observations as well as the communications. Thus, extra attention must be paid to payload requirements and data transfer.
- Position knowledge requirements increase with reducing altitude and thus flow down into more stringent requirements on AOCS.
- Drag reduces mission lifetime significantly if not accounted for by a propulsion system. This system should operate throughout the entire mission lifetime and increases satellite mass and volume. Drag also challenges attitude control. Geometry optimization and material selection were found to be critical for drag minimization. Especially the development of specular reflecting materials has great potential. A rear tail could further enhance aerodynamic performance.
- Propulsion and AOCS design suffer from very complex atmospheric modeling in VLEO due to large uncertainties and variations in atmospheric density and composition.
- Atomic oxygen in VLEO degrades exposed materials and could lead to contaminant deposition on critical surfaces such as optical lenses. Application of a thin film protective layer which contains for example silicon could mitigate such risks.
- Plasma that is present in VLEO or results from EP could induce charge buildup in the satellite. Integration of a Faraday Cage and designing the power subsystem accordingly is therefore important.
- Orbit design in VLEO is challenged by several contradicting requirements coming from payload, communications, power and aerodynamics, calling for a careful trade-off.

Nevertheless, VLEO presents interesting opportunities such as aerodynamic attitude control (even though it was concluded that additional 3-axis attitude control is still required) and atmosphere-breathing electric propulsion. This literature review discussed the most promising concepts in these fields. These novel concepts could enhance feasibility of spacecraft in VLEO.

2.3. Satellite Bus Volume Optimization

For the proposed mission, satellite bus volume optimization is of significant importance. Not only does a small volume enhance drag requirements on the spacecraft, it also maximizes the available payload volume, reduces launch cost and facilitates constellation deployment. Bus volume can be reduced in two ways: subsystem miniaturization and smart subsystem integration. This section first expands on different satellite form factors currently in use, followed by an analysis of the research done in the field of miniaturization and smart integration with the aim of satellite bus volume reduction.

2.3.1. Form Factors

CubeSats (units of $10\,\mathrm{cm}$ x $10\,\mathrm{cm}$ x $10\,\mathrm{cm}$ with a maximum weight of $1\,\mathrm{kg}$) have disrupted the satellite market by increasing space access for non-governmental parties such as universities and start-ups

[107]. The fundamental difference compared to traditional satellites is the implementation of standardization, miniaturization and modularity, as each subsystem is represented by one or multiple PCBs (Printed Circuit Board) in a central core stack. This methodology allows for the use of COTS components within the spacecraft, resulting in significant cost reduction and fast delivery [108]. Further developments have led to even smaller form factors such as PocketQubes with a base of $5\,\mathrm{cm}$.

However, the cubical configuration of these satellites has been challenged for its limited surface area. Alternatives such as the DiskSats and HexSats promise high power applications and low mass configurations, with the HexSat providing better packing efficiency for small satellites inside the launcher on top of full 3-axis control [109][108]. The proposed $2.5\,\mathrm{cm}$ thick, flat, stackable HexSats makes use of a distributed micro-propulsion system to operate in VLEO and can support payloads with an average power consumption of $100\,\mathrm{W}$ [108]. The limited thickness of these satellites constrains the payload options and thus, a Disk- or HexSat configuration is not feasible for every mission. As described in Chapter 1, the proposed payload would not fit the aforementioned thickness and thus, this exact concept does not carry over to the mission in question. Moreover, even if the payload could be accommodated, part of the payload is located on the satellite's external face and thus, the stackability advantage of Disk- and HexSats does not necessarily persist.

Nowadays, the CubeSat concept is still widely applied in the space industry and, together with the rise of smaller form factors, supports active research in subsystem miniaturization. This form factor is therefore preferred for the proposed mission. Bus volume optimization within the CubeSat is explored in the following subsections.

2.3.2. Subsystem Miniaturization

One interesting development for bus volume optimization is the miniaturization of subsystems, which has been a key enabler of CubeSats. By making use of embedded systems, advanced materials and microelectronics, subsystems can achieve similar performance for a much lower mass and volume budget. These developments have led to subsystems that fit on a single PCB that can be stacked in a CubeSat.

Miniaturization could also be achieved by relieving requirements, for example on data processing and transmission, to allow for smaller components. A study from 2022 introduced several methods to do so: intelligent perception disregards useless observations (for example, when clouds cover Earth's surface) [110]. Additionally, intelligently processing could be applied to only process variations in observations and disregard all similar information. Implementing these concepts could aid in miniaturization by lowering data rates and thus, expanding the range of component possibilities. For the mission proposed in this thesis, these methods could provide a significant reduction in the amount of data to be transmitted. Once a global map of marine plastic has been constructed, only changes are of interest and all other observations could be disregarded. Thus, implementing intelligent perception and processing would reduce the amount of payload data to be transmitted to Earth, relieving the requirements on transmission rate and potentially allowing for a smaller sized transmitter.

2.3.3. Lean Interfacing

Lean electrical interfaces improve system compatibility by standardizing the electrical interface connector or removing it altogether to become wireless [111]. Delfi C^3 housed a wireless Sun sensor that transmitted data over a radio link and gained its energy directly form the Sun [112]. Furthermore, a self-powered temperature sensor was developed to make use of the thermoelectric energy harvesting concept [113][114]. Important disadvantages of wireless sensors are the potential radio interference with other systems, conditional power source (Sun or temperature gradient), lower TRL and bigger size compared to wired sensors [111]. Wireless sensors are most advantageous in bigger satellites, where the wiring is more complex and adds significant weight. However, in small satellites such as CubeSats, their added value is less and thus, these sensor types are not explored for the proposed mission.

Next to miniaturization and lean interfacing, further volume optimization can be achieved by a different method of subsystem integration. Even though the standardization approach used in CubeSats enhances modularity and thus reduces cost and development time, it does not necessarily lead to a volume-optimized satellite. Therefore, the stacked subsystem configuration has been challenged by several concepts, which are introduced below.

2.3.4. Cellularization

Cellularized satellite architectures, composed of modular satlet units, offer an alternative to traditional CubeSat stacks by emphasizing miniaturization, modularity, and cost reduction [115]. Unlike stacked configurations, single-function satlets reduce single points of failure and enable graceful degradation. This concept also supports in-space assembly and self-reconfiguration, improving launch flexibility [116]. However, these advantages often come at the expense of increased power, mass, and volume.

Several subsystems have been explored for cellularization, with mixed success in optimizing volume. Cellular reaction wheels tested on Delfi-n3Xt demonstrated graceful degradation, lower power consumption and finer control, but implied significant volume penalties [117]. Similarly, solar acquisition units that integrate solar cells and MPPT circuitry successfully improved system scalability and shadow resistance, but increased wiring complexity [118][119][120].

The cellular flat radio is a notable exception, offering volume efficiency by integrating the directional patch antenna and its electronic circuit [118]. Mounted on the satellite's outer panel, it minimizes core stack usage. Omni-directionality and beam steering are feasible through strategic placement and phased-array technology, making it a promising candidate for the proposed mission [121].

Other concepts, such as cellular magnetorquers and Artificial Stem Cells (ASCs), improve system reliability but increase volume and power requirements [118][122]. A Nano-Modular Format (NMF), while simplifying integration by already having all subsystems mounted on the faces in a pyramid shape, constrains geometry and is less suited for volume optimization [123].

In summary, cellularization enhances system reliability, but often compromises volume efficiency. For the proposed mission, the cellular flat radio stands out as a viable option, while other applications require careful trade-offs due to their volume-related disadvantages.

2.3.5. Smart Subsystem Integration

Integration of different subsystems into a single PCB within the core stack offers significant volume optimization benefits, reduces power requirements and shortens integration time [124]. For instance, BeEagleSat's OBCOMS board houses both the On-Board Computer (OBC) and a beacon modem [125]. Extending this concept, critical subsystems like power conversion, monitoring, and Maximum Power Point Tracking (MPPT) could also be integrated alongside the OBC. Additional sensors such as MEMS (Micro-ElectroMechanical System) units and magnetometers may be included, though mission requirements could limit standardization and scalability [118].

Another approach involves advanced integrated outer panels that combine cellular, NMF, and smart integration concepts without consuming internal volume. These panels incorporate external-facing subsystems like solar cells, MPPTs, antennas, and attitude sensors, retaining ease of integration while minimizing volume [118]. Multi-functionality further supports volume reduction. Shared use of transmission systems and antennas for SAR and data signals, or leveraging a single microcontroller for both OBC and attitude control, exemplifies this approach [118][126]. However, compatibility and interference issues must be carefully addressed [110].

Extreme miniaturization as seen in ChipSats pushes volume optimization to its limits [127]. These spacecraft, sized like computer chips ($3.5\,\mathrm{cm}$ x $3.5\,\mathrm{cm}$), enable cost-effective swarm deployments [128]. However, their limited payload capabilities make them unsuitable for missions requiring larger instruments such as the marine plastic monitoring with a foreseen aperture of $20\,\mathrm{cm}$ to $40\,\mathrm{cm}$ (see Chapter 1).

In conclusion, CubeSat platforms emerge as the most feasible option for the proposed mission, balancing volume optimization and payload capacity. For marine plastic debris monitoring specifically, intelligent perception and processing could aid in minimizing the volume for data processing and transmission. A cellular flat radio and advanced integrated outer panel are also of particular interest. Cellularization, lean interfacing, and mission-specific trade-offs between modularity and smart integration are key to achieving an efficient design.

3

Problem Statement

This chapter details the problem that is fundamental to this thesis. In Section 3.1, a research gap is identified which reveals the need for this study. The next section then derives the research question and subsequent sub-questions that this thesis aims to answer.

3.1. Research Gap

From Chapter 2, one can conclude that a mission dedicated to marine plastic debris monitoring will significantly improve the available data on this matter. An improved dataset in terms of spatial and temporal resolution allows for better understanding of the problem at hand and will enhance solution strategy development.

Moreover, it became clear that VLEO presents great characteristics for such mission. Primarily, it improves spatial resolution without increasing payload size. Combining this with the implementation of deployable optics reduces spacecraft volume. Volume reduction was not only found to aid launch cost reduction, constellation deployment and thus temporal resolution, it is also critical to a mission in VLEO in terms of drag management as noted in Subsection 2.2.2. The increased drag in VLEO namely presents one of the key challenges of this mission. It is expected to size the AOCS and propulsion subsystem and negatively affect their volume budgets.

Lastly, recent developments in subsystem smart integration offer further volume budget-optimization possibilities, reducing launch cost and supporting constellation deployment. However, several methods were identified and combinations of these were also proposed. Therefore, the final configuration depends on the mission and should be carefully traded off.

In conclusion, absence of a dedicated mission for marine plastic debris monitoring limits our solution development. With research already being done on the payload for such mission (see Section 1.1), focus should be on satellite platform development. A deployable optical payload in combination with VLEO and a smartly integrated bus could namely greatly improve system performance as well as volume budgets, which are critical to the launch costs and thus mission feasibility. On the contrary, especially the increased drag in VLEO, as noted in Subsection 2.2.2, is expected to negatively affect volume budgets of the propulsion and attitude control subsystems. Therefore, there is a need for an evaluation of the net volume gain from the combination of these effects.

3.2. Research Question

The questions that drives this thesis is as follows:

How does the integration of deployable optics and VLEO affect satellite volume compared to a traditional LEO Earth observation satellite for monitoring marine plastic debris when taking into account their positive and negative effects on this budget?

Deployable optics and VLEO are referred to as budget-optimizing. However, it is important to note that these measures might not necessarily reduce satellite system volume. This namely, is the essence of the aforementioned research question that is answered in this thesis. In order to answer the research question, the following sub-questions were derived:

1. Which model is most applicable for the establishment of subsystem volume budgets?
2. How does uncertainty in the input parameters affect the system volume budget?
3. Which subsystems drive the system volume for a set of budget-optimization measures?
4. Which propulsion strategy is preferred for the proposed mission?
5. What is the optimal combination of budget-optimization strategies for the proposed mission?
6. Is the concept preferred over a traditional LEO Earth observation satellite in terms of expected return-on-investment and technical development risk?

This set of sub-questions aims to focus the work on the subsystems that are most affected by the implementation of the budget-optimization measures so that their budget estimation method can be adjusted accordingly. Moreover, special attention is given to the negative impact of these measured, leading to a complete overview of the net effect on the satellite system volume budget. This eventually allows for a realistic conclusion on concept feasibility while considering its technological readiness as well.

The work presented in this thesis intends to answer the aforementioned sub-questions and as a result, the research question. The answer to the research question depends on the input parameters to the design of the satellite platform. Major contributions are those of the instrument characteristics and requirements. However, as instrument design is outside the scope of this thesis, the methodology aims to include uncertainties in its parameters and follows a model-based design approach which allows for easy adjustment of input parameters as is explained in Chapter 4.

4

Methodology

This chapter lays the foundation for the work presented in this thesis. It establishes the methodology followed in order to answer the research questions stated in Section 3.2. Firstly, the general approach is outlined. Thereafter, criteria for the comparison of the novel and traditional approach are established. Then, the different satellite configurations competing in this comparison are outlined. The section closes with a description of the generation of the subsystem and subsequent system budgets.

4.1. Approach

The sub-questions listed in Section 3.2 make up the structure of the general approach. The overarching research question lists two volume budget-optimization measures; deployable optics and VLEO. All possible combinations of these parameters form the configurations that are studied in this thesis. Even though these measures intend to save on system volume, also their negative impact, especially on propulsion and attitude control, is explored. The goal is to evaluate the resulting net volume gain for a marine plastic debris monitoring satellite.

Firstly, the payload characteristics including their uncertainty are listed. From these, a set of key requirements forming the basis of the satellite design is deducted. Then, the budget optimization parameters are quantified and a model for the payload volume budget as a function of orbital altitude is constructed. Varying orbital altitude uniformly rather than setting a VLEO and LEO number allows for identification of a possible volume optimum. This is followed by the establishment of individual models for all subsystem volume budgets as a function of the budget-saving parameters. Some fundamental design decisions are made in this phase to define the subsystem concepts and allow budget development. A study on system modeling for VLEO set up a table containing some of these decisions for concept development and is depicted in Table 4.1 [39]. Chapter 2 already pointed at the need for three-axis pointing stability and expandability of the end-of-life system. Propulsion, drag compensation and control are extensively discussed in the following chapter. Payload design is not included in the scope of this thesis, but a static payload is considered for the bus design. Lastly, material GSI should be focused on in future work as noted in Section 7.8.

Table 4.1: A VLEO-specific concept technology development matrix [39]

Propulsion	**Drag Compensation**	**Material GSI**	**Stability**	**Control**	**Payload**	**End of life**
Chemical Electric ABEP None	Continuous Periodic None	Current (diffuse) Novel (quasi-specular)	Three-axis Aerostable Spinning Tumbling	Internal-actuators Control-surfaces Mixed	Static Steerable Hybrid	None Additional-device

Primarily, focus is put on the volume budget, though an evaluation of the power budget is essential for the design of the EPS and is thus incorporated as well. While constructing the subsystem volume models, the trade-off between performance and TRL is addressed when relevant.

Uncertainty in the input parameters of the subsystem budgets is a significant concern in this project. Firstly, as the instrument is outside the scope of this thesis, its characteristics such as aperture size, power consumption and data generation are unknown but highly relevant for for example drag, power budget and link budget analysis. Moreover, as concluded in Subsection 2.2.2, other parameters such as drag in VLEO are hard to model and thereby also introduce uncertainties. In order to model these input parameters as accurately as possible, appropriate probability distributions are defined and implemented in a Monte Carlo simulation that calculates the subsystem volume budgets for a combination of sampled inputs and combines them to a complete satellite volume sample. Repeating this process for different combinations of input samples results in the full satellite volume envelope. This way, the optimal configuration can be identified and compared to a traditional LEO satellite to evaluate the effectiveness of the budget-optimization measures and thereby, the viability of this novel concept for marine plastic debris monitoring.

Two different types of probability distributions are used. A uniform distribution is taken for values that have no best estimate and is written as $a - b$, whereas the log-normal distribution has a location parameter, $\mu*$, and a scale parameter, $\sigma*$, which are calculated based on the mean, m, and variance (or standard deviation squared), v and written as $m \pm \sqrt{v}$. [1]:

$$\mu^* = \ln\left(\frac{m^2}{\sqrt{v+m^2}}\right) \tag{4.1}$$

$$\sigma^* = \sqrt{\ln\left(\frac{v}{m^2}+1\right)} \tag{4.2}$$

4.2. Comparison

In order to establish wether or not a configuration is preferred over the traditional LEO satellite, a comparison criterion on the volume budget must be defined. For this thesis, a concept is preferred when it saves at least 50% on the system volume compared to a traditional LEO satellite.

The rationale behind this number is as follows: The Delft University of Technology foresees a constellation of about 50-100 satellites. The total cost of such mission is composed of investment, manufacturing, launch and operational segments. The novel concept primarily affects the investment and launch costs. Non-recurring investment costs are high compared to traditional LEO satellites due to the need for novel technologies and design, whereas the launch costs per satellite are expected to go down due to the aimed decrease in volume. This means that for a certain number of launched satellites, a break-even is reached, after which the total cost of the novel concept is lower than that of the traditional spacecraft. This break-even is expected to lie between 50 and 100 satellites, matching the foreseen constellation size, when a budget reduction of 50% is realized.

The concept for a traditional LEO spacecraft is one of the configurations that are evaluated in this thesis using the methodology defined in Section 4.1, leading to a fair comparison in terms of model uncertainties. Evaluating the TRL of the winning configuration allows for an estimation of the investment costs. Combining this with the achieved budget reduction and thus new launch costs makes validation of the assumption on the minimum 50% budget reduction possible.

4.3. Configurations

This section details the different configurations that are compared to find the optimal satellite design for marine plastic debris monitoring and determine concept feasibility of a volume optimized satellite in VLEO. As stated in Section 4.2, the novel design is considered favorable when it saves at least 50% on satellite volume compared to a traditional LEO satellite with static payload. The budget-optimization measures considered are: deployable optics and VLEO. While deployability is a discrete parameter, orbital altitude is not. Therefore, LEO is defined at $600\,\mathrm{km}$ and VLEO is considered at the volume optimum between $150\,\mathrm{km}$ and $450\,\mathrm{km}$. This leads to four possible configurations which are presented in the table below:

[1] https://nl.mathworks.com/help/stats/lognormal-distribution.html

Table 4.2: The four configurations that are compared

	1	2	3	4
Deployable optics		x		x
VLEO	x	x		

By comparing the four configurations, the effect of each of the measures is characterized (both positive and negative). This allows quantification of its effectiveness and thus evaluation of its costs and benefits. One should note that configuration 3 represents the 'traditional LEO satellite' and can be used for validation of the minimum 50% budget reduction assumption introduced in Section 4.2.

4.4. Budget Models

For each of the spacecraft subsystems, the volume budget is analyzed for the configurations in Section 4.3. However, the effects of the budget-optimization measures are different on each of the subsystems and can be both positive as well as negative. Therefore, the budget model is adapted to the subsystem inputs and the dependencies between the subsystem and measures.

For this, first, the inputs to the subsystem budget are identified. The characteristics of these inputs are important. In case any of the inputs is uncertain, a suitable probability distribution is established and randomly sampled. Then the inputs are fed to the subsystem budget tool. The subsystems budgets are finally added to a system budget, leading to one of many samples generated through this Monte Carlo approach. The subsystem budget tool is specific to each subsystem and can take several forms:

- **Scaling**: Scaling makes use of a baseline budget that is scaled to an input parameter.
- **Modeling**: Modeling is done based on established relations between input parameters that result in a budget.
- **Trade-off**: When a subsystem cannot be accurately scaled or modeled for the different input parameters, a discrete method is used. Budgets for the various design options are calculated using an applicable method and a trade-off is performed to converge to a design. This method is expected to be most applicable for propulsion budget evaluation as it drastically changes with uncertainty in drag and different propulsion types.

For each set of inputs, a budget is constructed in this way. Repetition of this method for various sampled input sets allows exploration of the volume envelope and reveals the spread of the subsystem budget for a specific configuration. Combining these subsystem budgets then sums to the total system budget. The three budget tool options are schematically depicted in Figure 4.1.

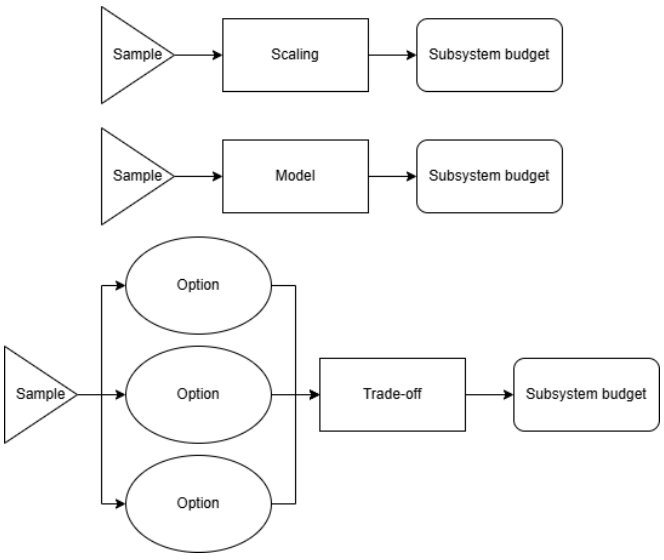

Figure 4.1: The three methods for subsystem budget analysis

5

Model Definition

This chapter aims at establishment of the relationships between the budget-optimization parameters and the satellite volume budget. From the payload characteristics listed in Section 5.1, key requirements for the satellite bus are derived. These flow down to functional requirements which are divided among the subsystems. Then, the effect of VLEO and deployable optics on the payload and subsystem volume budgets is analyzed. For this, each subsystem is considered separately and a model for its volume budget is proposed. Power consumption of each subsystem is evaluated as well, due to its direct effect on EPS (Electrical Power Subsystem) volume. The inputs to the subsystem models are identified as well, so that an N2 chart can be generated, which then forms the basis of the system model architecture.

5.1. Payload Characteristics and Requirements

In this section, the characteristics and requirements of the payload are listed. Table 5.1 gives an overview of the preliminary values for several parameters.

Table 5.1: The payload characteristics

Parameter	Value	Rationale
Mission lifetime	$3-7$ years	In terms of return on investment, a longer lifetime is preferred. Propulsion for orbit maintenance and total ionization dose are limiting factors. Numbers are based on VLEO mission concepts in Table 2.3.
Payload duty cycle	$25\,\%$	Based on the area of interest
Aperture size at $300\,\mathrm{km}$	$0.3\,\mathrm{m}$	Taken from the DST concept study [2].
Field of view	$3.8 \cdot 3.8\,^\circ$	Based on the AOTF concept [129].
Power consumption	$10\,\mathrm{W}$	Based on the AOTF concept [129].
Raw data rate	$840\,\mathrm{Mbps}$	Based on the calculation in Table 5.2
Ground sampling distance	$4\,\mathrm{m}$	Defined in the AOTF concept study [129].
Required attitude knowledge	$10\,\mathrm{m}$	Required for acceptable observations of size and evolution of plastic debris.
Required attitude control	$\pm\,15^\circ$ pointing	Pointing of the instrument for sufficient spectral resolution

Aperture size scales with altitude as explained in the next section and is here defined as approximation at an orbital altitude of $300\,\mathrm{km}$. Although this value is considered fixed by the model, a sensitivity analysis is performed later on to assess the effect of a change in this requirement. The raw data rate followed from a calculation presented in Table 5.2. The numbers in this table are based on the AOTF concept study and required Ground Sampling Distance (GSD) [3]. Indeed, the hyperspectral capabilities and GSD match the needs found in Section 2.1.

The average power consumption P_{PL} over one orbital period is computed based on the payload duty cycle and its power consumption as stated in Table 5.1. Reason for this approach is the variable consumption profile per pass due to different areas of interest.

$$P_{PL} = 10 \cdot 0.25 = 2.5\ W$$

Table 5.2: The calculation of the raw payload data rate

Parameter	Value
Spectral resolution	24
Bit-depth	$10\,\mathrm{bit}$
Swath width	$5000\,\mathrm{pixels}$
Line frequency	$700\,\mathrm{Hz}$
Raw data rate	$840\ \mathrm{Mbps}$

The payload concept assumes a satellite of $27\,\mathrm{U}$ at an altitude of $300\,\mathrm{km}$ and a constellation of 60 spacecraft over 12 different orbital planes in a polar, Sun-Synchronous Orbit (SSO) to reach hourly revisit of areas of interest [3]. Table 5.3 lists the key requirements for the satellite bus to support the payload and finally, successfully monitor marine plastic debris.

Table 5.3: The key requirements for the satellite bus

ID	Requirement	Rationale
SYS-01	The satellite bus shall provide the payload with $10\,\mathrm{W}$ of power in the payload operational phases	This power is required by the payload to perform its function.
SYS-02	The satellite bus shall keep payload temperatures within the operational range	Low payload temperatures are required for detection of wavelengths in the thermal infrared spectrum.
SYS-03	The satellite bus shall handle data coming from the payload	The generated images need to be stored and/or processed.
SYS-04	The satellite bus shall transmit relevant payload data to ground	The data from the payload needs to be transmitted to the ground in order to monitor plastic debris.
SYS-05	The satellite bus shall provide attitude knowledge with an accuracy of $10\,\mathrm{m}$ on ground	This is needed for sufficient information on the size and evolution of plastic debris.
SYS-06	The satellite bus shall support pointing of the instrument from $+\,15°$ to $-\,15°$ in $10\,\mathrm{s}$	This is necessary for sufficient spectral resolution in the areas of interest.
SYS-07	The satellite bus shall support a mission lifetime of $3\,\mathrm{years}$ to $7\,\mathrm{years}$	The system must remain in orbit and survive the environmental conditions.

5.2. Budget-Optimization Parameters

In Chapter 3, VLEO and deployable optics were listed as feasible budget-optimization parameters. Moreover, smart integration promised to enhance mission feasibility. This section elaborates more on the aforementioned strategies in order to specify their relations to the system volume budget.

5.2.1. VLEO

In order to evaluate VLEO and LEO as well as all possibilities in between, altitude is modeled as a continuous uniform distribution:

$$h = 150 - 600\ km$$

VLEO (usually considered between $150\,\mathrm{km}$ and $450\,\mathrm{km}$) is primarily expected to affect the volume budgets of the AOCS and propulsion subsystem. The increased drag due to residual atmosphere poses

higher requirements on the amount of ΔV to be delivered. The effect on AOCS and propulsion budgets is quantified in their respective subsections. Also, the volume of the payload is affected by the orbit to keep a consistent spatial resolution. Lastly, power for communications reveals a dependency on altitude due to the free space loss and communication window, as described in Section 5.8.

Orbital period T and orbital velocity v_{sat} are fixed by orbital altitude according to:

$$T = 2\pi\sqrt{\frac{(Re+h)^3}{GM}} \tag{5.1}$$

$$v_{sat} = \sqrt{\frac{GM}{R_e+h}} \tag{5.2}$$

Where GM is equal to $3.986 \times 10^5\,\mathrm{km^3 s^{-1}}$ is the gravitational constant multiplied with Earth's mass and $R_e = 6378\,\mathrm{km}$ is Earth's radius [130].

5.2.2. Deployable optics

Deployable optics is the second of the budget-optimization parameters investigated in this thesis. As mentioned in Section 1.1, the Delft University of Technology is developing a Deployable Space Telescope (DST) that aims to reduce the instrument stowed volume and thereby enhances mission cost and constellation deployment. The design features an instrumentation box and a Secondary Mirror (M2) that is positioned on three inwards hinging struts at a specific distance from the Primary Mirror (M1). A telescopic baffle shields the system from the Sun and controls the field of view. The number of segments that compose this baffle is modeled as a variable so that a system optimum can be found.

In order to investigate the effect of deployable optics on the satellite volume budget, a Ground Sampling Distance (GSD) is defined for performance consistency and the instrument is sized and scaled to the concepts' orbital altitude accordingly. Primarily, the aperture dimensions as well as the baffle length vary with orbital altitude and need to be modeled. The payload model is described in Section 5.3.

5.2.3. Core Spacecraft Bus Electronics Unit

Smart integration is assumed for all configurations under investigation. The reason for this is two-fold: firstly, it limits the parameter space significantly and makes the project more manageable in the given time frame. Secondly, this parameter is considered least important among the budget-optimization parameters. Therefore, the level of smart integration is not explored here and focus is placed on deployability of the telescope and orbital altitude.

Integration of the foreseen Command and Data Handling (CDH) unit, EPS control and distribution unit, AOCS computations and communication electronics, as suggested in [118], defines the core spacecraft bus electronics unit and is implemented in every design. This unit does not scale to instrument deployment or orbital altitude and thus consumes a constant volume throughout all configurations. For this, $0.25 - 1\ \mathrm{U}$ (uniformly distributed) is reserved, as stated in Table 5.4.

The power consumption of the EPS control and distribution unit as well as the communication electronics depends on orbital altitude and is thus variable in the model. Both are discussed in the subsystem's sections (Section 5.5 and Section 5.8 respectively). For the CDH unit and AOCS computations, a fixed power consumption is assumed as discussed in Section 5.7. The CDH has a $100\,\%$ duty cycle.

Table 5.4: The core spacecraft bus electronics unit model

Relations	Inputs	Outputs
$V_{ICU} = 0.25 - 1\mathrm{U}$		V_{ICU}
Validity	Smartly integrated small satellites	

5.3. Payload Model

The payload as proposed by the Delft University of Technology consists of an instrumentation box located in the satellite body, and a baffle segment that houses the primary and secondary mirror as well as the struts separating the two. The instrumentation box $V_{instrumentationbox}$ measures $11\,\mathrm{cm}$ x $12\,\mathrm{cm}$ x $19\,\mathrm{cm}$. The other part of the payload scales wit altitude: the aperture and baffle dimensions increase with altitude to keep the same GSD as mentioned in Section 5.2. Their models are described below.

Aperture Dimensions

Aperture dimensions depend on the required resolution and determine to a great extend the instrument volume budget. They are derived from the ground sampling distance, which is defined as follows:

$$GSD = h\theta_{res} \tag{5.3}$$

Where h is the orbital altitude and θ_{res} the angular resolution. Thus, increasing orbital altitude requires a decrease of the angular resolution to retain the same ground sampling distance. The angular resolution in turn depends on the diameter of M1, D (aperture), in case of a diffraction limited telescope:

$$\theta_{res} = 1.22 \cdot \frac{\lambda_{wave}}{D} \tag{5.4}$$

To observe a certain wavelength λ_{wave}, a higher orbit then implies the need for a bigger aperture. It thus scales proportionally to the orbital altitude in case of a diffraction limited telescope. If a SNR approach is taken, the same relation holds. Signal namely scales quadratically with distance due to the free space loss (see Equation 5.40). The area of M1 thus also needs to scale quadratically, leading to proportionality between the M1 diameter and distance or orbital altitude. Following these relationships and given an aperture of $0.3\,\mathrm{m}$ at $300\,\mathrm{km}$, the aperture dimensions are calculated with Equation 5.5 (in SI Units). Table 5.5 summarizes the model for the aperture dimensions.

$$D = 10^{-6}h \tag{5.5}$$

Table 5.5: The aperture model

Relations	Inputs	Outputs
$D = 10^{-6}h$	h	D
Validity	$4\,\mathrm{m}$ GSD	

Baffle Dimensions

The baffle aims to minimize stray light (abberation), provide thermal stability and protect the optics. It is sized to fit the M1-M2 structure and prevent sunlight from directly hitting M2 and its spider (which connects M2 to the deployable booms) [131]. For this, the baffle must exceed the distance between M1 and M2, d_{M1-M2} with a height h_x, defined by the orbital altitude and maximum diameter of the baffle. d_{M1-M2} is typically determined by a trade-off on instrument performance. As the instrument design is outside the scope of this thesis, the model uses information on existing telescope designs for Earth observation to derive a feasible M1-M2 distance. As depicted in Figure 5.1, no clear relation between orbital altitude and the design ratio, d_{M1-M2}/D, was identified. Therefore, the model uses a calculated mean and standard deviation of $0.9\ \pm\ 0.239$ for d_{M1-M2}/D:

$$d_{M1-M2} = (0.9\ \pm\ 0.239) \cdot D \tag{5.6}$$

The maximum diameter is the addition of the M1 diameter D, the extra space required to fit the deployable booms next to M1 (four times the boom radius R_{boom}) and the widening of the baffle due to its concentric segmentation R_x, as depicted in Figure 5.2.

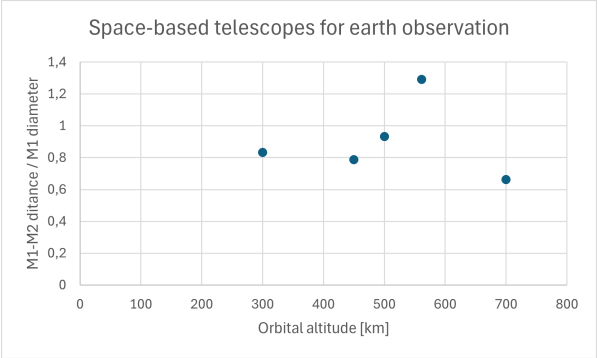

Figure 5.1: A plot of the ratio between the M1-M2 distance and M1 diameter d_{M1-M2}/D against orbital altitude h for several Earth observation telescope designs [132][133][134][135][136]

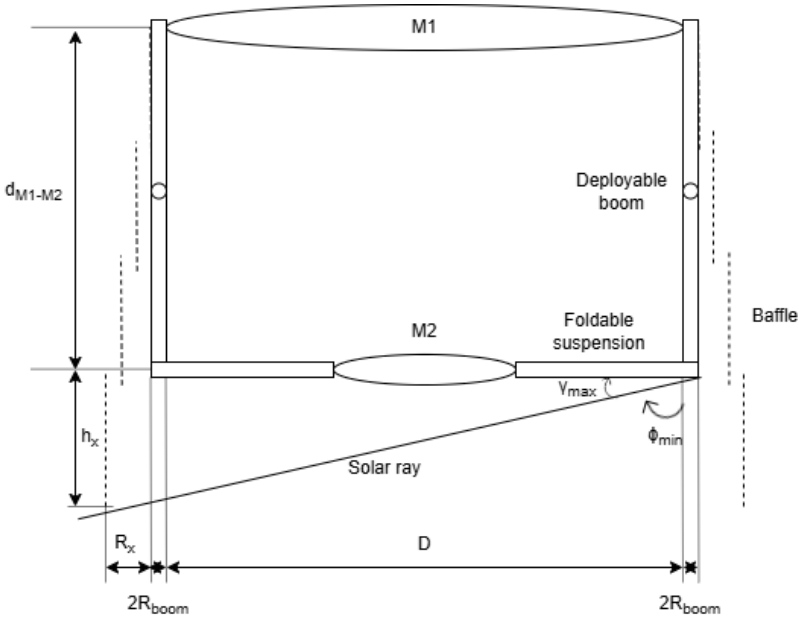

Figure 5.2: A graphical representation of h_x, D_{outer}, ϕ_{min} and γ_{max}

R_{boom} scales with orbital altitude h due to optical requirements on the maximum deflection angle of the suspension system. This angle is related to the square of d_{M1-M2} and the inverse of the moment of inertia. Due to proportionality between d_{M1-M2} and h (Equation 5.5 and Equation 5.6) and a third power relationship between moment of inertia and boom radius, the following formula for the suspension system's boom radius R_{boom} was obtained (given a boom radius of $12.5\,\mathrm{mm}$ at $300\,\mathrm{km}$ [132]):

$$R_{boom} = \left(\frac{h}{300}\right)^{\frac{2}{3}} \cdot 0.0125 \tag{5.7}$$

R_x is a function of the number of segments $n_{segments}$ with an assumed thickness of $3.5\,\mathrm{mm}$ [132]:

$$R_x = 0.0035 \cdot (n_{segments} - 1) \tag{5.8}$$

h_x is then computed using the geometry introduced in Figure 5.2 where ϕ_{min} represents the minimum angle between the nadir direction and incoming sunlight, which happens just before/after eclipse. γ_{max} is the maximum angle between the solar rays and M2. h_x is calculated such that it prevents the solar rays in this condition from hitting M2 or its spider (also see Figure 5.2):

$$\phi_{min} = \arcsin\left(\frac{Re}{Re + h}\right) \tag{5.9}$$

$$\gamma_{max} = \frac{\pi}{2} - \phi_{min} \tag{5.10}$$

$$h_x = (D + 4 \cdot R_{boom} + R_x) \tan \gamma_{max} \tag{5.11}$$

$$l_{baffle} = d_{M1-M2} + h_x \tag{5.12}$$

For the deployable baffle, preliminary design work suggests three segmented cylindrical concentric shells [2]. This number of segments is, however, not yet optimized for stowed-to-deployed volume. In such design, the height of the stowed baffle (and that of the individual segments), h_{min}, equals the height of the stowed M2. This height is solely determined by R_{boom} in case the suspension system has one hinge in the middle:

$$h_{min} = 4 \cdot R_{boom} \tag{5.13}$$

h_{min} thus determines the feasible maximum number of segments $n_{segments,max}$ to achieve the baffle length l_{baffle} needed to shield M2 and the spider from direct sunlight. The segments are assumed to overlap $1\,\mathrm{cm}$, resulting in the following relation for the maximum number of segments [132]:

$$n_{segments,max} = \left\lceil \frac{d_{M1-M2} + (D + h_{min} - 0.0035) \cdot \tan \gamma_{max}}{h_{min} - 0.01 - 0.0035 \cdot \tan \gamma_{max}} \right\rceil \tag{5.14}$$

As $n_{segments}$ affects the diameter of the telescope and thus also the surface area of the nadir- and zenith-pointing faces of the satellite, its value implies consequences on the other subsystems as well. Therefore, the number of segments $n_{segments}$ is uniformly distributed: $1 - n_{segments,max}$. This way, the volume is evaluated for all feasible baffle configurations to finally, after Monte Carlo simulation, find the optimal number at a specific altitude resulting in the lowest satellite volume. The height of the segments is computed as (again, assuming a $1\,\mathrm{cm}$ overlap between segments):

$$h_{segment} = \frac{l_{baffle}}{n_{segments}} + 0.01 \tag{5.15}$$

The stowed volume of the baffle is then obtained with the baffle outer diameter:

$$D_{max} = D + 4 \cdot R_{boom} + 2 \cdot R_x \tag{5.16}$$

$$V_{baffle} = h_{segment} \cdot \frac{1}{4} \pi \cdot D_{max}^2 \tag{5.17}$$

Also, the deployed frontal area of the baffle A_{baffle} is computed, as this is an input to the AOCS and propulsion design:

$$A_{baffle} = n_{segments} \cdot h_{segment} \cdot (D + 4 \cdot R_{boom} + R_x) \tag{5.18}$$

In conclusion, $n_{segments}$ is modeled by a uniform distribution, bounded by $n_{segments,max}$. This maximum follows from a minimum segment height that corresponds to the stowed height of M2 and is thus linked to R_{boom}, which scales with altitude. The segments add up to l_{baffle}, designed to shield the M2 and the spider from direct sunlight.

It was verified that even when using only one segment (and thus having a non-deployable telescope), the FoV of the baffle exceeds that of the instrument and thus does not limit payload performance. The model of baffle is summarized in Table 5.6.

Table 5.6: The baffle model

Relations	Inputs	Outputs
$d_{M1-M2} = (0.9 \pm 0.239) \cdot D$	D	
$R_{boom} = \left(\frac{h}{300}\right)^{\frac{2}{3}} \cdot 0.0125$	h	
$\phi_{min} = \arcsin\left(\frac{Re}{Re+h}\right)$		
$\gamma_{max} = \frac{\pi}{2} - \phi_{min}$		
$h_x = D \tan \gamma_{max}$		
$l_{baffle} = d_{M1-M2} + h_x$		
$h_{min} = 4 \cdot R_{boom}$		
$n_{segments,max} = \left\lceil \frac{d_{M1-M2}+(D+h_{min}-0.0035)\cdot\tan\gamma_{max}}{h_{min}-0.01-0.0035\cdot\tan\gamma_{max}} \right\rceil$		
$R_x = 0.0035 \cdot (n_{segments} - 1)$	$n_{segments} = 1 - n_{segments,max}$	
$h_{segment} = \frac{l_{baffle}}{n_{segments}} + 0.01$		$h_{segment}$
$D_{max} = D + 4 \cdot R_{boom} + 2 \cdot R_x$		
$V_{baffle} = h_{segment} \cdot \frac{1}{4}\pi \cdot D_{max}^2$		V_{baffle}
$A_{baffle} = l_{baffle} \cdot (D + 4 \cdot R_{boom} + R_x)$		A_{baffle}
Validity	Circular baffle with segment thickness $0.0035\,\mathrm{m}$ Dominant Sun shielding requirement One hinge in the middle of the booms	

5.4. Satellite Geometry

The geometry of the satellite affects the frontal area and thus the drag experienced. Moreover, a convenient form factor aids ease of launch. Therefore, based on the satellite volume, a distinction in geometry is made as explained below. A complementary decision tree is depicted in Figure 5.3. The effective stowed volume $V_{eff,stowed}$ here describes the volume of the smallest box that can be drawn around the satellite including its payload. The bus volume V_{bus} is the summation of all subsystem volumes including a $90\,\%$ fill factor and excluding payload. Nomenclature of the body geometry parameters is depicted in Figure 5.4.

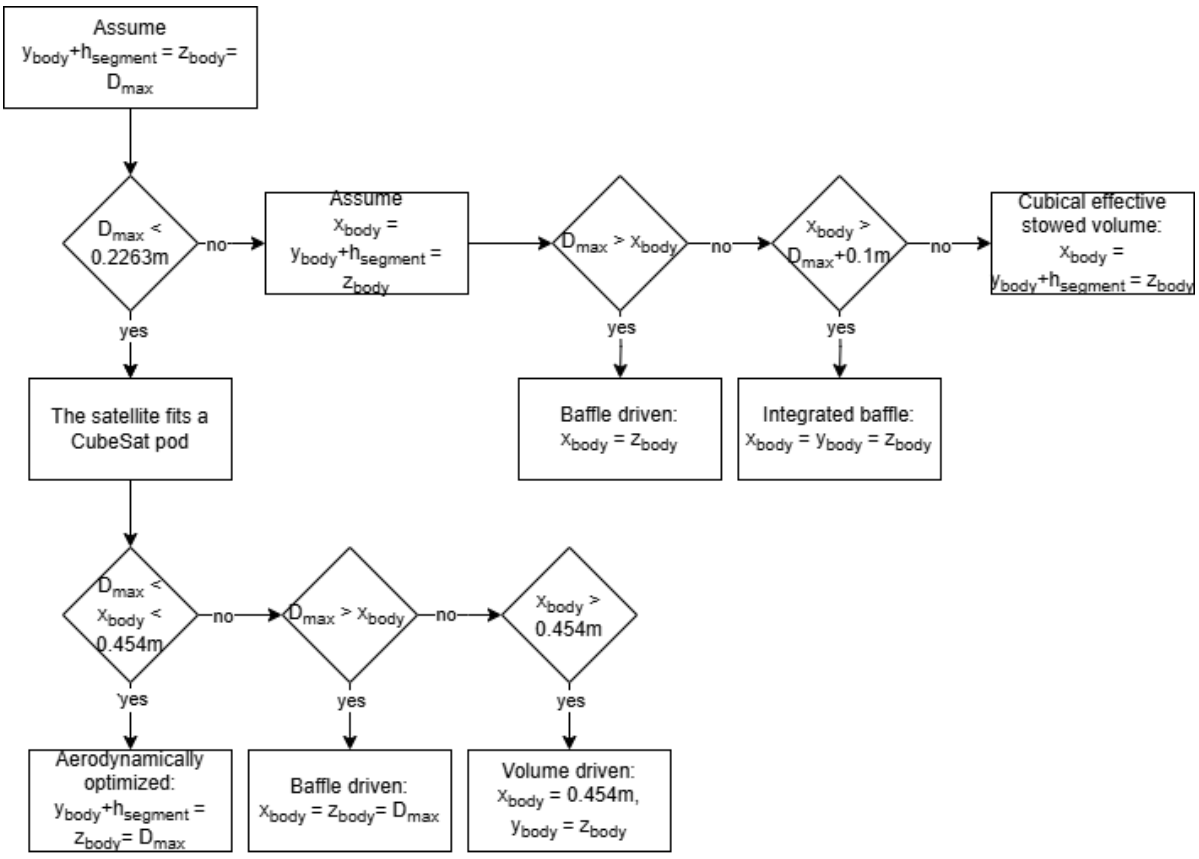

Figure 5.3: A decision tree on the satellite geometry

Case I: CubeSat

If $V_{eff,stowed}$ < $16\,\mathrm{U}$ or $23\,\mathrm{L}$ when the $y_{body}+h_{segment}$ and z_{body} are set equal to the baffle outer diameter and the $D_{max} < 0.2263\,\mathrm{m}$:

Then, the satellite fits within a CubeSat pod in the launch vehicle. In line with Section 2.3, this geometry is preferred. Maximum dimensions measure $0.2263\,\mathrm{m}$ x $0.2263\,\mathrm{m}$ x $0.454\,\mathrm{m}$. In order to improve aerodynamics of the design, x_{body} is maximized. For this, $y_{body}+h_{segment}$ and z_{body} are set equal to D_{max} to fit the instrument and it is checked that $D_{max} < x_{body} < 0.454\,\mathrm{m}$. This results in a square effective stowed frontal area. If $D_{max} > x_{body}$, then x_{body} and z_{body} are set equal to D_{max} and y_{body} reduces, resulting in a horizontal rectangular effective stowed frontal area. If $x_{body} > 0.454\,\mathrm{m}$, then x_{body} is set to $0.454\,\mathrm{m}$ and $y_{body}+h_{segment}$ and z_{body} are made equal, again resulting in a square effective stowed frontal area.

Case II: Baffle driven

If the D_{max} exceeds $x_{body} = y_{body}+h_{segment} = z_{body}$ (cubical effective stowed volume):

Then, the baffle drives the geometry and thus determines x_{body} and z_{body}. This leads to a horizontal rectangular effective stowed frontal area. In this case, y_{body} has a minimum value of $0.11\,\mathrm{m}$ to house the instrumentation box (see Subsection 5.2.2).

Else, a cubical effective stowed volume is aimed for to aid launch.

Case III: Integrated baffle
If $x_{body} = y_{body} + h_{segment} = z_{body} > D_{max} + 0.1\ \mathrm{m}$*:*
Then there is a significant amount of volume unused adjacent to the stowed baffle. Therefore, The baffle is integrated in the body in this case. V_{bus} and V_{baffle} are summed and $x_{body} = y_{body} = z_{body}$. In deployed conditions, this reduces the distance between the center of mass and center of pressure (see Section 5.9).

Case IV: Cubical
In all other cases:
$x_{body} = y_{body} + h_{segment} = z_{body}$ so that the effective stowed volume is cubical.

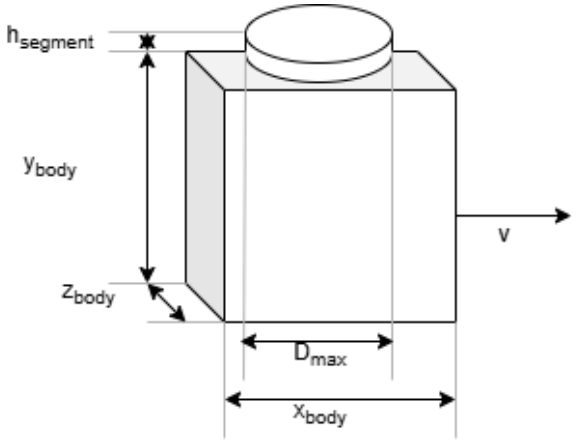

Figure 5.4: A graphical representation of x_{body}, y_{body}, z_{body}, $h_{segments}$ and D_{max},

5.5. EPS Model

The Electrical Power Subsystem (EPS) is composed of several components. Most important for the volume budget are the solar panels and batteries. As mentioned in Subsection 5.2.3, the power control and distribution is part of the core spacecraft bus electronics unit, though its losses are discussed at the end of this section.

The EPS is defined by the power consumption of all other subsystems as well as the eclipse time. Based on these, the battery volume, V_{bat}, and solar panel area, A_{sp}, are computed. Power consumption of the payload and bus subsystems is discussed in their respective sections. Important to note is that the thermal control is fully passive and is thus not included here (see Section 5.6). Subsystem powers are averaged over one orbit and summed to a total average power consumption P_{tot} as input to the EPS model:

$$P_{tot} = P_{PL} + P_{CDH} + P_{com} + P_{AOCS} + P_{prop} \tag{5.19}$$

In terms of volume and drag, body mounted solar panels are preferred. However, especially when electric propulsion is used, the need for deployable solar panels is foreseen. As already stated in Subsection 2.2.3, it was found that such solar panels are most efficient in VLEO when aligned with the velocity vector to minimize the drag [90]. The model thus assumes this configuration for all orbital altitudes. In LEO, drag is less prominent and thus, Sun-pointing panels might be advantageous. However, as the satellite body dimensions x_{body}, y_{body} and z_{body} (see Figure 5.4) are expected to increase with altitude, increased solar panel dimensions are predicted to have a lower relative impact on the volume budget and thus, this methodology is still assumed to be representative.

The average power generated by the deployable panels over one orbit in any SSO undergoes seasonal variations, where Solstice (when the Sun vector makes a ± $23.5°$ angle with the equatorial plane) represents the worst case due to longer periods of eclipse and higher cosine losses. The difference in relative average power generation between the two extremes, Equinox ($\lambda = 0°$) and Solstice ($\lambda = 90°$), can be observed in Figure 5.5 [90]. A relative average power generation, P_{avg}, of 1 is achieved for a $90°$ solar ray incidence angle on the panels for the full duration of the sunlit section of the orbit. The figure does not consider power loss due to eclipses and is thus independent of orbital altitude. Moreover, this figure clarifies that especially for a SSO with a longitude of the ascending node between Noon-Midnight ($\Omega - \lambda$ = $0°$) and Dusk-Dawn ($\Omega - \lambda$ = $90°$), the ability to rotate the panels ('movable') around the velocity vector improves power generation compared to 'fixed' panels.

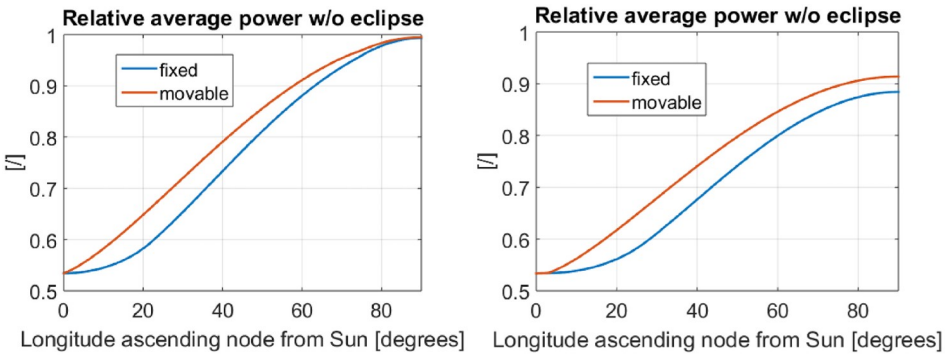

(a) Equinox **(b)** Solstice

Figure 5.5: The relative average power P_{avg} for velocity aligned solar panels as a function of the longitude of the ascending node $\Omega - \lambda$ without eclipse losses [90]

In order to model the average power generation P_{avg}, the longitude of the ascending node $\Omega - \lambda$ of the SSO is sampled at $0°$, $30°$, $60°$ and $90°$. Then P_{avg} at Solstice (taken from Figure 5.5b) is considered, as it implies the longest period of eclipse that a spacecraft with a lifetime over just $0.5\,\text{years}$ will experience. Depending on the orbital altitude and longitude of the ascending node, a loss due to eclipse at Solstice is added to finally obtain the relative average power generation including eclipse $P_{avg,e}$ for any orbit at

Solstice. The worst case scenario in terms of longitude of the ascending node is identified and put into the model as this forms the baseline design for the constellation.

As noted, the eclipse time varies with the seasons as well as with the orbital altitude h and longitude of the ascending node $\Omega - \lambda$. A plot representing the relation between the latter two and average eclipse fraction over one year, $\bar{f}$, is depicted in Figure 5.6 [137] (note that the orbital altitude h is expressed in Nautical Miles here).

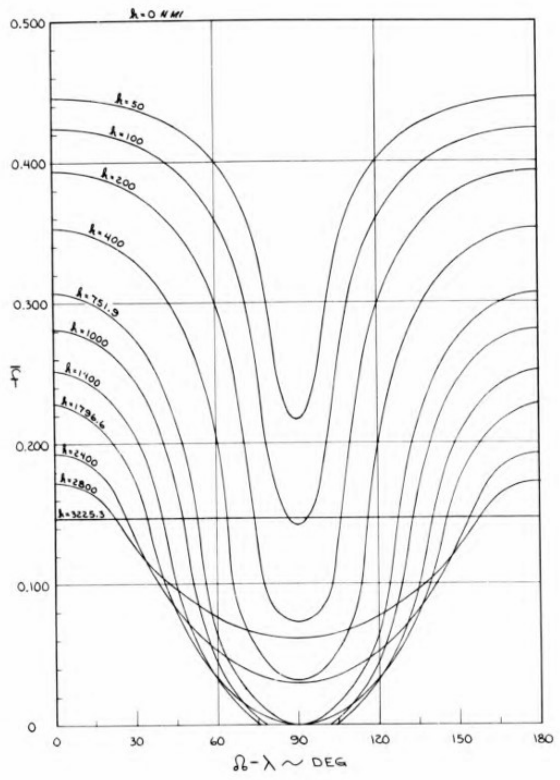

Figure 5.6: The average eclipse fraction $\bar{f}$ as a function of the longitude of the ascending node $\Omega - \lambda$ for various orbital altitudes h (in Nautical Miles) [137]

In order to model the worst case eclipse fraction (which happens at Solstice), the maximum seasonal variation has to be added to the average eclipse fraction $\bar{f}$. These variations are maximum for a Dusk-Dawn orbit, whereas for a Noon-Midnight orbit these are negligible, as clear from Figure 5.7 (again, h is in Nautical Miles).

Therefore, the seasonal variation of the eclipse fraction in a Dusk-Dawn orbit is evaluated for different orbital altitudes. From Figure 5.7b, the difference between the average and maximum eclipse fractions were plotted against orbital altitude in Figure 5.8. A maximum difference of 0.21 was found for an orbit at $285\,\mathrm{km}$. Therefore, 0.21 was added to $\bar{f}$ for a Dusk-Dawn orbit ($\Omega - \lambda = 90°$), 0.14 for a $60°$ orbit, 0.07 for a $30°$ orbit and 0 to a Noon-Midnight orbit ($\Omega - \lambda = 0°$) (as consistent with Figure 5.7a).

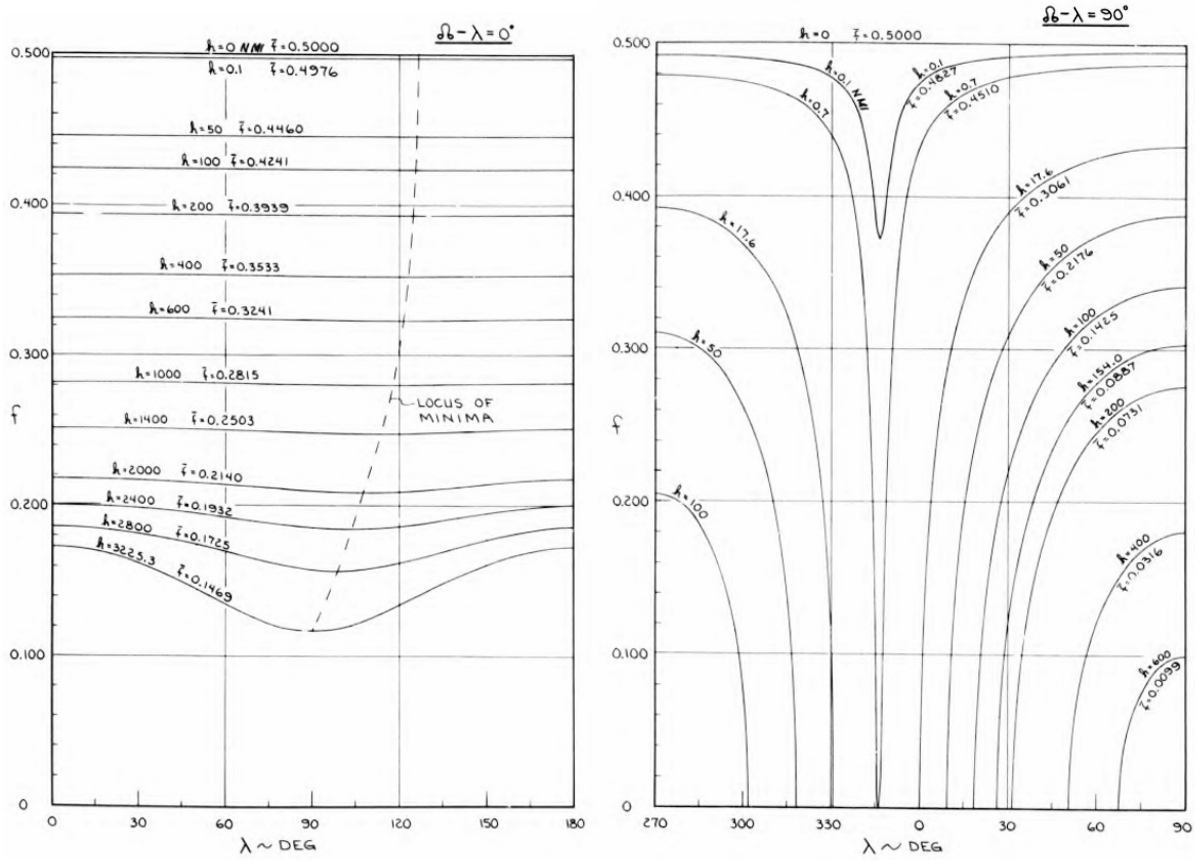

(a) Noon-Midnight **(b)** Dusk-Dawn

Figure 5.7: The seasonal variations of eclipse fractions f for different orbital altitudes h (in Nautical Miles) [137]

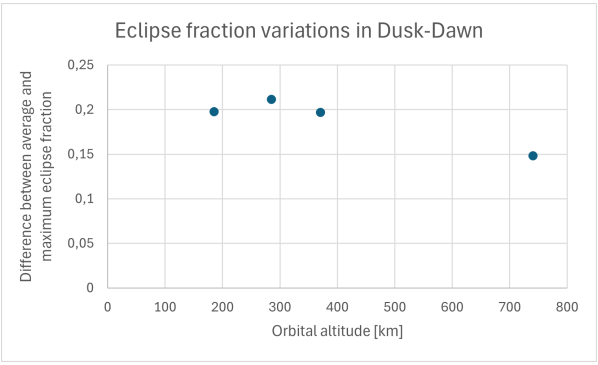

Figure 5.8: The difference between the average and maximum eclipse fractions $\bar{f}$ and $f_{Solstice}$ in a Dusk-Dawn orbit as a function of orbital altitude h

Combining these additions at Solstice with the average eclipse fractions found in Figure 5.6, the plots in Figure 5.9 were generated. They represent the Solstice eclipse fractions $f_{Solstice}$ as a function of orbital altitude for different longitudes of the ascending node.

Both Figure 5.5 (in terms of cosine loss) and Figure 5.9 (in terms of eclipse fraction) suggest that the worst case scenario for solar power generation occurs in a Noon-Midnight orbit ($\Omega - \lambda = 0°$) at Solstice. Therefore, a linear empirical relation for the eclipse fraction in this orbit as a function of orbital altitude was derived:

$$f_{Solstice} = -0.0001 \cdot h + 0.4535 \ \pm \ 0.0132 \tag{5.20}$$

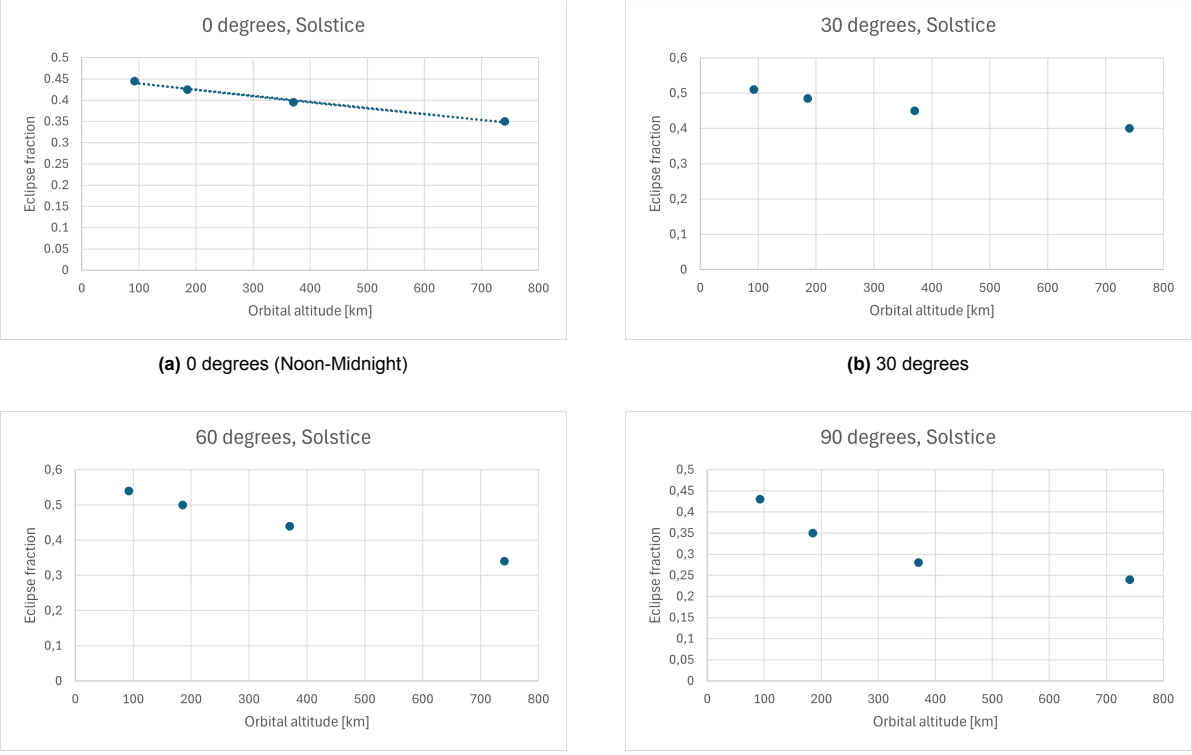

(a) 0 degrees (Noon-Midnight)

(b) 30 degrees

(c) 60 degrees

(d) 90 degrees (Dusk-Dawn)

Figure 5.9: The eclipse fractions at Solstice $f_{Solstice}$ as a function of orbital altitude h for four different longitudes of the ascending node $\Omega - \lambda$

Then, P_{avg} in this orbit at Solstice, which is 0.54 (Figure 5.5b), is multiplied with $1 - f_{Solstice}$ to obtain the relative average power at Solstice including eclipse, $P_{avg,e}$:

$$P_{avg,e} = 0.54 \cdot (1 - f_{Solstice}) \tag{5.21}$$

The solar panel area is then computed with Equation 5.28. For the end-of-life solar cell efficiency and fill factor, a value of $28\,\%$ and 0.8 are assumed respectively [138][139]. The solar constant is taken to be $1366.1\,\mathrm{Wm}^{-2}$ in accordance with ASTM E-490 [140]. For the maximum power point tracker efficiency and distribution losses, a factor of 0.85 is included [141].

The thickness of the deployable panels t_{sp} scales with their length $l_{sp,max}$ (elaborated on below) in order to limit static deflection and retain acceptable dynamic behavior. Assuming clamped hinges, a cantilever, thin walled solar panel, and a distributed load q_{load}, the tip deflection δ is related to length $l_{sp,max}$ and thickness t_{sp} as follows (where E is the Young's modulus and ν in Poisson's ratio) [142]:

$$\delta \sim \frac{12 \cdot (1 - \nu^2) \cdot q l_{sp,max}^4}{E t_{sp}^3} \tag{5.22}$$

$$t_{sp} \sim l_{sp,max}^{\frac{4}{3}} \tag{5.23}$$

However, the dynamic behavior of the panel should be considered as well (ρ is the material density) [142]:

$$f_1 \sim \frac{t_{sp}}{l_{sp,max}^2}\sqrt{\frac{E}{\rho \cdot (1-\nu^2)}} \tag{5.24}$$

$$t_{sp} \sim l_{sp,max}^2 \tag{5.25}$$

A third consideration is mass optimization, where mass is directly related to panel thickness and ideally minimized. Combining these three factors, it was decided to use the following scaling law for this phase of the mission design (a sensitivity analysis will be performed on this assumption in Section 7.6):

$$t_{sp} \sim l_{sp,max}^{1.5} \tag{5.26}$$

Given a $1.8\,\mathrm{mm}$ thickness for a $0.1\,\mathrm{m}$ panel and a $2.5\,\mathrm{mm}$ thickness for a $0.34\,\mathrm{m}$ panel and fitting these to the scaling law, the relation is as follows [143]:

$$t_{sp} = 0.00420 \cdot l_{sp,max}^{1.5} + 0.00167 \tag{5.27}$$

The two deployable solar panel arrays fold flat to the satellite and match the dimensions of the satellite side panel ($(y_{body} + h_{segments})z_{body}$ for geometry case I (CubeSat), II (Baffle driven) and IV (Cubical) and $y_{body}z_{body}$ for geometry case III (Integrated baffle), which are determined iteratively based on the total satellite volume, see Section 5.11) so that their length L_{sp} and volume V_{sp} are computed with Equation 5.29 and Equation 5.31. Due to the fact that there is no advantage in having half a panel from a launch volume perspective, the number of deployable segments is rounded up to add power redundancy. In case there is an uneven number of panels, the thickness is adjusted to the longest array $l_{sp,max}$.

$$A_{sp} = \frac{P_{tot}}{1366.1 \cdot P_{avg,e} \cdot 0.28 \cdot 0.8 \cdot 0.85} \tag{5.28}$$

$$l_{sp} = \left\lceil \frac{A_{sp}}{(y_{body}(+h_{segment}))z_{body})} \right\rceil (y_{body}(+h_{segment})) \tag{5.29}$$

$$l_{sp,max} = \left\lceil \frac{\left\lceil \frac{A_{sp}}{(y_{body}(+h_{segment}))z_{body})} \right\rceil}{2} \right\rceil (y_{body}(+h_{segment})) \tag{5.30}$$

$$V_{sp} = l_{sp} t_{sp} z_{body} \tag{5.31}$$

For sizing of the batteries, the total energy consumption during the calculated eclipse fraction is computed. This energy is then related to battery volume by the specific energy density and depth of discharge DoD, which is uniformly distributed as $20\% - 40\%$ [144]. For the discharge efficiency and power control and distribution losses, $12\,\%$ additional energy is included [141]. Assuming Lithium-ion batteries, the energy density is taken to be $7.62 \times 10^5\,\mathrm{Whm}^{-3}$[145].

$$E_{bat} = P_{tot} f_{Solstice} T \tag{5.32}$$

$$V_{bat} = \frac{1}{0.762} \cdot \frac{E_{bat}}{3600} \cdot \frac{1.12}{DoD} \tag{5.33}$$

The model is summarized in Table 5.7.

Table 5.7: The EPS model

Relations	Inputs	Outputs
$P_{tot} = P_{PL} + P_{CDH} + P_{com} + P_{AOCS} + P_{prop}$	P_{PL}, P_{CDH}, P_{com}, P_{AOCS}, P_{prop}	
$f_{Solstice} = -0.0001 \cdot h + 0.4535 \ \pm \ 0.0132$	h	
$P_{avg,e} = 0.54 \cdot (1 - f_{Solstice})$		
$A_{sp} = \frac{P_{tot}}{1366.1 \cdot P_{avg,e} \cdot 0.28 \cdot 0.8 \cdot 0.85}$		
$l_{sp} = \left\lceil \frac{A_{sp}}{(y_{body}(+h_{segment}))z_{body})} \right\rceil (y_{body}(+h_{segment}))$		
$l_{sp,max} = \left\lceil \frac{\left\lceil \frac{A_{sp}}{(y_{body}(+h_{segment}))z_{body})} \right\rceil}{2} \right\rceil (y_{body}(+h_{segment}))$		
$t_{sp} = 0.00420 \cdot l_{sp,max}^{1.5} + 0.00167$		
$V_{sp} = l_{sp} t_{sp} z_{body}$	y_{body}, z_{body}, $h_{segments}$ (iterative)	V_{sp}
$E_{bat} = P_{tot} f_{Solstice} T$	T	
$V_{bat} = \frac{1}{762000} \cdot \frac{E_{bat}}{3600} \cdot \frac{1.12}{DoD}$	$DoD = 0.2 - 0.4$	V_{bat}
Validity	$150\,\mathrm{km}$ to $600\,\mathrm{km}$ polar SSO Velocity aligned solar panels Lithium-ion batteries	

5.6. Thermal Control Model

The satellite's thermal control is assumed to be fully passive, based on the research presented in [132]. The instrumentation box is cooled by a cold-stage radiator. By implementation of an additional passive cryo-stage radiator with Earth shade door and side covers, the DST detector can successfully be cooled down to $150\,\mathrm{K}$, needed to make observations in the thermal-infrared domain. Both radiators measure $7\,\mathrm{cm}$ x $36\,\mathrm{cm}$ and do not scale with any of the budget-saving parameters. The Earth shade door has dimensions of $19\,\mathrm{cm}$ x $39\,\mathrm{cm}$ with side covers of $A_{tc} = 0.5 \cdot 0.19 \cdot 0.19\ \mathrm{m}$ and folds flat to the spacecraft's side panel in launch configuration. The volume of this system is negligible, though the side covers on the Earth shade door are part of the frontal area in the worst case scenario and thus, contribute to the drag as listed in Table 5.8. The design is depicted in Figure 5.10.

Table 5.8: The thermal control model

Relations	**Inputs**	**Outputs**
$A_{tc} = 0.0181\,\mathrm{m}^2$		A_{tc}
Validity	Passive thermal control design for DST concept	

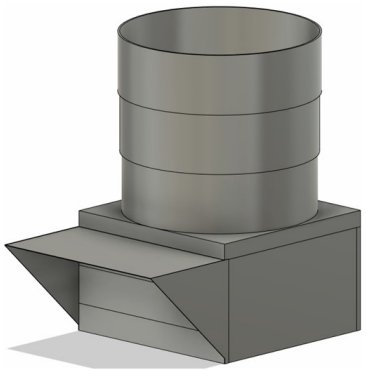

Figure 5.10: The thermal subsystem including Earth shade door integrated in a preliminary design of the satellite in deployed configuration [132]. The radiators are located underneath the Earth shade door with the cryo-stage cooler being the top one.

5.7. CDH Model

As noted in Subsection 5.2.3, the CDH unit is part of the core spacecraft bus electronics unit and is thus independent from the budget-saving parameters. Its volume is fixed along with the rest of the core spacecraft bus electronics unit unit. The power consumption of the CDH unit (including AOCS computations) is expected to be relatively high compared to CubeSats due to the large amount of payload data and stringent requirements on AOCS. Therefore, it is based on COTS CDH units that are capable of intelligent image processing due to high performance payload data processing or AI acceleration. The COTS CDH units considered are plotted in Figure 5.11 and the average power consumption was found to be 13.16 ± 5.936 W [146]. The CDH model is summarized in Table 5.9.

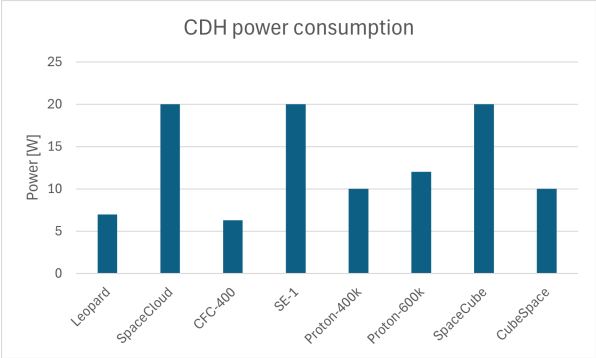

Figure 5.11: The power consumption P_{CDH} of several COTS CDH units

Table 5.9: The CDH model

Relations	Inputs	Outputs
$P_{CDH} = 13.16 \pm 5.936$		P_{CDH}
Validity	Smallsat with large amount of payload data and possibly intelligent image processing	

5.8. Communications Model

As discussed in Subsection 5.2.3, the communication electronics are part of the core spacecraft bus electronics unit. Therefore, the volume of this subsystem is not discussed here. However, its power consumption P_{com} does affect EPS volume and is thus analyzed in more detail. It is related to the transmission power P_{Tx} via the DC-to-RF efficiency η_{DC-RF} and an additional base power consumption P_{basis}. Combined, these form the transmitter input power P_{in}. P_{Tx} is determined by closing the link budget, which is discussed in more detail below. $1\,\mathrm{W}$ is added for housekeeping transmission and command reception as it does not scale with the budget-saving parameters and thus, is not of significant interest. As the EPS model requires the average power consumption over one orbit P_{com}, the communication window t_{com} has to be evaluated using the geometry sketched in Figure 5.12. It assumes one communication window per orbit and depends on the orbital altitude h and half-power beamwidth angle β. In line with the conclusions drawn in Section 2.2, a lower orbital altitude negatively impacts the communication window.

$$\alpha = \pi - \arcsin\left(\frac{(R_e + h)\sin(\beta)}{Re}\right) \tag{5.34}$$

$$\theta = \pi - \alpha - \beta \tag{5.35}$$

$$t_{com} = \frac{T\theta}{\pi} \tag{5.36}$$

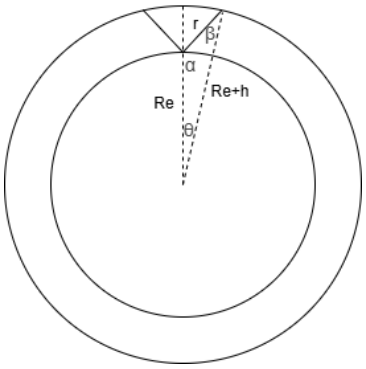

Figure 5.12: A graphical representation of R_e, h, r, α, β and θ

$$P_{com} = \frac{t_{com} \cdot \left(1 + P_{basis} + \frac{P_{Tx}}{\eta_{DC-RF}}\right)}{T} = \frac{t_{com} \cdot (1 + Pin)}{T} \tag{5.37}$$

SYS-04 drives the design of the communication subsystem and thus P_{Tx}. The average data rate DR_{avg} is a combination of the raw payload data rate ($840\ \mathrm{Mbps}$) with the addition of metadata and packet overhead (assumed to account for $25\,\%$ of the total data) and data reducing factors. The latter includes duty cycle ($25\,\%$, Table 5.1), compression (mathematically lossless: $2:1$ [147]) and intelligent perception and processing as introduced in Subsection 2.3.2. Intelligent perception and processing allow omission of useless images (due to for example clouds [1], absence of plastic and image similarity). Assuming plastic presence in the order of $10\,\%$ and detectable changes in $\frac{1}{3} \pm \frac{1}{3}$ of the images, the combination of these effects is expected to establish a reduction factor of 0.0013 ± 0.0013, leading to an average data rate of $1.493 \pm 1.493\ \mathrm{Mbps}$:

$$DR_{avg} = 1.493 \pm 1.493 \ \ Mbps$$

The worst case contact time occurs at the lowest altitude, where it takes approximately $0.6\,\%$ of the orbital period assuming an antenna beamwidth of $74°$. Considering DR_{avg}, the downlink data rate DR_{down} then needs to be $250\,\mathrm{Mbps}$. For larger orbital altitudes, the contact time as a fraction of the

[1] Between 1954-2008, average cloud coverage of oceans was found to be $68\,\%$ [148].

orbital period increases and thus, DR_{down} is lower. A plot of DR_{down} as a function of h for COTS antennas with different half-power beamwidths is depicted in Figure 5.13 where the average data rate of $1.493\,\mathrm{Mbps}$ was used. Clearly, a higher half-power beamwidth reduces the required downlink data rate.

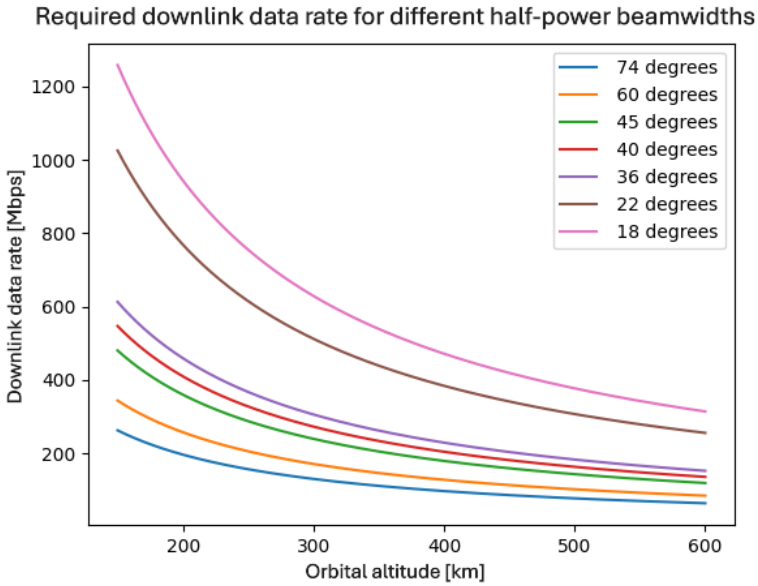

Figure 5.13: The downlink data rate DR_{down} as a function of orbital altitude h for different antenna half-power beamwidths using the mean average data rate DR_{avg}

The downlink data rate is thus relatively large compared to CubeSat missions due to the demanding payload and VLEO altitude. Traditionally, small- and CubeSats occupy the VHF-, UHF-, S-, X- and Ka-band [149]. Though, a shift to higher frequency bands (S-band and upwards) is observed due to crowdedness and advantageous data rates. Also for this mission, high frequency bands are attractive for their improved data rates. Higher frequencies, however, are restricted by the increased rain attenuation (especially in Ka-band) [150]. Moreover, limited COTS systems for Ka-band transmission are currently on the market, outperform X-band data rates and consume comparable power [151]. Therefore, the model assumes data transmission over the X-band.

As concluded from Figure 5.13, the antenna's half-power beamwidth β significantly affects the downlink data rate. Two methodologies are considered: either the antenna is defined and data rate is matched with the required data rate by changing modulation scheme, or the data rate is fixed and the antenna is matched with the required beamwidth. In terms of gain, changing modulation has a slight advantage over changing antenna, saving $9.5\,\mathrm{dB}$ compared to $7\,\mathrm{dB}$ at $600\,\mathrm{km}$ compared to $150\,\mathrm{km}$ [2]. In light of comparing configurations at different altitudes in a fair manner, the first option is implemented so that the transmitter and antenna components remain the same and modulation of the signal changes with datarate to limit the required bandwidth.

The X-band patch antenna from Endurosat is chosen as a reference antenna [3]. Its characteristics are summarized in Table 5.10. For transmission, the XTXG2 (Next Generation X-band Transmitter) from Cubecom is considered as reference [4]. Specifics of this system are summarized in Table 5.11. In order to determine P_{basis} and η_{DC-RF} for this X-band transmitter, a plot of RF power P_{Tx} as a function of

[2] Gain of $6\,\mathrm{dB}$ for $\beta = 74°$: `https://www.endurosat.com/products/x-band-patch-antenna/`. Gain of $13\,\mathrm{dB}$ for $\beta = 36°$ (XANT AIR): `https://cubecom.space/x-band/`. For modulation, see Table 5.12.

[3] `https://www.endurosat.com/products/x-band-patch-antenna/`

[4] `https://cubecom.space/x-band/`

input power P_{in} for several state-of-the-art X-band transmitters is generated in Figure 5.14 [5][6][7][8][9]. A linear empirical relation based on the least-squares method for P_{in} was found:

$$P_{in} = 3.9058 \cdot P_{Tx} + 9.8514 \ \pm \ 2.516 \tag{5.38}$$

Table 5.10: The characteristics of the X-band patch antenna[3]

Parameter	Value
Frequency range	$8025\,\mathrm{MHz}$ to $8400\,\mathrm{MHz}$
RF power handling	up to $4\,\mathrm{W}$
Mass	$<0.003\,\mathrm{kg}$
Half-power beamwidth	$72°$
Gain G_{Tx}	$6\,\mathrm{dBi}$ + over beamwidth

Table 5.11: The characteristics of the XTXG2[4]

Parameter	Value
Frequency range	$8025\,\mathrm{MHz}$ to $8400\,\mathrm{MHz}$
Maximum RF power	$2\,\mathrm{W}$ $(33\,\mathrm{dBm})$
Volume	$1.12 \times 10^{-4}\,\mathrm{m}$
Power consumption	$16\,\mathrm{W}$
Mass	$0.137\,\mathrm{kg}$
Symbol rate	$5\,\mathrm{Msps}$ to $50\,\mathrm{Msps}$

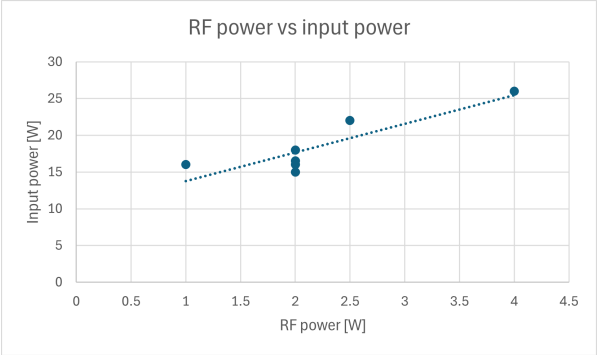

Figure 5.14: The RF power P_{Tx} as a function of input power P_{in} to the transmitter

Using these COTS components, the required data rate DR_{down} can be expressed as an empirical exponential function of orbital altitude. The fitted curve is depicted in Figure 5.15, has a standard deviation of $\left(2.718 + 1.493 \cdot \left(\frac{T}{t_{com}}\right)\right)$ (propagated from the data rate and increased by the curve fitting process) and its formula is as follows:

$$DR_{down} = 566.6 \cdot e^{-0.0069 \cdot h} + 59.06 \ \pm \ \left(2.718 + 1.493 \cdot \left(\frac{T}{t_{com}}\right)\right) \tag{5.39}$$

XTXG2 implements the DVB-S2 standard and supports QPSK, 8-PSK, 16-APSK and 32-APSK modulation. As depicted in Figure 5.13, data rates vary with orbital altitude. In order to limit the required bandwidth and keep the required Bit Energy to Noise Ratio E_b/N_0 (and thus P_{Tx}) as low as possible, different modulation schemes are used for different data rates. An overview is provided in Table 5.12, based on the highest code rate for optimal throughput [152].

Assuming a near-polar orbit for the mission, the KSAT ground station network is very suitable. KSAT is a ground station network with X-band antennas that are located near the poles (Tromsø at 69°N, Svalbard (SvalSat) at 78°N and Antarctic TrollSat Station at 72°S) to support communication with satellites in polar orbit [153]. Taking the most northern ground station, the receiving-antenna Gain to noise Temperature G/T is $35.7\,\mathrm{dBK}^{-1}$.

[5] https://satsearch.co/products/endurosat-x-band-transmitter
[6] https://www.syrlinks.com/en/space/x-band-transmitter
[7] https://cubecom.space/x-band/
[8] https://www.cubesatshop.com/product/iq-spacecom-x-link-x/
[9] https://4e97eb45-dc48-4580-af38-dd9ba35299e9.filesusr.com/ugd/3473d8_84af107a92c649d1b5729ad2e89ce4f9.pdf?index=true

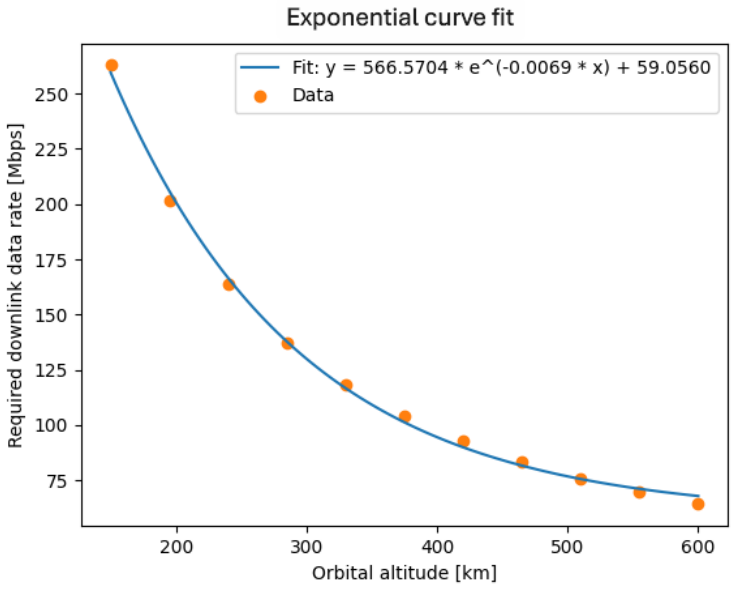

Figure 5.15: The required downlink data rate DR_{down} as a function of orbital altitude h fitted to an exponential decay function

Table 5.12: The modulation scheme and subsequent bit energy to noise ratios E_b/N_0 for different orbital altitudes h

Downlink data rate DR_{down}	Modulation scheme	Required bit energy to noise ratio E_b/N_0
> $200\,\mathrm{Mbps}$	32-APSK 9/10	$16.05\,\mathrm{dB}$
$150\,\mathrm{Mbps}$ to $200\,\mathrm{Mbps}$	16-APSK 9/10	$13.13\,\mathrm{dB}$
$100\,\mathrm{Mbps}$ to $150\,\mathrm{Mbps}$	8-PSK 9/10	$10.98\,\mathrm{dB}$
< $100\,\mathrm{Mbps}$	QPSK 9/10	$6.41\,\mathrm{dB}$

The link budget is also subject to several losses. Most influential is the free space loss, L_S, caused by 2-dimensional beam spread. Other losses include the effects of pointing (L_P), the atmosphere (L_A) and hardware (L_{Tl} and L_{Rl}). Scintillation loss is not considered here as it was found to be negligible for links beyond $1\,\mathrm{GHz}$ [154].

The free space loss L_S is calculated using the following formula, where L_S is expressed in dB, r denotes the distance between the two antennas in km and f is the frequency in GHz [154]:

$$L_S = 92.45 + 20 \cdot \log_{10}(r) + 20 \cdot \log_{10}(f) \tag{5.40}$$

The distance r depends on the orbital altitude as well as the elevation angle. Free space loss thus varies during the pass. A plot of the distance between the satellite and ground station during contact for various orbital altitudes is shown in Figure 5.16a. For the generation of the plot, a frequency f of $8400\,\mathrm{MHz}$ was assumed, as this represents the worst case loss in the X-band. The associated free space loss is plotted in Figure 5.16b. According to expectation, these figures reveal that with an increasing orbital altitude, the distance as well as the free space loss increases.

Now, the average free space loss as a function of altitude is derived. For this, the computed average free space loss was fitted to a polynomial. The fit is depicted in Figure 5.17. The standard deviation is calculated to be 0.1572 and the formula is as follows:

$$\bar{L}_S = -0.000038 \cdot h^2 + 0.0538 \cdot h + 148.3518 \ \pm \ 0.1572 \tag{5.41}$$

Pointing loss L_P occurs both on the transmission as well as on the receiving side. It is related to the pointing error of the AOCS onboard the satellite and ground station, as well as to the beam shape. The pointing accuracy of the satellite is scaled to its altitude and this thus reduces the dependency between

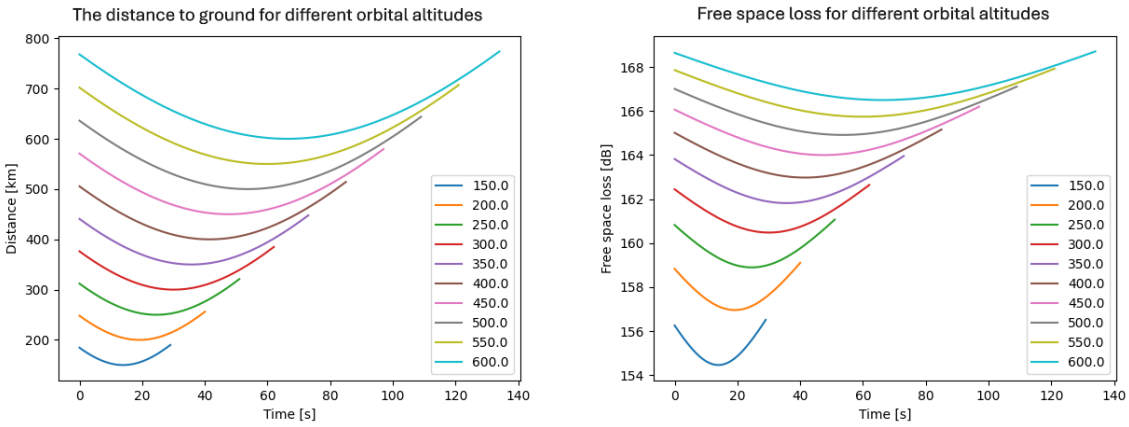

(a) Distance r **(b)** Free space loss L_S

Figure 5.16: The distance r between the satellite and ground station and the associated free space loss L_S during contact for various orbital altitudes h [km]

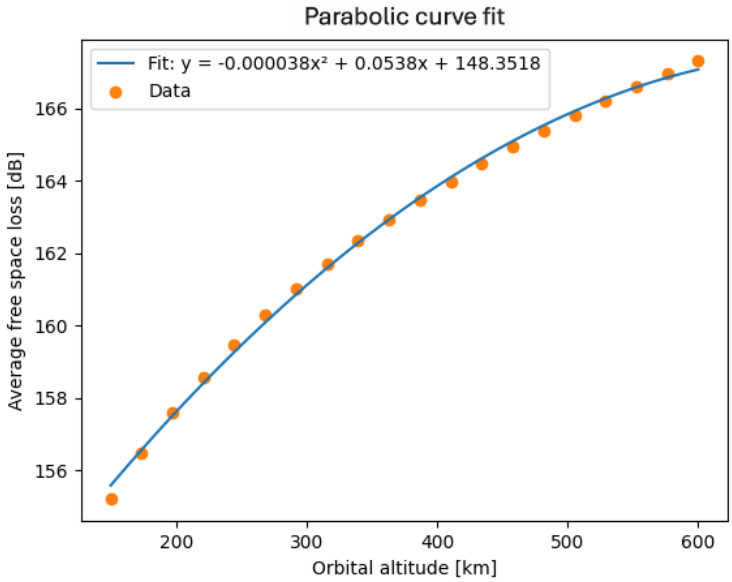

Figure 5.17: The average free space loss $\bar{L}_S$ as a function of orbital altitude h fitted to a second degree polynomial

pointing loss and orbital altitude too. Therefore, pointing loss in this model is included in the form of a constant estimate of $0.5\,\mathrm{dB}$ [155].

Atmospheric attenuation L_A is the result of absorption of the communication signal, mainly by oxygen and water vapor, and happens primarily in the troposphere and stratosphere (up to $100\,\mathrm{km}$ so that there is no dependency on orbital altitude of the satellite) [156]. It is primarily dependent on the transmission frequency as well as the elevation angle. A link in the X-band experiences about $0.35\,\mathrm{dB}$ of loss due to the atmosphere [157]. It needs to be corrected for by the cosecant of the elevation angle, which in the worst case is equal to $37°$ [154]. For this angle, the loss is $1.33\,\mathrm{dB}$. The link budget thus assumes the average loss over one pass of $0.87\,\mathrm{dB}$.

The last loss that is considered by the model is the line loss on the transmission and reception side, L_{Tl} and L_{Rl} respectively. This loss includes contributions of all hardware components. As it is independent of the budget-saving parameters, the model takes an estimate of $5.5\,\mathrm{dB}$ and $2\,\mathrm{dB}$ on the transmitting and receiving side respectively, based on typical values [154].

All factors that contribute to the link budget are summarized in Table 5.13.

Table 5.13: The link budget

Parameter	Value	Unit
Orbital altitude	$150 - 600$	km
Half-power beamwidth	74	$^\circ$
Frequency	8400	MHz
Downlink data rate	(Equation 5.39)	Mbps
Satellite		
Amplifier output power	TBD	W
Line loss	5.5	dB
Antenna peak gain	6	dBi
Antenna pointing loss	0.5	dB
Path		
Free space loss	(Equation 5.41)	dB
Atmospheric loss	0.87	dB
Ground station		
G/T (KSAT SG3 [158])	35.7	dBK^{-1}
Line loss	2	dB
Eb/No	(Table 5.12)	dB
Link margin	3	dB

In order to close the link budget with a link margin of $3\,\mathrm{dB}$, E_b/N_0 must be equal to the value stated in Table 5.12 + $3\,\mathrm{dB}$ [159]. It is calculated by expressing the data rate in $\mathrm{dB-Hz}$ and using it as follows [154]:

$$R_b = 10 \cdot \log(DR_{dowm} \cdot 10^6) \tag{5.42}$$

$$(E_b/N_0 + 3) = C/N_0 - R_b \tag{5.43}$$

$$C/N_0 = EIRP + G/T - (\bar{L}_S + L_P + L_A + L_{Rl}) + 228.6 \tag{5.44}$$

$$EIRP = P_{Tx} + G_{Tx} - L_{Tl} \tag{5.45}$$

Rewriting for the transmission power:

$$P_{Tx,dB} = (E_b/N_0 + 3) + DR_{down} - G/T + (\bar{L}_S + L_P + L_A + L_{Rl}) - 228.6 - G_{Tx} + L_{Tl} \tag{5.46}$$

The link budget was evaluated using mean values for the downlink data rate and average free space loss. The found relation between P_{Tx} (in dBm) and h is visualized in Figure 5.18. The bumps in the graph are a result of the change in modulation. Clearly, the required output power in order to close the link budget is within the capability of the chosen X-band transmitter (Table 5.11).

Finally, the complete model is captured in Table 5.14.

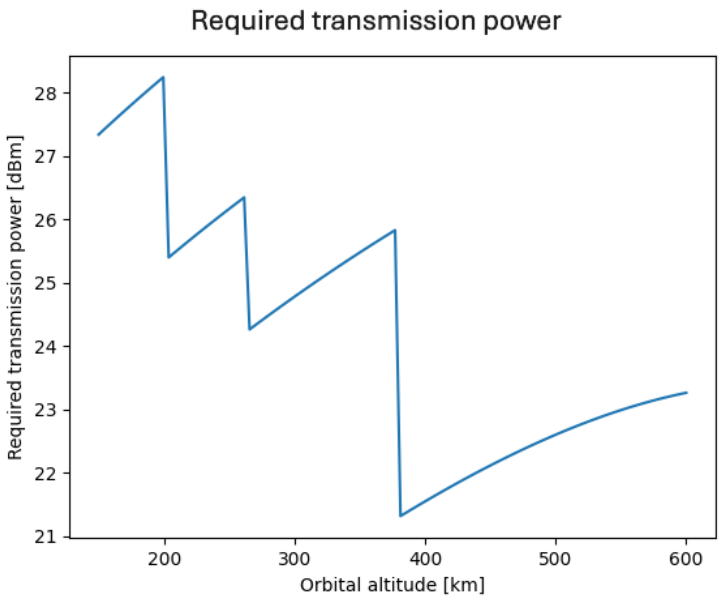

Figure 5.18: The required transmission power P_{Tx} as a function of orbital altitude h using mean values for downlink data rate DR_{down} and average free space loss $\bar{L}_S$

Table 5.14: The communications model

Relations	Inputs	Outputs
$\alpha = \pi - \arcsin\left(\frac{(R_e+h)\sin(\beta)}{Re}\right)$	h	
	$\beta = 74\ °$	
$\theta = \pi - \alpha - \beta$		
$t_{com} = \frac{T\theta}{\pi}$	T	
$DR_{down} = 566.6 \cdot e^{-0.0069 \cdot h} + 59.06\ \pm\ \left(2.718 + 1.493 \cdot \left(\frac{T}{t_{com}}\right)\right)$		
$R_b = 10\log(DR_{dowm} \cdot 10^6)$		
$\bar{L}_S = -0.000038 \cdot h^2 + 0.0538 \cdot h + 148.3518\ \pm\ 0.1572$		
$E_b/N_0 = f(h)$	Table 5.12	
$L_{loss} = \bar{L}_S + L_P + L_A + L_{Rl}$		
$P_{Tx,dB} = (E_b/N_0 + 3) + R_b - G/T + L_{loss} - 228.6 - G_{Tx} + L_{Tl}$	$G/T = 35.7\ \mathrm{dBK}^{-1}$	
	$L_P = 0.5\ \mathrm{dB}$	
	$L_A = 0.87\ \mathrm{dB}$	
	$L_{Rl} = 2\ \mathrm{dB}$	
	$G_{Tx} = 6\ \mathrm{dB}$	
	$L_{Tl} = 5.5\ \mathrm{dB}$	
$P_{Tx} = 10^{\frac{P_{Tx,dB}}{10}}$		
$P_{in} = 3.9058 \cdot P_{Tx} + 9.8514\ \pm\ 2.516$		
$P_{com} = \frac{t_{com} \cdot (1+Pin)}{T}$		P_{com}
Validity	25 % metadata/packet overhead 150 km to 600 km polar orbit 1 communication window per orbit 74° beamwidth X-band 8400 Hz 1 W to 2 W transmission power 75 Mbps to 250 Mbps data rate KSAT ground station 155 dB to 167 dB free space loss	

5.9. AOCS Model

The AOCS is split up in sensors and actuators. For both, an evaluation of their volume and power is presented.

5.9.1. Sensors

The sensors determine an absolute attitude and location with respect to an external reference frame, or a relative attitude compared to an initial attitude. The accuracy of relative sensors is usually higher, although they show drift over time and thus require frequent calibration by absolute sensors. Therefore, this design considers the use of absolute sensors.

Input to the sensor system design is requirement SYS-05. As pointing knowledge needs to translate to at least $10\,\mathrm{m}$ on ground for all configurations, an indication for the pointing knowledge requirement at different altitudes can be obtained as follows:

$$\theta_{point} = \frac{10}{h}$$

For the altitudes investigated in this thesis ($150\,\mathrm{km}$ to $600\,\mathrm{km}$), necessary pointing knowledge thus ranges from $0.001\,^\circ$ to $0.004\,^\circ$ or $3\,\mathrm{arcsec}$ to $14\,\mathrm{arcsec}$ cross-boresight. Comparing these numbers to typical absolute sensor performance as stated in Table 5.15, immediately the need for star trackers is evident [160]. For COTS star trackers with such accuracies, no clear relation was found between boresight accuracy and volume, as can be concluded from Table 5.16. Therefore, the volume of this sensor is assumed constant among the different configurations investigated and is considered to be independent of the budget-saving parameters.

Table 5.15: The performance of typical AOCS sensors

Sensor	Accuracy
Earth horizon sensor	0.05° to 1°
Sun sensor	0.005° to 3°
Star tracker	$3 \times 10^{-4\circ}$ to 0.01°
Magnetometer	0.5° to 3°

Table 5.16: The characteristics of some COTS star trackers

Star tracker (manufacturer)	Accuracy cross boresight	Volume	Power
Sagitta high-precision star tracker (Arcsec) [10]	$2\,\mathrm{arcsec}$	$2.09 \times 10^{-4}\,\mathrm{m}^3$	$1.5\,\mathrm{W}$
Star Tracker (Redwire Space) [11]	$10\,\mathrm{arcsec}$	$4.47 \times 10^{-4}\,\mathrm{m}^3$	$2.5\,\mathrm{W}$
ST400 (AAC Clydespace) [12]	$10\,\mathrm{arcsec}$	$2.65 \times 10^{-4}\,\mathrm{m}^3$	$0.7\,\mathrm{W}$
KSST-01 Star Tracker (Kairospace) [13]	$5\,\mathrm{arcsec}$	$3.62 \times 10^{-4}\,\mathrm{m}^3$	$0.3\,\mathrm{W}$

The model considers two Sagitta high-precision star trackers and thus reserves $418\ \mathrm{cm}^3$ in total for these components, which together consume $3\,\mathrm{W}$ of power. Two star trackers assure that there is always one that is not blinded by Earth or the Sun. Primarily, this specific sensor is considered as it meets the pointing accuracy requirement of $3\,\mathrm{arcsec}$ for a $600\,\mathrm{km}$ orbit. Moreover, it has a relatively low volume compared to the other sensors while still providing an acceptable around boresight accuracy of $10\,\mathrm{arcsec}$.

This, however, does not complete the sensor package. A star tracker namely only measures angles with respect to the stars. The satellite thus also needs knowledge on its position with respect to Earth to complete localization. For this, a GNSS receiver is integrated. Again, position knowledge needs to

[10] https://www.arcsec.space/sagitta/
[11] https://redwirespace.com/wp-content/uploads/2023/06/redwire-spectratrac-flysheet.pdf
[12] https://www.aac-clyde.space/what-we-do/space-products-components/AOCS/st400
[13] https://www.kairo.space/products/ksst-01-star-tracker

be better than $10\,\mathrm{m}$, which is within the range of the GNSS receiver Celeste supplied by Spacemanic and therefore, this one is considered in the model [14]. The receiver measures $6.7\,\mathrm{cm}$ x $4.2\,\mathrm{cm}$ x $0.7\,\mathrm{cm}$ and consumes $0.1\,\mathrm{W}$ of power.

Lastly, redundant sensors such as Sun sensors could be added to the design to improve system reliability. These consume negligible volume and power and are thus not explicitly included in the model. The complete sensor package used to model the attitude sensors is listed in Table 5.17.

Table 5.17: The AOCS sensors considered in the model

Sensor	Quantity	Volume	Power
Sagitta high-precision star tracker (Arcsec)	2	$2.09 \times 10^{-4}\,\mathrm{m}^3$	$1.5\,\mathrm{W}$
Celeste GNSS receiver (Spacemaniac)	1	$1.97 \times 10^{-5}\,\mathrm{m}^3$	$0.1\,\mathrm{W}$
Total	3	$4.38 \times 10^{-4}\,\mathrm{m}^3$	$3.1\,\mathrm{W}$

5.9.2. Actuators

The actuators, on the other hand, do scale with the budget saving parameters as predicted in Subsection 5.2.1 and are thus modeled mathematically. They enable pointing of the instrument according to SYS-06 and counteract disturbances. Due to the precision of the payload and the importance of its spatial resolution for the mission, three-axis active attitude control is deemed necessary. Although passive aerodynamic control as discussed in Subsection 2.2.2 could complement the system when located in VLEO, this technique does not provide the control accuracy and agility required for the mission and its low TRL demands significant research effort which is not feasible for the scope of this study [37].

Although the instrument is used in a push-broom configuration, pointing cross-track is deemed necessary for coverage of all areas of interest within the constellation. SYS-06 expresses this need and imposes a minimum slew rate (SR) requirement on the AOCS. The slew rate translates to a requirement on the torque to be delivered by the actuators.

$$SR = \frac{\frac{\Delta\iota \cdot \pi}{180}}{\Delta t} = 0.0524\ rad/s \tag{5.47}$$

The disturbance torques imposed on the satellite originate from aerodynamic interactions, gravity gradients, solar radiation and magnetic dipoles. Gravity gradient torque is not considered explicitly as its magnitude is relatively low and it is only relevant during pointing maneuvers, which account for just a small fraction of the orbital period. The other toques are continuous and therefore quantified below.

Aerodynamic Torque

Aerodynamic torque follows from Equation 5.48, where cp_a denotes the aerodynamic center of pressure and cm is the center of mass of the satellite.

$$T_a = \frac{1}{2}\rho_{atm} C_D A v_{sat}^2 (cp_a - cm) \tag{5.48}$$

A, cp_a and cm depend on the satellite's configuration. In order to calculate the frontal area A, a simplified geometry of the spacecraft is assumed as depicted in Figure 5.19. It considers the satellite side panel and (deployed) baffle area, $y_{body} z_{body}$ and A_{baffle} (if the baffle is not integrated in the satellite body). As the deployed baffle area is expected to dominate that of the Earth shade door A_{tc}, torque around the z-axis is considered for sizing of the actuators. The solar panels are not taken into account as they are aligned with the velocity vector. In the final model, x_{body}, y_{body} and z_{body} are iterated upon based on the satellite volume. A_{baffle} was found to be a function of h and is an output of the payload model outlined in Table 5.6.

The mismatch between the aerodynamic center of pressure cp_a and the center of mass cm is computed for the DST concept design and taken as a percentage of y_{body}. For this, the payload mass is assumed to be $\frac{1}{3} - \frac{1}{2}$ of the total mass with its center of pressure at $\frac{1}{4} - \frac{1}{3}$ of the deployed baffle length l_{baffle}. The

[14] https://www.spacemanic.com/celeste-gnss-receiver/

mass in the body is assumed to be homogeneously distributed. By smartly distributing the mass in the body, the arm between cp_a and cm can be reduced and the AOCS design could be optimized. The DST concept assumes a cubical effective stowed volume similar to geometry case III (Integrated baffle) and IV (Cubical) in Section 5.4. The deviant geometries assume a horizontal rectangular effective stowed frontal area, which implies a lower $cp_a - cm$ mismatch. This model is therefore conservative in those cases.

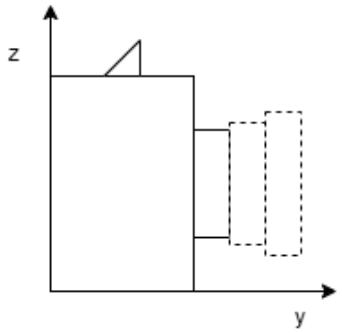

Figure 5.19: The simplified geometry of the satellite for evaluation of the aerodynamic center of pressure cp_a

The $cp_a - cm$ mismatch for the DST concept, a $27\,\mathrm{U}$ satellite at $300\,\mathrm{km}$, is calculated to be $0.1486 - 0.2606$ of y_{body}:

$$cp_a - cm = (0.1486 - 0.2606) \cdot y_{body} \tag{5.49}$$

C_D contains information on the satellite geometry and is assumed to be equal to that of a flat plate. However, this parameter also changes as a result of atmospheric conditions (Section 2.2). At high altitudes, the flow is sufficiently rarefied such that gas surface interactions dominate inter-molecular collisions, a condition called Free Molecular Flow (FMF). On the contrary, at lower altitudes, atmospheric density is larger and thus, flow cannot be accurately modeled as being FMF. The discrepancy is visualized in Figure 5.20 [34]. Based on C_D analysis done in other studies, the following relation was obtained for $h = 150\,\mathrm{km}$ to $600\,\mathrm{km}$ [34][161]:

$$C_D = 0.0005 \cdot h + 2.0169 \ \pm \ 0.02 \tag{5.50}$$

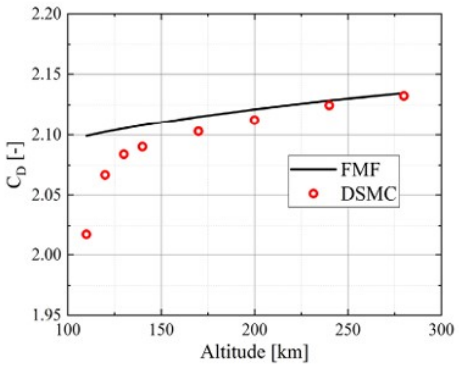

Figure 5.20: The drag coefficient C_D for a flat plate as a function of orbital altitude h when assuming free molecular flow (FMF) and using direct Monte Carlo simulation (DMCS) [34]

ρ_{atm} does not only vary with h, it is also susceptible to the solar cycle, day-to-night variations, seasonal-latitudinal and (semi-)annual variations and was found to be complex to capture in a model (see Section 2.2) [40]. In order to simulate all these effects, the mean atmospheric density during high solar

activity as a function of h is used in the model and is depicted in Figure 5.21 [162]. Assuming a maximum lifetime of $7\,\text{years}$ and solar cycle of $11\,\text{years}$, high solar activity was found to be the most likely worst-case scenario. The graph is captured by the following power law:

$$\rho_{atm} = 15742 \cdot h^{-5.847} \tag{5.51}$$

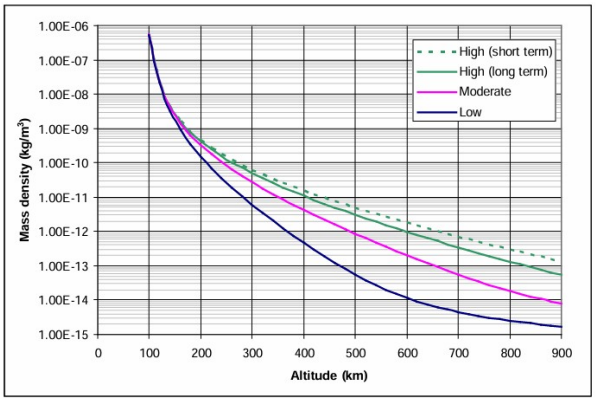

Figure 5.21: The mean atmospheric density as a function of altitude for low, moderate and high solar activity [162]

This preliminary analysis assumes linear proportionality between the satellite's body dimensions x_{body}, y_{body} and z_{body} and h, based on the linear proportional relationship between the M1 diameter D and h. Moreover, a cubical body is assumed here so that $x_{body} = y_{body} = z_{body}$ and the body dimension is taken to be $0.35\,\text{m}$ at $300\,\text{km}$ in line with the concept design [132]. Using mean values for d_{M1-M2}, C_D and $cp_a - cm$ and assuming a three-segmented baffle design reveals a torque starting at $1.5 \times 10^{-4}\,\text{Nm}$ and reducing to $3.2 \times 10^{-6}\,\text{Nm}$ as depicted in Figure 5.22. These assumptions are solely used to generate the aforementioned plot and gain insight in the orders of magnitude. The final model iteratively calculates x_{body}, y_{body} and z_{body} based on the satellite volume until convergence is achieved as explained in Section 5.11. Moreover, $n_{segments}$ is uniformly distributed in the final model to find a system optimum.

Solar Radiation Torque

Solar radiation induces torque due to the momentum exchange between the satellite and the absorbed photons. For a right angle of incidence, it is defined as [154]:

$$T_s = \frac{\Phi}{c} A \cdot (1 + q_{refl})(cp_s - cm) \tag{5.52}$$

The largest torque is experienced on the least symmetrical face of the satellite, which is the same face that was considered for the aerodynamic torque analysis. Therefore, $cp_s - cm = cp_a - cm$. Φ is the solar constant, which is equal to $1366.1\,\text{Wm}^{-2}$ [140]. c is the speed of light, $3 \times 10^8\,\text{ms}^{-1}$, and q_{refl} represents the unitless reflectance factor ranging from 0 to 1, where a value of 1 is taken as a worst case. As depicted in the bottom line in Figure 5.22, torque values range from $5 \times 10^{-8}\,\text{Nm}$ to $4 \times 10^{-6}\,\text{Nm}$.

Magnetic Dipole Torque

The magnetic torque is a result of the interaction between Earth's magnetic field and the currents inside the satellite. Its magnitude depends on the residual dipole moment of the satellite DP_{sat}, orbital altitude h, and a unitless function of the magnetic latitude ranging from $1 - 2$ from magnetic equator to poles, λ_{mag} (see Equation 5.53) [154]. M_{mag} stands for the magnetic moment of the Earth, which is $7.8 \times 10^{15}\,\text{Tm}^3$. Considering the highest torque experienced, which occurs at the magnetic poles where $\lambda_{mag} = 2$, and estimating $DP_{sat} = 10\,\text{Am}^2\text{m}^{-3}$ based on measurements of real satellites, this torque is a function of altitude and satellite volume as depicted in Figure 5.22: magnetic dipole torque starts at $3 \times 10^{-6}\,\text{Nm}$ and increases to $1.6 \times 10^{-4}\,\text{Nm}$.

$$T_m = DP_{sat}\left(\frac{M_{mag}}{(Re + h)^3}\lambda_{mag}\right) \tag{5.53}$$

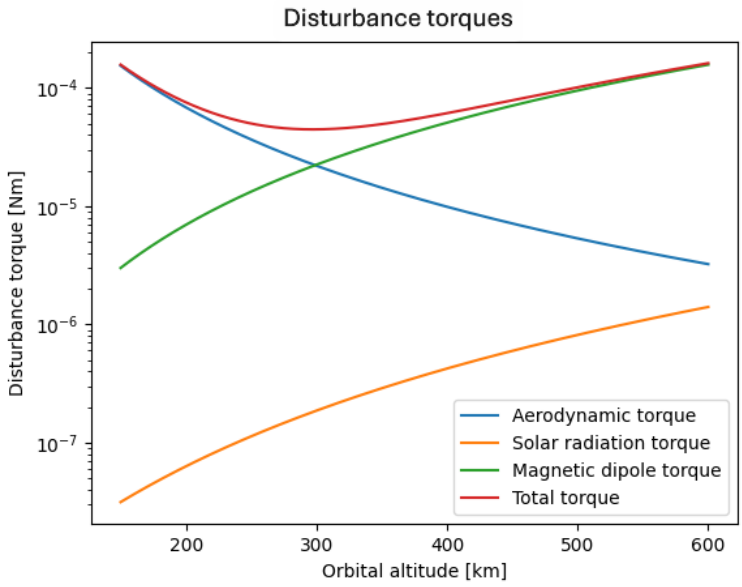

Figure 5.22: The disturbance torques as a function of orbital altitude h assuming linear proportionality between between the satellite's body dimensions x_{body}, y_{body} and z_{body} and h, a cubical body, mean values for d_{M1-M2}, C_D, $cp_a - cm$ and a three-segmented baffle

This preliminary analysis predicts a combined disturbance torque from $4.7 \times 10^{-5}\,\mathrm{Nm}$ to $1.8 \times 10^{-4}\,\mathrm{Nm}$ with a negligible contribution from the solar radiation torque. Therefore, the model computes T_a and T_m and adds 10% to account for solar radiation and gravity gradient torque. It should be noted that here, the worst case is considered and the highest torques are added up, where in reality, this rarely happens.

The actuators must accumulate momentum for disturbance torque correction for at least half an orbit before desaturation over a maximum of half an orbit and provide the torque for instrument pointing. The accumulated momentum is calculated with Equation 5.54 and is plotted against orbital altitude in Figure 5.23. The momentum that is built up in the actuators over half an orbit to compensate for the total torque ranges from $0.13\,\mathrm{Nms}$ to $0.51\,\mathrm{Nms}$ assuming linear proportionality between the satellite's body dimensions x_{body}, y_{body} and z_{body} and h, a cubical body and mean values for d_{M1-M2}, C_D, $cp_a - cm$ and a three-segmented baffle.

$$M_{accumulated} = 1.1 \cdot (T_a + T_m)\frac{1}{2}T \tag{5.54}$$

Both Reaction Wheels (RWs) and Control Moment Gyros (CMGs) are considered for momentum accumulation. A rough order of magnitude calculation showed that at low altitudes, the accumulated momentum pushes the limits of COTS RWs whereas at high altitudes, the torque required for the pointing maneuver drives the system sizing. CMGs on the other hand can comfortably assist both. Another advantage that comes with CMGs is the increased agility and power efficency compared to RWs [163]. However, the preferable performance of the CMG comes at the cost of slightly increased volume. A comparison of volume, power and mass for some COTS RWs and CMGs is depicted in Figure 5.24a, Figure 5.24b and Figure 5.24c [15][16][17][18][19][20][21].

[15] https://www.rocketlabusa.com/space-systems/satellite-components/reaction-wheels/
[16] https://www.satcatalog.com/component/gen2-cubewheel-cw0500/
[17] https://www.satcatalog.com/component/microwheel-4000/
[18] https://www.aspina-group.com/en/technologies/014/
[19] https://ocetechnology.com/satellite-subsystems/
[20] https://www.researchgate.net/publication/341304204_Design_and_Structural_Analysis_of_a_Control_Moment_Gyroscope_CMG_Actuator_for_CubeSats
[21] https://tensortech.co/product/detail/cmg_for_over_30_kg

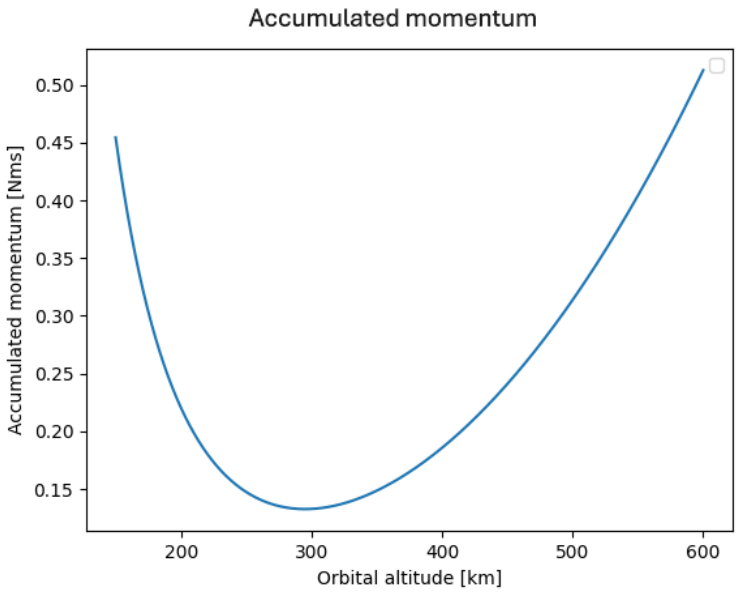

Figure 5.23: The accumulated momentum over half an orbit as a function of orbital altitude h assuming linear proportionality between the satellite's body dimensions x_{body}, y_{body} and z_{body} and h, a cubical body, mean values for d_{M1-M2}, C_D, $cp_a - cm$ and a three-segmented baffle

In order to make a decision on actuator type, a trade-off is performed. The criteria are **Volume** and **Power**, both with a weight of 0.3 due to their direct affect on satellite volume and thus mission feasibility. **Mass** is assigned a weight of 0.2, just like **Agility**, as these parameters are important to cost and performance of the mission, but are not the main focus of this research. The options are scored on a scale from 1 (lowest) to 5 (highest) and the trade-off table is presented in Table 5.18.

Table 5.18: The trade-off table for AOCS actuators

Criteria / Options	*Volume*	*Power*	*Mass*	*Agility*	*Total score*
Weights	0.3	0.3	0.2	0.2	-
Reaction wheel	L: Slightly better than CMG (Figure 5.24a).	Y: Higher power consumption.	G: Low mass (Figure 5.24c).	Y: Lower agility.	3.7
Control moment gyro	Y: Variable but slightly worse in general (Figure 5.24a).	G: Very power efficient (Figure 5.24b).	L: Slightly higher mass (Figure 5.24c).	G: Very agile.	4.2

To conclude, CMGs are preferred based on these criteria and are thus used by the model. Four of these actuators are implemented for redundancy. Sizing is driven by amount of momentum to be stored rather than torque required for pointing due to the relatively high torque capabilities of COTS CMGs.

From Figure 5.24a and Figure 5.24b, linear empirical relations following the least squares method are generated for volume and average power consumption of the CMGs based on their maximum momentum storage (the linearity of this relationship is based on the linearity between mass and momentum):

$$V_{CMG} = 7.221 \cdot 10^{-4} \cdot M_{accumulated} + 8.801 \cdot 10^{-4} \pm 4.026 \cdot 10^{-4} \tag{5.55}$$

$$P_{CMG} = 2.312 \cdot M_{accumulated} + 5.795 \pm 4.132 \tag{5.56}$$

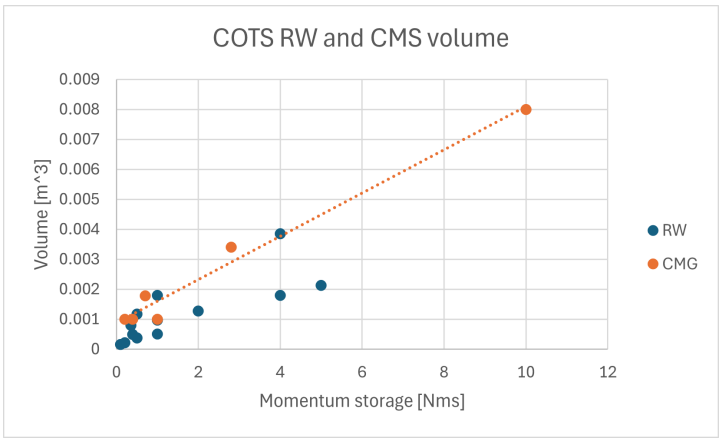

(a) Volume

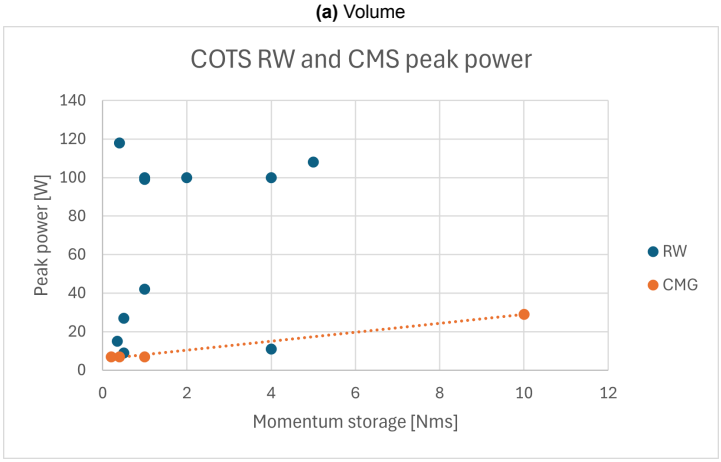

(b) Peak power

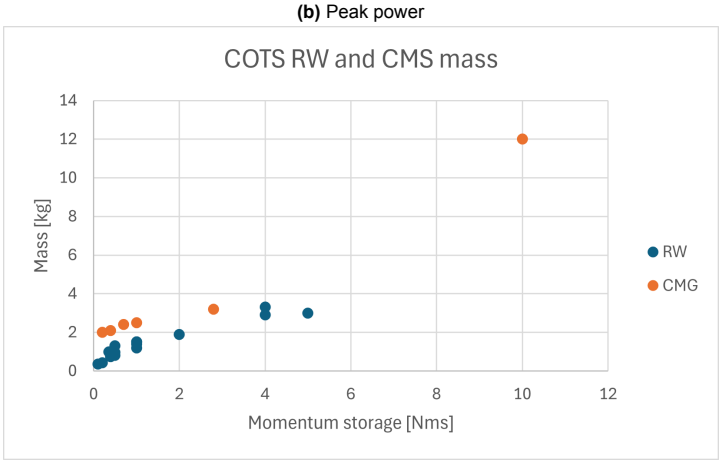

(c) Mass

Figure 5.24: Comparison of COTS RWs and CMGs in terms of volume, peak power, and mass plotted against momentum storage capability.

For low power desaturation of the actuators, three magnetorquers are used. Their power consumption scales with the amount of momentum dumping required. The torque to be provided by the magnetorquers is the summation of the disturbance torque and desaturation torque:

$$T_{MTQ} = 1.1 \cdot (T_a + T_m) + T_{desat} \tag{5.57}$$

When requiring desaturation within half an orbit, the minimum magnetic dipole is a function of orbital altitude, where $\lambda_{mag,avg}$ is equal to $2 - \frac{2}{\pi}$:

$$T_{MTQ} = 1.1 \cdot (T_a + T_m) + \frac{M_{accumulated}}{\frac{1}{2}T} = DP\left(\frac{M}{(Re+h)^3}\lambda_{mag,avg}\right) \tag{5.58}$$

$$DP = \frac{(Re+h)^3}{M\lambda_{mag,avg}}\left(\frac{M_{accumulated}}{\frac{1}{2}T} + 1.1 \cdot (T_a + T_m)\right) \tag{5.59}$$

This function is plotted assuming linear proportionality between the satellite's body dimensions x_{body}, y_{body} and z_{body} and h, a cubical body, mean values for d_{M1-M2}, C_D, $cp_a - cm$ and a three-segmented baffle in Figure 5.25. The required magnetic dipole follows the shape of the accumulated momentum $M_{accumulated}$ in Figure 5.23.

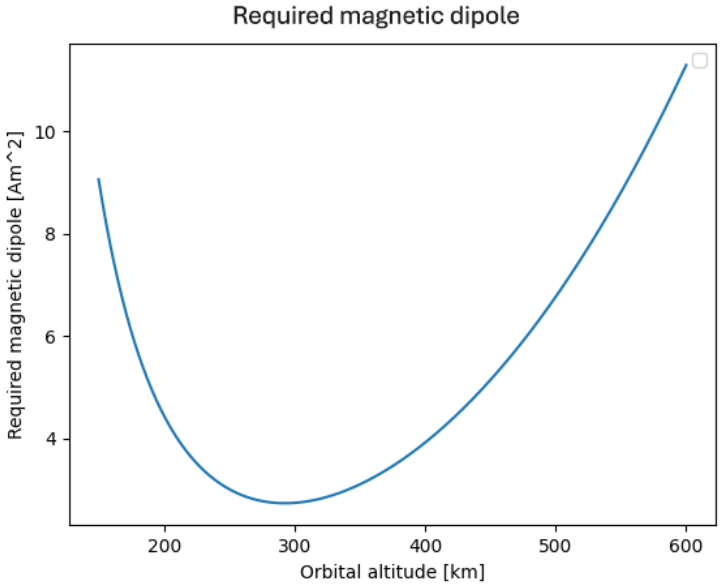

Figure 5.25: The magnetic dipole DP for a half-orbit desaturation as a function of orbital altitude h assuming linear proportionality between the satellite's body dimensions x_{body}, y_{body} and z_{body} and h, a cubical body, mean values for d_{M1-M2}, C_D, $cp_a - cm$ and a three-segmented baffle

The magnetorquers are sized based on the MTQ series from Tensor Tech of which linear empirical relations for volume and power are derived based on the least squares method [22]. The characteristics of this series are outlined in Table 5.19.

$$V_{MTQ} = 6.435 \cdot 10^{-6} \cdot DP + 1.795 \cdot 10^{-6} \ \pm \ 2.972 \cdot 10^{-5} \tag{5.60}$$

$$P_{MTQ} = 0.0858 \cdot DP + 0.0677 \ \pm \ 0.320 \tag{5.61}$$

The complete model along with the in- and outputs is summarized in Table 5.20.

[22] https://tensortech.co/product/category/mtq

Table 5.19: The characteristics of the Tensor Tech MTQ series [22]

	TensorMTQ-200m	TensorMTQ-2	TensorMTQ-20	TensorMTQ-20
Magnetic dipole [Am^2]	0.2	2	10	20
Volume [m^3]	$7 \cdot 10^{-6}$	$2 \cdot 10^{-5}$	$1.26 \cdot 10^{-4}$	$1.26 \cdot 10^{-4}$
Power [W]	0.36	0.173	0.5	2

Table 5.20: The AOCS model

Relations	Inputs	Outputs
$V_{sensors} = 4.38 \cdot 10^{-4} \mathrm{m}^3$		
$P_{sensors} = 3.1\,\mathrm{W}$		
$\rho_{atm} = 15742 \cdot h^{-5.847}$	h	
$C_D = 0.0005 \cdot h + 2.0169 \ \pm \ 0.02$		
$A = A_{baffle} + y_{body} z_{body}$	A_{baffle}, y_{body}, z_{body} (iterative)	
$cp_a - cm = (0.1486 - 0.2606) \cdot y_{body}$		
$T_a = \frac{1}{2} \rho_{atm} C_D A v_{sat}^2 (cp_a - cm)$	v	
$DP_{sat} = 10 \cdot x_{body} y_{body} z_{body}$	x_{body}	
$T_m = DP_{sat} \left(\frac{M_{mag}}{(Re+h)^3} \lambda_{mag} \right)$		
	$M = 7.8 \cdot 10^{15}\ \mathrm{Tm}^3$	
	$\lambda_{mag} = 2$ (worst case)	
$M_{accumulated} = 1.1 \cdot (T_a + T_m) \frac{1}{2} T$	T	
$V_{CMG} = 7.221 \cdot 10^{-4} \cdot M_{accumulated} + 8.801 \cdot 10^{-4} \ \pm \ 4.026 \cdot 10^{-4}$		
$P_{CMG} = 2.312 \cdot M_{accumulated} + 5.795 \ \pm \ 4.132$		
$DP = \frac{(Re+h)^3}{M \lambda_{mag,avg}} \left(\frac{M_{accumulated}}{\frac{1}{2} T} + 1.1 \cdot (T_a + T_m) \right)$	$\lambda_{mag,avg} = 2 - \frac{2}{\pi}$	
$V_{MTQ} = 6.435 \cdot 10^{-6} \cdot DP + 1.795 \cdot 10^{-6} \ \pm \ 2.972 \cdot 10^{-5}$		
$P_{MTQ} = 0.0858 \cdot DP + 0.0677 \ \pm \ 0.320$		
$V_{AOCS} = V_{sensors} + 4 \cdot V_{CMG} + 3 \cdot V_{MTQ}$		V_{AOCS}
$P_{AOCS} = P_{sesnors} + 4 \cdot P_{CMG} + 3 \cdot P_{MTQ}$		P_{AOCS}
Validity	$4\,\mathrm{m}$ GSD Velocity aligned solar panels Payload mass = $\frac{1}{3} - \frac{1}{2}$ total mass Payload center of mass at $\frac{1}{4} - \frac{1}{3}$ baffle length Homogeneous body mass distribution Flat plate drag coefficient $1\,\mathrm{Nms}$ to $10\,\mathrm{Nms}$ accumulated momentum $0.2\,\mathrm{Am}^2$ to $20\,\mathrm{Am}^2$ required dipole moment	

5.10. Propulsion Model

For the propulsion subsystem, three main categories can be distinguished as suggested by Table 4.1: ABEP, regular EP and chemical propulsion. The decision on which system to implement is mainly dependent on the altitude regime that the satellite will fly in, as well as its geometry and lifetime t_{life}. Together they define the ΔV that must be provided to maintain the orbit and counteract the drag F_{drag}. F_{drag} is calculated as follows:

$$F_{drag} = \frac{1}{2}\rho_{atm} C_D A v_{sat}^2 \tag{5.62}$$

A plot of the drag as a function of orbital altitude is depicted in Figure 5.26 (assuming the satellite's body dimensions x_{body}, y_{body} and z_{body}, scale proportional with altitude, the body has a cubical shape and the baffle is composed of three segments). It ranges between $6.7\,\mathrm{mN}$ at $150\,\mathrm{km}$ and $0.023\,\mathrm{mN}$ at $600\,\mathrm{km}$. For these drag levels, a continuous thrust strategy is feasible for ABEP and regular EP. For chemical propulsion, a periodic strategy is considered.

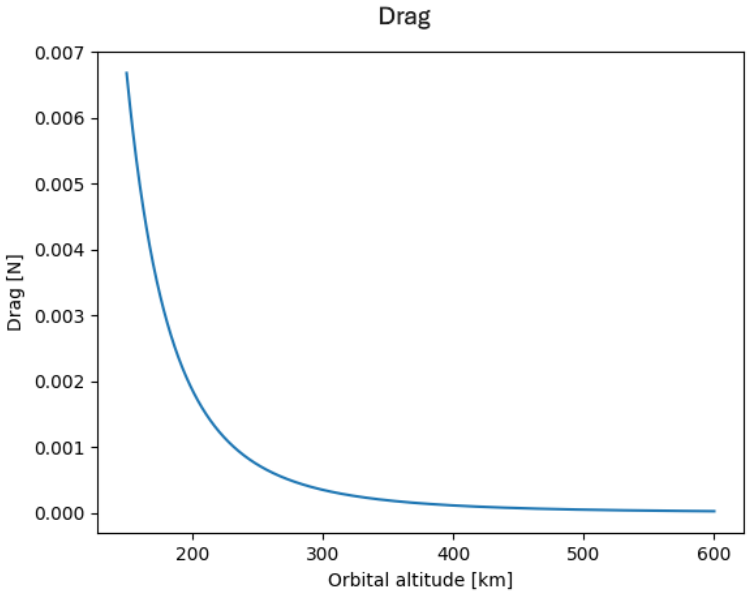

Figure 5.26: The drag F_{drag} as a function of orbital altitude h assuming linear proportionality between the satellite's body dimensions x_{body}, y_{body} and z_{body} and h, a cubical body, mean values for d_{M1-M2} and C_D and a three-segmented baffle

For a defined specific impulse I_{sp} and thrust level F_{thrust}, the propellant mass of the system m_{prop} is computed based on the amount of time the thruster fires, t_{prop}:

$$m_{prop} = \frac{F_{thrust}}{I_{sp} g_0} t_{prop} \tag{5.63}$$

As noted in Section 2.2, ABEP is only feasible in orbits from $150\,\mathrm{km}$ to $250\,\mathrm{km}$. For altitudes beyond this range, ABEP is excluded. From data on the experimentally tested ABEP systems defined in Table 2.2, a linear empirical relation based on the least squares method between F_{drag} and ABEP power consumption P_{ABEP} is established:

$$P_{ABEP} = 29240 \cdot F_{drag} + 155.6 \ \pm \ 257.4 \tag{5.64}$$

The volume of such ABEP system is defined by the thruster and intake only, as the residual atmosphere takes the role of propellant. Due to the deficiency of information on this novel type of technology and its similarity to regular EP, the dry volume is carried over from regular EP and an additional margin of 50% is included to account for the low TRL. Intake area and volume, A_c and V_{intake}, are derived from a bottom-up calculation. The area is based on the drag and collection efficiency η_c [164]:

$$A_c = \frac{F_d}{\eta_c I_{sp,ABEP} g_0 \rho_{atm} v_{sat}} \tag{5.65}$$

The intake design is characterized by balancing η_c with the compression ratio. Optimal intake aspect ratios $L/\sqrt{A}$ between $5-10$ ensure sufficient compression at $\eta_c = 0.25-0.4$ [164]. Using an array of inlet ducts rather than a single inlet duct boosts $L/\sqrt{A}$ without increasing intake volume. A maximum of 1000 ducts is assumed for this analysis, following from manufacturing and mass considerations. The volume of the intake V_{intake} is then computed as follows:

$$V_{intake} = 1000^{-0.5} \cdot A_c^{1.5} L/\sqrt{A} \tag{5.66}$$

Analyzing the intake area assuming a typical $I_{sp,ABEP}$ of $4000\,\mathrm{s}$ for Hall-effect and ion thrusters and optimistic $\eta_c = 0.4$ & $L/\sqrt{A} = 5$ results in Figure 5.27a, Figure 5.27b and Figure 5.27c, where the body is assumed to have a constant area. The baffle area of a three-segmented baffle is plotted alongside the body area for reference and turns out to be always smaller than the intake. Clearly, feasibility of ABEP depends on $y_{body} z_{body}$ and is thus only considered when the body area exceeds the necessary intake area so that the intake does not drive the effective stowed volume. From the aforementioned figures, one can conclude that this occurs more often for larger satellites.

In order to evaluate the characteristics of regular EP for this mission, a similar approach to ABEP is taken, where the power P_{EP} relates to the drag as follows [165][166]:

$$P_{EP} = 15409 \cdot F_{drag} + 25.6 \ \pm \ 29.51 \tag{5.67}$$

Propellant mass is calculated with Equation 5.63, where I_{sp} is uniformly distributed $1150-7852\,\mathrm{s}$ and t_{prop} is equal to t_{life}. Assuming Xenon propellant with a density of $1350\,\mathrm{kgm}^{-3}$, the propellant volume is computed as well [167]. For dry volume, no clear relationship with thrust level was found. Therefore, an average dry volume including a 10% margin of $0.86\,\mathrm{U}$ is decided upon.

For chemical propulsion, the fire time t_{prop} is calculated with:

$$t_{prop} = \frac{F_{drag} t_{life}}{F_{thrust}} \tag{5.68}$$

The thrust of such systems for CubeSats specifically varies between $0.1\,\mathrm{N}$ and $1\,\mathrm{N}$ and is thus taken as a continuous distribution [165]. Similarly, I_{sp} is varied between $200\,\mathrm{s}$ and $258\,\mathrm{s}$. For dry volume, $1\,\mathrm{U}$ (average) is defined. Assuming HAN propellant with a density of $1430\,\mathrm{kgm}^{-3}$, propellant mass and volume are computed [168]. Power consumption of such systems is negligible.

In order to select the best propulsion type for the mission, the volumes of all three options are compared. For this, the subsystem wet volume and battery + solar panel volume required to run the system are evaluated:

$$V = V_{dry} + V_{prop} + V_{intake} + \frac{P t_{eclipse} \cdot 1.12}{762000 \cdot 3600 \cdot DoD} + \frac{0.02 \cdot P_{EP}}{1366.1 \cdot 0.54 \cdot (1 - f_{Solstice}) \cdot 0.28 \cdot 0.8 \cdot 0.85} \tag{5.69}$$

Similarly to what was done in Section 5.9, this preliminary analysis assumes linear proportionality between the satellite's body dimensions x_{body}, y_{body} and z_{body} and h, a cubical body, mean values for all uncertain parameters and a three-segmented baffle. The final model uses the iteratively determined x_{body}, y_{body} and z_{body} as explained in Section 5.11 and considers a uniform distribution for $n_{segments}$. The total volume of the ABEP, regular EP and chemical propulsion including battery and solar panels is plotted in Figure 5.28: ABEP was only considered in its feasible altitude range from $150\,\mathrm{km}$ to $250\,\mathrm{km}$ and chemical propulsion only becomes the preferred strategy beyond $400\,\mathrm{km}$. The assumed increasing body dimensions drive the volume of the ABEP system so that it cannot compete with regular EP. Though, the final model iterates on these dimensions, possibly resulting in ABEP feasibility as well. Therefore, all three types of propulsion are evaluated in every iteration of the final model. The complete propulsion model is captured in Table 5.21.

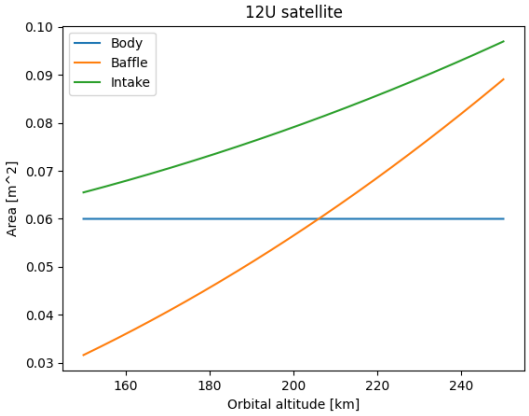

(a) 12U CubeSat

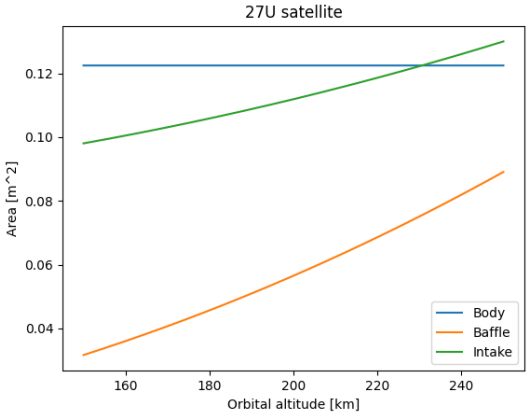

(b) 27U CubeSat

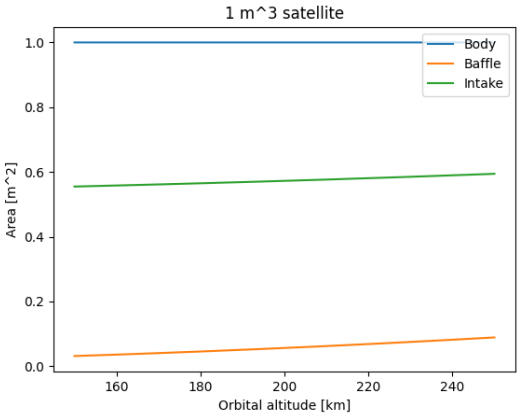

(c) $1\ \mathrm{m}^3$ Small satellite

Figure 5.27: The body, baffle and intake area for different satellite volumes

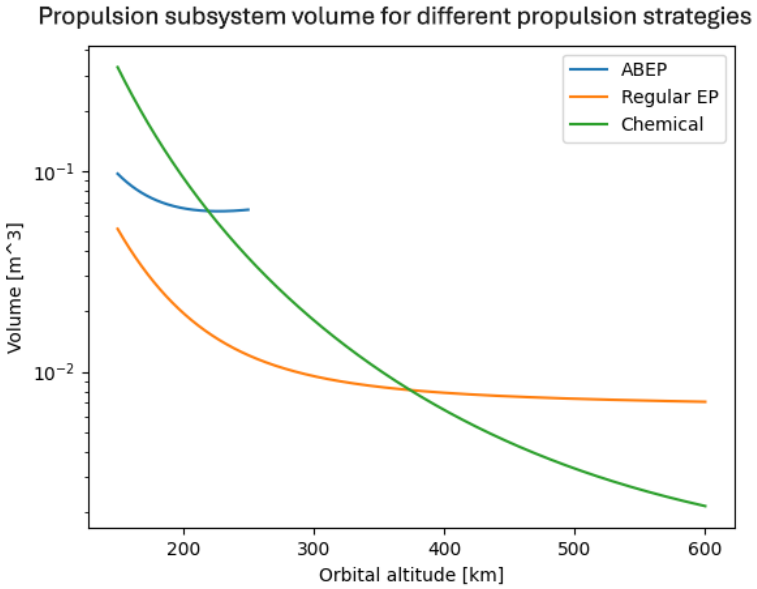

Figure 5.28: The total volume of the propulsion system V_{prop} including battery and solar panel volume assuming linear proportionality between the satellite's body dimensions x_{body}, y_{body} and z_{body} and h, a cubical body, mean values for all uncertain parameters and a three-segmented baffle

Table 5.21: The propulsion model

	Relations	Inputs	Outputs
	$F_{drag} = \frac{1}{2}\rho_{atm} C_D A v_{sat}^2$	ρ_{atm} (Equation 5.51) C_D (Equation 5.50) $A = y_{body} z_{body} + A_{baffle} + A_{tc}$ (iterative) v	
ABEP	$V_{ABEP,dry} = 1.29$ U $A_c = \frac{F_d}{\eta_c I_{sp,ABEP} g_0 \rho_{atm} v_{sat}}$ $V_{intake} = 1000^{-0.5} \cdot A_c^{1.5} L/\sqrt{A}$ $V_{ABEP} = V_{ABEP,dry} + V_{intake}$ $P_{ABEP} = 29240 \cdot F_{drag} + 155.6 \pm 257.4$	$\eta_c = 0.25 - 0.4$ $I_{sp,ABEP} = 2000 - 4000$ s $L/\sqrt{A} = 5 - 10$	V_{ABEP} P_{ABEP}
Regular EP	$V_{EP,dry} = 0.86$ U $m_{EP,prop} = \frac{F_{drag}}{I_{sp,EP} g_0} t_{life}$ $V_{EP,prop} = \frac{m_{EP,prop}}{1350}$ $V_{EP} = V_{EP,dry} + V_{EP,prop}$ $P_{EP} = 15409 \cdot F_{drag} + 25.6 \pm 29.5$	$I_{sp,EP} = 1150 - 7852$ s	V_{EP} P_{EP}
Chemical propulsion	$V_{ch,dry} = 1$ U $t_{prop} = \frac{F_{drag} t_{life}}{F_{thrust}}$ $m_{ch,prop} = \frac{F_{T,ch}}{I_{sp,ch} g_0} t_{prop}$ $V_{ch,prop} = \frac{m_{ch,prop}}{1430}$ $V_{ch} = V_{ch,dry} + V_{ch,prop}$	$F_{T,ch} = 0.1 - 1$ N, t_{life} $I_{sp,ch} = 200 - 258$ s	V_{ch}
Validity	Velocity aligned solar panels Flat plate drag coefficient <70 mN for ABEP 1000 ABEP ducts <18 mN for regular EP <1000 mN for chemical propulsion		

5.11. Activity Flow

With all subsystem volume budgets defined, the total subsystem volume is computed, accounting for a volume fill factor of $90\,\%$:

$$V_{bus} = \frac{V_{instumentbox} + V_{ICU} + V_{AOCS} + V_{prop} + V_{bat} + V_{sp}}{0.9} \tag{5.70}$$

x_{body}, y_{body} and z_{body} are then determined based on the rules established in Section 5.4. If the payload is external to the satellite bus (all cases but III in Section 5.4):

$$V_{eff,stowed} = x_{body} y_{body} z_{body} + h_{segment} x_{body} z_{body} \tag{5.71}$$

And for case III (integrated baffle):

$$V_{eff,stowed} = x_{body} y_{body} z_{body} \tag{5.72}$$

An N2 chart is generated to gain insight into how the subsystem models are connected and is depicted in Table 5.22.

Table 5.22: The N2 chart showing relations between the subsystem models

Sample payload					$n_{segments}$			t_{life}		
	ICU model									V_{ICU}
		Thermal model						A_{tc}		
			CDH model						P_{CDH}	
				Sample h	h	h	h	h	h	
					Payload model		A_{baffle}	A_{baffle}	P_{PL}, $h_{segments}$	V_{baffle}
						Com. model			P_{com}	
							AOCS model		P_{AOCS}	V_{AOCS}
								Propulsion model	P_{prop}	V_{prop}
									EPS model	V_{sp}, V_{bat}
							x_{body} y_{body} z_{body}	y_{body} z_{body}	y_{body} z_{body}	Volume budget

From the table, it is obvious that the generation of a system volume budget is iterative due to the relation between system volume and aerodynamic torque/drag. Therefore, x_{body}, y_{body} and z_{body} are iterated upon until a $1\,\%$ convergence in $y_{body} z_{body}$ is achieved.

6

Monte Carlo Simulation

The subsystem models defined in Chapter 5 form the basis of the satellite volume model. They are connected according to Table 5.22, resulting in a system model that computes the satellite's effective stowed volume as a function of altitude for a deployable and non-deployable space telescope while considering uncertainties in the input parameters by sampling their distributions. This chapter elaborates on the characteristics and use of this model in a Monte Carlo simulation.

6.1. Verification and Validation

Before proceeding to the Monte Carlo simulation, the model is validated: it is checked whether the model represents the correct real-life case by evaluating trends in the outcomes and matching results to expectations. Moreover, four reference cases are analyzed manually and compared to the model output in order to verify the outcome. This way, the face validity of the model is assessed. The assumptions made by the subsystem models are verified in this section as well.

6.1.1. Trend Validity

A single run of the model loops over the entire altitude range from $150\,\mathrm{km}$ to $600\,\mathrm{km}$ and attempts to arrive at a converged design at every altitude instance (every $1\,\mathrm{km}$ in this analysis). The final Monte Carlo simulation executes a multitude of these runs as described in Section 6.2. Plots of a single run of the model are depicted in Figure 6.1 to Figure 6.5.

As anticipated by the concept design and in line with the hypothesis in Chapter 3, a volume optimum exists in the VLEO regime around $250\,\mathrm{km}$ to $300\,\mathrm{km}$. Below, the effective stowed volume increases due to the increased atmospheric density and thus larger AOCS and propulsion subsystem (leading to bigger solar panels and batteries as well) as can be concluded from Figure 6.1. Contrastingly, at higher altitudes, the payload (the baffle specifically) dominates the effective stowed volume, driven by the aperture size. This is the case especially for a low number of baffle segments as seen in Figure 6.2, where the top line corresponds to a non-deployable configuration and the number of segments increases going down. The increase in the number of segments corresponding to a lower effective stowed volume is in agreement with the analysis plotted in Figure 6.6 (although an optimum baffle volume is not reached due to the constraint imposed by the deployable booms, see Subsection 5.2.2).

The effect of the mission lifetime on the effective stowed volume in Figure 6.3 seems very limited and only shows vague dependency at very low altitudes, again pointing at a lower relative AOCS and propulsion volume at high altitudes. Moreover, referring to Figure 6.4, chemical propulsion is preferred at higher altitudes whereas regular EP wins in lower orbits, matching what was concluded in Subsection 2.2.3. The two different trends in propulsion volume between $350\,\mathrm{km}$ to $550\,\mathrm{km}$ in Figure 6.1 are explained by this transition from regular EP to chemical propulsion, which in some cases appears to be beneficial in terms of total volume (a summation of propulsion subsystem volume as well as the additional battery and solar panel volume). None of the data points converges to ABEP, which is a logical trend considering the preliminary analysis and Figure 5.28.

Also interesting to note is the distribution of geometry cases in Figure 6.5, where the majority of the converged designs is driven by the outer diameter of the baffle (case II). At lower altitudes, when the aperture size and thus baffle outer diameter decreases, there is a regime that results in a cubical effective stowed volume (case IV), followed by designs that integrate the baffle within the body due to excessive unused volume adjacent to the baffle in a cubical configuration. This also means neither of the cases assessed in this sanity analysis is suitable for integration in a CubeSat pod (case I).

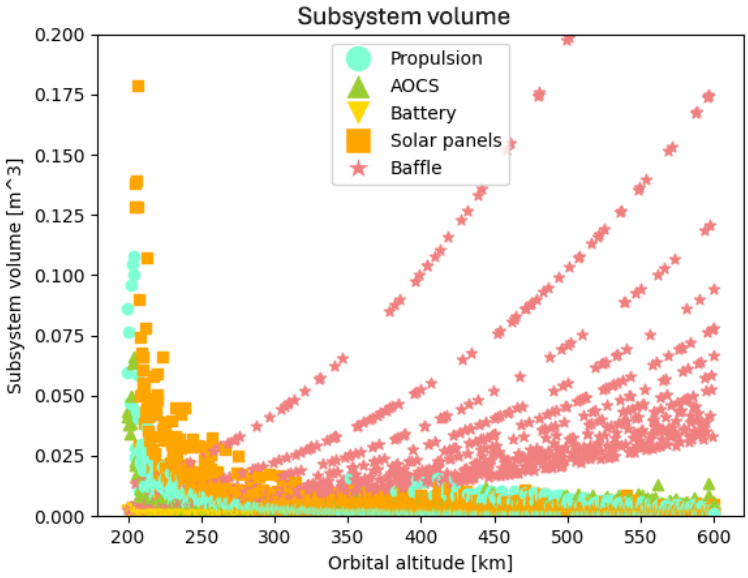

Figure 6.1: The subsystem volumes V_{prop}, V_{AOCS}, V_{bat}, V_{sp} and V_{baffle} for different input variables as a function of orbital altitude h

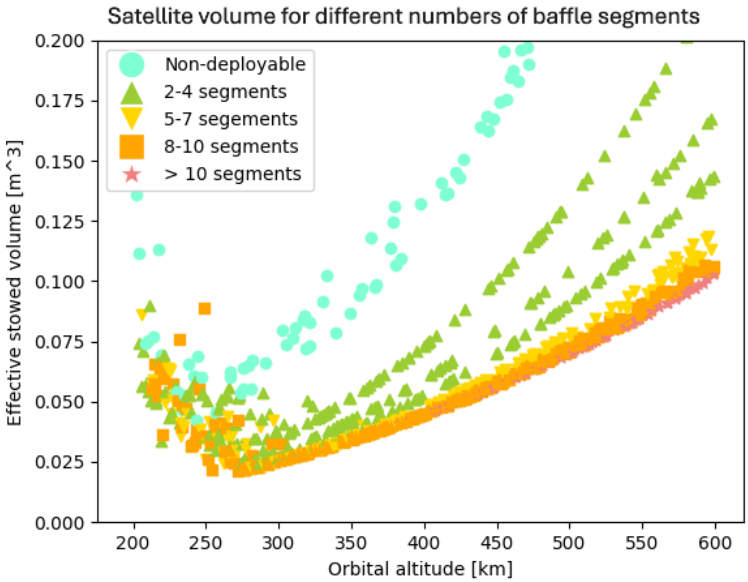

Figure 6.2: The effective stowed volume $V_{eff,stowed}$ as a function of orbital altitude h for different numbers of segments $n_{segments}$

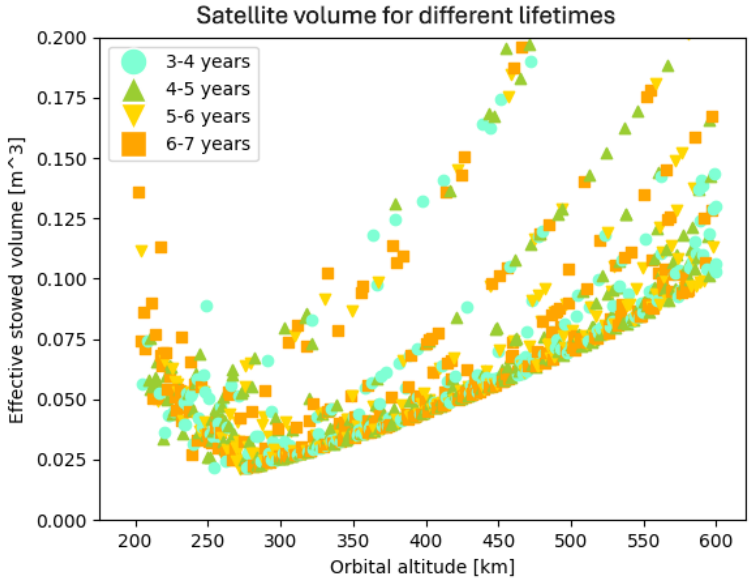

Figure 6.3: The effective stowed volume $V_{eff,stowed}$ as a function of orbital altitude h for different lifetimes t_{life}

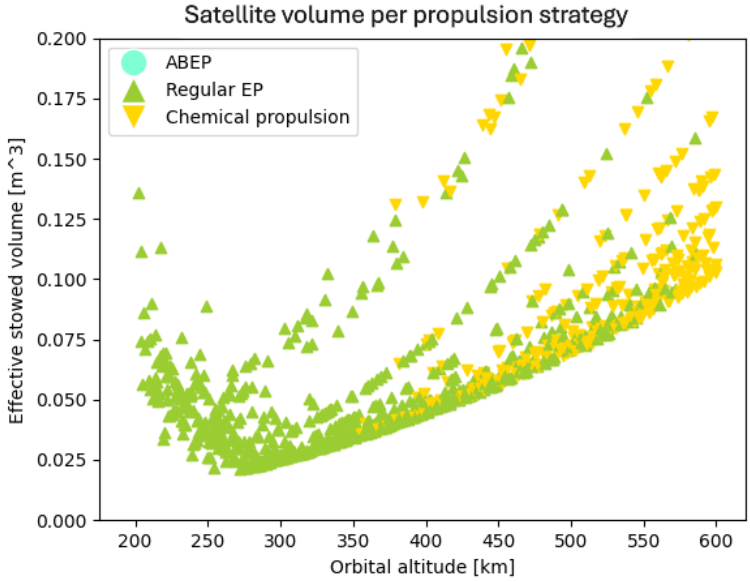

Figure 6.4: The effective stowed volume $V_{eff,stowed}$ as a function of orbital altitude h for different propulsion types

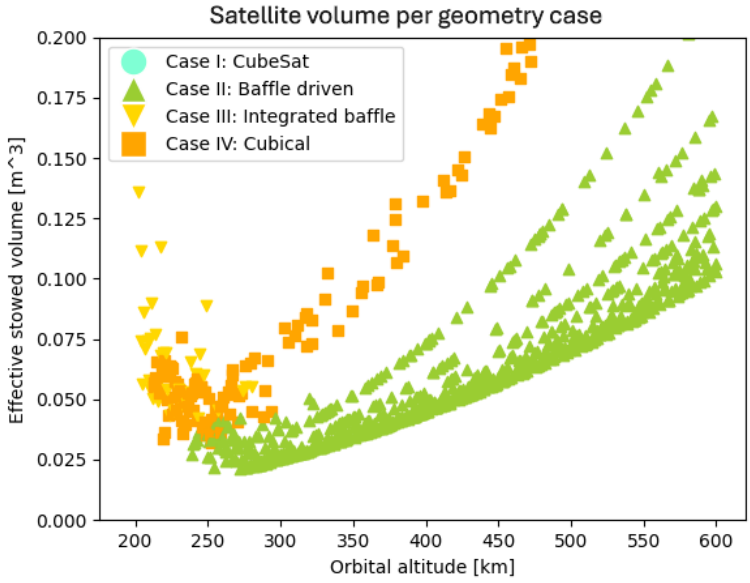

Figure 6.5: The effective stowed volume $V_{eff,stowed}$ as a function of orbital altitude h and the used geometry case

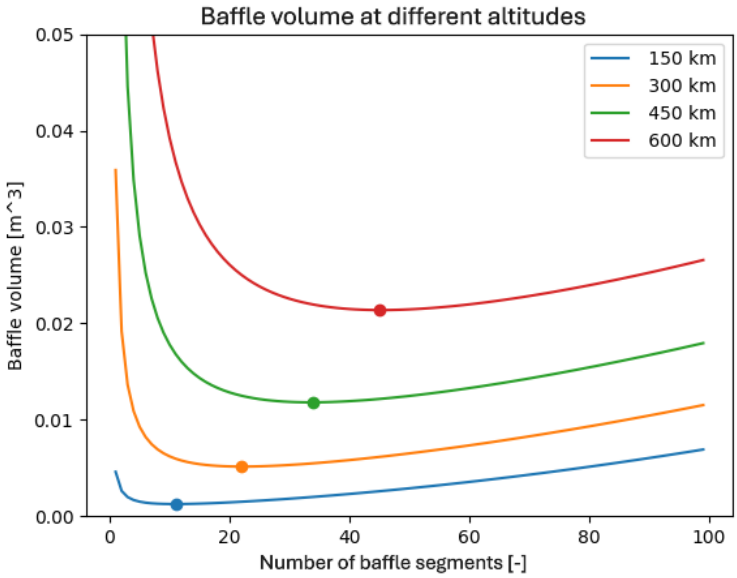

Figure 6.6: The baffle volume V_{baffle} as a function of the number of segments $n_{segments}$ for different orbital altitudes h assuming $\frac{d_{M1-M2}}{D} = 0.9$

Along with the increasing AOCS and propulsion volumes at low altitudes, their power consumption dominates this regime as depicted in Figure 6.7, leading to the driving solar panel volume revealed in Figure 6.1. Furthermore, as expected, the average communications power consumption increases with altitude due to the increased free space loss. In contrast to Figure 5.18, which depicts the instantaneous power consumption during transmission, the average power consumption takes into account the communication window and orbital period according to Equation 5.37. Due to the larger communication window with respect to orbital period in higher orbits, Figure 6.7 shows a different trend.

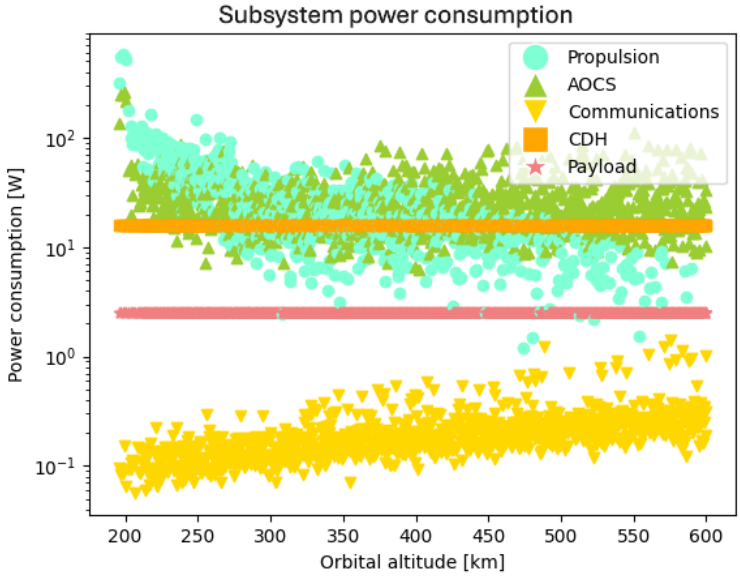

Figure 6.7: The subsystem power consumptions P_{prop}, P_{AOCS}, P_{com}, P_{CDH} and P_{PL} for different input variables as a function of orbital altitude h

6.1.2. Reference Cases

4 reference cases were analyzed manually. Their sampled variables were chosen randomly to replicate the model and are listed in Table 6.1. The first iteration assumes x_{body}, y_{body} and z_{body} equal to $0.34\,\mathrm{m}$, $0.35\,\mathrm{m}$ and $0.36\,\mathrm{m}$ respectively and geometry case IV ($27\,\mathrm{U}$ CubeSat).

Table 6.1: The variable inputs to the reference cases

Variable	Symbol	Case 1	Case 2	Case 3	Case 4
Orbital altitude	h	150 km	300 km	450 km	600 km
Mission lifetime	t_{life}	5 years	3 years	7 years	6 years
M1-M2 distance	d_{M1-M2}	0.121 m	0.301 m	0.222 m	0.591 m
Number of baffle segments	$n_{segments}$	7	3	2	10
ICU volume	V_{ICU}	0.34 U	0.86 U	0.25 U	0.75 U
Solstice eclipse fraction	$f_{Solstice}$	0.45	0.49	0.49	0.54
Depth of discharge	DoD	0.38	0.29	0.21	0.34
CHD power	P_{CDH}	15.5 W	6.75 W	9.19 W	17 W
Downlink data rate	DR_{down}	200 Mbps	221 Mbps	95 Mbps	163 Mbps
Average free space loss	$\bar{L}_S$	166 dB	168 dB	180 dB	167 dB
Drag coefficient	C_D	2.06	2.13	2.15	2.30
Percentage mismatch	$cp_a - cm$	0.204	0.157	0.193	0.235
Collection efficiency	η_c	0.40	–	–	–
ABEP Specific impulse	$I_{sp,ABEP}$	3000 s	–	–	–
Aspect ratio	$L/\sqrt{A}$	7	–	–	–
Regular EP specific impulse	$I_{sp,EP}$	480 s	6780 s	4830 s	1390 s
Chemical propulsion thrust	$F_{T,ch}$	0.4 N	0.2 N	0.9 N	0.7 N
Chemical propulsion specific impulse	$I_{sp,ch}$	233 s	209 s	247 s	258 s

Case 1
The results of for case 1 are tabulated in Table 6.2. This case did not converge as numbers exploded quickly. For the given set of inputs, there is thus no solution using the generated model. Therefore, convergence is a point of attention and should be analyzed. However, this makes it an interesting case to see what exactly drives the solution to the impossible.

As detailed in Table 5.22, the payload and communication characteristics are independent of the final body dimensions and only need to be computed once. The calculated baffle volume falls within the range seen in Figure 6.1 at $150\,\mathrm{km}$. The transmission power slightly exceeds the capabilities of the XTXG2 transmitter which was chosen as a reference (see Table 5.11). Though, the transmitter input power falls within the limits of the empirical model used (see Figure 5.14) and matches the trend in Figure 6.7.

Already in the first iteration, the aerodynamic torque is significantly higher than the value predicted by Figure 5.22. This can be explained by the difference in frontal area and $cp_a - cm$ mismatch. Where Figure 5.22 assumes linear proportionality between the body dimensions and altitude with a $27\,\mathrm{U}$ CubeSat at $300\,\mathrm{km}$ and thus effective stowed volume dimensions of $0.175\,\mathrm{m}$ at $150\,\mathrm{km}$, this run results in much larger body dimensions and an additional baffle area of $0.0330\,\mathrm{m}^2$. Hence, the frontal area in the first iteration is about six times larger and the $cp_a - cm$ mismatch multiplies this value by four. The same holds for the magnetic torque, which is computed based on the satellite bus volume. These discrepancies also explain the relatively high accumulated momentum compared to Figure 5.23, resulting in a required magnetic dipole that largely exceeds the model validity boundaries. Only the AOCS volume and power consumption in the first iteration roughly match Figure 6.1 and Figure 6.7. Contrastingly, the subsequent iterations cope with increasing frontal area and thus unreasonably large AOCS volumes and power consumptions.

The propulsion subsystem suffers from similar differences to the preliminary analysis in Section 5.10 as the AOCS, where the increased frontal area translates to more drag. From the second iteration onward, this drag exceeds the thrusting capabilities ABEP as stated in Table 2.2. Due to the increased frontal area however, ABEP becomes feasible by extrapolating the thrust as the intake does not extend beyond the satellite body anymore. This reduces the propulsion subsystem volume at the cost of an extreme increase in power consumption, which translates to an extremely large solar panel area and greater battery capacity. The extreme required solar panel volume cascades to even more drag in the following iterations, blowing up the propulsion subsystem further.

In terms of volume, the solar panels are clearly driving the effective stowed volume critically. This, in turn, is the result of extreme power consumption, initially by the propulsion subsystem but later on taken over by the AOCS. Conform expectations, these subsystems suffer from the increased drag in VLEO that was not considered in the linear scaling of the body dimensions assumed in Chapter 5, leading to a higher and higher effective stowed volume with every iteration. In order to cope with the large frontal area, the AOCS and propulsion model had to be extrapolated from the first iteration onward. Therefore, these variables are given extra attention to in Subsection 6.1.3. The fact that all iterations lead to geometry case III (integrated baffle) is a logical result of the extreme bus volume compared to the payload.

In conclusion, given the input values, the iterated values make sense but do not lead to a valid design. Convergence and extrapolation of the AOCS and propulsion model are the main concerns for this lowest orbit case.

Case 2
Case 2 is designed for an altitude of $300\,\mathrm{km}$, similar to the reference payload concept, and converged to a rectangular configuration after 52 iterations as listed in Table 6.3 [3] (based on a $1\,\%$ convergence criterion for the body dimensions). The stowed baffle volume corresponds to the outcome of the model for a baffle consisting of three segments in Figure 6.1. Transmission power again exceeds the capabilities of the XTXG2 but the communications power consumption resembles the high end of the plot in Figure 6.7. The main driver here is the downlink data rate, which is almost twice the predicted mean value in Figure 5.15, combined with a relatively high free space loss ($168\,\mathrm{dB}$ compared to the mean $161\,\mathrm{dB}$ as depicted in Figure 5.17).

The AOCS is significantly smaller than in case 1 due to a combination of lower atmospheric density and smaller frontal area. Both aerodynamic torque and magnetic dipole torque are in the same order of magnitude as predicted in Figure 5.22. The aerodynamic torque matches up really well as the dimensions of the effective stowed volume closely resemble a $27\,\mathrm{U}$ CubeSat. The magnetic dipole torque is slightly smaller than predicted due to the smaller bus volume. Thus, the accumulated momentum and required magnetorquer dipole remain within bounds and there is no need for extrapolation of the AOCS model. Volume and power consumption of the AOCS are much lower than the previous case and correspond to was is observed in Figure 6.1 and Figure 6.7.

Also the drag resembles Figure 5.26 due to the similar dimensions to the preliminary analysis. Regular EP in this case excels in specific impulse, causing it to have a lower volume than chemical propulsion and to be the propulsion type of choice. Volume and power of the converged propulsion subsystem compare to those in Figure 6.1 and Figure 6.7.

With the non-cubical geometry, fitting of sufficient solar panel area could be slightly more challenging as it results in a larger amount of panels. However, this case only required a total of eight segments, four on each side, to close the power budget which is almost equally driven by the AOCS and propulsion subsystem. Solar panels dominate the bus volume. Also interesting to note is that the baffle as part of the payload is the primary driver of the effective stowed volume geometry, hence geometry case II. The body height (y-dimension exluding exterior baffle) is already limited by the height of the instrumentation box. Only the communications model was extrapolated to reach a converged design.

Thus, the results from this case are plausible, though the extrapolation of the communication model is a point of attention.

Case 3

The third reference case is characterized in Table 6.4 and converged already after two iterations. Due to the relatively short M1-M2 distance ($0.222\,\mathrm{m}$ compared to a mean of $0.405\,\mathrm{m}$ as stated in Table 6.1), the baffle volume is less than outputted by the model in Figure 6.1. Transmission power on the other hand is closer to the capabilities of the XTXG2 (see Table 5.11) than case 2, while still relatively high due to an extreme free space loss prediction ($180\,\mathrm{dB}$ compared to the mean of $165\,\mathrm{dB}$ as in Figure 5.17). The resulting communications power consumption is in line with the prediction made by the model in Figure 6.7.

AOCS volume and power are slightly different from case 2, which is primarily caused by the standard deviation imposed on these models. The lower atmospheric density is mostly compensated for by the larger bus volume so that the total torque is in the same order of magnitude as in case 2. Simultaneously, the total torque is slightly smaller than what is predicted by the preliminary analysis in Figure 5.22, as the frontal area and bus volume of the satellite converge to smaller dimensions than anticipated. For the same reason, the drag is also somewhat smaller than what was predicted by the preliminary analysis. In contrast to Figure 5.28, regular EP is preferred at this altitude, although chemical propulsion is very competitive here. This can be explained by uncertainty on the regular EP power, which causes a decrease of almost $10\,\mathrm{W}$ compared to the mean power value for this drag level. Calculated volume and power of both of these subsystems are in line with Figure 6.1 and Figure 6.7.

Main driver of the effective stowed volume is the payload and the large baffle outer diameter causes geometry II to be preferred. Again, body height is defined by the height of the instrumentation box. Considering the bus only, AOCS plays a primary role and also drives the volume of the EPS. This trend of AOCS becoming the primary power consumer over propulsion matches Figure 6.7. Still, the number of solar panel segments is limited to seven. Therefore, similar to the previous case, the results are realistic: Only the communications model was extrapolated to finalize this design.

Case 4

The final reference case in Table 6.5 considers a traditional LEO orbit and also converged after two iterations. Due to the use of 10 segments, the baffle volume is managed and corresponds to the 10-segment line in Figure 6.1. A relatively high downlink data rate of $163\,\mathrm{dB}$ pushes the required transmission power, which exceeds the XTXG2 capabilities by $20\,\%$. Communications power consumption does match Figure 6.7.

AOCS and propulsion have reduced even further, as expected by the decreasing atmospheric density and distance to Earth. The aerodynamic torque matches Figure 5.22 really well while the magnetic torque turns out lower than anticipated due to a significantly smaller bus volume. Due to the lower strength of Earth's magnetic field, the required dipole is somewhat larger than in case 3, but falls comfortably within the boundaries of the model. The AOCS volume matches the forecast made by the model in Figure 6.1. In this case, the AOCS power consumption together with that of the CDH subsystem dominates the power budget which is in line with Figure 6.7.

Chemical propulsion is preferred as was hypothesized in Figure 5.28. Therefore, propulsion plays an insignificant role in the power budget. Its volume aligns with Figure 6.1 and is driven by the volume of the propellant. Moreover, it is in the same order of magnitude as calculated in the preliminary analysis in Figure 5.28. The slight deviation can be blamed on the higher-than-average lifetime of the mission in this reference case.

Also this case converged to a type II geometry, which is driven by the baffle outer diameter. The number of solar panels, six, is feasible. Propulsion and AOCS are less dominant than previously and other subsystems such as the CHD become more prominent. Only the communications models was slightly extrapolated in this design.

In conclusion, these reference cases provide insight in how the volume budget is built up. In general, the calculations match the model outcomes depicted in Figure 6.1 to Figure 6.7. Deviations from the preliminary analyses performed in Chapter 5 can be justified by considering the input parameters and converged design characteristics. The different geometries of the converged reference cases are depicted in Figure 6.8.

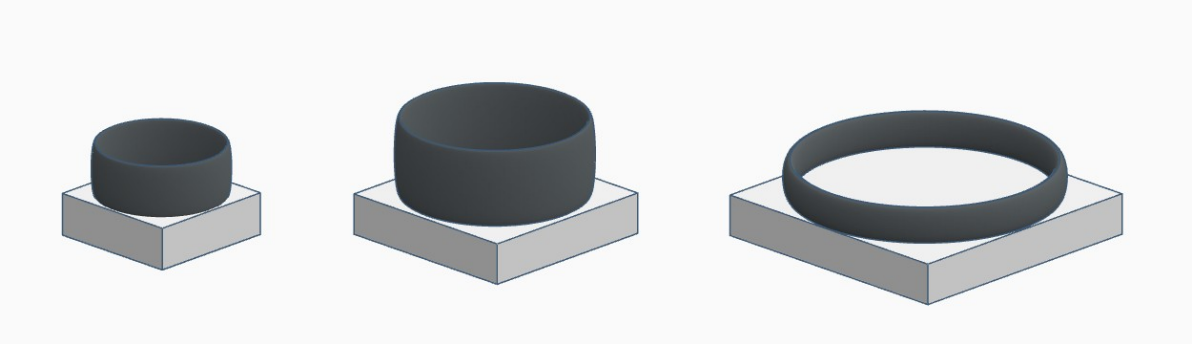

Figure 6.8: The geometry of the converged reference cases. From left to right: case 2, case 3, case 4

Some conclusions can be drawn with respect to the model:

- The transmission power required to close the link budget consistently exceeds the capabilities of the chosen reference system XTXG2 in the analyzed cases. Therefore, an additional analysis is performed in Subsection 6.1.3 to see what percentage of runs lead to such exceedance.
- In the majority of the cases, the geometry of the effective stowed volume is constrained by the outer diameter of the baffle as part of the payload, leading to a non-cubical configuration. Inherent consequences of this are lower-than-expected aerodynamic torque and drag. However, this configuration also could make fitting of solar panels more challenging due to the relatively smaller frontal area. Thus, the total number of segments was analyzed and plotted as a function of orbital altitude for the different geometry cases in Figure 6.9. With some exceptions, the majority of the designs do not exceed 10 segments and thus, this variable is not of particular concern here, but will be considered in the feasibility of the design outcomes.
- Considering reference case 1, ABEP pushes the power budget to infeasible limits, leading to concerns about the feasibility of ABEP as a propulsion strategy in general. Figure 6.10, confirms high power consumption of ABEP, though differences with regular EP are not extreme.
- As the body dimensions do not follow the linear proportionality with altitude that was assumed in Chapter 5, the aerodynamic torque, magnetic dipole torque and drag deviate from what was predicted in that same chapter. In low orbits, the body dimensions exceed the anticipated range,

resulting in high torques and drag. In terms of model validity, the accumulated momentum and required magnetorquer dipole are a concern at such altitudes. Additionally, thrust in case 1 extrapolates the data used for the propulsion model. Therefore, these topics are elaborated on in Subsection 6.1.3. Contrastingly, in high orbits, torque and drag are lower than expected, not directly raising concerns on model validity.

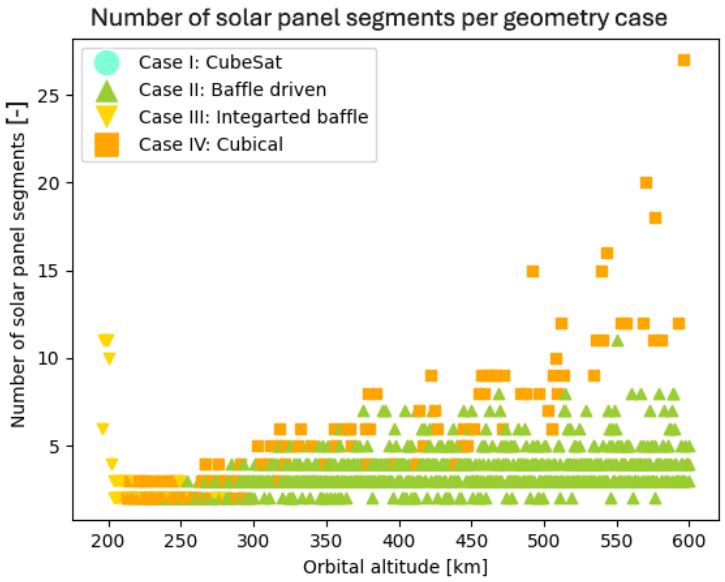

Figure 6.9: The total number of solar panel segments as a function of orbital altitude h for the different geometry cases

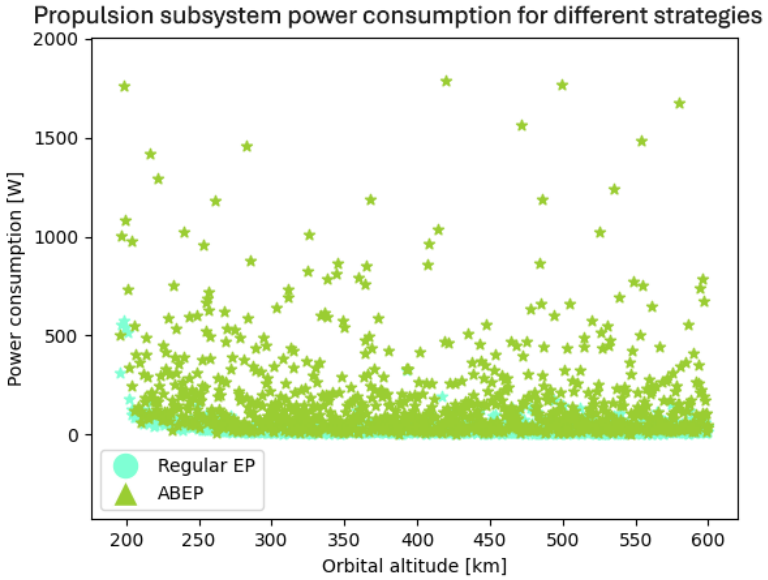

Figure 6.10: The power consumption of ABEP P_{ABEP} as a function of orbital altitude h

Table 6.2: The calculated results for case 1 per iteration

Variable	Symbol	Iteration 1	Iteration 2	Iteration 3	Iteration 4
Orbital period	T	$5249\,\mathrm{s}$			
Orbital velocity	v	$7814\,\mathrm{ms}^{-1}$			
M1 diameter	D	$0.150\,\mathrm{m}$			
Boom radius	R_{booom}	$0.007\,87\,\mathrm{m}$			
Sun shielding height	h_x	$0.0327\,\mathrm{m}$			
Baffle length	l_{baffle}	$0.154\,\mathrm{m}$			
Segmentation width	R_x	$0.0210\,\mathrm{m}$			
Segment height	$h_{segment}$	$0.0320\,\mathrm{m}$			
Outer diameter	D_{max}	$0.223\,\mathrm{m}$			
Stowed baffle volume	V_{baffle}	$0.003\,13\,\mathrm{m}^3$			
Deployed baffle area	A_{baffle}	$0.0330\,\mathrm{m}^2$			
Communication time	t_{com}	$29.8\,\mathrm{s}$			
Required bit energy to noise ratio	E_b/N_0	$13.13\,\mathrm{dB}$			
Transmission power	P_{Tx}	$2.35\,\mathrm{W}$			
Transmission input power	P_{in}	$19\,\mathrm{W}$			
Average communication power	P_{com}	$0.114\,\mathrm{W}$			
Atmospheric density	ρ	$2.97 \times 10^{-9}\,\mathrm{kgm}^{-3}$			
Frontal area	A	$0.159\,\mathrm{m}^2$	$3.51\,\mathrm{m}^2$	$157\,\mathrm{m}^2$	$8.13 \times 10^4\,\mathrm{m}^2$
$cp_a - cm$ mismatch	$cp_a - cm$	$0.0714\,\mathrm{m}$	$0.382\,\mathrm{m}$	$2.56\,\mathrm{m}$	$58.2\,\mathrm{m}$
Aerodynamic torque	T_a	$0.002\,12\,\mathrm{N}$	$0.251\,\mathrm{N}$	$75.3\,\mathrm{N}$	$8.84 \times 10^5\,\mathrm{N}$
Magnetic torque	T_m	$2.4 \times 10^{-5}\,\mathrm{N}$	$0.003\,68\,\mathrm{N}$	$1.11\,\mathrm{N}$	$1.3 \times 10^4\,\mathrm{N}$
Accumulated momentum	$M_{accumulated}$	$6.2\,\mathrm{Nms}$	$735\,\mathrm{Nms}$	$2.21 \times 10^5\,\mathrm{Nms}$	$2.59 \times 10^9\,\mathrm{Nms}$
CMG volume	V_{CMG}	$0.005\,51\,\mathrm{m}^3$	$0.531\,\mathrm{m}^3$	$159\,\mathrm{m}^3$	$1.87 \times 10^6\,\mathrm{m}^3$
CMG power	P_{CMG}	$13.2\,\mathrm{W}$	$1.7 \times 10^3\,\mathrm{W}$	$5.1 \times 10^5\,\mathrm{W}$	$5.99 \times 10^9\,\mathrm{W}$
Required dipole	DP	$124\,\mathrm{Am}^2$	$1.46 \times 10^4\,\mathrm{Am}^2$	$4.4 \times 10^6\,\mathrm{Am}^2$	$5.16 \times 10^{10}\,\mathrm{Am}^2$
MTQ volume	V_{MTQ}	$8.29 \times 10^{-4}\,\mathrm{m}^3$	$0.0942\,\mathrm{m}^3$	$28.3\,\mathrm{m}^3$	$3.32 \times 10^5\,\mathrm{m}^3$
MTQ power	P_{MTQ}	$10.9\,\mathrm{W}$	$1.26 \times 10^3\,\mathrm{W}$	$3.77 \times 10^5\,\mathrm{W}$	$4.43 \times 10^9\,\mathrm{W}$
AOCS volume	V_{AOCS}	$0.025\,\mathrm{m}^3$	$2.41\,\mathrm{m}^3$	$722\,\mathrm{m}^3$	$8.48 \times 10^6\,\mathrm{m}^3$
AOCS power	P_{AOCS}	$88.7\,\mathrm{W}$	$1.06 \times 10^4\,\mathrm{W}$	$3.17 \times 10^6\,\mathrm{W}$	$3.72 \times 10^{10}\,\mathrm{W}$
Drag force	F_{drag}	$0.0331\,\mathrm{N}$	$0.66\,\mathrm{N}$	$29.4\,\mathrm{N}$	$1.52 \times 10^4\,\mathrm{N}$
Collection area	A_c	$0.121\,\mathrm{m}^2$	$2.41\,\mathrm{m}^2$	$108\,\mathrm{m}^2$	$5.56 \times 10^4\,\mathrm{m}^2$
Intake volume	V_{intake}	$0.009\,32\,\mathrm{m}^3$	$0.829\,\mathrm{m}^3$	$247\,\mathrm{m}^3$	$2.9 \times 10^6\,\mathrm{m}^3$
ABEP volume	V_{ABEP}	$0.28\,\mathrm{m}^3$	$5.96\,\mathrm{m}^3$	$472\,\mathrm{m}^3$	$3.02 \times 10^6\,\mathrm{m}^3$
ABEP power	P_{ABEP}	$1.03 \times 10^3\,\mathrm{W}$	$1.96 \times 10^4\,\mathrm{W}$	$8.61 \times 10^5\,\mathrm{W}$	$4.45 \times 10^8\,\mathrm{W}$
Regular EP prop. mass	$m_{EP,prop}$	$1.11 \times 10^3\,\mathrm{kg}$	$2.21 \times 10^4\,\mathrm{kg}$	$9.86 \times 10^5\,\mathrm{kg}$	$5.09 \times 10^8\,\mathrm{kg}$
Regular EP prop. volume	$V_{EP,prop}$	$0.822\,\mathrm{m}^3$	$16.4\,\mathrm{m}^3$	$731\,\mathrm{m}^3$	$3.77 \times 10^5\,\mathrm{m}^3$
Regular EP volume	V_{EP}	$0.956\,\mathrm{m}^3$	$19\,\mathrm{m}^3$	$849\,\mathrm{m}^3$	$4.39 \times 10^5\,\mathrm{m}^3$
Regular EP power	P_{EP}	$508\,\mathrm{W}$	$1.02 \times 10^4\,\mathrm{W}$	$4.54 \times 10^5\,\mathrm{W}$	$2.34 \times 10^8\,\mathrm{W}$
Propulsion time	t_{prop}	$1.31 \times 10^7\,\mathrm{s}$	$2.6 \times 10^8\,\mathrm{s}$	$1.16 \times 10^{10}\,\mathrm{s}$	$5.99 \times 10^{12}\,\mathrm{s}$
Chemical propulsion prop. mass	$m_{ch,prop}$	$2.29 \times 10^3\,\mathrm{kg}$	$4.55 \times 10^4\,\mathrm{kg}$	$2.03 \times 10^6\,\mathrm{kg}$	$1.05 \times 10^9\,\mathrm{kg}$
Chemical propulsion prop. volume	$V_{ch,prop}$	$1.6\,\mathrm{m}^3$	$31.8\,\mathrm{m}^3$	$1.42 \times 10^3\,\mathrm{m}^3$	$7.34 \times 10^5\,\mathrm{m}^3$
Chemical prop. volume	V_{ch}	$1.6\,\mathrm{m}^3$	$31.8\,\mathrm{m}^3$	$1.42 \times 10^3\,\mathrm{m}^3$	$7.34 \times 10^5\,\mathrm{m}^3$
Propulsion type		ABEP	ABEP	ABEP	Regular EP
Propulsion volume	V_{prop}	$0.0106\,\mathrm{m}^3$	$0.83\,\mathrm{m}^3$	$247\,\mathrm{m}^3$	$3.77 \times 10^5\,\mathrm{m}^3$
Total power consumption	P_{tot}	$1.14 \times 10^3\,\mathrm{W}$	$3.02 \times 10^4\,\mathrm{W}$	$4.03 \times 10^6\,\mathrm{W}$	$3.75 \times 10^{10}\,\mathrm{W}$
Relative avg power generation	$P_{avg,e}$	$0.297\,\mathrm{W}$	$0.297\,\mathrm{W}$	$0.297\,\mathrm{W}$	$0.297\,\mathrm{W}$
Solar panel area	A_{sp}	$14.7\,\mathrm{m}^2$	$391\,\mathrm{m}^2$	$5.22 \times 10^4\,\mathrm{m}^2$	$4.85 \times 10^8\,\mathrm{m}^2$
Solar panel volume	V_{sp}	$5.87\,\mathrm{m}^3$	$1.77 \times 10^3\,\mathrm{m}^3$	$2.08 \times 10^7\,\mathrm{m}^3$	$1.6 \times 10^{15}\,\mathrm{m}^3$
Battery energy	E_{bat}	$2.69 \times 10^6\,\mathrm{J}$	$7.14 \times 10^7\,\mathrm{J}$	$9.53 \times 10^9\,\mathrm{J}$	$8.85 \times 10^{13}\,\mathrm{J}$
Battery volume	V_{bat}	$0.002\,89\,\mathrm{m}^3$	$0.0767\,\mathrm{m}^3$	$10.2\,\mathrm{m}^3$	$9.51 \times 10^4\,\mathrm{m}^3$
Subsystem volume	V_{bus}	$6.57\,\mathrm{m}^3$	$1.97 \times 10^3\,\mathrm{m}^3$	$2.32 \times 10^7\,\mathrm{m}^3$	$1.78 \times 10^{15}\,\mathrm{m}^3$
Geometry case		III	III	III	III
Body dimensions	x_{body}	$1.87\,\mathrm{m}$	$12.5\,\mathrm{m}$	$285\,\mathrm{m}$	$1.21 \times 10^5\,\mathrm{m}$
	y_{body}	$1.87\,\mathrm{m}$	$12.5\,\mathrm{m}$	$285\,\mathrm{m}$	$1.21 \times 10^5\,\mathrm{m}$
	z_{body}	$1.87\,\mathrm{m}$	$12.5\,\mathrm{m}$	$285\,\mathrm{m}$	$1.21 \times 10^5\,\mathrm{m}$

Table 6.3: The calculated results for case 2 per iteration

Variable	Symbol	Iteration 1	Iteration 2	Iteration 3	Iteration 52
Orbital period	T	$5431\,\mathrm{s}$			
Orbital velocity	v	$7726\,\mathrm{ms}^{-1}$			
M1 diameter	D	$0.300\,\mathrm{m}$			
Boom radius	R_{booom}	$0.0125\,\mathrm{m}$			
Sun shielding height	h_x	$0.093\,\mathrm{m}$			
Baffle length	l_{baffle}	$0.394\,\mathrm{m}$			
Segmentation width	R_x	$0.007\,00\,\mathrm{m}$			
Segment height	$h_{segment}$	$0.141\,\mathrm{m}$			
Outer diameter	D_{max}	$0.364\,\mathrm{m}$			
Stowed baffle volume	V_{baffle}	$0.0147\,\mathrm{m}^3$			
Deployed baffle area	A_{baffle}	$0.175\,\mathrm{m}^2$			
Communication time	t_{com}	$62.1\,\mathrm{s}$			
Required bit energy to noise ratio	E_b/N_0	$16.05\,\mathrm{dB}$			
Transmission power	P_{Tx}	$8.06\,\mathrm{W}$			
Transmission input power	P_{in}	$41.1\,\mathrm{W}$			
Average communication power	P_{com}	$0.482\,\mathrm{W}$			
Atmospheric density	ρ	$5.17 \times 10^{-11}\,\mathrm{kgm}^{-3}$			
Frontal area	A	$0.301\,\mathrm{m}^2$	$0.23\,\mathrm{m}^2$	$0.226\,\mathrm{m}^2$	$0.215\,\mathrm{m}^2$
$cp_a - cm$ mismatch	$cp_a - cm$	$0.0549\,\mathrm{m}$	$0.0237\,\mathrm{m}$	$0.022\,\mathrm{m}$	$0.0173\,\mathrm{m}$
Aerodynamic torque	T_a	$5.43 \times 10^{-5}\,\mathrm{N}$	$1.79 \times 10^{-5}\,\mathrm{N}$	$1.64 \times 10^{-5}\,\mathrm{N}$	$1.22 \times 10^{-5}\,\mathrm{N}$
Magnetic torque	T_m	$2.24 \times 10^{-5}\,\mathrm{N}$	$1.05 \times 10^{-5}\,\mathrm{N}$	$9.74 \times 10^{-6}\,\mathrm{N}$	$7.63 \times 10^{-6}\,\mathrm{N}$
Accumulated momentum	$M_{accumulated}$	$0.229\,\mathrm{Nms}$	$0.0847\,\mathrm{Nms}$	$0.078\,\mathrm{Nms}$	$0.0592\,\mathrm{Nms}$
CMG volume	V_{CMG}	$9.50 \times 10^{-4}\,\mathrm{m}^3$	$0.001\,95\,\mathrm{m}^3$	$4.81 \times 10^{-4}\,\mathrm{m}^3$	$6.60 \times 10^{-4}\,\mathrm{m}^3$
CMG power	P_{CMG}	$1.92\,\mathrm{W}$	$4.47\,\mathrm{W}$	$12.1\,\mathrm{W}$	$4.83\,\mathrm{W}$
Required dipole	DP	$4.73\,\mathrm{Am}^2$	$1.75\,\mathrm{Am}^2$	$1.61\,\mathrm{Am}^2$	$1.22\,\mathrm{Am}^2$
MTQ volume	V_{MTQ}	$3.81 \times 10^{-5}\,\mathrm{m}^3$	$1.03 \times 10^{-6}\,\mathrm{m}^3$	$2.31 \times 10^{-6}\,\mathrm{m}^3$	$4.92 \times 10^{-6}\,\mathrm{m}^3$
MTQ power	P_{MTQ}	$0.441\,\mathrm{W}$	$0.0331\,\mathrm{W}$	$0.343\,\mathrm{W}$	$0.006\,31\,\mathrm{W}$
AOCS volume	V_{AOCS}	$0.004\,35\,\mathrm{m}^3$	$0.008\,22\,\mathrm{m}^3$	$0.002\,37\,\mathrm{m}^3$	$0.003\,09\,\mathrm{m}^3$
AOCS power	P_{AOCS}	$12.1\,\mathrm{W}$	$21.1\,\mathrm{W}$	$52.7\,\mathrm{W}$	$22.4\,\mathrm{W}$
Drag force	F_{drag}	$0.001\,05\,\mathrm{N}$	$8.15 \times 10^{-4}\,\mathrm{N}$	$8.02 \times 10^{-4}\,\mathrm{N}$	$7.66 \times 10^{-4}\,\mathrm{N}$
Regular EP prop. mass	$m_{EP,prop}$	$1.49\,\mathrm{kg}$	$1.16\,\mathrm{kg}$	$1.14\,\mathrm{kg}$	$1.09\,\mathrm{kg}$
Regular EP prop. volume	$V_{EP,prop}$	$0.0011\,\mathrm{m}^3$	$8.59 \times 10^{-4}\,\mathrm{m}^3$	$8.45 \times 10^{-4}\,\mathrm{m}^3$	$8.07 \times 10^{-4}\,\mathrm{m}^3$
Regular EP volume	V_{EP}	$0.0106\,\mathrm{m}^3$	$0.005\,41\,\mathrm{m}^3$	$0.0161\,\mathrm{m}^3$	$0.007\,21\,\mathrm{m}^3$
Regular EP power	P_{EP}	$30.4\,\mathrm{W}$	$13.1\,\mathrm{W}$	$50.8\,\mathrm{W}$	$19.6\,\mathrm{W}$
Propulsion time	t_{prop}	$4.96 \times 10^5\,\mathrm{s}$	$3.85 \times 10^5\,\mathrm{s}$	$3.79 \times 10^5\,\mathrm{s}$	$3.62 \times 10^5\,\mathrm{s}$
Chemical propulsion prop. mass	$m_{ch,prop}$	$48.4\,\mathrm{kg}$	$37.6\,\mathrm{kg}$	$37\,\mathrm{kg}$	$35.3\,\mathrm{kg}$
Chemical propulsion prop. volume	$V_{ch,prop}$	$0.0338\,\mathrm{m}^3$	$0.0263\,\mathrm{m}^3$	$0.0259\,\mathrm{m}^3$	$0.0247\,\mathrm{m}^3$
Chemical prop. volume	V_{ch}	$0.0348\,\mathrm{m}^3$	$0.0273\,\mathrm{m}^3$	$0.0269\,\mathrm{m}^3$	$0.0257\,\mathrm{m}^3$
Propulsion type		Regular EP	Regular EP	Regular EP	Regular EP
Propulsion volume	V_{prop}	$0.001\,96\,\mathrm{m}^3$	$0.001\,72\,\mathrm{m}^3$	$0.001\,71\,\mathrm{m}^3$	$0.001\,67\,\mathrm{m}^3$
Total power consumption	P_{tot}	$52.2\,\mathrm{W}$	$43.9\,\mathrm{W}$	$113\,\mathrm{W}$	$51.8\,\mathrm{W}$
Relative avg power generation	$P_{avg,e}$	$0.275\,\mathrm{W}$	$0.275\,\mathrm{W}$	$0.275\,\mathrm{W}$	$0.275\,\mathrm{W}$
Solar panel area	A_{sp}	$0.729\,\mathrm{m}^2$	$0.612\,\mathrm{m}^2$	$1.58\,\mathrm{m}^2$	$0.722\,\mathrm{m}^2$
Solar panel volume	V_{sp}	$0.008\,11\,\mathrm{m}^3$	$0.003\,26\,\mathrm{m}^3$	$0.026\,\mathrm{m}^3$	$0.004\,31\,\mathrm{m}^3$
Battery energy	E_{bat}	$1.39 \times 10^5\,\mathrm{J}$	$1.17 \times 10^5\,\mathrm{J}$	$3.01 \times 10^5\,\mathrm{J}$	$1.38 \times 10^5\,\mathrm{J}$
Battery volume	V_{bat}	$1.96 \times 10^{-4}\,\mathrm{m}^3$	$1.64 \times 10^{-4}\,\mathrm{m}^3$	$4.24 \times 10^{-4}\,\mathrm{m}^3$	$1.94 \times 10^{-4}\,\mathrm{m}^3$
Subsystem volume	V_{bus}	$0.02\,\mathrm{m}^3$	$0.0186\,\mathrm{m}^3$	$0.0376\,\mathrm{m}^3$	$0.014\,\mathrm{m}^3$
Geometry case		II	II	IV	II
Body dimensions	x_{body}	$0.364\,\mathrm{m}$	$0.364\,\mathrm{m}$	$0.389\,\mathrm{m}$	$0.364\,\mathrm{m}$
	y_{body}	$0.151\,\mathrm{m}$	$0.14\,\mathrm{m}$	$0.248\,\mathrm{m}$	$0.11\,\mathrm{m}$
	z_{body}	$0.364\,\mathrm{m}$	$0.364\,\mathrm{m}$	$0.389\,\mathrm{m}$	$0.364\,\mathrm{m}$

Table 6.4: The calculated results for case 3 per iteration

Variable	Symbol	Iteration 1	Iteration 2	Iteration 3
Orbital period	T	$5615\,\mathrm{s}$		
Orbital velocity	v	$7641\,\mathrm{ms}^{-1}$		
M1 diameter	D	$0.450\,\mathrm{m}$		
Boom radius	R_{booom}	$0.0164\,\mathrm{m}$		
Sun shielding height	h_x	$0.172\,\mathrm{m}$		
Baffle length	l_{baffle}	$0.394\,\mathrm{m}$		
Segmentation width	R_x	$0.003\,50\,\mathrm{m}$		
Segment height	$h_{segment}$	$0.207\,\mathrm{m}$		
Outer diameter	D_{max}	$0.523\,\mathrm{m}$		
Stowed baffle volume	V_{baffle}	$0.0445\,\mathrm{m}^3$		
Deployed baffle area	A_{baffle}	$0.271\,\mathrm{m}^2$		
Communication time	t_{com}	$97.1\,\mathrm{s}$		
Required bit energy to noise ratio	E_b/N_0	$6.41\,\mathrm{dB}$		
Transmission power	P_{Tx}	$5.97\,\mathrm{W}$		
Transmission input power	P_{in}	$31.8\,\mathrm{W}$		
Average communication power	P_{com}	$0.567\,\mathrm{W}$		
Atmospheric density	ρ	$4.83 \times 10^{-12}\,\mathrm{kgm}^{-3}$		
Frontal area	A	$0.397\,\mathrm{m}^2$	$0.329\,\mathrm{m}^2$	$0.329\,\mathrm{m}^2$
$cp_a - cm$ mismatch	$cp_a - cm$	$0.0675\,\mathrm{m}$	$0.0212\,\mathrm{m}$	$0.0212\,\mathrm{m}$
Aerodynamic torque	T_a	$8.12 \times 10^{-6}\,\mathrm{N}$	$2.11 \times 10^{-6}\,\mathrm{N}$	$2.11 \times 10^{-6}\,\mathrm{N}$
Magnetic torque	T_m	$2.1 \times 10^{-5}\,\mathrm{N}$	$1.47 \times 10^{-5}\,\mathrm{N}$	$1.47 \times 10^{-5}\,\mathrm{N}$
Accumulated momentum	$M_{accumulated}$	$0.0899\,\mathrm{Nms}$	$0.0521\,\mathrm{Nms}$	$0.0521\,\mathrm{Nms}$
CMG volume	V_{CMG}	$6.67 \times 10^{-4}\,\mathrm{m}^3$	$0.002\,67\,\mathrm{m}^3$	$0.002\,67\,\mathrm{m}^3$
CMG power	P_{CMG}	$2.24\,\mathrm{W}$	$10.4\,\mathrm{W}$	$10.4\,\mathrm{W}$
Required dipole	DP	$1.92\,\mathrm{Am}^2$	$1.11\,\mathrm{Am}^2$	$1.11\,\mathrm{Am}^2$
MTQ volume	V_{MTQ}	$1.11 \times 10^{-5}\,\mathrm{m}^3$	$1.03 \times 10^{-6}\,\mathrm{m}^3$	$1.03 \times 10^{-6}\,\mathrm{m}^3$
MTQ power	P_{MTQ}	$0.0336\,\mathrm{W}$	$0.14\,\mathrm{W}$	$0.14\,\mathrm{W}$
AOCS volume	V_{AOCS}	$0.003\,14\,\mathrm{m}^3$	$0.0111\,\mathrm{m}^3$	$0.0111\,\mathrm{m}^3$
AOCS power	P_{AOCS}	$12.1\,\mathrm{W}$	$45.1\,\mathrm{W}$	$45.1\,\mathrm{W}$
Drag force	F_{drag}	$1.26 \times 10^{-4}\,\mathrm{N}$	$1.05 \times 10^{-4}\,\mathrm{N}$	$1.05 \times 10^{-4}\,\mathrm{N}$
Regular EP prop. mass	$m_{EP,prop}$	$0.586\,\mathrm{kg}$	$0.489\,\mathrm{kg}$	$0.489\,\mathrm{kg}$
Regular EP prop. volume	$V_{EP,prop}$	$4.34 \times 10^{-4}\,\mathrm{m}^3$	$3.62 \times 10^{-4}\,\mathrm{m}^3$	$3.62 \times 10^{-4}\,\mathrm{m}^3$
Regular EP volume	V_{EP}	$0.008\,29\,\mathrm{m}^3$	$0.006\,73\,\mathrm{m}^3$	$0.006\,73\,\mathrm{m}^3$
Regular EP power	P_{EP}	$24.6\,\mathrm{W}$	$19.4\,\mathrm{W}$	$19.4\,\mathrm{W}$
Propulsion time	t_{prop}	$3.08 \times 10^4\,\mathrm{s}$	$2.58 \times 10^4\,\mathrm{s}$	$2.58 \times 10^4\,\mathrm{s}$
Chemical propulsion prop. mass	$m_{ch,prop}$	$11.5\,\mathrm{kg}$	$9.57\,\mathrm{kg}$	$9.57\,\mathrm{kg}$
Chemical propulsion prop. volume	$V_{ch,prop}$	$0.008\,01\,\mathrm{m}^3$	$0.006\,69\,\mathrm{m}^3$	$0.006\,69\,\mathrm{m}^3$
Chemical prop. volume	V_{ch}	$0.009\,01\,\mathrm{m}^3$	$0.007\,69\,\mathrm{m}^3$	$0.007\,69\,\mathrm{m}^3$
Propulsion type		Regular EP	Regular EP	Regular EP
Propulsion volume	V_{prop}	$0.001\,29\,\mathrm{m}^3$	$0.001\,22\,\mathrm{m}^3$	$0.001\,22\,\mathrm{m}^3$
Total power consumption	P_{tot}	$49\,\mathrm{W}$	$76.7\,\mathrm{W}$	$76.7\,\mathrm{W}$
Relative avg power generation	$P_{avg,e}$	$0.275\,\mathrm{W}$	$0.275\,\mathrm{W}$	$0.275\,\mathrm{W}$
Solar panel area	A_{sp}	$0.684\,\mathrm{m}^2$	$1.07\,\mathrm{m}^2$	$1.07\,\mathrm{m}^2$
Solar panel volume	V_{sp}	$0.0053\,\mathrm{m}^3$	$0.0089\,\mathrm{m}^3$	$0.0089\,\mathrm{m}^3$
Battery energy	E_{bat}	$1.35 \times 10^5\,\mathrm{J}$	$2.11 \times 10^5\,\mathrm{J}$	$2.11 \times 10^5\,\mathrm{J}$
Battery volume	V_{bat}	$2.62 \times 10^{-4}\,\mathrm{m}^3$	$4.10 \times 10^{-4}\,\mathrm{m}^3$	$4.10 \times 10^{-4}\,\mathrm{m}^3$
Subsystem volume	V_{bus}	$0.0142\,\mathrm{m}^3$	$0.0271\,\mathrm{m}^3$	$0.0271\,\mathrm{m}^3$
Geometry case		II	II	II
Body dimensions	x_{body}	$0.523\,\mathrm{m}$	$0.523\,\mathrm{m}$	$0.523\,\mathrm{m}$
	y_{body}	$0.11\,\mathrm{m}$	$0.11\,\mathrm{m}$	$0.11\,\mathrm{m}$
	z_{body}	$0.523\,\mathrm{m}$	$0.523\,\mathrm{m}$	$0.523\,\mathrm{m}$

Table 6.5: The calculated results for case 4 per iteration

Variable	Symbol	Iteration 1	Iteration 2	Iteration 3
Orbital period	T	$5801\,\mathrm{s}$		
Orbital velocity	v	$7558\,\mathrm{ms}^{-1}$		
M1 diameter	D	$0.600\,\mathrm{m}$		
Boom radius	R_{booom}	$0.0198\,\mathrm{m}$		
Sun shielding height	h_x	$0.266\,\mathrm{m}$		
Baffle length	l_{baffle}	$0.857\,\mathrm{m}$		
Segmentation width	R_x	$0.0315\,\mathrm{m}$		
Segment height	$h_{segment}$	$0.0957\,\mathrm{m}$		
Outer diameter	D_{max}	$0.742\,\mathrm{m}$		
Stowed baffle volume	V_{baffle}	$0.0414\,\mathrm{m}^3$		
Deployed baffle area	A_{baffle}	$0.810\,\mathrm{m}^2$		
Communication time	t_{com}	$135\,\mathrm{s}$		
Required bit energy to noise ratio	E_b/N_0	$13.13\,\mathrm{dB}$		
Transmission power	P_{Tx}	$2.41\,\mathrm{W}$		
Transmission input power	P_{in}	$17.3\,\mathrm{W}$		
Average communication power	P_{com}	$0.426\,\mathrm{W}$		
Atmospheric density	ρ	$8.98 \times 10^{-13}\,\mathrm{kgm}^{-3}$		
Frontal area	A	$0.936\,\mathrm{m}^2$	$0.892\,\mathrm{m}^2$	$0.892\,\mathrm{m}^2$
$cp_a - cm$ mismatch	$cp_a - cm$	$0.0822\,\mathrm{m}$	$0.0258\,\mathrm{m}$	$0.0258\,\mathrm{m}$
Aerodynamic torque	T_a	$4.54 \times 10^{-6}\,\mathrm{N}$	$1.36 \times 10^{-6}\,\mathrm{N}$	$1.36 \times 10^{-6}\,\mathrm{N}$
Magnetic torque	T_m	$1.97 \times 10^{-5}\,\mathrm{N}$	$2.78 \times 10^{-5}\,\mathrm{N}$	$2.78 \times 10^{-5}\,\mathrm{N}$
Accumulated momentum	$M_{accumulated}$	$0.0772\,\mathrm{Nms}$	$0.0931\,\mathrm{Nms}$	$0.0931\,\mathrm{Nms}$
CMG volume	V_{CMG}	$4.98 \times 10^{-4}\,\mathrm{m}^3$	$5.33 \times 10^{-4}\,\mathrm{m}^3$	$5.33 \times 10^{-4}\,\mathrm{m}^3$
CMG power	P_{CMG}	$13.8\,\mathrm{W}$	$4.05\,\mathrm{W}$	$4.05\,\mathrm{W}$
Required dipole	DP	$1.7\,\mathrm{Am}^2$	$2.05\,\mathrm{Am}^2$	$2.05\,\mathrm{Am}^2$
MTQ volume	V_{MTQ}	$2.58 \times 10^{-6}\,\mathrm{m}^3$	$7.35 \times 10^{-6}\,\mathrm{m}^3$	$7.35 \times 10^{-6}\,\mathrm{m}^3$
MTQ power	P_{MTQ}	$0.0957\,\mathrm{W}$	$0.0482\,\mathrm{W}$	$0.0482\,\mathrm{W}$
AOCS volume	V_{AOCS}	$0.002\,44\,\mathrm{m}^3$	$0.002\,59\,\mathrm{m}^3$	$0.002\,59\,\mathrm{m}^3$
AOCS power	P_{AOCS}	$58.5\,\mathrm{W}$	$19.5\,\mathrm{W}$	$19.5\,\mathrm{W}$
Drag force	F_{drag}	$5.63 \times 10^{-5}\,\mathrm{N}$	$5.37 \times 10^{-5}\,\mathrm{N}$	$5.37 \times 10^{-5}\,\mathrm{N}$
Regular EP prop. mass	$m_{EP,prop}$	$0.781\,\mathrm{kg}$	$0.745\,\mathrm{kg}$	$0.745\,\mathrm{kg}$
Regular EP prop. volume	$V_{EP,prop}$	$5.79 \times 10^{-4}\,\mathrm{m}^3$	$5.52 \times 10^{-4}\,\mathrm{m}^3$	$5.52 \times 10^{-4}\,\mathrm{m}^3$
Regular EP volume	V_{EP}	$0.004\,27\,\mathrm{m}^3$	$0.002\,06\,\mathrm{m}^3$	$0.002\,06\,\mathrm{m}^3$
Regular EP power	P_{EP}	$9.03\,\mathrm{W}$	$2.07\,\mathrm{W}$	$2.07\,\mathrm{W}$
Propulsion time	t_{prop}	$1.52 \times 10^4\,\mathrm{s}$	$1.45 \times 10^4\,\mathrm{s}$	$1.45 \times 10^4\,\mathrm{s}$
Chemical propulsion prop. mass	$m_{ch,prop}$	$4.21\,\mathrm{kg}$	$4.01\,\mathrm{kg}$	$4.01\,\mathrm{kg}$
Chemical propulsion prop. volume	$V_{ch,prop}$	$0.002\,94\,\mathrm{m}^3$	$0.002\,81\,\mathrm{m}^3$	$0.002\,81\,\mathrm{m}^3$
Chemical prop. volume	V_{ch}	$0.003\,94\,\mathrm{m}^3$	$0.003\,81\,\mathrm{m}^3$	$0.003\,81\,\mathrm{m}^3$
Propulsion type		Chemical propulsion	Regular EP	Regular EP
Propulsion volume	V_{prop}	$0.003\,94\,\mathrm{m}^3$	$0.001\,41\,\mathrm{m}^3$	$0.001\,41\,\mathrm{m}^3$
Total power consumption	P_{tot}	$78.4\,\mathrm{W}$	$41.5\,\mathrm{W}$	$41.5\,\mathrm{W}$
Relative avg power generation	$P_{avg,e}$	$0.248\,\mathrm{W}$	$0.248\,\mathrm{W}$	$0.248\,\mathrm{W}$
Solar panel area	A_{sp}	$1.21\,\mathrm{m}^2$	$0.642\,\mathrm{m}^2$	$0.642\,\mathrm{m}^2$
Solar panel volume	V_{sp}	$0.015\,\mathrm{m}^3$	$0.002\,83\,\mathrm{m}^3$	$0.002\,83\,\mathrm{m}^3$
Battery energy	E_{bat}	$2.46 \times 10^5\,\mathrm{J}$	$1.3 \times 10^5\,\mathrm{J}$	$1.3 \times 10^5\,\mathrm{J}$
Battery volume	V_{bat}	$2.95 \times 10^{-4}\,\mathrm{m}^3$	$1.56 \times 10^{-4}\,\mathrm{m}^3$	$1.56 \times 10^{-4}\,\mathrm{m}^3$
Subsystem volume	V_{bus}	$0.0277\,\mathrm{m}^3$	$0.0114\,\mathrm{m}^3$	$0.0114\,\mathrm{m}^3$
Geometry case		II	II	II
Body dimensions	x_{body}	$0.742\,\mathrm{m}$	$0.742\,\mathrm{m}$	$0.742\,\mathrm{m}$
	y_{body}	$0.11\,\mathrm{m}$	$0.11\,\mathrm{m}$	$0.11\,\mathrm{m}$
	z_{body}	$0.742\,\mathrm{m}$	$0.742\,\mathrm{m}$	$0.742\,\mathrm{m}$

6.1.3. Assumption Verification

As already touched upon in Subsection 6.1.2, it should be checked whether the results produced by the model are within the validity ranges of the subsystem models themselves, which are indicated in the bottom row of each subsystem model table in Chapter 5. The majority of these assumptions relate to design decisions on the concept side and are thus met automatically. However, for some, the numbers need to be verified explicitly. This is done by running the model and evaluating the results.

The ICU and CDH models are only valid for small satellites. Considering Figure 6.11, less than $2\,\%$ of the cases exceeds $0.3\,\mathrm{m}^3$, translating to cubical body dimensions below $0.67\,\mathrm{m}$. Such dimensions do not exceed the small satellite class and thus, this assumption is valid for the model. Simultaneously, this analysis verifies the EPS model, which states that the body dimensions may not exceed $1\,\mathrm{m}$. The EPS model also assumes velocity aligned solar panels at all altitudes, arguing that even though in LEO drag is less prominent and thus, Sun-pointing panels might be advantageous, the satellite body dimensions x_{body}, y_{body} and z_{body} are expected to increase with altitude, resulting in a lower relative impact of the increased solar panel dimensions on the system volume budget. Indeed, Figure 6.1 reveals a negligible contribution of solar panels to the system volume at higher altitudes.

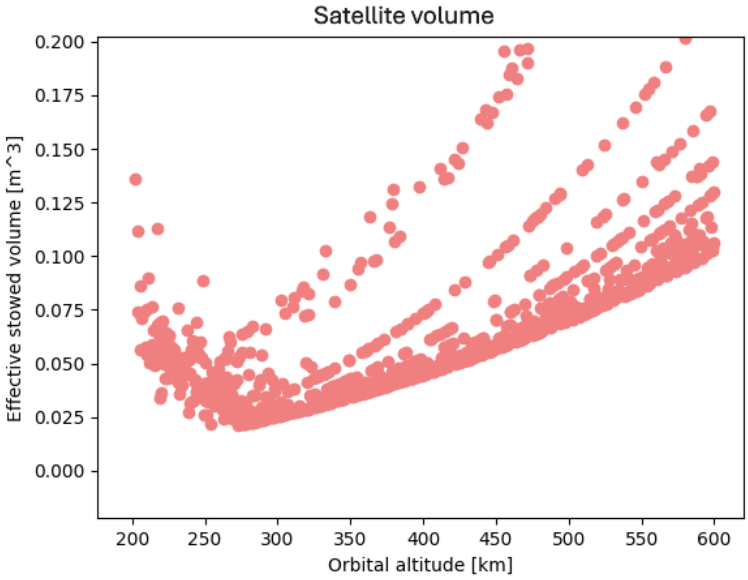

Figure 6.11: The effective stowed volume $V_{eff,stowed}$ as a function of orbital altitude h including outliers

The communications subsystem is modeled assuming the transmission power does not exceed $2\,\mathrm{W}$ (see Table 5.11). A plot of the transmission power as a function of orbital altitude is depicted in Figure 6.12. Different bands can be distinguished, corresponding to the different E_b/N_0 ranges. It turns out that in less than $10\,\%$ of the cases, the $2\,\mathrm{W}$ maximum transmission power is exceeded as was thus coincidentally observed in all reference cases. As clear from Figure 6.12, data rate drives this transmission power.

Furthermore, the communication model assumes a maximum downlink data rate of $250\,\mathrm{Mbps}$. Figure 6.13 shows the relationship between the downlink data rate and orbital altitude for one run. From analysis, it is concluded that less than $9\,\%$ of the cases exceeds data rate threshold.

The AOCS model assumes the accumulated momentum (for CMG evaluation) to remain below $10\,\mathrm{Nms}$ and is based on a magnetorquer dipole moment (for magnetorquer characterization) up to $20\,\mathrm{Am}^2$. The plots in Figure 6.14 visualize these parameters as a function of orbital altitude. Less than $1\,\%$ of the sampled cases accumulated more than $10\,\mathrm{Nms}$ and not more than $6\,\%$ requires a magnetorquer dipole moment over $20\,\mathrm{Am}^2$. These extrapolations occur mostly at low altitudes. Furthermore, extrapolation of the CMG model only occurs below $170\,\mathrm{km}$ altitude, compared to $250\,\mathrm{km}$ for the magnetorquer model.

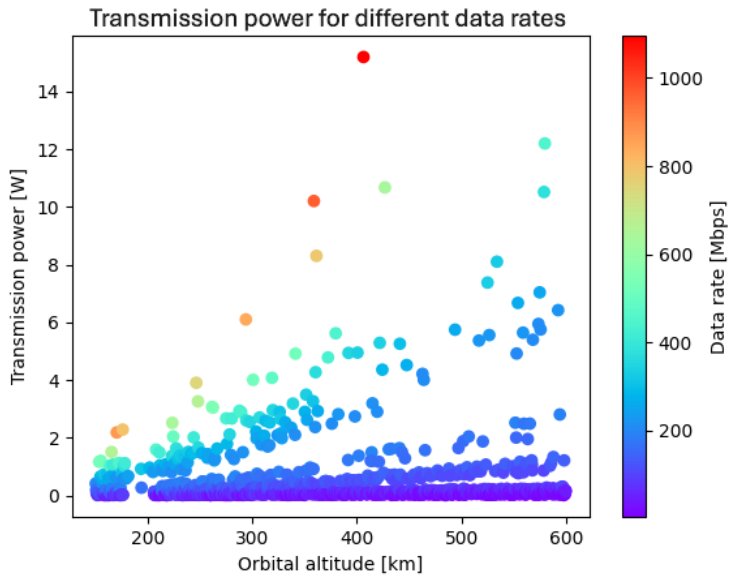

Figure 6.12: The required transmission power P_{Tx} as a function of orbital altitude h

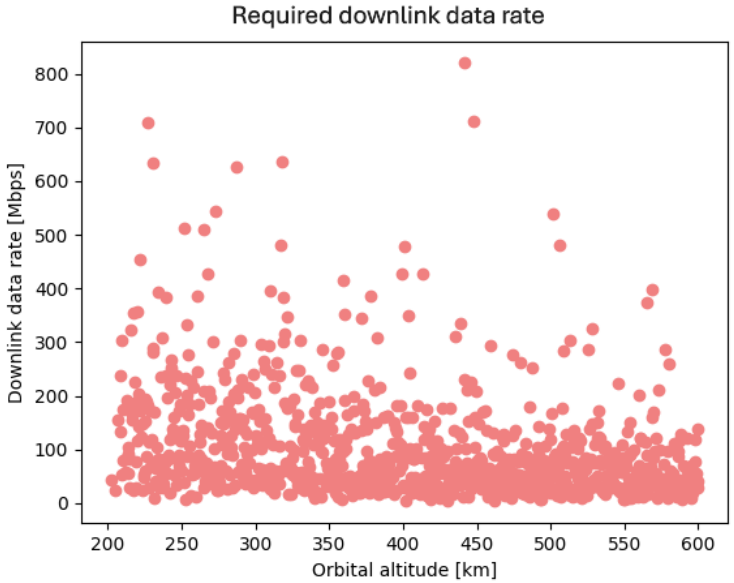

Figure 6.13: The downlink data rate DR_{down} as a function of orbital altitude h

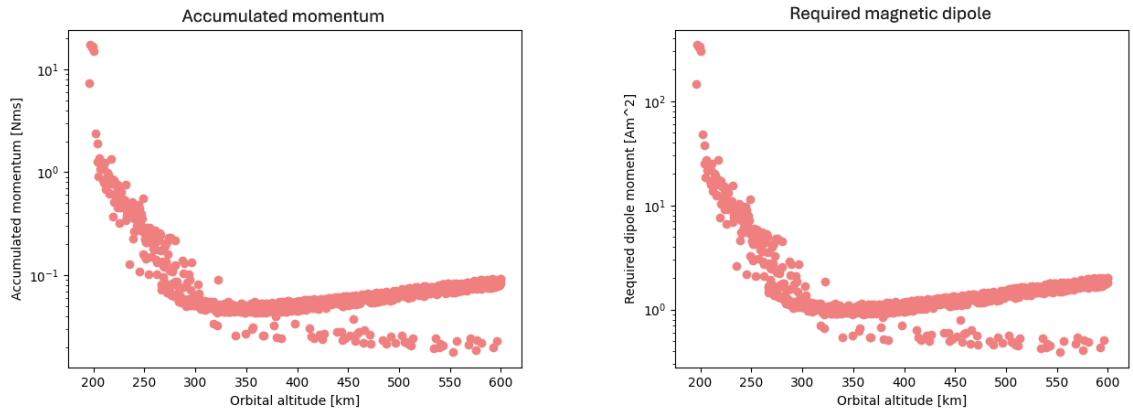

(a) The accumulated momentum $M_{accumulated}$

(b) The magnetorquer dipole moment DP

Figure 6.14: The accumulated momentum $M_{accumulated}$ and magnetorquer dipole moment DP as a function of orbital altitude h

Lastly, the assumptions used by the propulsion model are evaluated. The thrust levels are constrained per propulsion type, but most stringent is the one on the regular EP. In about $1\,\%$ of the cases depicted in Figure 6.15, the value of $18\,\mathrm{mN}$ is exceeded.

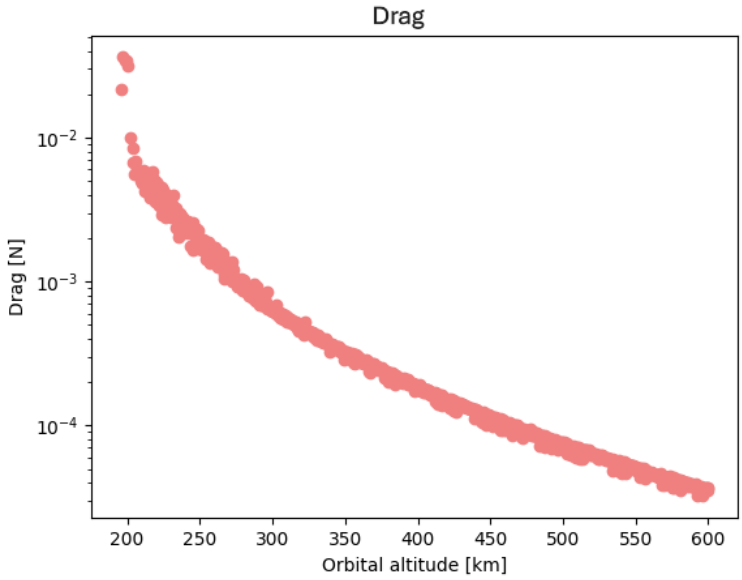

Figure 6.15: The drag and thus required thrust F_T to be delivered by the propulsion subsystem as a function of orbital altitude h

6.2. Monte Carlo Approach

The model is integrated into a Monte Carlo simulation in Python. The effect of uncertainty in the input parameters is included in the simulation by the use of dedicated probability distributions as assigned in Chapter 5 and summarized in Table 6.6. The goal is to run the model for many sets of sampled input parameters to obtain an envelope of the satellite volume as a function of orbital altitude. This is done for the DST as well as for the non-deployable telescope ($n_{segments} = 1$) in order to finally answer the research question. Furthermore, the volume of the individual subsystems is analyzed to evaluate the impact of deployability and orbital altitude. This way, an optimal combination of deployability and orbital altitude can be extracted and feasibility of a DST in VLEO is assessed. Moreover, the effects of t_{life}, $n_{segments}$ and propulsion strategy on the satellite volume are of particular interest for the mission design (as other considerations rather than volume come into play, such as technological readiness) and are thus evaluated explicitly.

Finally, the sensitivity of the model on the aperture diameter D, solar panel thickness t_{sp} and other uncertain input parameters is assessed in a sensitivity analysis. D was found to drive the design at high altitudes in Section 6.1 and is subject to change due to the preliminary stage of this study. Therefore, the reference diameter at $300\,\mathrm{km}$ is varied between $20\,\mathrm{cm}$ to $40\,\mathrm{cm}$. The other variables are explored to reveal underlying sensitive dependencies. The feasibility of the results is discussed and the optimal design is extracted.

As was presented in Chapter 5, some distributions are independent of h, such as the ICU volume detailed in Table 5.4. Other distributions such as the downlink data rate in Table 5.14 are intrinsically dependent on orbital altitude. An overview of all uncertain input parameters and their dependency on h is presented in Table 6.6. In order to make the model as consistent as possible, all input parameters that are independent of h are sampled before looping over h, leading to a full run of the model with one single set of these inputs for all sampled altitudes. h-dependent parameters do vary within one run of the model. This is also the explanation for the propulsion volume discrepancy observed around $350\,\mathrm{km}$ to $550\,\mathrm{km}$ in Figure 6.1, where for some combinations of inputs chemical propulsion outperforms regular EP.

As noted in Section 6.1, some samples result in extrapolation of the subsystem models. These data points are flagged to discriminate them from those that are completely within the model validity range. Moreover, not all sample sets lead to a converging design. In the Monte Carlo Simulation, in order to limit computation time and prevent overflow in Python, a sample set is disregarded if 100 iterations of the body dimensions are executed or body volume exceeds $100\,\mathrm{m}^3$.

The amount of model runs N required to obtain a certain level of precision ϵ for a distribution with a standard deviation σ is defined by the following formula, where z is related to the confidence interval [169]:

$$N = \left(\frac{z\sigma}{\epsilon}\right)^2 \tag{6.1}$$

In order to determine σ, the model was ran 1000 times with $1\,\mathrm{km}$ altitude intervals. Per altitude, the mean average effective stowed volume and standard deviation were recorded. Outliers were removed conform the z-score method with a threshold of $Z = 3$, resulting in removal of data points that fall beyond three standard deviations from the mean (which was $1.53\,\%$ in this analysis). The model standard deviation was estimated by treating the standard deviations per altitude as independent errors and combining them according to the mean square method, resulting in $\sigma = 0.0434$. For a confidence interval of $95\,\%$ ($z = 1.96$) and a precision of $0.001\,\mathrm{m}^3$ (less than $5\,\%$ of the minimum mean average effective stowed volume recorded), at least 7236 individual runs of the model are thus required. Computation time of the Monte Carlo Simulation is limited by using $5\,\mathrm{km}$ altitude intervals.

Table 6.6: The uncertain inputs

Parameter	Symbol	Distribution	h-dependent
Mission lifetime	t_{life}	$3-7$ years	No
M1-M2 distance	d_{M1-M2}	$(0.9 \pm 0.239) \cdot D$	No
Number of baffle segments	$n_{segments}$	$1 - n_{segments,max}$	Yes
ICU volume	V_{ICU}	$0.25 - 1$ U	No
Solstice eclipse fraction	$f_{Solstice}$	$0.0001 \cdot h + 0.4535 \pm 0.0132$	Yes
Depth of discharge	DoD	$0.2 - 0.4$	No
CHD power	P_{CDH}	13.16 ± 5.936 W	No
Downlink data rate	DR_{down}	$566.6 \cdot e^{-0.0069 \cdot h} + 59.06 \pm \left(2.718 + 1.493 \cdot \left(\frac{T}{t_{com}}\right)\right)$	Yes
Average free space loss	$\bar{L}_S$	$0.000038 \cdot h^2 + 0.0538 \cdot h + 148.3518 \pm 0.157$	Yes
Transmitter input power	P_{in}	$3.9058 \cdot P_{Tx} + 9.8514 \pm 2.516$	Yes
Drag coefficient	C_D	$0.0005 \cdot h + 2.0169 \pm 0.02$	Yes
Percentage mismatch	$cp_a - cm$	$0.1486 - 0.2606$	No
CMG volume	V_{CMG}	$7.221 \cdot 10^{-4} \cdot M_{accumulated} + 8.801 \cdot 10^{-4} \pm 4.026 \cdot 10^{-4}$	Yes
CMG power	P_{CMG}	$2.312 \cdot M_{accumulated} + 5.795 \pm 4.132$	Yes
MTQ volume	V_{MTQ}	$6.435 \cdot 10^{-6} \cdot DP + 1.795 \cdot 10^{-6} \pm 2.972 \cdot 10^{-5}$	Yes
MTQ power	P_{MTQ}	$0.0858 \cdot DP + 0.0677 \pm 0.320$	Yes
Collection efficiency	η_c	$0.25 - 0.4$	No
ABEP Specific impulse	$I_{sp,ABEP}$	$2000 - 4000$ s	No
Aspect ratio	$L/\sqrt{A}$	$5 - 10$	No
ABEP power	P_{ABEP}	$29240 \cdot F_{drag} + 155.6 \pm 257.4$	Yes
Regular EP specific impulse	$I_{sp,EP}$	$150 - 7852$ s	No
Regular EP power	P_{EP}	$15409 \cdot F_{drag} + 25.6 \pm 29.5$	Yes
Chemical propulsion thrust	$F_{T,ch}$	$0.1 - 1$ N	No
Chemical propulsion specific impulse	$I_{sp,ch}$	$200 - 258$ s	No

7

Simulation Results and Analysis

This chapter presents the results of the Monte Carlo analysis through various plots. They are used to extract the satellite (effective stowed) volume envelope, identify the driving subsystems and expose the dependency of satellite volume on input uncertainty to finally determine the optimal combination of budget-optimization parameters in terms of satellite volume, taking into account feasibility as well. Moreover, the propulsion subsystem gets additional attention and a sensitivity analysis is outlined to visualize the effect of changing design parameters and put the results into the perspective for the proposed mission.

7.1. Data Refinement

This section refines the data produced by the Monte Carlo simulation outlined in Chapter 6. The data is plotted and filtered to gain better insight into how the effective stowed volume of the satellite depends on altitude and deployability of its payload. In line with the calculations done in Section 6.2, the model was ran 7236 times to generate data with a $0.001\,\mathrm{m}^2$ accuracy and $95\,\%$ confidence interval. h was simulated by a uniformly spaced array from $150\,\mathrm{km}$ to $600\,\mathrm{km}$ in $5\,\mathrm{km}$ intervals. $86.4\,\%$ of the data converged to a solution.

Figure 7.1a depicts the raw data on the satellite volume $V_{eff,stowed}$ as a function of orbital altitude h. In Figure 7.1b, outliers were filtered out using a z-score threshold of 3, similar to what was done in Section 6.2. One can observe that removal of the outliers, which account for $1.66\,\%$ of the converged data points, has an almost invisible affect on the plot, though it reduces the standard deviation from 0.0639 to 0.0423. The latter matches the standard deviation found in Chapter 6 reasonably well, confirming correctness of the number of Monte Carlo runs.

Furthermore, as touched upon in Subsection 6.1.3, some data points are generated by extrapolation of the model. They account for $14.4\,\%$ of the total amount of data points. Removal of these leads to Figure 7.2b, which significantly differs from Figure 7.2a (which excludes outliers) at altitudes below $200\,\mathrm{km}$: all data is removed. Therefore, both data sets are used in further analysis.

In Figure 7.3, the top line corresponding to 'With outliers' depicts the distribution of converged cases as a function of altitude. Clearly, little to no datasets converged below $200\,\mathrm{km}$, which is in line with the manually computed reference case 1 in Subsection 6.1.2. The 'With extrapolation'-line just below shows that primarily beyond $500\,\mathrm{km}$ outliers are removed. Reason for this is that the spread introduced by the baffle segmentation causes outliers (see Section 7.2). Extrapolation occurs throughout the entire altitude range as concluded by comparison of the 'With extrapolation'- and 'Without extrapolation'-line, but mostly affects the data around $200\,\mathrm{km}$. When considering Figure 7.4, the extrapolated cases that were removed in the 'Without extrapolation'-category represented by the lower line can be explained. The majority of the data points at low altitudes is removed due to extrapolation of the AOCS model (the magnetic dipole moment specifically). Data rate shows a significantly smaller peak and transmission power remains more or less constant. An important conclusion to draw here is that none of the data below $200\,\mathrm{km}$ can be considered reliable.

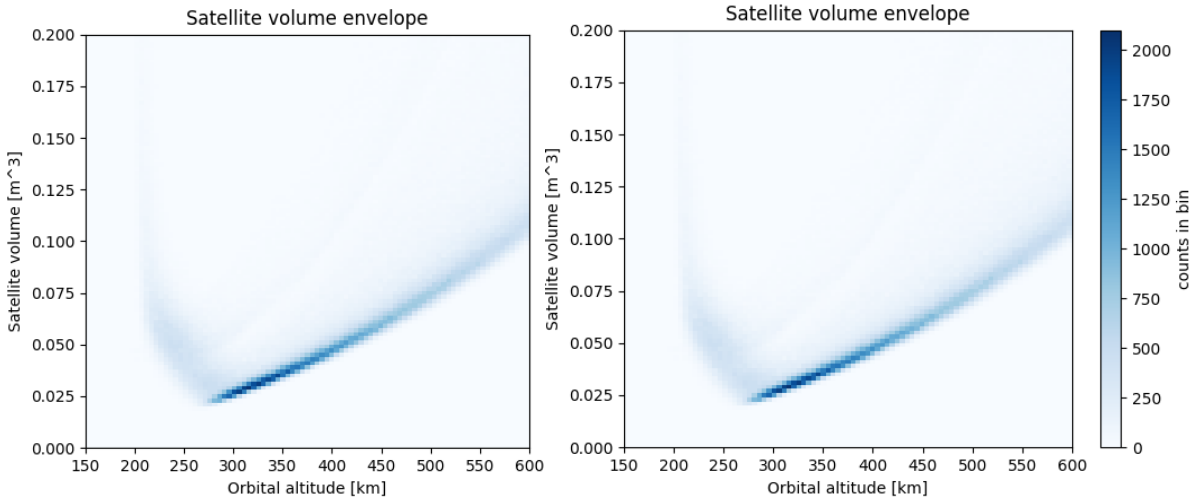

(a) Including outliers

(b) Excluding outliers

Figure 7.1: The Monte Carlo simulation result of the satellite volume envelope $V_{stowed,eff}$ as a function of orbital altitude h with and without outliers (bin size = $(5\,\mathrm{km},\, 0.002\,\mathrm{m}^3)$)

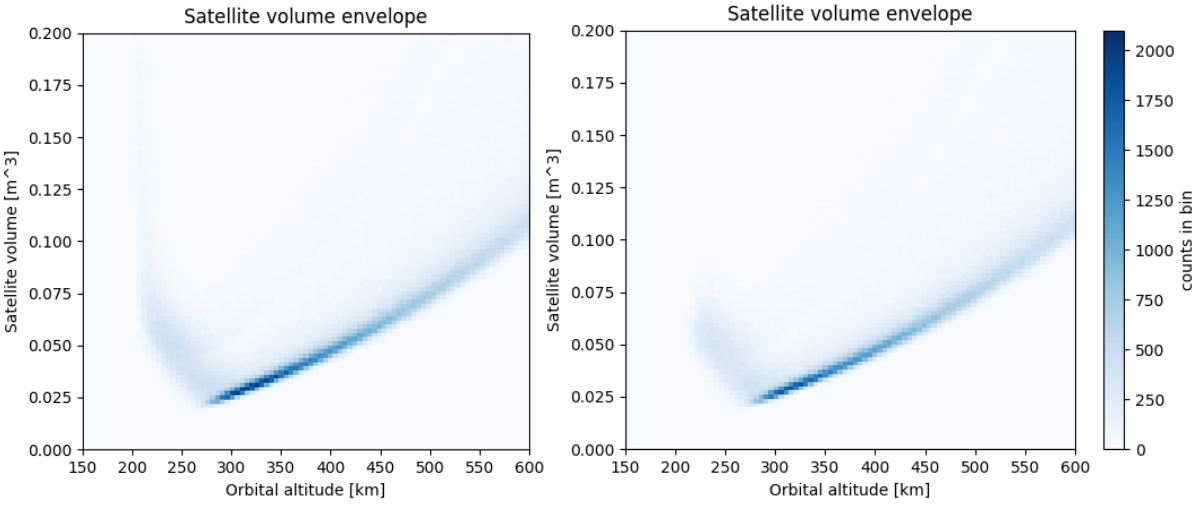

(a) Including extrapolation

(b) Excluding extrapolation

Figure 7.2: The Monte Carlo simulation result of the satellite volume envelope $V_{stowed,eff}$ as a function of orbital altitude h without outliers and with and without extrapolated data points (bin size = $(5\,\mathrm{km},\, 0.002\,\mathrm{m}^3)$)

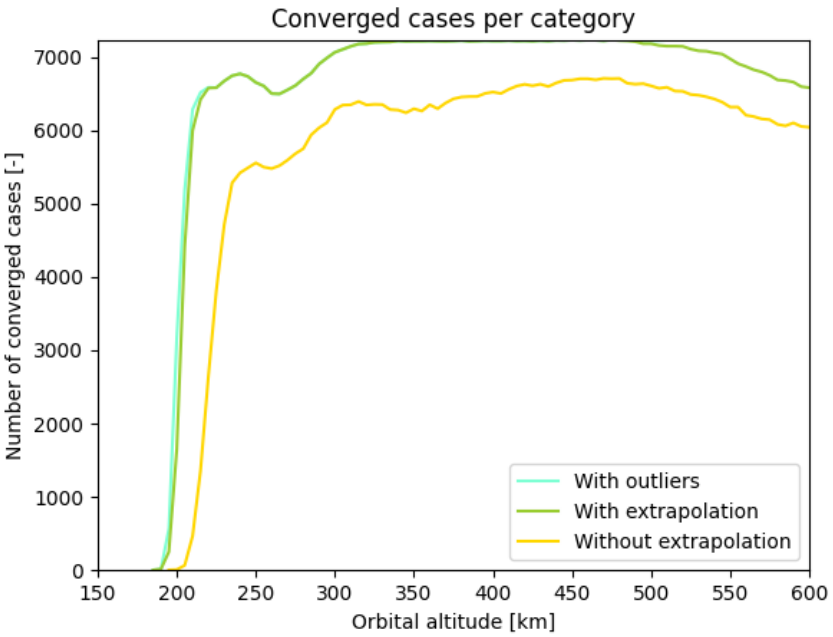

Figure 7.3: The Monte Carlo simulation result of the number of converged cases as a function of orbital altitude h with and without extrapolated data points

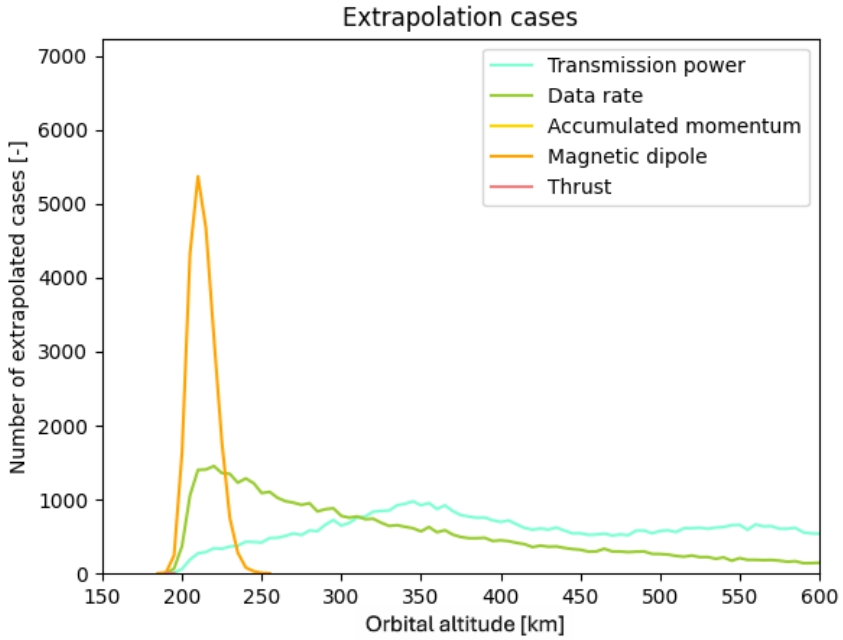

Figure 7.4: The Monte Carlo simulation result of the number of extrapolated cases per category as a function of orbital altitude h

7.2. System Budgets

Now, the results of the Monte Carlo simulation for the system budget are analyzed, both volume as well as power. For this, two plotting methods are used: a two-dimensional histogram that visualizes the envelope of the data, and a line formed by the average and modal value at every altitude. The satellite volume is broken down into the individual subsystem contributions, so that the driving subsystems can be identified.

Firstly, the volume envelopes in-and excluding extrapolated data were already depicted in Figure 7.2. In order to visualize the spread in a different manner, Figure 7.5 depicts plots of the average and median effective stowed satellite volume as a function of orbital altitude. The median is slightly lower than the average in both plots.

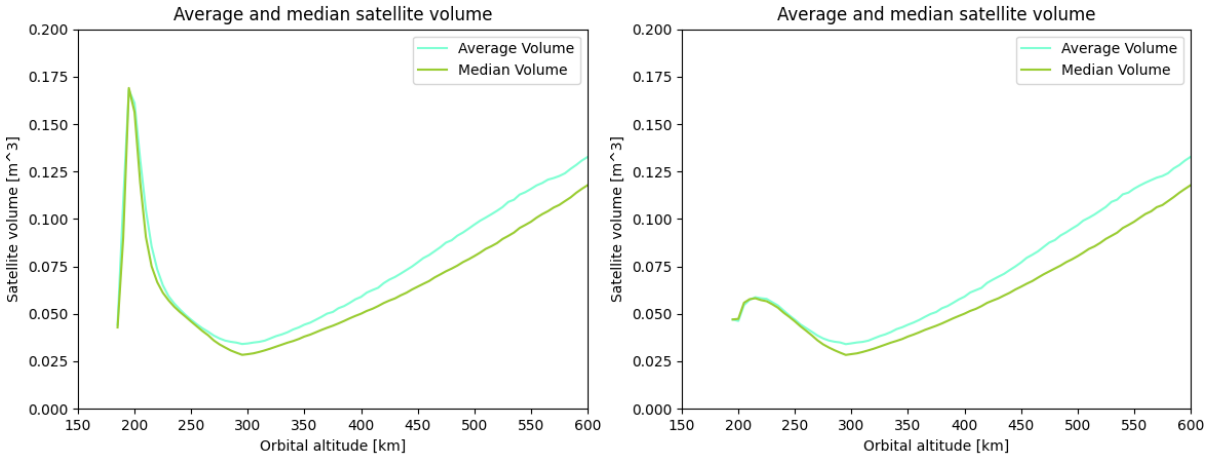

(a) Including extrapolation

(b) Excluding extrapolation

Figure 7.5: The Monte Carlo simulation result of the average and median satellite volume $V_{stowed,eff}$ as a function of orbital altitude h with and without extrapolated data points

Several observations can be made in the aforementioned figures. Their shape is similar to what was found in Section 6.1, with an optimal altitude at $295\,\mathrm{km}$ corresponding to the average minimum effective stowed volume of $0.0341\,\mathrm{m}^3$ with a standard deviation of $0.0128\,\mathrm{m}^3$. The volume increases exponentially below the optimum altitude and shows an almost linear relationship beyond. Furthermore, the uncertainty in effective stowed volume is lowest around the optimum, with a rapid increase below $280\,\mathrm{km}$ and a gradual increase at higher altitudes. The plots show faint lines above the dense optimum, corresponding to different numbers of baffle segments as explained in Section 7.3. Looking at the volume envelopes, most values cluster at the lower end of the volume, pointing at a positively skewed distribution. As the average is sensitive to large values, it is pulled upwards. This effect is caused by the baffle segmentation as discussed in Section 7.3. Therefore, both the average and median volume will be documented in Section 7.8.

The satellite's effective stowed volume is composed of that of the satellite bus and payload. The former consists of the integrated core unit, modeled by a uniform distribution, and the computed volumes of the propulsion subsystem V_{prop}, AOCS V_{AOCS} and EPS V_{bat} and V_{sp}. The latter is the sum of the instrumentation box $V_{instrumentationbox}$, which occupies a fixed volume in the model, and the stowed baffle volume V_{baffle}. The average volume of the altitude-dependent variables are plotted in Figure 7.6.

Again, trends match Figure 6.1. Clearly, removal of outliers drastically reduces propulsion and AOCS volume, leading to reduction of the battery and solar panel volume as well. At low altitudes, volume is driven by these systems (solar panel, propulsion and AOCS respectively), whereas the the payload instrument, particularly the baffle component, dominates beyond $290\,\mathrm{km}$. The individual volume envelopes are depicted in Figure 7.7, Figure 7.8, Figure 7.9, Figure 7.10 and Figure 7.11.

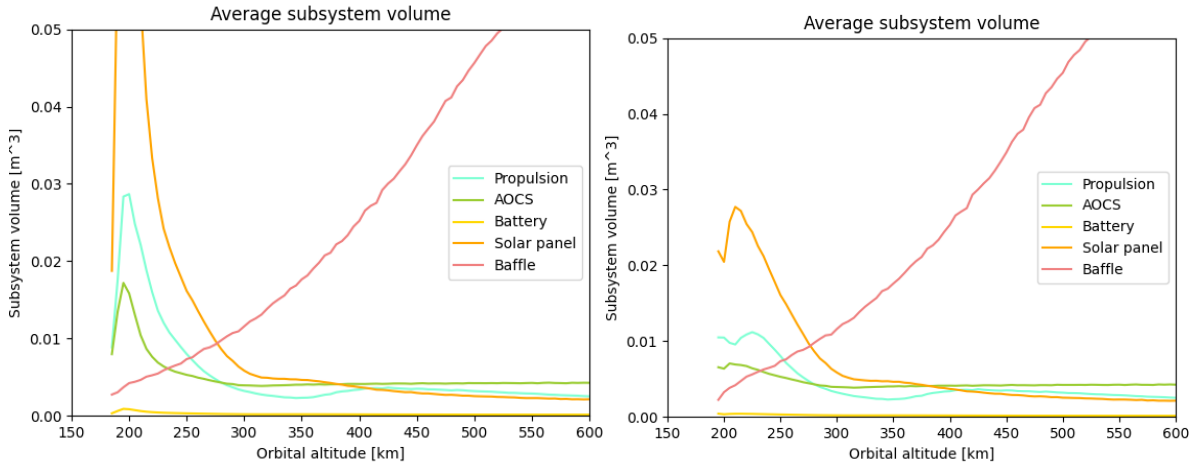

(a) Including extrapolation

(b) Excluding extrapolation

Figure 7.6: The Monte Carlo simulation result of the average subsystem volume budgets V_{prop}, V_{AOCS}, V_{bat}, V_{sp} and V_{baffle} as a function of orbital altitude h with and without extrapolated data points

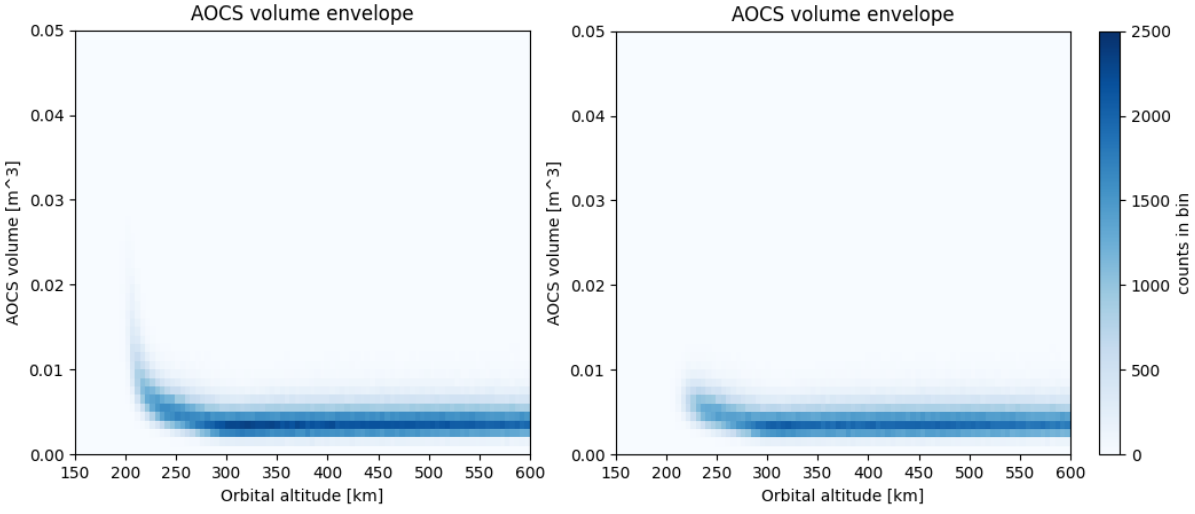

(a) Including extrapolation

(b) Excluding extrapolation

Figure 7.7: The Monte Carlo simulation result of the AOCS volume envelope V_{AOCS} as a function of orbital altitude h with and without extrapolated data points (bin size = $(5\,\mathrm{km},\ 0.001\,\mathrm{m}^3)$)

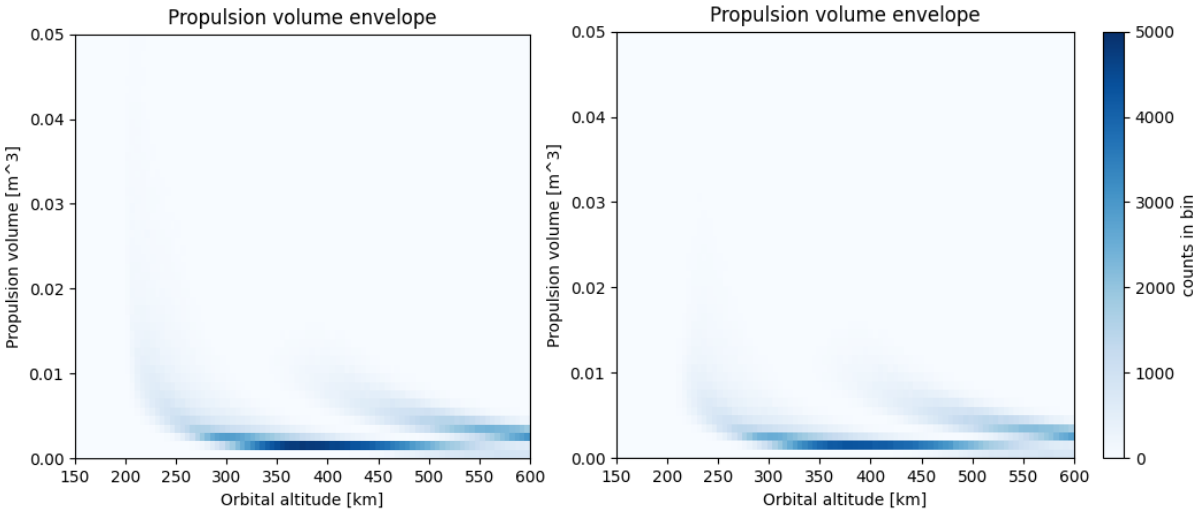

(a) Including extrapolation

(b) Excluding extrapolation

Figure 7.8: The Monte Carlo simulation result of the propulsion system volume envelope V_{prop} as a function of orbital altitude h with and without extrapolated data points (bin size = $(5\,\mathrm{km}, 0.001\,\mathrm{m}^3)$)

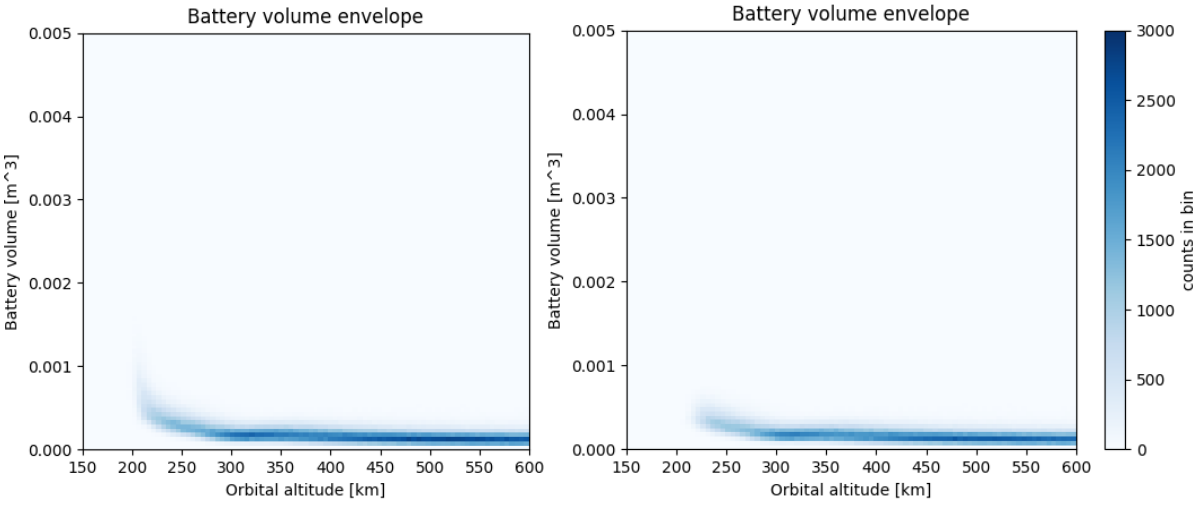

(a) Including extrapolation

(b) Excluding extrapolation

Figure 7.9: The Monte Carlo simulation result of the battery volume envelope V_{bat} as a function of orbital altitude h with and without extrapolated data points (bin size = $(5\,\mathrm{km}, 0.000\,05\,\mathrm{m}^3)$)

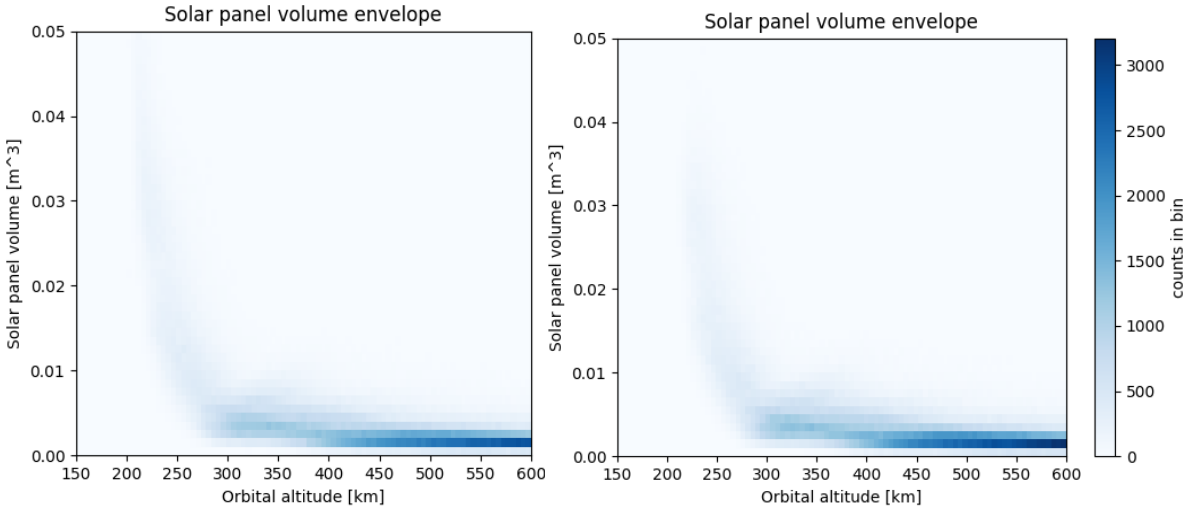

(a) Including extrapolation

(b) Excluding extrapolation

Figure 7.10: The Monte Carlo simulation result of the solar panel volume envelope V_{sp} as a function of orbital altitude h with and without extrapolated data points (bin size = $(5\,\mathrm{km}, 0.001\,\mathrm{m}^3)$)

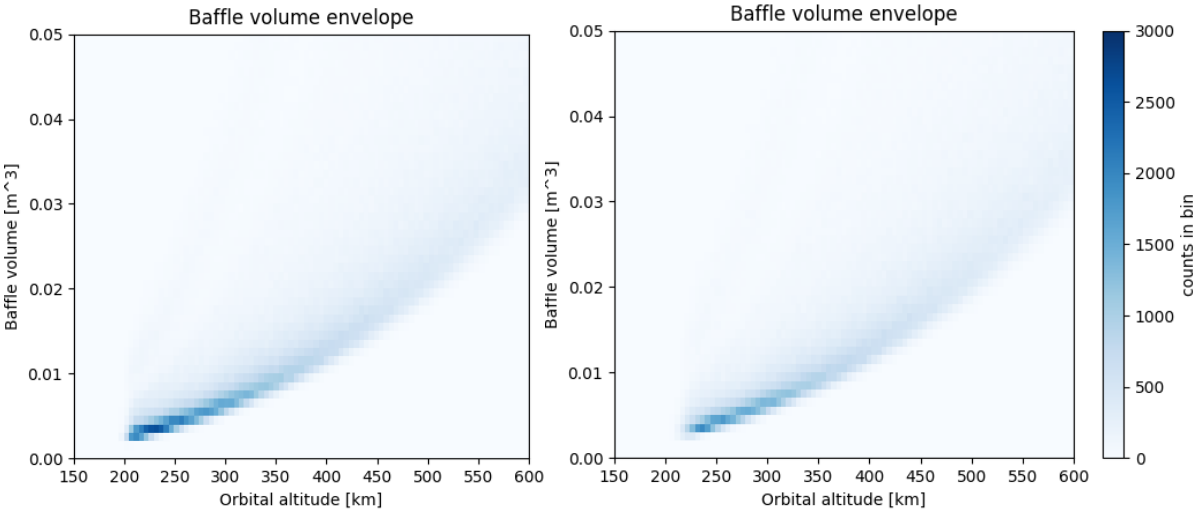

(a) Including extrapolation

(b) Excluding extrapolation

Figure 7.11: The Monte Carlo simulation result of the baffle volume envelope V_{baffle} as a function of orbital altitude h with and without extrapolated data points (bin size = $(5\,\mathrm{km}, 0.001\,\mathrm{m}^3)$)

Evidently, the uncertainty in the satellite volume observed in Figure 7.2a and Figure 7.2b mainly comes from the propulsion subsystem and solar panels at low altitudes, and the optical payload at high altitudes. Reason for the first is the uncertainty in regular EP volume and power, which is further detailed in Section 7.4. The two different trends between $350\,\mathrm{km}$ and $550\,\mathrm{km}$ in Figure 7.8 as well as the wave of the propulsion volume in this same region in Figure 7.6 are the result of the transition between regular EP and chemical propulsion, where the additional EPS volume for regular EP is not taken into account in this plot. On system level however, regular EP implies a larger EPS and thus competes with chemical propulsion in this altitude region. This transition also causes a reduction in solar panel and battery volume as observed in Figure 7.6. The baffle as part of the optical payload introduces uncertainty by the variation of the amount of baffle segments, which is explained in Section 7.3.

The average power consumption of the individual subsystems is depicted in Figure 7.12. Considering the logarithmic scale, power consumption is dominated by the propulsion subsystem at low altitudes where regular EP is the preferred strategy (see Section 7.4). Beyond $300\,\mathrm{km}$, AOCS takes over as the primary power consumer, requiring about $20\,\mathrm{W}$ to $30\,\mathrm{W}$. Indeed, propulsion power consumption decreases exponentially from $350\,\mathrm{km}$ onward, where the transition to chemical propulsion takes place. The plateau in propulsion power consumption before this decrease matches the base power consumption of regular EP as established in Section 5.10. Communications power consumption is relatively low due to the high gain of the receiving antenna (KSAT) and the X-band frequency used.

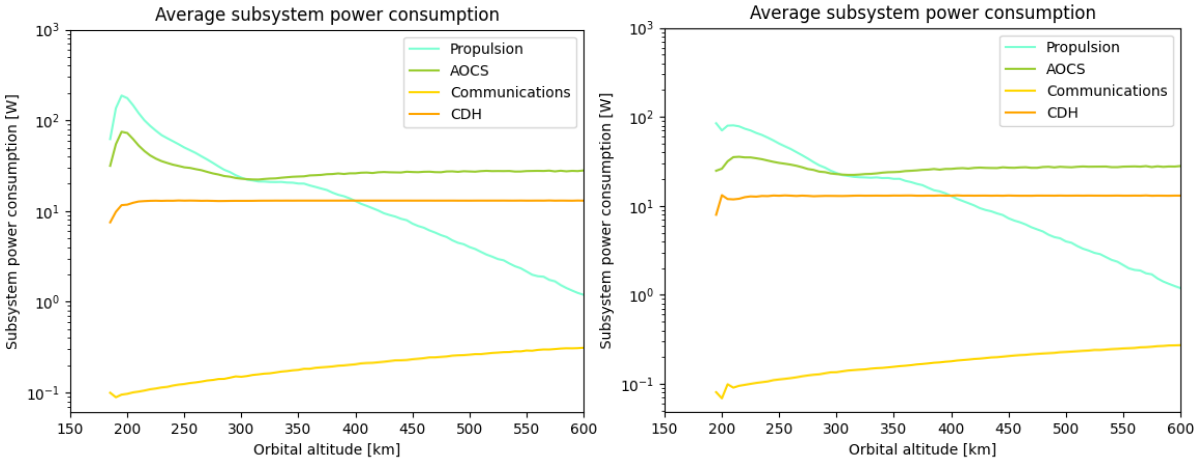

(a) Including extrapolation

(b) Excluding extrapolation

Figure 7.12: The Monte Carlo simulation result of the average subsystem power budgets P_{prop}, P_{AOCS}, P_{com} and P_{CDH} as a function of orbital altitude h with and without extrapolated data points

As AOCS and propulsion are primary design drivers and their model is based on empirical relations, it is important to verify their reliability in the results. Starting with the AOCS, the accumulated momentum and required magnetic dipole are plotted in Figure 7.13a and Figure 7.13b. As explained in Section 5.9, the volume and power models of the CMG and magnetorquer are based on series ranging from $1\,\mathrm{Nms}$ to $10\,\mathrm{Nms}$ and $0.2\,\mathrm{Am}^2$ to $20\,\mathrm{Am}^2$ respectively. In line with what was concluded from Figure 7.4, the accumulated momentum does not exceed $10\,\mathrm{Nms}$. The required magnetic dipole does exceed its model validity range below $220\,\mathrm{km}$. Furthermore, the CMG model is extrapolated at the low end for the majority of the cases. Hence, the AOCS volume and power consumption are likely over-estimated due to a base volume and power consumption targeted towards over-sized actuators. This also explains the flat AOCS lines from $350\,\mathrm{km}$ onward in Figure 7.6 and Figure 7.12. To put this into perspective: taking the CMG's from Veoware, which can accumulate up to $0.1\,\mathrm{Nms}$ [1], as an example, each CMG can save about $5\,\mathrm{W}$. This in turn leads to a total power consumption reduction of $20\,\mathrm{W}$.

[1] `https://veowarespace.com/vw-products/reaction-wheel-whl-100.`

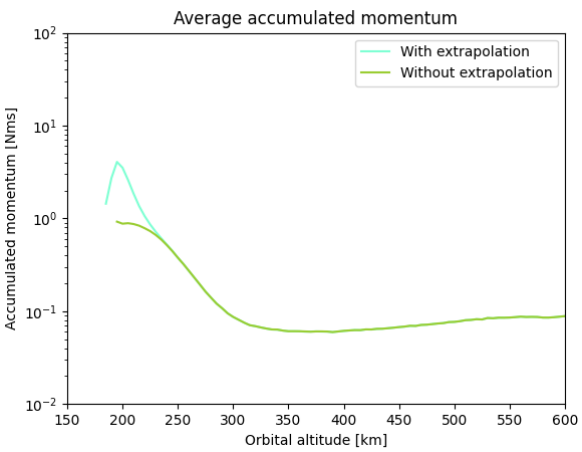

(a) Average accumulated momentum M_{acc} as a function of orbital altitude h with and without extrapolated data points.

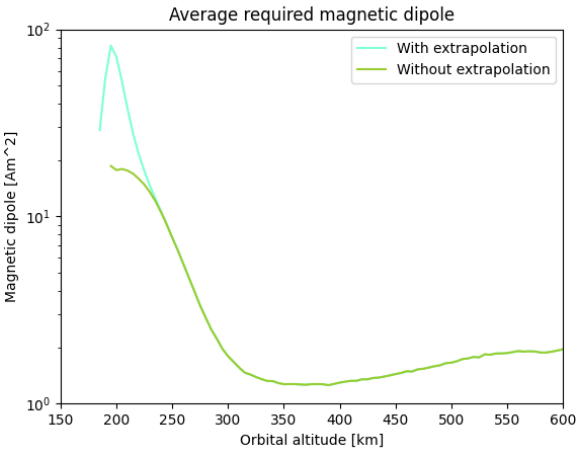

(b) Average required magnetic dipole DP as a function of orbital altitude h with and without extrapolated data points.

Figure 7.13: Comparison of Monte Carlo simulation results for M_{acc} and DP with and without extrapolated data points.

Now, for propulsion, extrapolation does not occur. This model is namely based on a large set regular EP of samples that covers a wide range thrust levels from $0.003\,\mathrm{mN}$ to $18\,\mathrm{mN}$. According to Figure 7.14, this covers all possible average thrust levels. For chemical propulsion, the approach is different as the thrust level is sampled and the amount of thrust-time is computed, making the model valid for all drag levels below $1\,\mathrm{N}$.

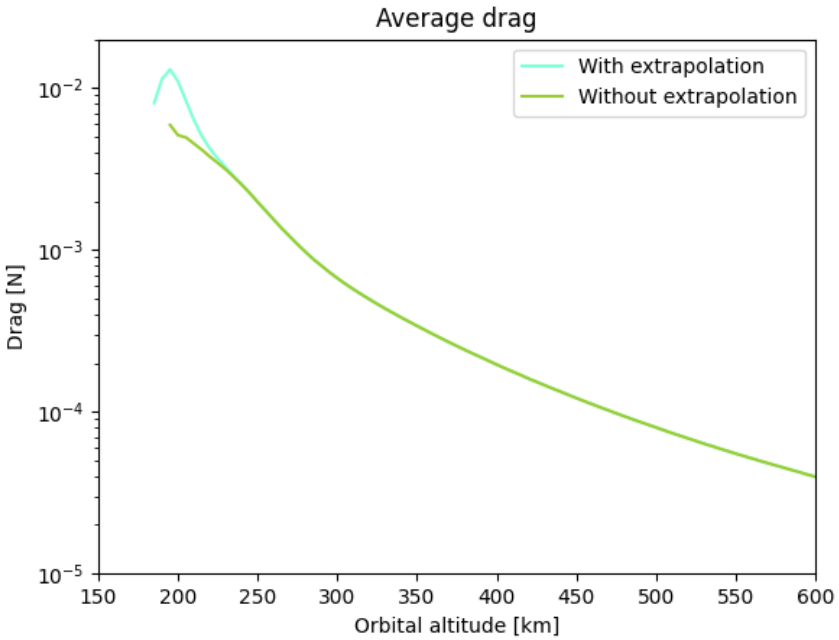

Figure 7.14: The Monte Carlo simulation result of the average required magnetic dipole DP as a function of orbital altitude h without extrapolated data points

7.3. Input Dependencies

As mentioned in Section 6.2 the mission lifetime t_{life} and number of baffle segments $n_{segments}$ are of particular interest for the mission design. This section analyzes these parameters in more detail. A plot of the average satellite volume for different mission lifetimes is depicted in Figure 7.15. It can be concluded that mission lifetime has more impact at lower orbital altitudes, where a longer mission corresponds to a larger satellite volume. Reason for this is the increased propellant volume, though differences on system level are small compared to the effect of the number of baffle segments due to the high specific impulse of regular EP propellants.

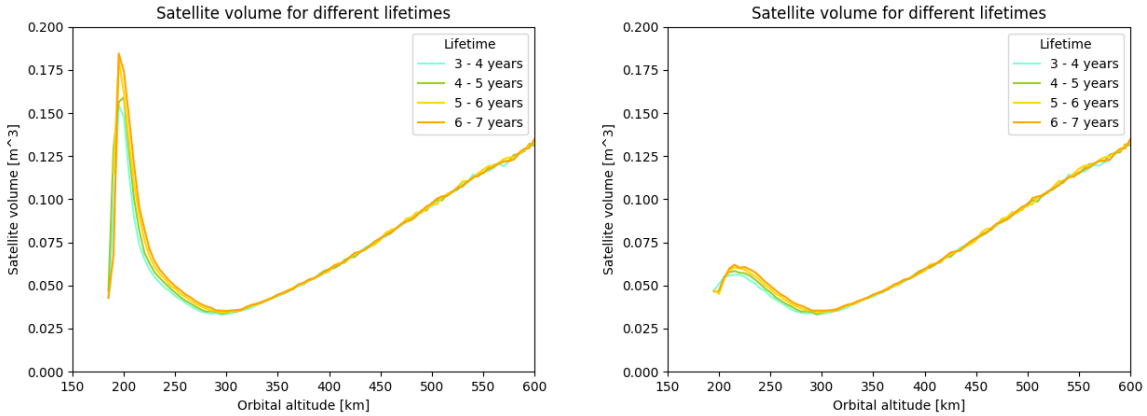

(a) Including extrapolation

(b) Excluding extrapolation

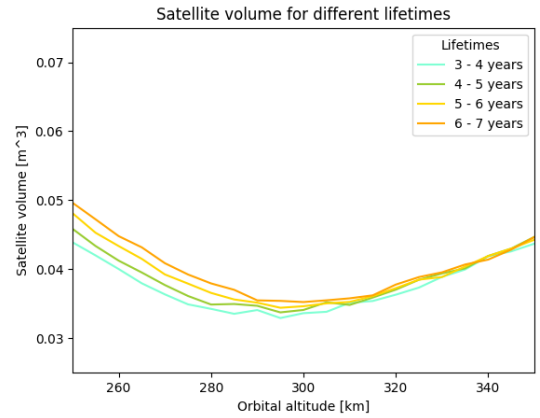

(c) Including extrapolation, zoomed in

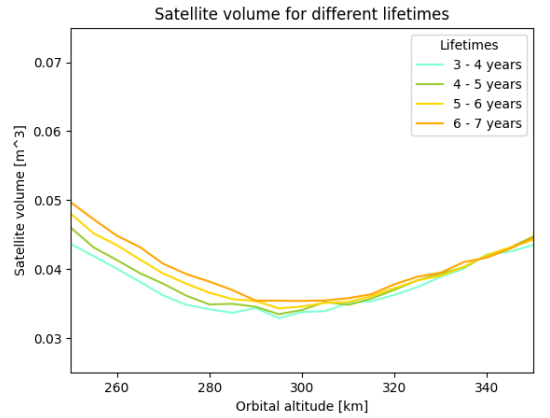

(d) Excluding extrapolation, zoomed in

Figure 7.15: The Monte Carlo simulation result of the average satellite volume $V_{eff,stowed}$ as a function of orbital altitude h for different mission lifetimes t_{life}, with and without extrapolated data points.

The effect of the number of baffle segments can be observed in Figure 7.16: indeed, an increasing number of segments reduces the effective stowed volume. In contrast to the mission lifetime, the impact of this parameter grows with orbital altitude, making it a primary contributor to the satellite volume uncertainty at high altitudes observed in Figure 7.2. Furthermore, its effect on satellite volume is significant, revealing the true power of a deployable payload instrument. The satellite volume reduces with an increasing amount of segments, though the gain per added segment lowers. This calls for a trade-off between satellite volume optimization and other factors such as complexity.

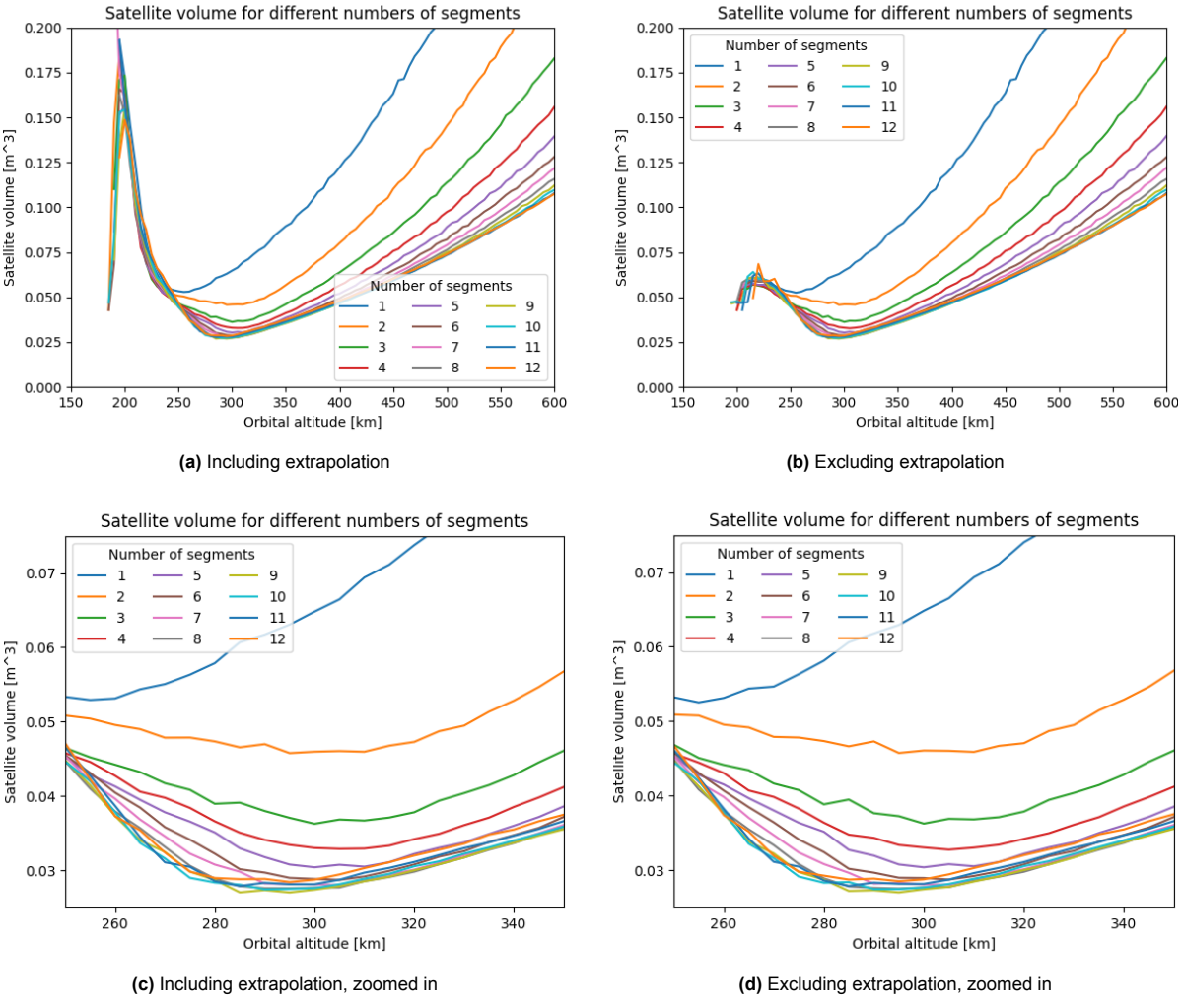

(a) Including extrapolation

(b) Excluding extrapolation

(c) Including extrapolation, zoomed in

(d) Excluding extrapolation, zoomed in

Figure 7.16: The Monte Carlo simulation result of the average satellite volume as a function of orbital altitude h for different numbers of baffle segments $n_{segments}$, with and without extrapolated data points.

7.4. Propulsion Strategy

The propulsion strategy is important for the mission design as factors such as TRL, complexity and regulation come into play here as well. The average volume and power consumption of the different propulsion strategies are plotted in Figure 7.17 and Figure 7.18, which are based only on the data points that converged to that specific propulsion strategy (the line ranging from $150\,\mathrm{km}$ to $250\,\mathrm{km}$ represents ABEP, the lower line is for regular EP and the upper one for chemical propulsion). Figure 7.19 visualizes how many runs converged to a specific propulsion strategy as a function of altitude where the first big peak in both plots corresponds to regular EP and the second one to chemical propulsion.

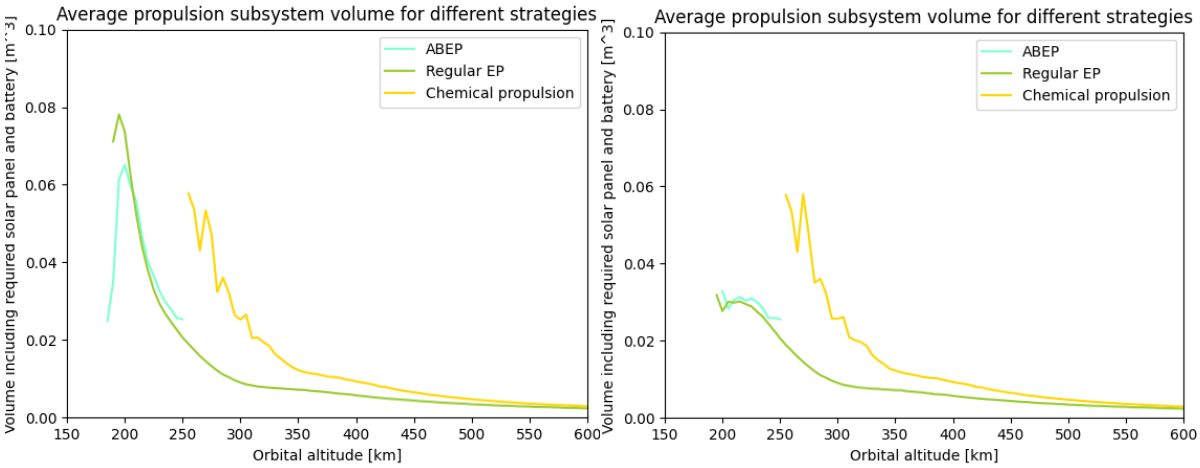

(a) Including extrapolation

(b) Excluding extrapolation

Figure 7.17: The Monte Carlo simulation result of the average propulsion subsystem volume including additional solar panel and battery volume as a function of orbital altitude h for different propulsion strategies at converged data points with and without extrapolated data points

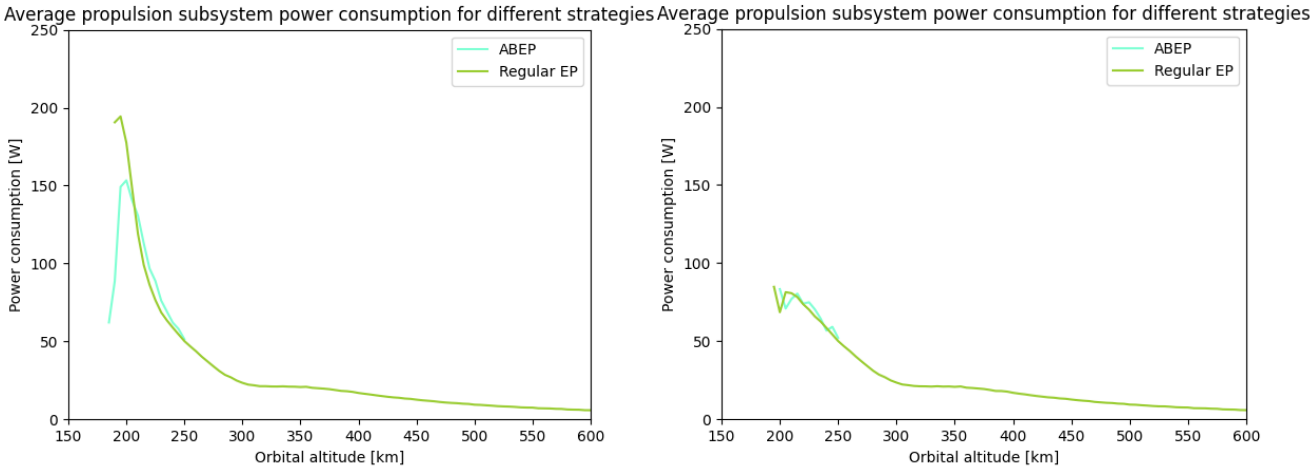

(a) Including extrapolation

(b) Excluding extrapolation

Figure 7.18: The Monte Carlo simulation result of the average propulsion subsystem power P_{prop} as a function of orbital altitude h for different propulsion strategies at converged data points with and without extrapolated data points

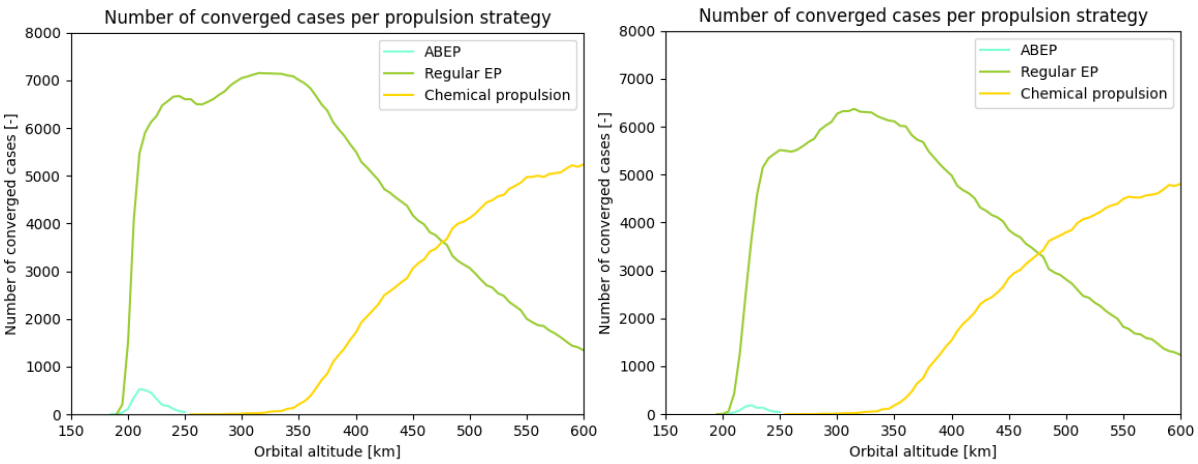

(a) Including extrapolation

(b) Excluding extrapolation

Figure 7.19: The Monte Carlo simulation result of the propulsion strategy count as a function of orbital altitude h with and without extrapolated data points

Clearly, ABEP feasibility is extremely low, as very little runs converged to this strategy. Reason for this is its great power consumption combined with the constraints related to the intake area that may not exceed spacecraft dimensions. Furthermore, regular EP performs considerably better than chemical propulsion in the VLEO regime in terms of volume, hence the high count of converged regular EP cases in Figure 7.19. At the optimal altitude of $295\,\mathrm{km}$, regular EP is thus the preferred propulsion strategy in terms of volume.

Interestingly, regular EP consumes lower volume at all altitudes when the design converges to this strategy. However, at higher altitudes, its volume advantage decreases so that more and more often, chemical propulsion wins. This transition also becomes visible when plotting the average propulsion volume of all types at all data points as done in Figure 7.20 rather than only the converged ones in Figure 7.17. The discrepancy in transition altitude between Figure 7.19 and Figure 7.20 is the result of skewed data: a few extreme regular EP volumes around $400\,\mathrm{km}$ to $450\,\mathrm{km}$ increase the average volume while not yet affecting the convergence count as much.

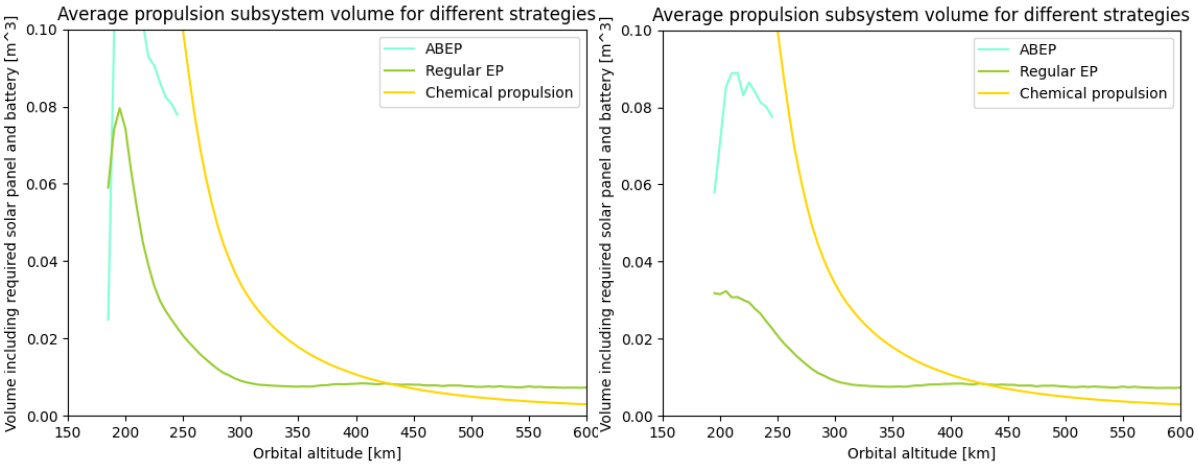

(a) Including extrapolation

(b) Excluding extrapolation

Figure 7.20: The Monte Carlo simulation result of the average propulsion subsystem volume including additional solar panel and battery volume as a function of orbital altitude h for different propulsion strategies at all data points with and without extrapolated data points

An important note here is the average power consumption of regular EP, depicted in Figure 7.18. The relatively high power required namely drives the power budget in VLEO as was observed in Figure 7.12, resulting in a significant solar panel volume, which is elaborated more on in Section 7.5.

As mentioned before and plotted in Figure 7.8, the propulsion subsystem introduces uncertainty into the model at low altitudes and around $350\,\mathrm{km}$ to $550\,\mathrm{km}$. The latter is related to the regular EP - chemical propulsion transition in accordance with Figure 7.19, as the volume of chemical propulsion is larger than that of regular EP when additional EPS volume is not taken into account. The uncertainty at low altitudes is a result of the different geometries that occur in this range, hence an uncertainty in the amount of drag to be compensated by this subsystem. The satellite geometry is discussed in more detail in Section 7.5. Figure 7.21 depicts the regular EP volume envelope. Indeed, uncertainty increases with decreasing altitude due to a spread in the drag that must be compensated.

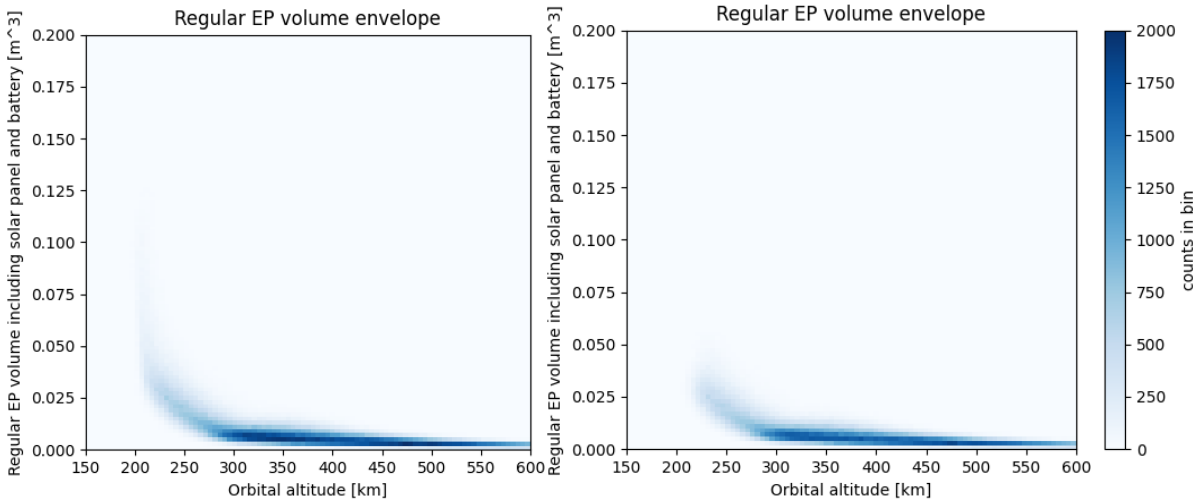

(a) Including extrapolation

(b) Excluding extrapolation

Figure 7.21: The Monte Carlo simulation result of the regular EP volume envelope as a function of orbital altitude h with and without extrapolated data points (bin size = $(5\,\mathrm{km},\ 0.002\,\mathrm{m}^3)$)

7.5. Result Feasibility

As noted in Subsection 6.1.2, the number of solar panel segments could introduce feasibility issues. Therefore, it is explicitly analyzed in the Monte Carlo simulation and plotted in Figure 7.22.

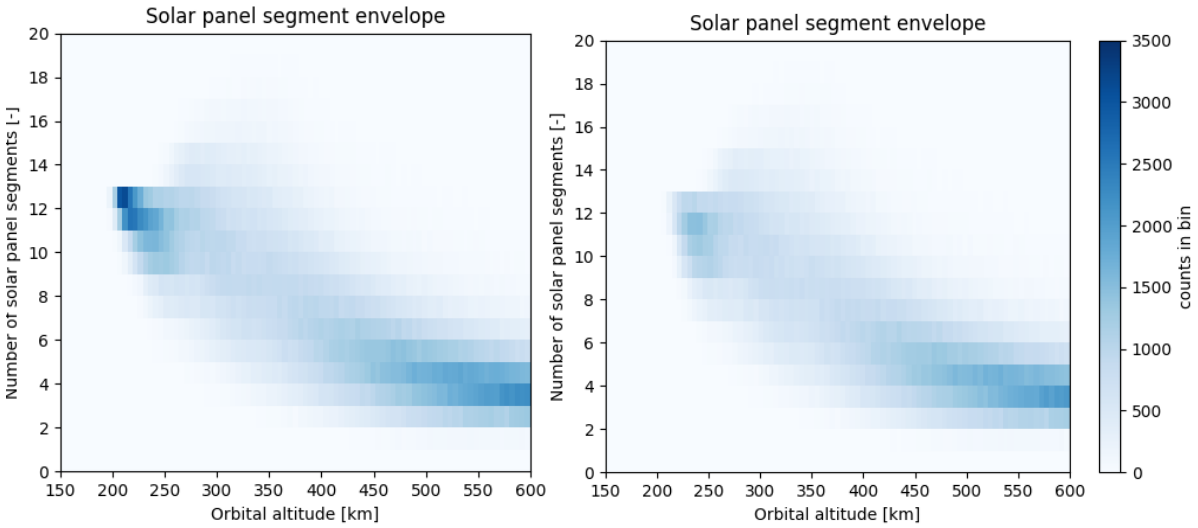

(a) Including extrapolation

(b) Excluding extrapolation

Figure 7.22: The Monte Carlo simulation result of the solar panel segment envelope as a function of orbital altitude h with and without extrapolated data points (bin size = ($5\,\mathrm{km}$, 1 segment))

The increased spread in the required number of solar panels around $250\,\mathrm{km}$ to $450\,\mathrm{km}$ is the result of baffle segmentation. The number of baffle segments is namely related to their height and thus, the total available area for solar panels. To visualize this, Figure 7.23 plots the average number of solar panels for different numbers of baffle segments. It is clear that the number of solar panel segments suffers from the decrease in baffle segment height as the amount of baffle segments increases.

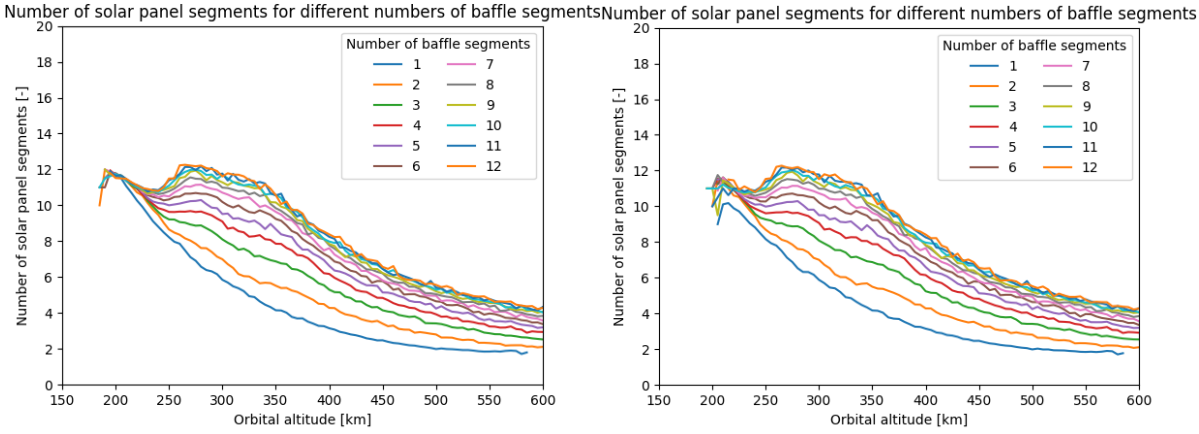

(a) Including extrapolation

(b) Excluding extrapolation

Figure 7.23: The Monte Carlo simulation result of the average number of solar panel segments for different numbers of baffle segments $n_{segments}$ as a function of orbital altitude h with and without extrapolated data points

Ten segments, five on each side of the satellite, push the practical feasibility of the solar panel design as a larger number of segments is rarely encountered in real-life. Thus, from Figure 7.23, one can conclude that the majority of designs below $300\,\mathrm{km}$ deal with challenges concerning solar panel integration. The need for a large number of solar panels is the result of a combination of power demand, especially by the propulsion subsystem, and the satellite geometry.

In line with Section 5.4, the satellite takes any of the four geometry cases, depending on the stowed payload dimensions and bus volume. The average volume of the converged designs for the different geometry cases is depicted in Figure 7.24. The count of the geometry cases is depicted in Figure 7.25.

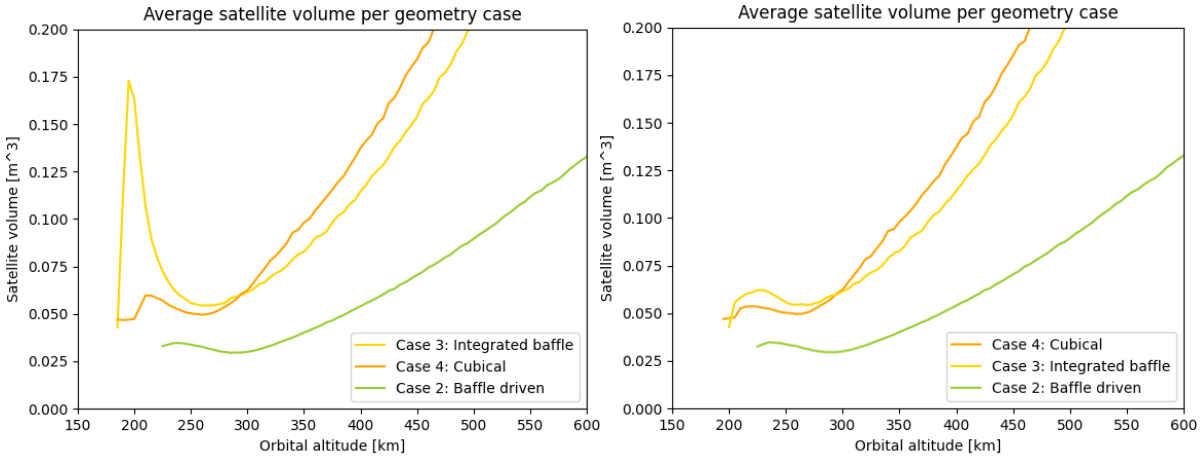

(a) Including extrapolation

(b) Excluding extrapolation

Figure 7.24: The Monte Carlo simulation result of the average satellite volume $V_{stowed,eff}$ for the different geometry cases as a function of orbital altitude h with and without extrapolated data points

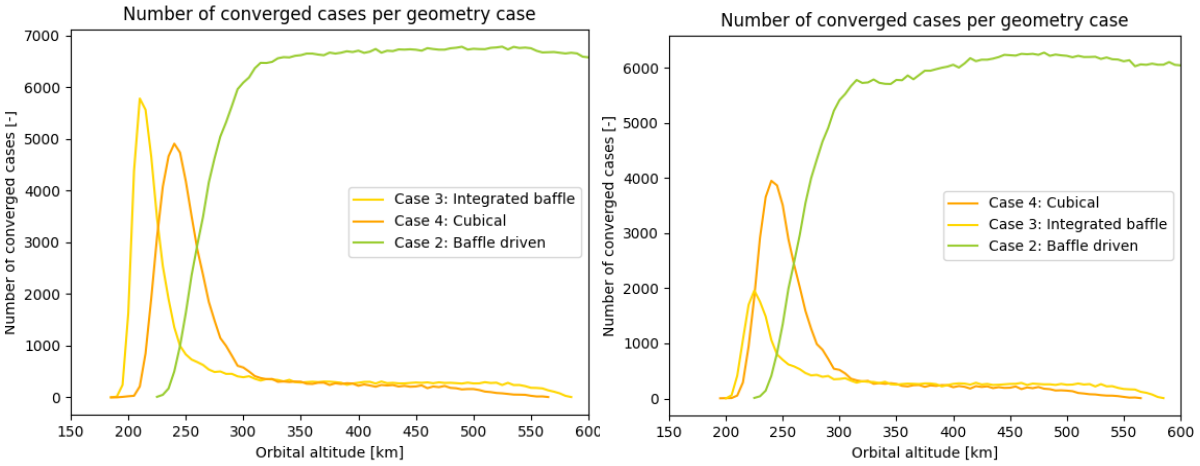

(a) Including extrapolation

(b) Excluding extrapolation

Figure 7.25: The Monte Carlo simulation result of the geometry case count as a function of orbital altitude h with and without extrapolated data points

Geometry case I (CubeSat) does not occur at all. Therefore, a CubeSat geometry is deemed unfeasible for this mission. Case III (Integrated baffle) and IV (Cubical) are implemented in a minority of cases, primarily at low altitudes when the baffle does not drive the satellite dimensions, They are also preferred when the effective stowed volume is relatively large. For the far majority of sample sets however, geometry case II (Baffle driven) is implemented, meaning the payload is driving and the satellite takes a rectangular shape that reduces drag. Indeed, this geometry leads to relatively small solar panel segments, as the height of the satellite is adjusted to add up to the required bus volume (with a minimum imposed by the instrumentation box). A plot of the satellite body dimensions is depicted in Figure 7.26.

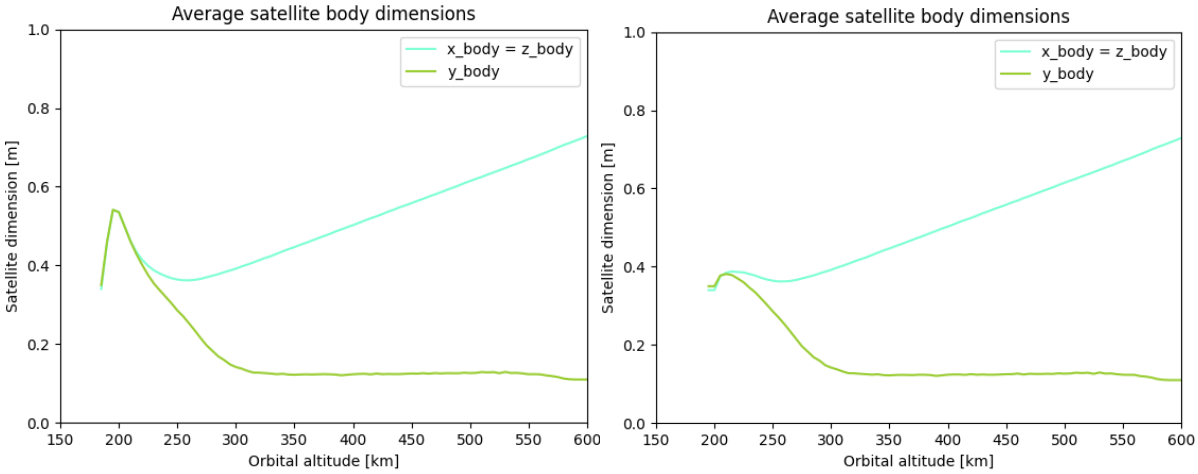

(a) Including extrapolation

(b) Excluding extrapolation

Figure 7.26: The Monte Carlo simulation result of the satellite body dimensions x_{body}, y_{body} and z_{body} as a function of orbital altitude h with and without extrapolated data points

From the plot, it is clear that the average height (y-dimension along nadir direction excluding exterior baffle) of the satellite is significantly less than the other two dimensions, due to the dominant role of the baffle. At the volume optimum of $295\,\mathrm{km}$, the height is about $0.2\,\mathrm{m}$, compared to the other dimensions (x- and z-dimension) of $0.4\,\mathrm{m}$. The model thus outputs flatter satellites at higher altitudes, constrained by the minimum height for the instrumentation box, closely resembling the Disk/HexSat concept introduced in Section 2.3. While diverging from the initially intended CubeSat concept, these form factors seem to be more suitable for this mission. This calls for a reconsideration of the most suitable geometry and the possibility of stacking flat satellites with such payload.

A second concern that resulted from Subsection 6.1.2 was the extrapolation of the communication model, and, more specifically, the transmission power. An envelope of the transmission power as a function of orbital altitude is depicted in Figure 7.27. Similar to Figure 5.18, bands corresponding to the different E_b/N_0 ranges can be identified. Only $8.86\,\%$ of the data uses extrapolation of the communications model.

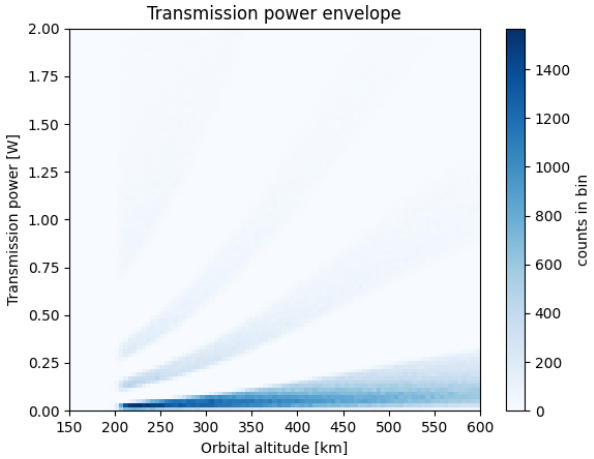

Figure 7.27: The Monte Carlo simulation result of the transmission power envelope P_{Tx} as a function of orbital altitude h with extrapolated data points (bin size = (5 km, $0.02\,\mathrm{W}$)

7.6. Sensitivity Analysis

The goal of this research is to identify the effects of deployable optics and VLEO on satellite volume. In order to do this, the DST concept proposed by the Delft University of Technology was taken as a starting point. However, this preliminary concept is based on several assumptions that might change in the course of mission development. Therefore, it is important to assess the sensitivity of the generated model to changes in this concept design. This section maps the sensitivities of the simulation results to the volume driving subsystems.

7.6.1. Aperture Sensitivity

A fundamental assumption on which the model is based is related to the diameter of the primary mirror. As explained in Subsection 5.2.2, a diameter of $30\,\mathrm{cm}$ at $300\,\mathrm{km}$ is taken as a reference. However, re-evaluation of the optical considerations could lead to the adjustment of this reference dimension, hence the sensitivity of the model on this parameter is assessed. In order to do so, the Monte Carlo simulation was ran with a M1 reference diameter of $20\,\mathrm{cm}$ and $40\,\mathrm{cm}$ at $300\,\mathrm{km}$. Figure 7.28 depicts the resulting satellite volume envelopes (the data is filtered according to Section 7.1 and extrapolated data is included). The first analysis converged to a solution in $84.1\,\%$ of the sample sets while the latter did so in $86.7\,\%$, both fairly close to the original model at $86.2\,\%$. As expected, the standard deviation of the model increases with increasing M1; from $0.0221\,\mathrm{m}^3$ for the $20\,\mathrm{cm}$ case to $0.0725\,\mathrm{m}^3$ for the $40\,\mathrm{cm}$ case, compared to $0.0421\,\mathrm{m}^3$ for the original model.

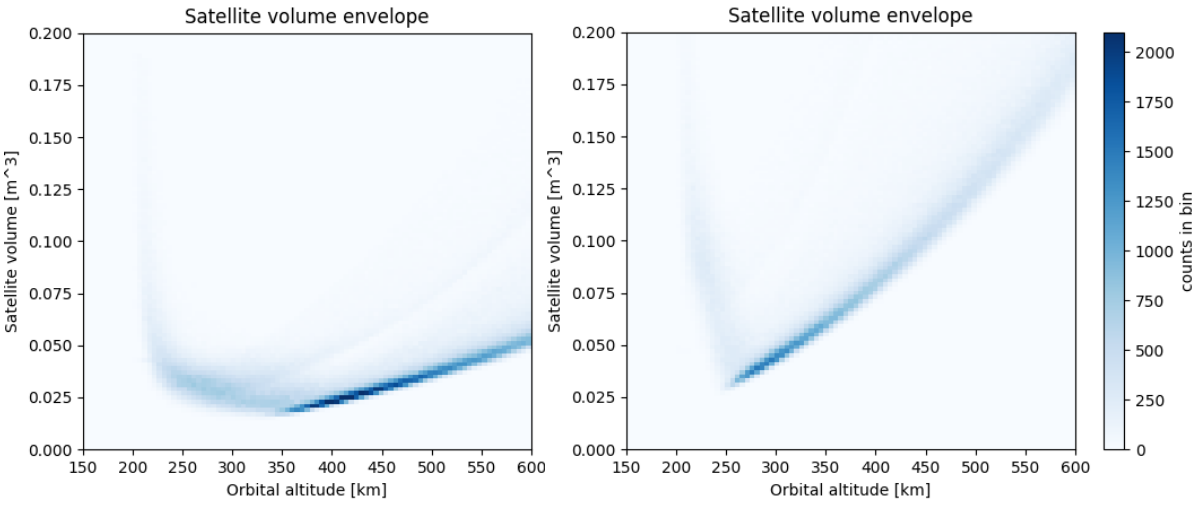

(a) Reference aperture of $20\,\mathrm{cm}$ at $300\,\mathrm{km}$

(b) Reference aperture of $40\,\mathrm{cm}$ at $300\,\mathrm{km}$

Figure 7.28: The Monte Carlo simulation result of the effective stowed volume $V_{eff,stowed}$ as a function of orbital altitude h with extrapolated data points (bin size = ($5\,\mathrm{km}$, $0.002\,\mathrm{m3}$))

It immediately becomes clear that the M1 diameter visibly affects the volume envelope. Both the minimum effective stowed volume shifts (see Table 7.1) and the shape of the plot evolves. With increasing M1 diameter, the minimum effective stowed volume increases and the optimal attitude decreases. Interestingly, the shape of the envelope also becomes sharper, meaning a larger volume increase for the same deviation from the optimum. The rapidly increasing payload volume (more specifically, the baffle) is responsible for this effect (see Figure 7.29 below). Again, the uncertainty for both is smallest around the optimum and faint lines indicating the volumes for different baffle segmentations can be distinguished.

The subsystem volume trends are plotted in Figure 7.29. As expected, the baffle volume increases with increasing M1 diameter. The other altitude-dependent subsystems are mostly affected at altitudes below $300\,\mathrm{km}$. AOCS increases with increasing aperture dimensions while propulsion transitions from regular EP to chemical propulsion at a higher altitude (seen as a wave in the propulsion volume line), affecting the EPS volume trend as well. The latter is clarified in Figure 7.30 and a direct consequence of the increased volume and thus drag due to a larger M1. In both cases, ABEP still shows little feasibility.

Table 7.1: The average minimum effective stowed volume for different primary mirror dimensions

M1 diameter at $300\,\mathrm{km}$ [m]	**Average optimal altitude** [km]	**Average effective stowed volume** [m^3]
0.2	370	0.0281
0.3	295	0.0341
0.4	270	0.0475

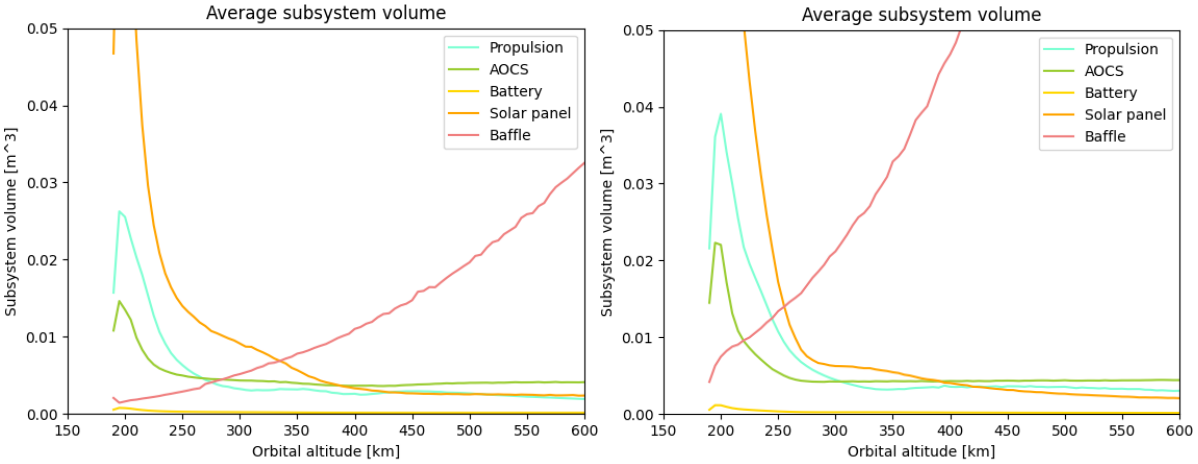

(a) Reference aperture of $20\,\mathrm{cm}$ at $300\,\mathrm{km}$

(b) Reference aperture of $40\,\mathrm{cm}$ at $300\,\mathrm{km}$

Figure 7.29: The Monte Carlo simulation result of the average subsystem volume budgets V_{prop}, V_{AOCS} , V_{bat}, V_{sp} and V_{baffle} as a function of orbital altitude h with extrapolated data points

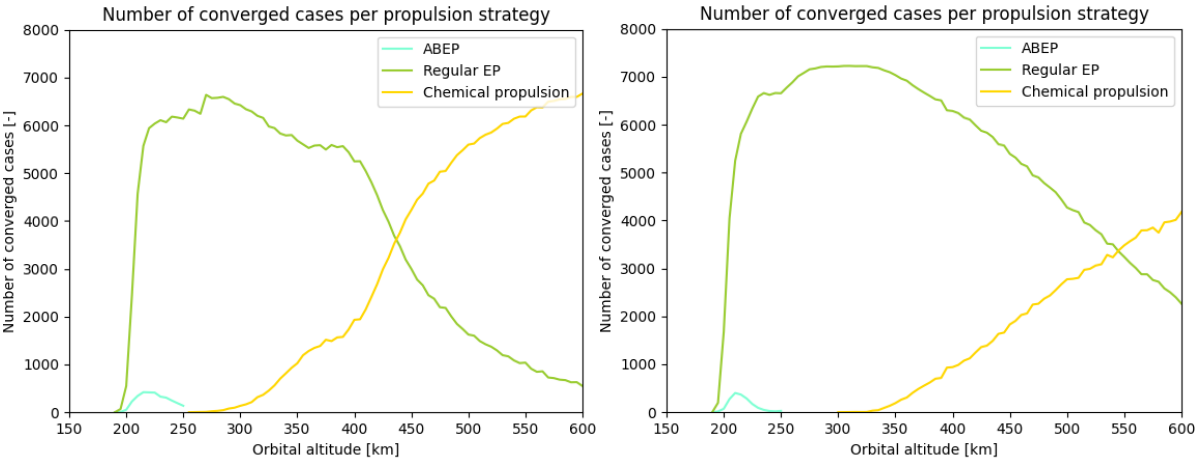

(a) Reference aperture of $20\,\mathrm{cm}$ at $300\,\mathrm{km}$

(b) Reference aperture of $40\,\mathrm{cm}$ at $300\,\mathrm{km}$

Figure 7.30: The Monte Carlo simulation result of the propulsion strategy count as a function of orbital altitude h with extrapolated data points

The propulsion subsystem power consumption follows the regular EP-chemical propulsion transition trend as seen in Figure 7.31. Solar panel volume reveals a dependency that cannot be explained by the power consumption, but rather is the effect of satellite geometry as depicted in Figure 7.32. A payload driven satellite namely allows for wider solar panels compared to a cubical configuration, reducing solar panel length and consequently, thickness as well.

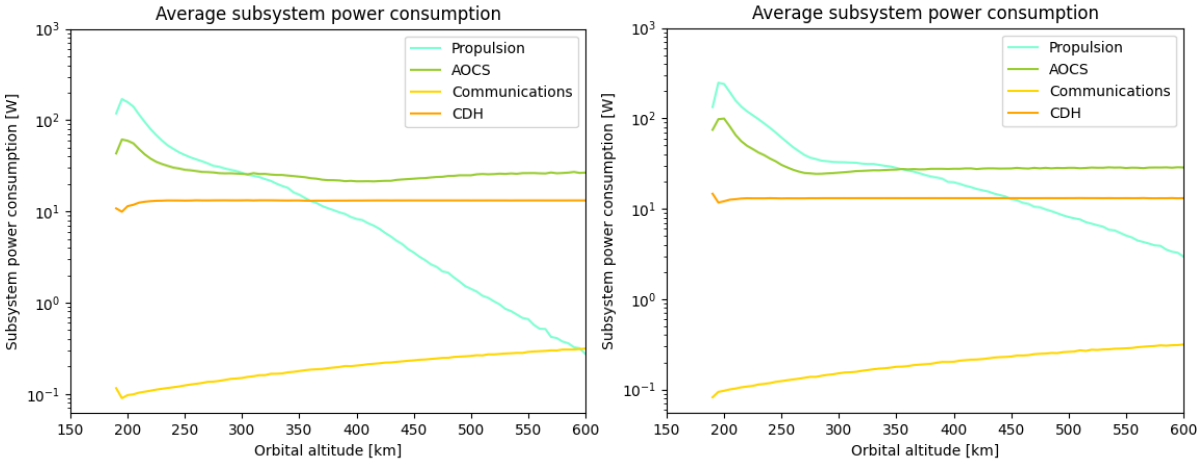

(a) Reference aperture of $20\,\mathrm{cm}$ at $300\,\mathrm{km}$

(b) Reference aperture of $40\,\mathrm{cm}$ at $300\,\mathrm{km}$

Figure 7.31: The Monte Carlo simulation result of the average subsystem power budgets P_{prop}, P_{AOCS} , P_{com} and P_{CDH} as a function of orbital altitude h with extrapolated data points

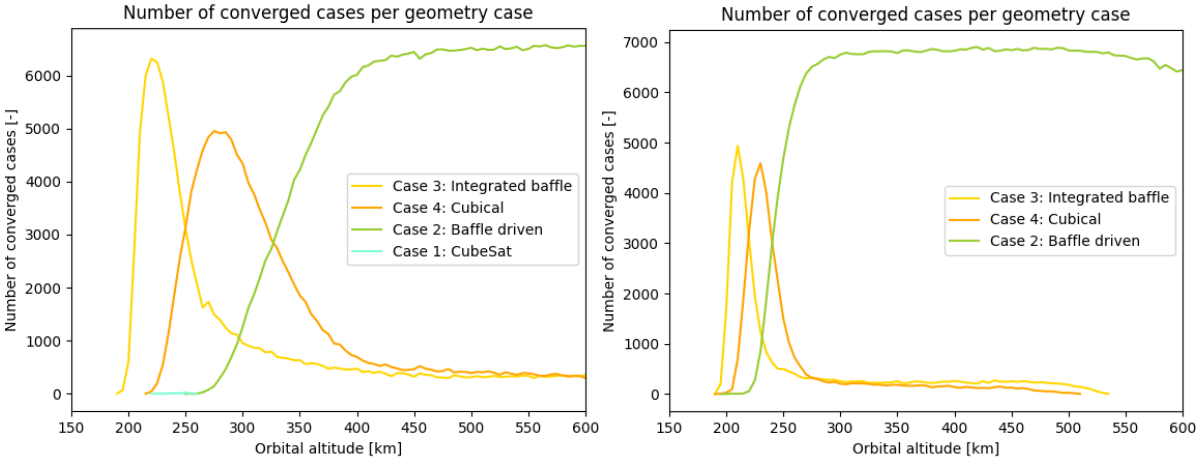

(a) Reference aperture of $20\,\mathrm{cm}$ at $300\,\mathrm{km}$

(b) Reference aperture of $40\,\mathrm{cm}$ at $300\,\mathrm{km}$

Figure 7.32: The Monte Carlo simulation result of the geometry case count as a function of orbital altitude h with and without extrapolated data points

For the number of baffle segments, an increased M1 causes more volume gain per added segment (see Figure 7.33).

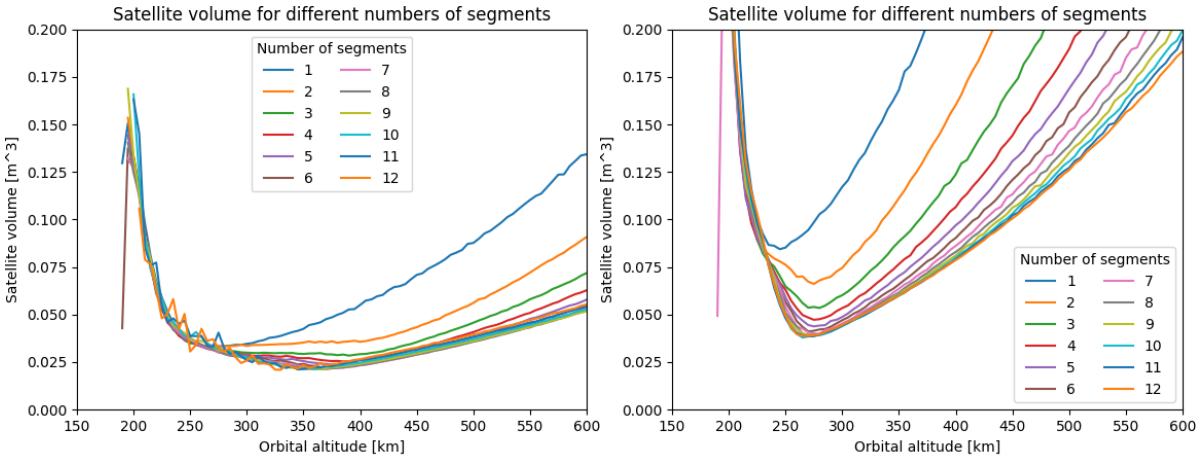

(a) Reference aperture of $20\,\mathrm{cm}$ at $300\,\mathrm{km}$

(b) Reference aperture of $40\,\mathrm{cm}$ at $300\,\mathrm{km}$

Figure 7.33: The Monte Carlo simulation result of the average satellite volume $V_{eff,stowed}$ as a function of orbital altitude h for different number of baffle segments $n_{segments}$ with extrapolated data points

Reliability of these results is related to the extend of extrapolation of the model. A plot indicating the number of extrapolations per category can be found in Figure 7.34. The same trends are observed, though a larger aperture diameter causes more extrapolation of the AOCS model.

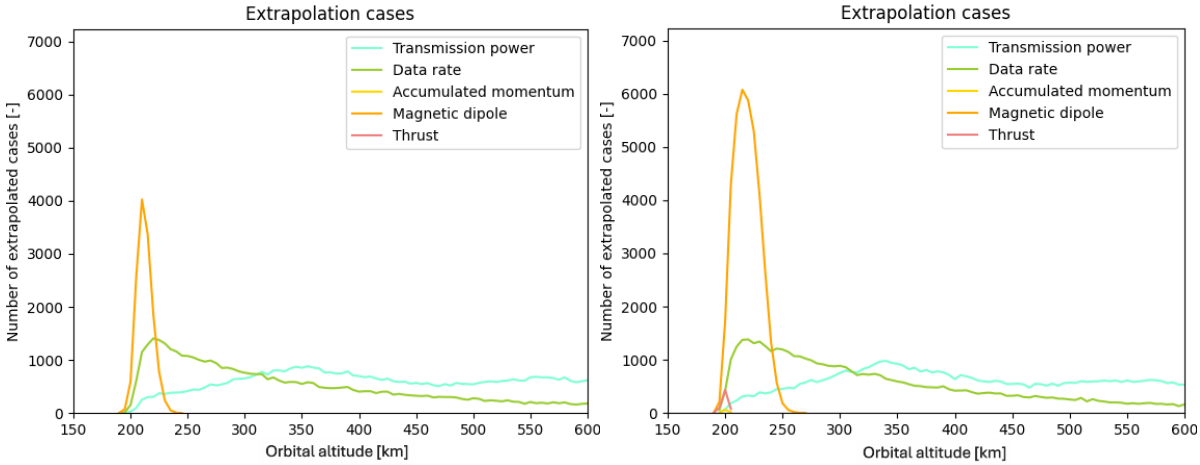

(a) Reference aperture of $20\,\mathrm{cm}$ at $300\,\mathrm{km}$

(b) Reference aperture of $40\,\mathrm{cm}$ at $300\,\mathrm{km}$

Figure 7.34: The Monte Carlo simulation result of the number of extrapolated cases per category as a function of orbital altitude h

7.6.2. Solar Panel Thickness Sensitivity

The dominance of solar panel volume observed in Figure 7.6 requires a critical analysis of the model used. Apart from the power budget itself, volume is heavily affected by the thickness of the panels. As shown in Section 5.5, the model balances static and dynamic considerations to land on a $t_{sp} \sim l_{sp,max}^{1.5}$ relation. However, the critical case is mission dependent. Therefore, both $t_{sp} \sim l_{sp,max}$ and $t_{sp} \sim l_{sp,max}^2$ are analyzed in this sensitivity study. Both use the same reference data points as the original model ($1.8\,\mathrm{mm}$ thickness for a $0.1\,\mathrm{m}$ long panel and $2.5\,\mathrm{mm}$ for a $0.34\,\mathrm{m}$ panel), leading to the following relations for solar panel thickness:

$$t_{sp} = 0.00292 \cdot l_{sp,max} + 0.00151 \tag{7.1}$$

$$t_{sp} = 0.00663 \cdot l_{sp,max}^2 + 0.00173 \tag{7.2}$$

The linear thickness-length relationship led to a relatively high convergence percentage of $91.56\,\%$, while the quadratic relation resulted only in $77.2\,\%$ convergence. Again, convergence predominantly occurred at altitudes above $250\,\mathrm{km}$ to $300\,\mathrm{km}$. An explanation for this is the high power demand at low altitudes resulting in a large solar panel area and thus increased thickness, snowballing to a larger effective stowed volume that requires more power for AOCS and propulsion. The standard deviation of both relations come close to that of the original model, with $0.0539\,\mathrm{m}^3$ for the linear one and $0.0457\,\mathrm{m}^3$ for the quadratic one.

Figure 7.35 depicts the filtered satellite volume envelope for both analyses, including extrapolated data points. Indeed, the majority of the data at low altitudes for the quadratic case got removed due to divergence. Moreover, the optimum has shifted to a higher altitude compared to the linear case. This observation is confirmed by Table 7.2. Both the envelope and table also show limited increase of the effective stowed volume as a result of a stronger thickness-length relation. Similar to the other volume envelopes discussed in this chapter, uncertainty in the effective stowed volume is least around the optimum and increases moving away from it.

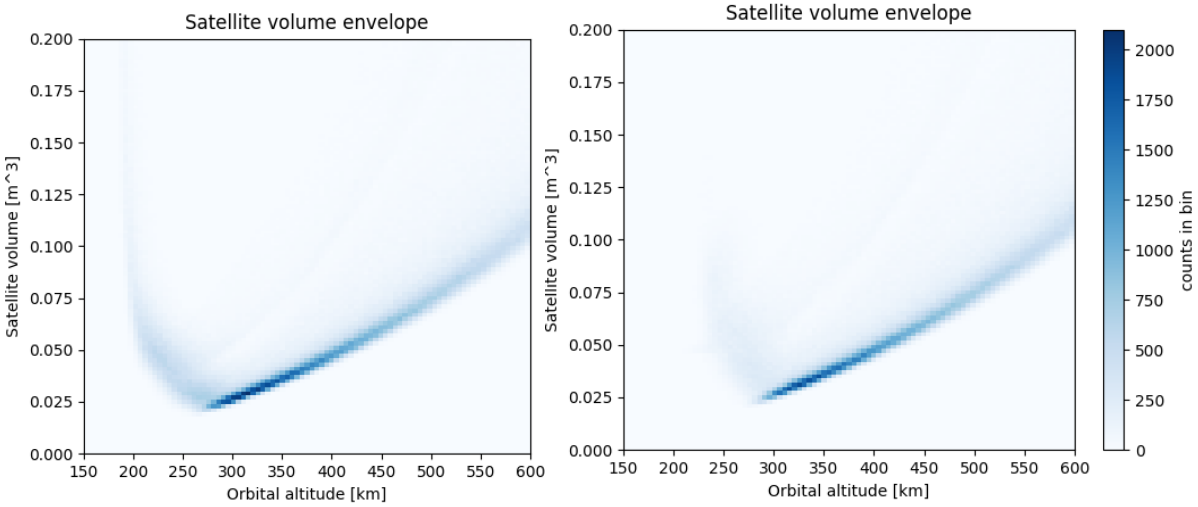

(a) $t_{sp} \sim l_{sp,max}$ **(b)** $t_{sp} \sim l_{sp,max}^2$

Figure 7.35: The Monte Carlo simulation result of the effective stowed volume $V_{eff,stowed}$ as a function of orbital altitude h with extrapolated data points (bin size = ($5\,\mathrm{km}$, $0.002\,\mathrm{m3}$))

Looking at the subsystem volume distribution in Figure 7.36, one should remember that the reliability of the results coming from the quadratic relation below $250\,\mathrm{km}$ is low. Clearly, the optimum shifts to higher altitudes due to an increased solar panel volume that negatively affects lower altitudes. According to Figure 7.37 and in line with earlier observations, the increased volume leads to an increase in chemical propulsion usage.

Table 7.2: The average minimum effective stowed volume for different primary mirror dimensions

Thickness relation at $300\,\mathrm{km}$ [m]	**Average minimum effective stowed volume** [m^3]	**Average optimal altitude** [km]
$t_{sp} \sim l_{sp,max}$	0.0322	285
$t_{sp} \sim l_{sp,max}^{1.5}$	0.0341	295
$t_{sp} \sim l_{sp,max}^{2}$	0.0382	310

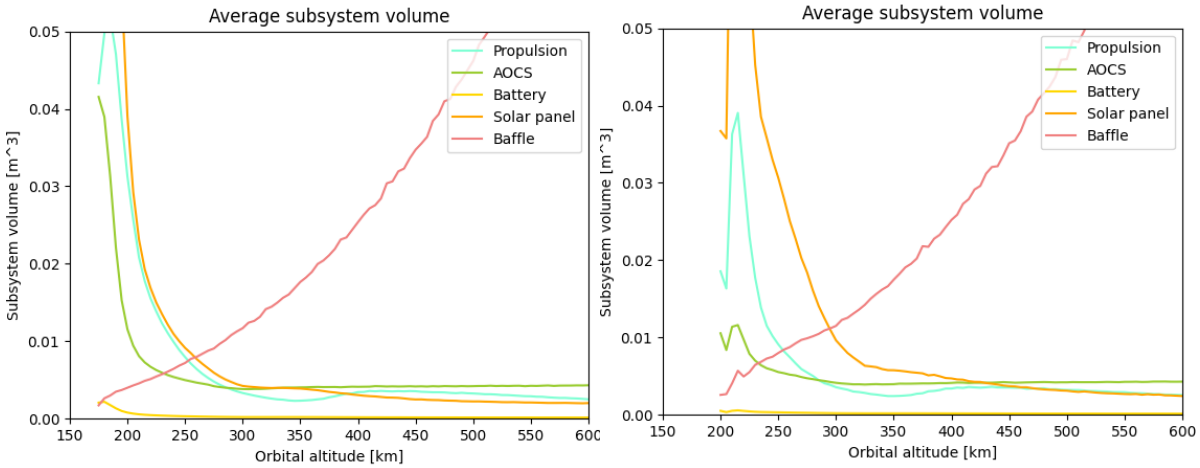

(a) $t_{sp} \sim l_{sp,max}$ **(b)** $t_{sp} \sim l_{sp,max}^2$

Figure 7.36: The Monte Carlo simulation result of the average subsystem volume budgets V_{prop}, V_{AOCS} , V_{bat}, V_{sp} and V_{baffle} as a function of orbital altitude h with extrapolated data points

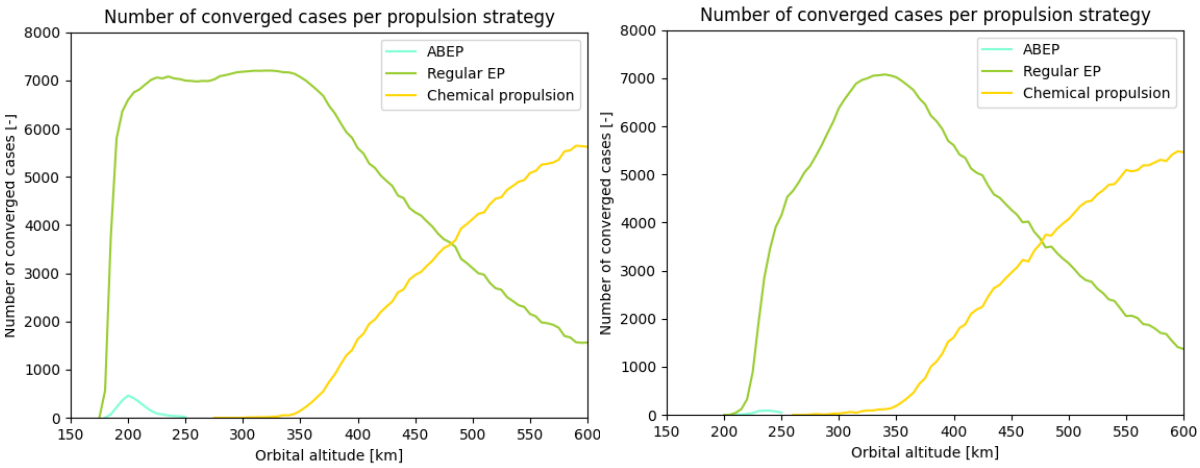

(a) $t_{sp} \sim l_{sp,max}$ **(b)** $t_{sp} \sim l_{sp,max}^2$

Figure 7.37: The Monte Carlo simulation result of the propulsion strategy count as a function of orbital altitude h with extrapolated data points

The distribution of geometry cases is also affected by the solar panel thickness relation, as depicted in Figure 7.38. An increased solar panel thickness causes an increase in satellite bus volume and thus slightly delays a dominant payload geometry to a higher altitude of about $275\,\mathrm{km}$. This implies that the y-dimension of the satellite, and thus the side panel area, is larger at lower altitudes for a quadratic case than for the linear one. Indeed, Figure 7.39 reveals that in this altitude range, a quadratic relation leads to less solar panel segments.

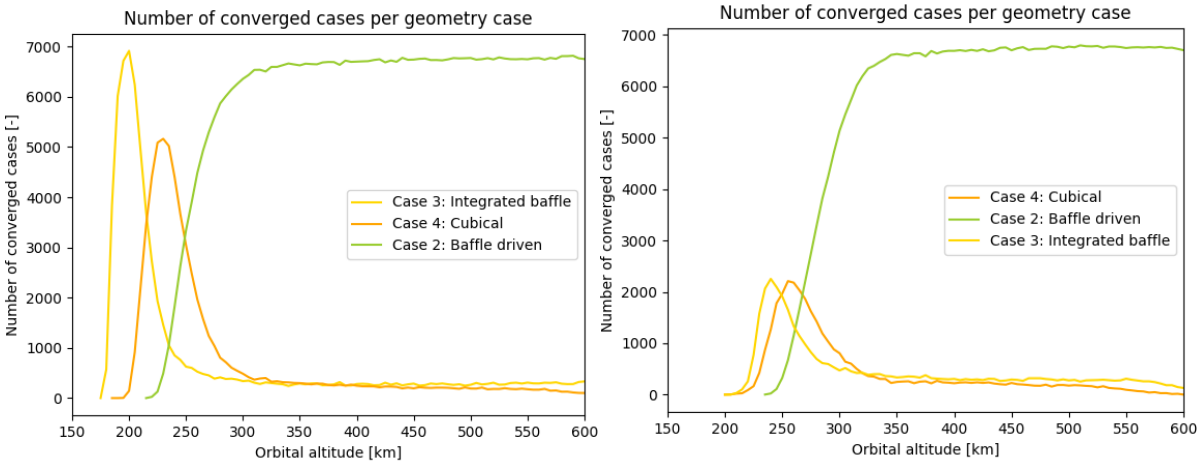

(a) $t_{sp} \sim l_{sp,max}$ **(b)** $t_{sp} \sim l_{sp,max}^2$

Figure 7.38: The Monte Carlo simulation result of the geometry case count as a function of orbital altitude h with and without extrapolated data points

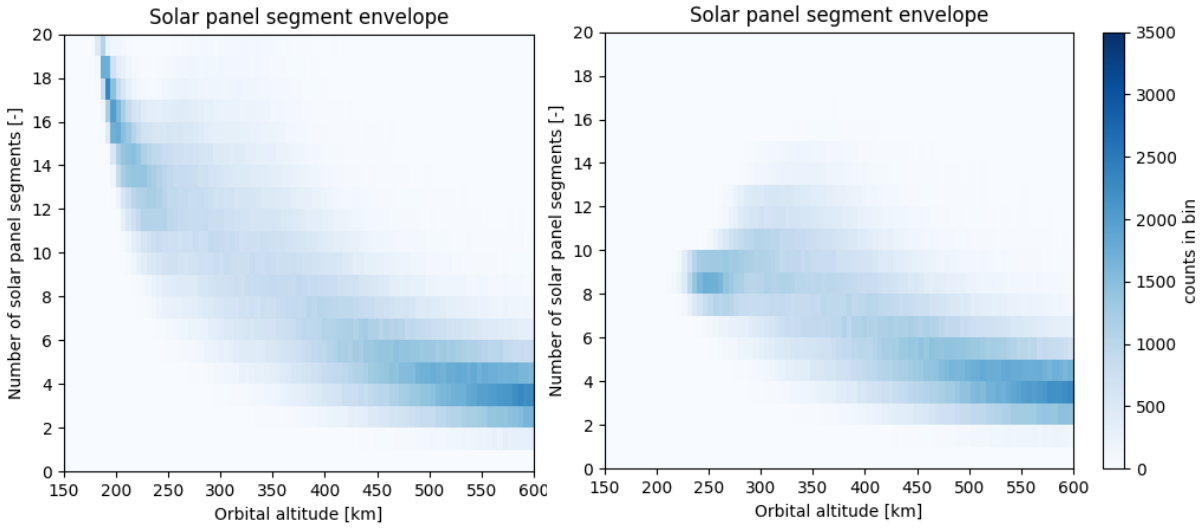

(a) $t_{sp} \sim l_{sp,max}$ **(b)** $t_{sp} \sim l_{sp,max}^2$

Figure 7.39: The Monte Carlo simulation result of the solar panel segment envelope as a function of orbital altitude h with extrapolated data points (bin size = ($5\,\mathrm{km}$, 1 segment))

7.6.3. Uncertain Input Sensitivity

The complete list of uncertain input parameters can be found in Table 6.6. The effect of t_{life} and $n_{segments}$ was discussed before (see Section 7.3). The other parameters were also analyzed and the most interesting ones are depicted in Figure 7.40. These namely reveal a remarkable relation with the effective stowed volume while other parameters did not. The figures depict the average effective stowed volume as a function of orbital altitude for different ranges of the uncertain parameters d_{M1-M2}/D and $I_{sp,EP}$.

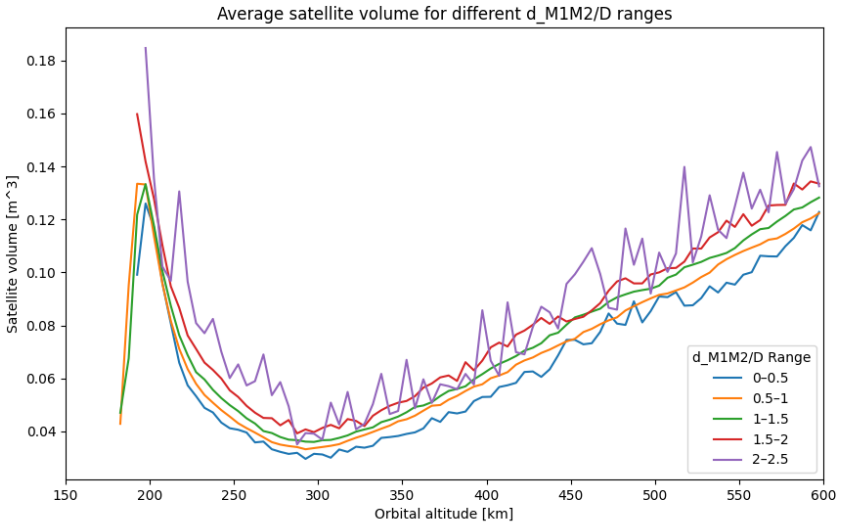

(a) d_{M1-M2}/D

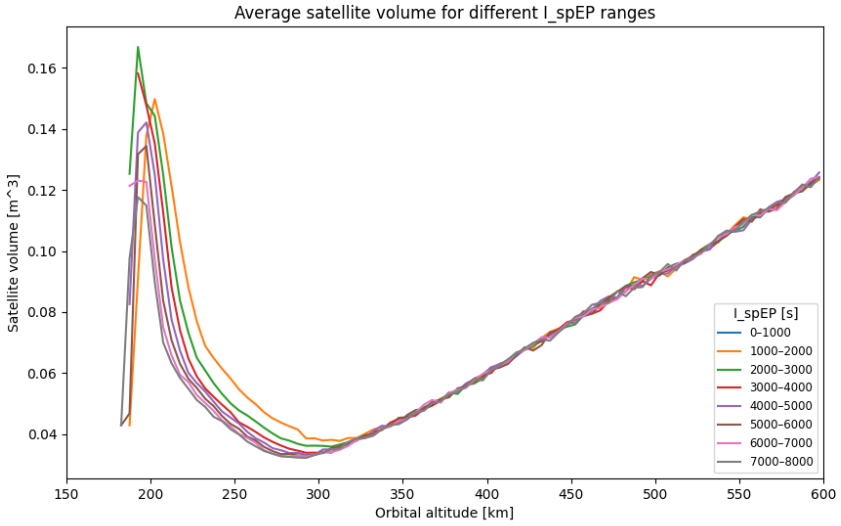

(b) $I_{sp,EP}$

Figure 7.40: The sensitivity of the average effective stowed volume $V_{eff,stowed}$ as a function of orbital altitude h for uncertain model inputs

Figure 7.40a shows the effect of the d_{M1-M2}/D parameter (the distance between the primary and secondary mirror over the aperture diameter), which is independent of orbital altitude. In general, a higher d_{M1-M2}/D implies a larger satellite volume, as expected. In order to further clarify the relationship between d_{M1-M2}/D and satellite volume, Figure 7.41 depicts the same plot, but separates by baffle segmentation. These separated plots show the least correlation between d_{M1-M2}/D and satellite volume for a non-deployable design ($n_{segments} = 1$) and at low altitudes. Both of these effects can be explained by satellite geometry. As depicted in Figure 7.42, the geometry case distribution for a non-deployable payload is very different from the others: case 2, a payload driven geometry, does not dominate at any altitude. Similarly, this happens for multiple numbers of baffle segments below $300\,\mathrm{km}$. Logically, baffle length has relatively little impact when the satellite geometry is not payload-driven.

Now focusing on Figure 7.40b, especially below $300\,\mathrm{km}$, the specific impulse of electric propulsion unveils a relationship with the satellite volume. As noticed in Section 7.2, propulsion has a significant volume contribution in this altitude regime. Moreover, regular EP is preferred in this region as concluded in Section 7.4. Therefore, a more efficient propellant directly translates to a noteworthy lower satellite volume below $300\,\mathrm{km}$.

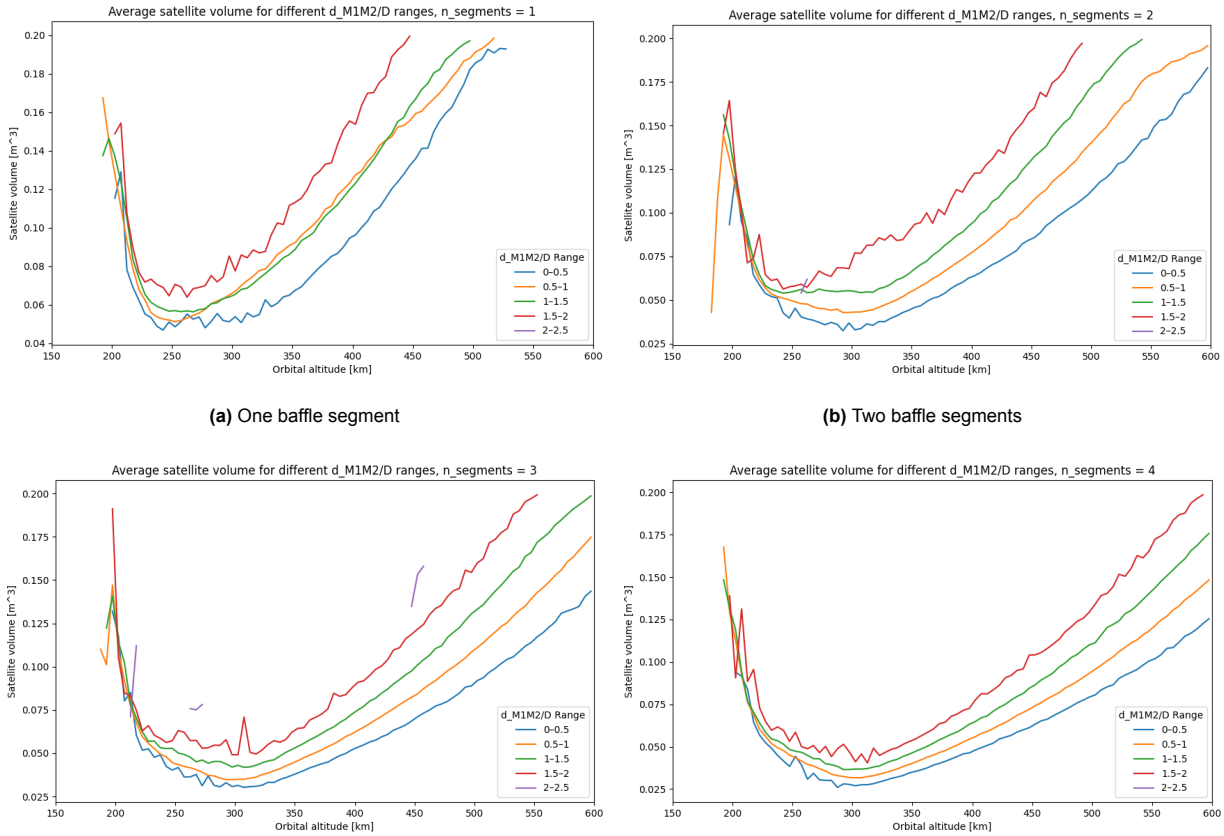

(a) One baffle segment

(b) Two baffle segments

(c) Three baffle segments

(d) Four baffle segments

Figure 7.41: The sensitivity of the average effective stowed volume $V_{eff,stowed}$ as a function of orbital altitude h for the uncertain parameter d_{M1-M2}/D only considering a specific amount of baffle segments

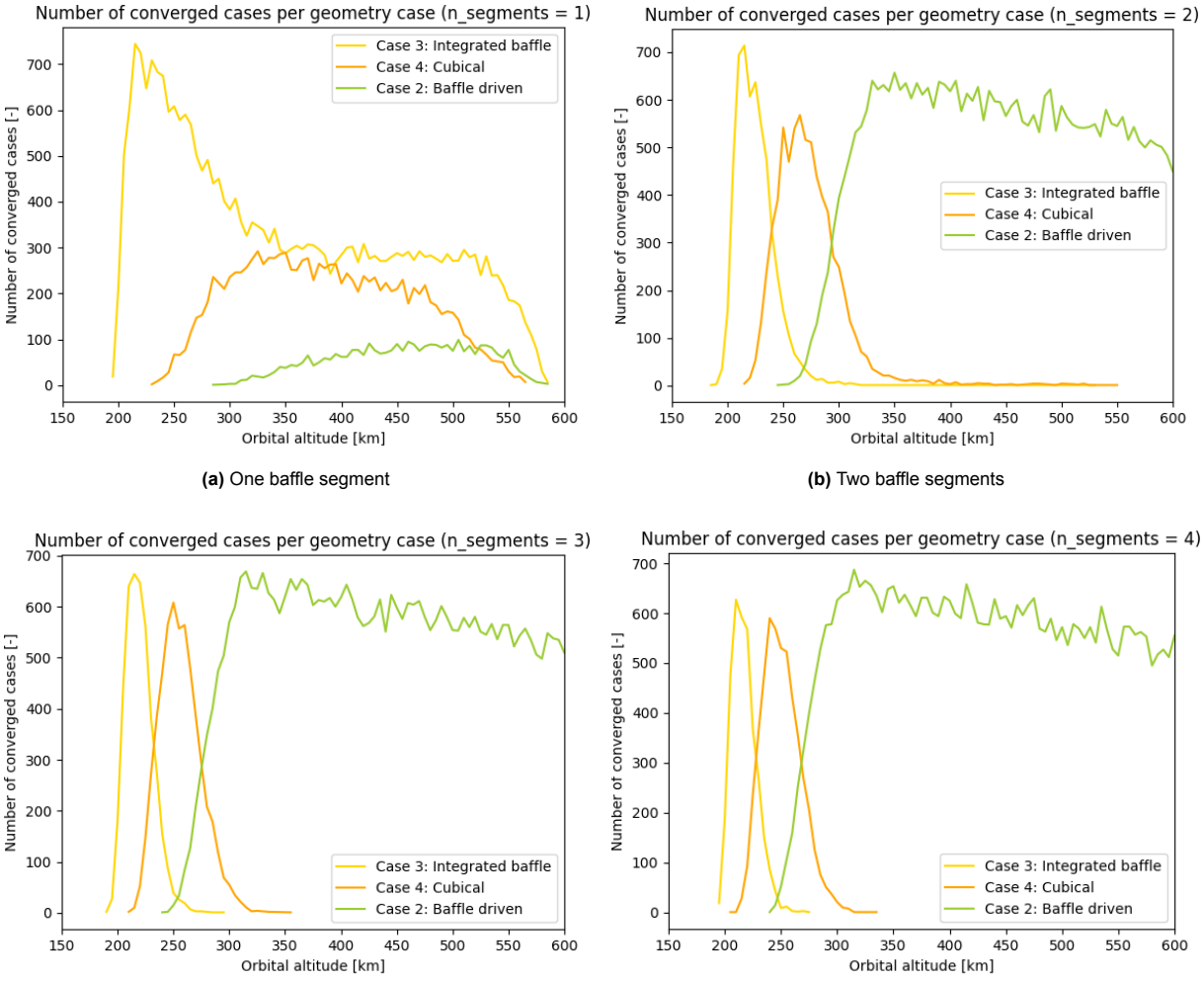

(a) One baffle segment

(b) Two baffle segments

(c) Three baffle segments

(d) Four baffle segments

Figure 7.42: The geometry case count as a function of orbital altitude h only considering a specific amount of baffle segments

7.6.4. Propulsion Strategy Sensitivity

Section 7.4 revealed that around the optimum, regular EP is preferred in terms of volume. However, several factors such as TRL, complexity and regulation could result in the decision not to use this type of propulsion. Therefore, the volume envelope of a satellite constrained to chemical propulsion is depicted in Figure 7.43b.

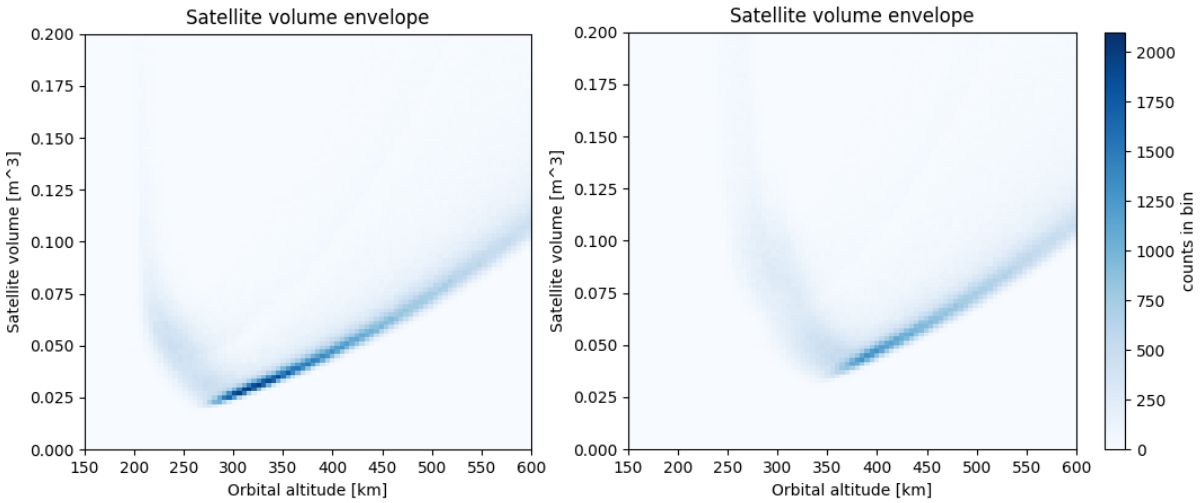

(a) Non-constrained propulsion type

(b) Constrained to chemical propulsion

Figure 7.43: The Monte Carlo simulation result of the effective stowed volume $V_{eff,stowed}$ as a function of orbital altitude h with extrapolated data points (bin size = $(5\,\mathrm{km},\, 0.002\,\mathrm{m3})$)

Clearly, the optimum altitude increases and so does the volume. The average minimum effective stowed volume is $0.0535\,\mathrm{m}^3$ at an altitude of $360\,\mathrm{km}$. The volume distribution among the subsystems is presented in Figure 7.44b.

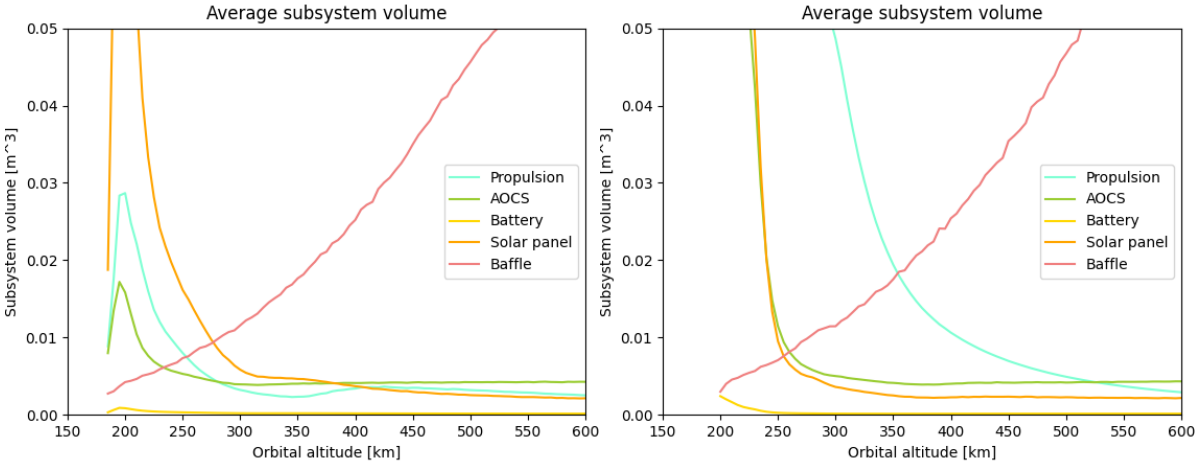

(a) Non-constrained propulsion typ

(b) Constrained to chemical propulsion

Figure 7.44: The Monte Carlo simulation result of the average subsystem volume budgets V_{prop}, V_{AOCS} , V_{bat}, V_{sp} and V_{baffe} as a function of orbital altitude h with extrapolated data points

Propulsion volume increases significantly when constrained to chemical propulsion due to the propellant. This effect is largest at lower altitudes. Although some reduction in EPS volume does occur, AOCS still requires large amounts of power at low altitudes.

From the sensitivity analyses performed, one can conclude that the aperture dimension significantly impacts the results of the simulation. With increasing aperture, the volume increases and the optimum altitude lowers, though the standard deviation of the model increases as well. Reason for this is the increasing dominance of the payload volume (which is a function of the aperture diameter) at higher altitudes. The preferred propulsion strategy at the optimum is not affected, but the geometry case is. Furthermore, the volume gain per additional baffle segment increases with aperture diameter.

On the contrary, solar panel thickness has a much smaller effect on the optimum effective stowed volume and optimal altitude. However, a quadratic relationship leads to significantly more divergence at low altitudes, making the reliability of the result here questionable. Still, the number of converged cases around the found optimum are comparable to the other analyses.

Out of the list of uncertain input parameters, only two showed a visible sensitivity relation to the effective stowed volume: d_{M1-M2}/D and $I_{sp,EP}$. The first leads to the logical correlation of an increased volume with an increased d_{M1-M2}/D, but a strong impact of the number of baffle segments and geometry case was observed. The latter primarily affects the results at altitudes below $300\,\mathrm{km}$.

Lastly, propulsion strategy has a significant impact on the volume envelope. When constrained to chemical propulsion, the average minimum effective stowed volume increases from $0.0341\,\mathrm{m}^3$ to $0.0535\,\mathrm{m}^3$ and the optimal altitude is raised to $360\,\mathrm{km}$.

7.7. Design for Volume Optimum

By the law of large numbers, the sample average of a Monte Carlo simulation approximates the expected value [170]. Following this logic, the optimal altitude for the envisioned mission is $295\,\mathrm{km}$. For this altitude, the average effective stowed volume is $0.0341\,\mathrm{m}^3$, close to all sample sets converged and about $17\,\%$ required model extrapolation. In order to give a sense of the spread, Table 7.3 presents the average as well as the first, second and third quartile (Q1, median and Q3) of the effective stowed volume at $295\,\mathrm{km}$. The standard deviation at this altitude was found to be $0.0128\,\mathrm{m}^3$. As visible in the volume envelope, the quartiles confirm more spread at the high-volume end, hence a positively skewed volume disttribution.

Table 7.3: The characteristics of the optimal design according to the Monte Carlo simulation

Statistical measure	Volume
Average	$0.0341\,\mathrm{m}^3$
Q1	$0.0258\,\mathrm{m}^3$
Median	$0.0284\,\mathrm{m}^3$
Q3	$0.0373\,\mathrm{m}^3$

Furthermore, the satellite volume at $295\,\mathrm{km}$ is equally dominated by the deployed payload instrument and solar panels, whereas the power consumption is driven by AOCS and propulsion. The mission lifetime has limited effect on the volume, hence a longer mission of $7\,\mathrm{years}$ is advised to optimize the amount of data that can be gathered. In terms of baffle segmentation, a trade-off between volume gain and complexity is necessary. For a proper analysis, the payload construction must be consolidated first. Nonetheless, the simulation results show significant improvement by the use of multiple segments. Adding a third segment reduces the average effective stowed volume by $17.6\,\%$, the fourth subtracts another $11.4\,\%$. From the fifth segment onward, gain drops below $6.8\,\%$.

According to the model, regular Electric Propulsion (EP) is preferred for the mission as $99.9\,\%$ of the data at $295\,\mathrm{km}$ converges to this propulsion strategy. Its specific impulse at this altitude has been shown to only have limited impact on the effective stowed volume. Propulsion power consumption at $295\,\mathrm{km}$ has decreased to about $25\,\mathrm{W}$, similar to AOCS (which is likely over-estimated according to Section 7.2). TRL is not directly of great concern for this technology: some $1\,\mathrm{mN}$ systems have reached TRL 9 such as the NPT30-I2-1U from ThrustMe and ENPULSION MICRO R³ from ENPULSION [171][172]. However, these systems are still associated with a relatively high power consumption. Therefore, reducing regular EP power consumption should be a key point of focus in the development of this mission. Fortunately, a lot of research is focused on optimizing regular EP thrust-to-power ratio. The Plasma Sources and Applications Centre/Space Propulsion Centre (PSAC/SPC) Singapore for example, investigated low-power Hall-effect thrusters and demonstrated a thrust of $3\,\mathrm{mN}$ at $25\,\mathrm{W}$ [173]. Therefore, improvements in the thrust-to-power ratio of commercially available EP systems are expected in the upcoming years. If practical considerations exclude regular EP as an option, chemical propulsion can be integrated at the expense of a $80.1\,\%$ volume increase. This adjustment also shifts the optimal altitude to $360\,\mathrm{km}$.

The number of solar panel segments at $295\,\mathrm{km}$ shows significant spread with a mean of 9.89 and quartiles of 8, 10 and 12. Now, focusing on concepts that are based on three and six payload baffle segments, numbers slightly reduce while still being at the upper limit to what is found in current satellites. Reason for this dependency is related to satellite geometry as detailed in Section 7.5. The satellite geometry at the optimal altitude is most likely driven by the payload, as geometry case II dominates with $85.4\,\%$ at this altitude. Only non-deployable designs differ in this aspect; they converge to geometry case III (Integrated baffle).

To quantify the design optimum for various design decisions, five cases are explored. They represent non-deployable and deployable designs in VLEO. The first four feature regular EP at $295\,\mathrm{km}$ while number five is limited to chemical propulsion at $360\,\mathrm{km}$, as in Subsection 7.6.4. In order to visualize the effect of the design decision on the number of baffle segments, the four cases at $295\,\mathrm{km}$ have one, three, six and 12 (the highest number analyzed) baffle segments respectively. The fifth case has three. All cases only consider data with a lifetime of $6.5\,\mathrm{years}$ to $7\,\mathrm{years}$, in accordance with the recommendation made above. Also, all DST designs use geometry case II (Baffle driven), so that x_{body} and z_{body} are

equal. Contrastingly, the first case, representing the non-deployable design in VLEO, takes the shape of geometry case III (integrated baffle). Their characteristics are tabulated in Table 7.4 next to a non-deployable and deployable LEO ($600\,\mathrm{km}$) satellite carrying the same payload. For the latter two, outlier filtering is not applied. Reason for this is that this type of filtering removes all non-deployable concepts at this altitude due to the great volume difference between a non-deployable and deployable concept (see Figure 7.16). The row called 'Relative' indicates the relative volume of that configuration with respect to a satellite in VLEO featuring a three-segmented baffle (which is taken as a reference in all comparisons).

Table 7.4: The model output for different design optima given a number of baffle segments and propulsion type next to the designs for LEO, all with a lifetime of $6.5\,\mathrm{years}$ to $7\,\mathrm{years}$

Design							
Baffle segments	1	3	6	12	3	1	3
Altitude	$295\,\mathrm{km}$	$295\,\mathrm{km}$	$295\,\mathrm{km}$	$295\,\mathrm{km}$	$360\,\mathrm{km}$	$600\,\mathrm{km}$	$600\,\mathrm{km}$
Propulsion	EP	EP	EP	EP	chemical	chemical	chemical
Geometry	III	II	II	II	II	III	II
Effective stowed volume							
Average	$0.0598\,\mathrm{m}^3$	$0.0361\,\mathrm{m}^3$	$0.0300\,\mathrm{m}^3$	$0.0293\,\mathrm{m}^3$	$0.0650\,\mathrm{m}^3$	$0.332\,\mathrm{m}^3$	$0.183\,\mathrm{m}^3$
Q1	$0.0551\,\mathrm{m}^3$	$0.0322\,\mathrm{m}^3$	$0.0252\,\mathrm{m}^3$	$0.0270\,\mathrm{m}^3$	$0.0585\,\mathrm{m}^3$	$0.302\,\mathrm{m}^3$	$0.167\,\mathrm{m}^3$
Median	$0.0580\,\mathrm{m}^3$	$0.0361\,\mathrm{m}^3$	$0.0284\,\mathrm{m}^3$	$0.0273\,\mathrm{m}^3$	$0.0648\,\mathrm{m}^3$	$0.321\,\mathrm{m}^3$	$0.180\,\mathrm{m}^3$
Q3	$0.0619\,\mathrm{m}^3$	$0.0403\,\mathrm{m}^3$	$0.0328\,\mathrm{m}^3$	$0.0282\,\mathrm{m}^3$	$0.0714\,\mathrm{m}^3$	$0.356\,\mathrm{m}^3$	$0.193\,\mathrm{m}^3$
Relative	$166\,\%$	$100\,\%$	$83.1\,\%$	$81.2\,\%$	$180\,\%$	$920\,\%$	$507\,\%$
x- & z- body dimension							
Average	$0.390\,\mathrm{m}$	$0.359\,\mathrm{m}$	$0.379\,\mathrm{m}$	$0.419\,\mathrm{m}$	$0.435\,\mathrm{m}$	$0.692\,\mathrm{m}$	$0.693\,\mathrm{m}$
Q1	$0.381\,\mathrm{m}$	$0.358\,\mathrm{m}$	$0.379\,\mathrm{m}$	$0.421\,\mathrm{m}$	$0.430\,\mathrm{m}$	$0.671\,\mathrm{m}$	$0.693\,\mathrm{m}$
Median	$0.387\,\mathrm{m}$	$0.358\,\mathrm{m}$	$0.379\,\mathrm{m}$	$0.421\,\mathrm{m}$	$0.430\,\mathrm{m}$	$0.685\,\mathrm{m}$	$0.693\,\mathrm{m}$
Q3	$0.396\,\mathrm{m}$	$0.358\,\mathrm{m}$	$0.379\,\mathrm{m}$	$0.421\,\mathrm{m}$	$0.430\,\mathrm{m}$	$0.709\,\mathrm{m}$	$0.693\,\mathrm{m}$
y-body dimension excluding exterior baffle							
Average	$0.390\,\mathrm{m}$	$0.159\,\mathrm{m}$	$0.140\,\mathrm{m}$	$0.112\,\mathrm{m}$	$0.190\,\mathrm{m}$	$0.692\,\mathrm{m}$	$0.110\,\mathrm{m}$
Q1	$0.381\,\mathrm{m}$	$0.135\,\mathrm{m}$	$0.110\,\mathrm{m}$	$0.110\,\mathrm{m}$	$0.171\,\mathrm{m}$	$0.671\,\mathrm{m}$	$0.110\,\mathrm{m}$
Median	$0.387\,\mathrm{m}$	$0.157\,\mathrm{m}$	$0.128\,\mathrm{m}$	$0.110\,\mathrm{m}$	$0.192\,\mathrm{m}$	$0.685\,\mathrm{m}$	$0.110\,\mathrm{m}$
Q3	$0.396\,\mathrm{m}$	$0.183\,\mathrm{m}$	$0.159\,\mathrm{m}$	$0.110\,\mathrm{m}$	$0.208\,\mathrm{m}$	$0.709\,\mathrm{m}$	$0.110\,\mathrm{m}$
Baffle							
Outer diameter	$0.344\,\mathrm{m}$	$0.358\,\mathrm{m}$	$0.379\,\mathrm{m}$	$0.421\,\mathrm{m}$	$0.430\,\mathrm{m}$	$0.679\,\mathrm{m}$	$0.693\,\mathrm{m}$
Stowed length	$0.356\,\mathrm{m}$	$0.129\,\mathrm{m}$	$0.069\,\mathrm{m}$	$0.0397\,\mathrm{m}$	$0.159\,\mathrm{m}$	$0.806\,\mathrm{m}$	$0.279\,\mathrm{m}$
Deployed length	$0.356\,\mathrm{m}$	$0.356\,\mathrm{m}$	$0.356\,\mathrm{m}$	$0.356\,\mathrm{m}$	$0.447\,\mathrm{m}$	$0.806\,\mathrm{m}$	$0.806\,\mathrm{m}$
Number of solar panel segments							
Average	6.72	8.18	10.3	12.2	3.73	1.74	2.43
Q1	6	7	9	10	3	1	2
Median	6	8	10	12	4	2	2
Q3	8	9	12	14	4	2	3

Conform expectations, EP leads to a lower volume in the VLEO regime. Moreover, a lower number of baffle segments as well as bigger body dimensions and chemical propulsion reduce the number of solar panels required. For the third and fourth case, featuring regular EP and six and 12 baffle segments respectively, the number of solar panels could be pushing practical feasibility. For the other cases, this number is not raising concerns. The significance of the a deployable payload becomes clear from these results, as well as the fact that the gain per added segment reduces. Figure 7.45 depicts the four most interesting cases as described in Section 4.3. From top to bottom: a non-deployable space telescope in VLEO, a DST in VLEO (three baffle segments), a non-deployable space telescope in LEO, a DST in LEO (three baffle segments).

An important observation can be made in the configurations with a non-deployable instrument: while their geometry prescribes an integrated baffle (case III), the baffle does not always fit the cubical geometry or leaves sufficient space for the instrumentation box ($11\,\mathrm{cm}$ as stated in Section 5.3). This topic is addressed in the following section.

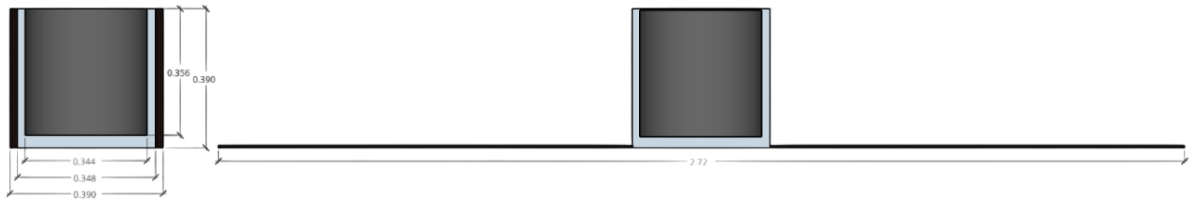

(a) Non-deployable space telescope in VLEO

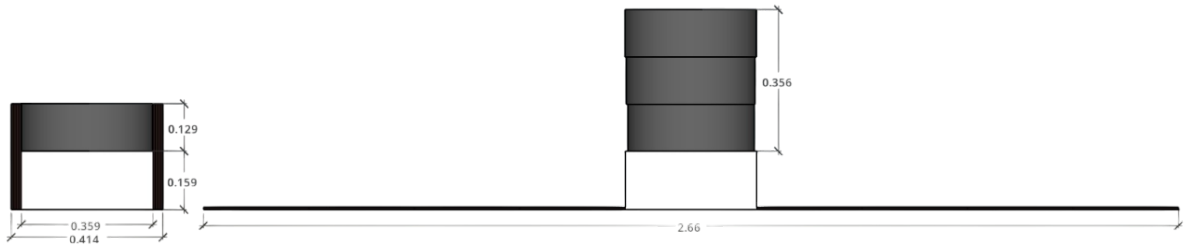

(b) DST in VLEO

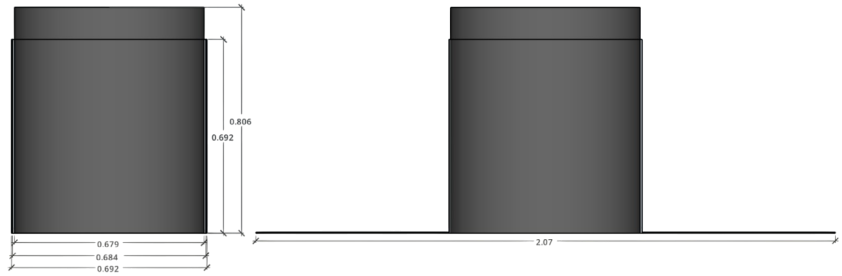

(c) Non-deployable space telescope in LEO

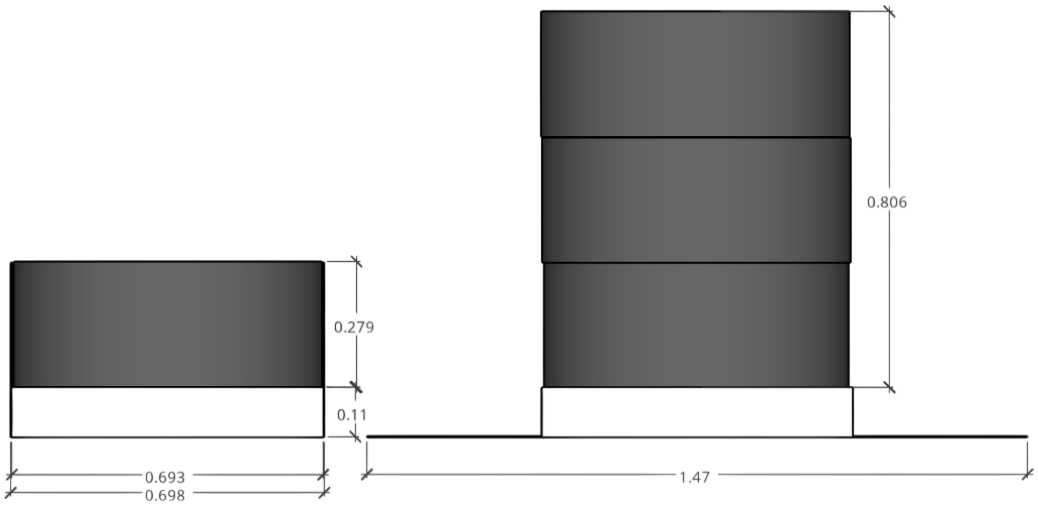

(d) DST in LEO

Figure 7.45: The four combinations of payload deployability and orbital altitude

7.8. Comparison and Discussion

To summarize, as hypothesized, VLEO presents great opportunities for lowering satellite volume, even when considering the negative effects on the AOCS and propulsion subsystem. A volume optimum was found at $295\,\mathrm{km}$, where electric propulsion has significant advantage over traditional chemical propulsion. Moreover, deployability of the instrument greatly enhances volume optimization. The optimum number of baffle segments exceeds practical feasibility and thus, it should be traded-off against complexity and the resulting number of solar panel segments. Comparing the optimal design from the Monte Carlo analysis (assuming three baffle segments) to the traditional LEO satellite with the same ground sampling distance, the budget-optimization parameters established a volume reduction of $89.1\,\%$.

The main reason for optimizing satellite volume is suppression of launch cost to stimulate constellation deployment, which in turn enhances temporal resolution of the marine plastic debris observations. Indeed, such suppression is realized when looking at the optimized satellite. To put this into perspective, a deployable telescope in VLEO would fit a 1/4 plate in Falcon 9's rideshare program while a traditional rigid LEO ($600\,\mathrm{km}$) design requires a full plate, hence launch cost can be reduced from $\$1,300,000$ to $\$325,000$ [174]. Furthermore, the optimized design primarily uses COTS components. Only the payload needs to be developed completely and thus scores low on TRL. In terms of propulsion, current technology could be used, though improvement of the thrust-to-power ratio promises further volume reduction. Therefore, the investments cost of this mission are kept to a minimum. This conclusion affects the assumption made in Section 4.2: the investments costs are relatively low while at the same time, volume reduction leads to a significant launch cost reduction. The minimum $50\,\%$ budget reduction in order to favor the novel concept might thus even be too stringent. In any case, as significantly more than $50\,\%$ is saved on the volume budget, a constellation of optimized satellites flying in VLEO and featuring a deployable payload largely outperform a traditional LEO satellite.

Improvements can be made on the volume and power models of the AOCS. As found in Section 7.2, these are currently based on over-sized actuators. Therefore, the computed volume and power budgets are expected to be over-estimated. Adjusting the model by using reference systems closer to the accumulated momentum and required magnetic dipole found in the Monte Carlo simulation would improve reliability of the outcome. However, even despite this deficiency, VLEO and deployable optics still prove to be promising, as this adjustment would only further reduce AOCS (and EPS) volume in VLEO.

On a critical note, the spatial integration requires additional attention. Firstly, as noted in the previous section, the configurations that are non-deployable and apply geometry case II (Integrated baffle) cannot always adhere to the cubical dimensions due to the length of the baffle and additional height required for the instrumentation box underneath. Figure 7.46a reveals that on average, all satellites carrying a non-deployable space telescope adhering to geometry case II beyond $230\,\mathrm{km}$ suffer this discrepancy. Looking at Figure 7.46b, one can see that this is the case for roughly half of all non-deployable space telescopes in LEO. Therefore, this subset of cases requires to let go of the cubical form factor and define the y-dimension y_{body} based on the addition of the baffle length l_{baffle} and height of the instrumentation box, which is $11\,\mathrm{cm}$ as stated in Section 5.3. This does not affect the effective stowed volume of this configuration as the subsystems can still be fitted in the empty space around the baffle and thus, the x- and z-dimensions can compensate the increased y- dimension. For this reason, the volume-based comparison of a DST in VLEO with a non-deployable payload in LEO remains valid.

Shifting focus to the exterior, the nadir pointing face carries the optical payload, the opposite face can be used to place a launcher interface while the side faces carry the velocity aligned solar panels and the passive thermal control subsystem. However, the optimal design (a DST in VLEO) does not have sufficient body width and height to fit these on one face (both the cold- and cryo-stage radiator measure $7\,\mathrm{cm}$ x $36\,\mathrm{cm}$) [132]. Therefore, re-evaluation of the thermal control subsystem is required and possibly, active cooling should be implemented.

Another slight discrepancy in subsystem integration must be highlighted here. The satellite dimensions are namely based on a summation of the individual subsystem volumes (including the solar panel). Thereafter, the solar panel dimensions are computed from these. In case the payload drives the satellite geometry, its outer dimensions define the satellite body dimensions as well. However, as the solar panels in this case extent beyond the satellite body up to the top of the stowed baffle, their volume is

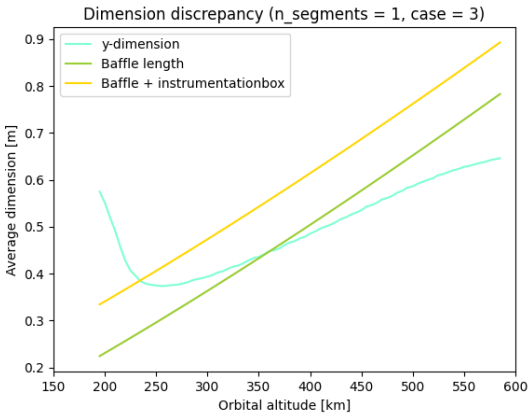

(a) The average value of y_{body}, l_{baffle} and $l_{baffle} + 0.11$ for non-deployable space telescopes that apply geometry case II (Integrated baffle)

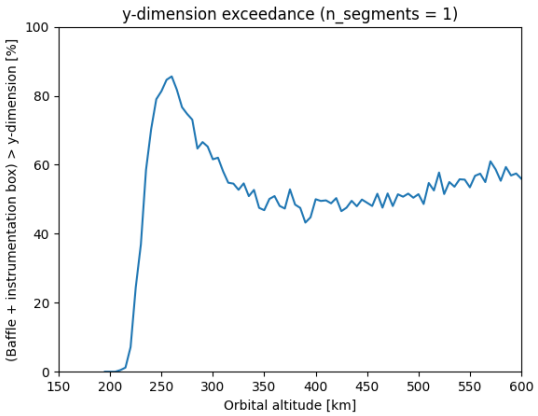

(b) The percentage of non-deployable space telescopes that cannot adhere to a cubical effective stowed volume

Figure 7.46: An analysis of the dimension discrepancy for the non-deployable space telescopes

not contained within the satellite bus 'box'. On one hand, this increases the effective stowed volume as the panels need to be placed adjacent to the baffle to prevent interference, causing an increase in body dimensions. On the other hand, extension of the solar panels beyond the body height reduces the volume occupied within the bus 'box', introducing the possibility to reduce its height. These effects are expected to balance each other to some extend and further analysis of this effect is outside the scope of this thesis.

Finally, the sensitivity analysis has shown that the aperture diameter is critical in determining the exact optimal altitude. So, establishing the final optical parameters and deriving the required M1 diameter is of utmost importance and must take priority in the subsequent design phases.

8

Conclusion and Recommendations

This thesis detailed a study on the feasibility of volume optimized satellites in Very Low Earth Orbit (VLEO) for marine plastic debris monitoring and aimed at answering the following research question:

How does the integration of deployable optics and VLEO affect satellite volume compared to a traditional LEO Earth observation satellite for monitoring marine plastic debris when taking into account their positive and negative effects on this budget?

As described in Subsection 2.2.1, VLEO ($150\,\mathrm{km}$ to $400\,\mathrm{km}$) is interesting for such Earth observation mission specifically as it allows for the improvement of spatial resolution without the need for an enlarged optical telescope, thereby decreasing satellite launch costs. This, in turn, enables deployment of a constellation, so that the temporal resolution can also be improved compared to current data coming from non-dedicated missions in Low Earth Orbit (LEO) such as Sentinel-2. In an attempt to further reduce satellite volume and launch costs in its wake, smart integration of the Command and Data Handling (CDH) unit, Electrical Power Subsystem (EPS) control and distribution unit, Attitude and orbit Control Subsystem (AOCS) computations and communication electronics as well as deployability of the optical payload were considered. However, due to the increased drag in VLEO, an increased propulsion and AOCS are foreseen. This connects the importance of volume optimization to the VLEO regime. For the mission to be feasible, the net effect of VLEO and payload deployability on system volume and the additional developments costs must balance the increased launch cost of a VLEO constellation with respect to a single LEO satellite. For this, a volume budget reduction criterion of 50% compared to a traditional LEO satellite was established in Section 4.2. Thus, in order to answer the research question, the volume of a VLEO satellite carrying a deployable payload was modeled and compared to a traditional LEO satellite. For this, the satellite volume was broken down into the payload and subsystem contributions, leading to the first sub-question:

Which model is most applicable for the establishment of subsystem volume budgets?

The deployable payload is currently in development at the Delft University of technology as the Deployable Space Telescope (DST) and consists of an instrumentation box and baffle segment. The latter contains the Primary and Secondary Mirror (M1 and M2), a foldable suspension in between, and a telescopic baffle. The number of baffle segments determines the stowed height of the instrument as M2 can be folded closely to M1, although a minimum distance exists. An increased segmentation thus reduces the stowed height, but simultaneously increases the outer diameter of the baffle. Modeling the payload volume as presented in Section 5.3 was done by varying the number of baffle segments from one (representing a non-deployable payload) to the maximum, which is determined by the minimum distance between M1 and M2. This way, an optimum number of segments can be determined.

The satellite bus volume was modeled using various approaches as detailed in Chapter 5. Subsystems that were expected to be less important in this study were modeled on a high level only: the dimensions of the thermal control were taken from an earlier study and the volume of the integrated core unit containing all smartly integrated components was represented by a uniform distribution. The communication

subsystem was modeled by evaluation of the link budget and matching it to Commercial Off-the-Shelf (COTS) components. Critical subsystem models (EPS, AOCS and propulsion) were worked out in more detail, combining fundamental physics with empirical relations based on existing systems. The subsystem models were combined in a system model that served as input to a Monte Carlo simulation which computes the satellite volume envelope as a function of orbital altitude from $150\,\mathrm{km}$ to $600\,\mathrm{km}$, taking into account uncertainties in the input parameters. Logically, the next sub-question reads:

How does uncertainty in the input parameters affect the system volume budget?

In the Monte Carlo Simulation, $86.4\,\%$ of the sample sets converged to a solution, after which outliers were removed using a z-score of 3. The resulting volume envelope is depicted in Figure 8.1. As outlined in Section 7.2, a clear volume optimum can be identified at $295\,\mathrm{km}$, where the expected effective stowed volume of the satellite is $0.0341\,\mathrm{m}^3$. The standard deviation of the effective stowed volume at this altitude was found to be $0.0128\,\mathrm{m}^3$.

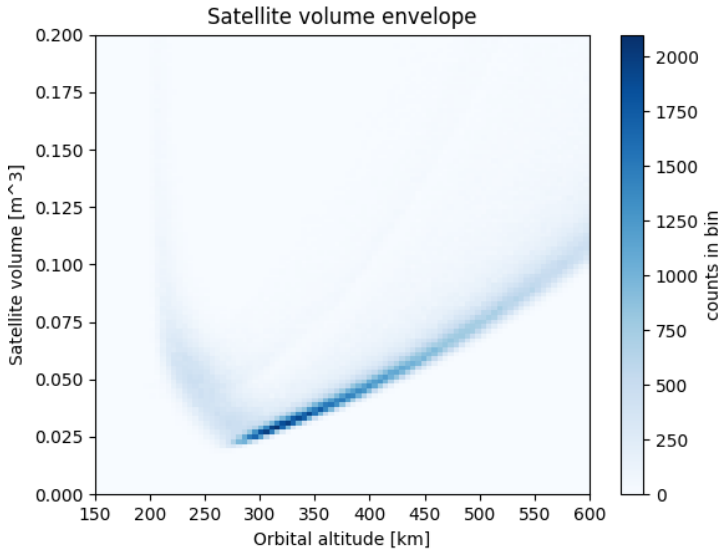

Figure 8.1: The Monte Carlo simulation result of the satellite volume envelope $V_{stowed,eff}$ as a function of orbital altitude without outliers (bin size = ($5\,\mathrm{km}$, $0.002\,\mathrm{m}^3$))

In terms of design input, mission lifetime was found to have limited effect on the volume budget according to Section 7.3. Only at low altitudes, some effect was visible due to the presence of residual atmosphere. Therefore, a mission of $6.5\,\mathrm{years}$ to $7\,\mathrm{years}$ is advised to extract as much debris observations as possible. However, the deployment of the secondary mirror and baffle was found to have a much more significant influence: comparing a DST featuring three baffle segments with a non-deployable instrument at the optimal altitude of $295\,\mathrm{km}$, the average effective stowed volume was reduced by $39.6\,\%$. The optimum number of baffle segments (starting with 12 segments at $150\,\mathrm{km}$ and increasing for higher altitudes) exceeds practical feasibility and thus, it must result from a trade-off between volume optimization, complexity and resulting number of solar panel segments. The latter relation relation exists due to the fact that, in order to maximize available solar panel area, the solar panels extend to the top of the stowed baffle in launch configuration. In order to investigate the individual subsystem contributions, the following sub-question was posed:

Which subsystems drive the system volume for a set of budget-optimization measures?

Figure 8.2 depicts the average subsystem volume as a function of altitude. Below the optimum altitude, the increased atmospheric density drives the power budget of AOCS and propulsion, hence solar panel volume dominates in this regime. Contrastingly, beyond the optimal altitude, the payload (primarily baffle) volume increases and drives the effective stowed volume. Due to the prominent role of the propulsion subsystem, one wonders which propulsion strategy out of the ones described in Subsection 2.2.3 is preferred:

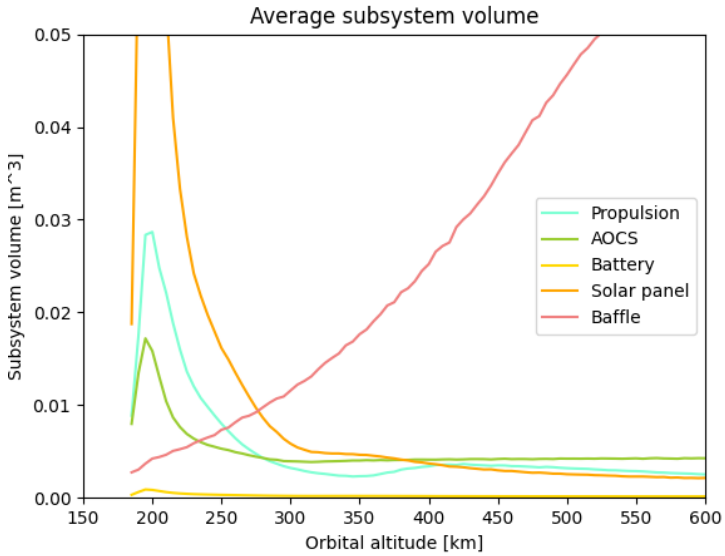

Figure 8.2: The Monte Carlo simulation result of the average subsystem volume budgets V_{prop}, V_{AOCS}, V_{bat}, V_{sp} and V_{baffle} as a function of orbital altitude h without outliers

Which propulsion strategy is preferred for the proposed mission?

As elaborated on in Section 7.4, regular Electric Propulsion (EP) was found to have a favorable volume at the optimal altitude compared to chemical propulsion. At $350\,\mathrm{km}$ to $550\,\mathrm{km}$, a transition from EP to chemical propulsion was observed. In case EP is excluded as an option, chemical propulsion can be implemented at the cost of a $80.1\,\%$ volume increase. Also, the optimal altitude then increases to $360\,\mathrm{km}$. Atmosphere Breathing Electric Propulsion (ABEP) was also investigated, but found to require too much power and intake volume to compete with EP at its current stage of development. As concluded in Subsection 2.2.3, ABEP is still in the experimental phase, with research being done on the improvement of the inlet efficiency and thrust-to-power ratio. Therefore, it might become competitive in the future and should be kept an eye on.

The payload volume on the other hand relates to the satellite geometry as highlighted in Section 5.4. In case of a non-deployable payload at $295\,\mathrm{km}$, the effective stowed volume takes a cubical shape and the baffle is integrated into the body, surrounded by the subsystems. For a DST, the outer diameter of the baffle drives the body dimensions and hence, the effective stowed volume converges to a flatter design. On one hand, this improves the ballistic coefficient, on the other it complicates fitting of sufficient solar panels area as discussed in Section 7.5. However, the latter was found not no be a major concern for the optimal design when balancing the number of baffle segments: assuming three baffle segments, a total of seven deployable solar panel segments were required (three to four on each side). With these primary relationships established, it is time to ask:

What is the optimal combination of budget-optimization strategies for the proposed mission?

Table 8.1 tabulates the effect of the VLEO and deployability of the instrument as analyzed in Section 7.8. The four configurations are also depicted in Figure 8.3. Conform expectations, both VLEO and the DST establish significant volume reduction and their combined integration leads to the optimal design. The greatest effect is that of the orbital altitude. The primary reason for this is shrinkage of the primary mirror, which scales proportional to altitude in order to preserve a Ground Sampling Distance (GSD) of $4\,\mathrm{m}$. Compared to the traditional, non-deployable space telescope in LEO, the combination of VLEO and deployable optics reduces volume by $89.1\,\%$. As this greatly exceed the $50\,\%$ criterion established, the final sub-question is answered:

Is the concept preferred over a traditional LEO Earth observation satellite in terms of expected return-on-investment and technical development risk?

Table 8.1: The average effective stowed volume of the four competing configurations

Orbital altitude	Deployability	Effective stowed volume
VLEO ($295\,\mathrm{km}$)	No	$0.0598\,\mathrm{m}^3$
VLEO ($295\,\mathrm{km}$)	Yes ($n_{segments} = 3$)	$0.0361\,\mathrm{m}^3$
LEO ($600\,\mathrm{km}$)	No	$0.332\,\mathrm{m}^3$
LEO ($600\,\mathrm{km}$)	Yes ($n_{segments} = 3$)	$0.183\,\mathrm{m}^3$

Related to the payload design, the sensitivity analysis in Section 7.6 revealed a strong dependency of the effective stowed volume on the aperture diameter. Even though the current baseline design assumes a reference diameter of $30\,\mathrm{cm}$ at $300\,\mathrm{km}$, re-evaluation of optical requirements could result in adjustment of this parameter. This directly impacts the optimal altitude as well as the effective stowed volume. Therefore, consolidating this dimension must take priority in future design activities.

Furthermore, an eye should be kept on the number of solar panel segments for it not to grow to an unfeasible number. This could be aided by advancements in the thrust-to-power ratio of EP, which is an active area of research. It is also recommended to establish a more applicable AOCS model. The model used in this study is largely extrapolated on the low end due to an over-estimation of satellite body dimensions, possibly resulting in an over-estimation of AOCS power consumption and thus number of solar panel segments. Therefore, focus must shift to lower-torque systems.

The EPS will also be affected by this over-estimation. As can be concluded from Section 5.9, the Control Moment Gyro's (CMG's) are the primary power consumer related to the AOCS. While the model assumed COTS CMG's that are capable of accumulating momentum from $1\,\mathrm{Nms}$ to $10\,\mathrm{Nms}$, Section 7.5 revealed that at the optimum altitude, only $0.1\,\mathrm{Nms}$ accumulates. Taking the CMG's from Veoware, which can accumulate up to $0.1\,\mathrm{Nms}$ [1], as an example, each CMG can save about $5\,\mathrm{W}$. This in turn leads to a power consumption reduction of $20\,\mathrm{W}$, which reduces the required number of solar panels to five. Important to evaluate is the effect of the asymmetrical solar panel configuration. Even though not considered in this work, such asymmetry could induce additional torques that drive the AOCS. Alternatives such as reduction of the solar panel dimensions could provide a solution.

Lastly, attention must be given to the thermal control design, as the current baseline subsystem does not fit the optimal satellite design. Redesign, relocation or different ways of passive cooling could provide solutions without extensive redesign of the entire satellite.

As this study proved feasibility of VLEO satellites in terms of volume, focus should shift to the geometry optimization of this concept satellite, as this was proven vital in VLEO missions (see Subsection 2.2.2). The possibilities of including a tail geometry and implementing aerodynamic attitude control to ease requirements on AOCS should be investigated next, along with the possibility of stacking the payload driven geometry. The latter would allow similar benefits to the Disk- and HexSat configuration discussed in Section 2.3. Material considerations come into play here as well.

This thesis is limited to the design of a marine plastic debris monitoring mission, though exploration of VLEO could open up many more possibilities in other research areas as well. Especially Earth Observation (EO) satellites could benefit from the higher achievable resolution. Other advantages not explored here are the fast orbital debris mitigation and low latency communication. The challenges addressed in this work primarily follow from the increased atmospheric drag related to the satellite geometry and altitude. However, the charge build-up and the consequences of material usage (such as Atomic Oxygen (AO) degradation and specular reflection for attitude control) shall not be underestimated and require careful consideration as well.

To conclude, this work has shown that the integration of deployable optics and VLEO leads to a significant net volume reduction compared to a traditional LEO Earth observation satellite. With that, it proves feasibility of the improvement of spatial and temporal resolution on data regarding marine plastic debris. This result does not limit to this specific application, but opens the doors to data improvement for a wide variety of Earth observation missions.

[1] `https://veowarespace.com/vw-products/reaction-wheel-whl-100.`

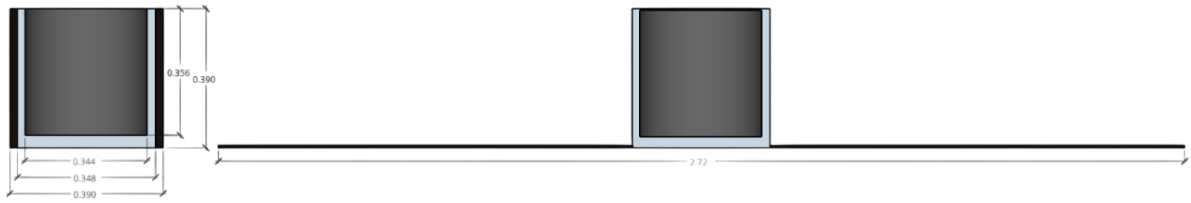

(a) Non-deployable space telescope in VLEO

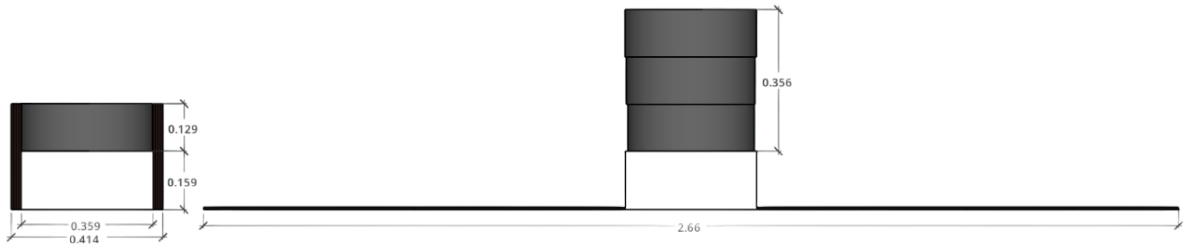

(b) DST in VLEO

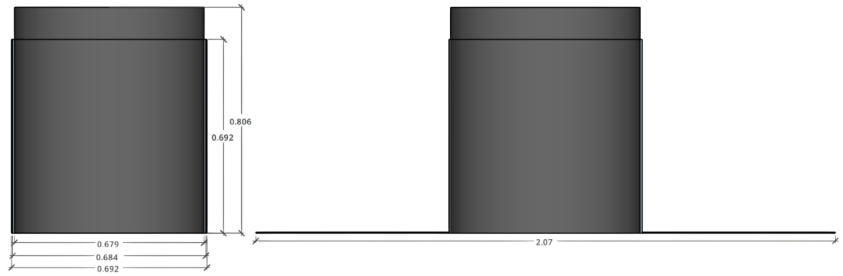

(c) Non-deployable space telescope in LEO

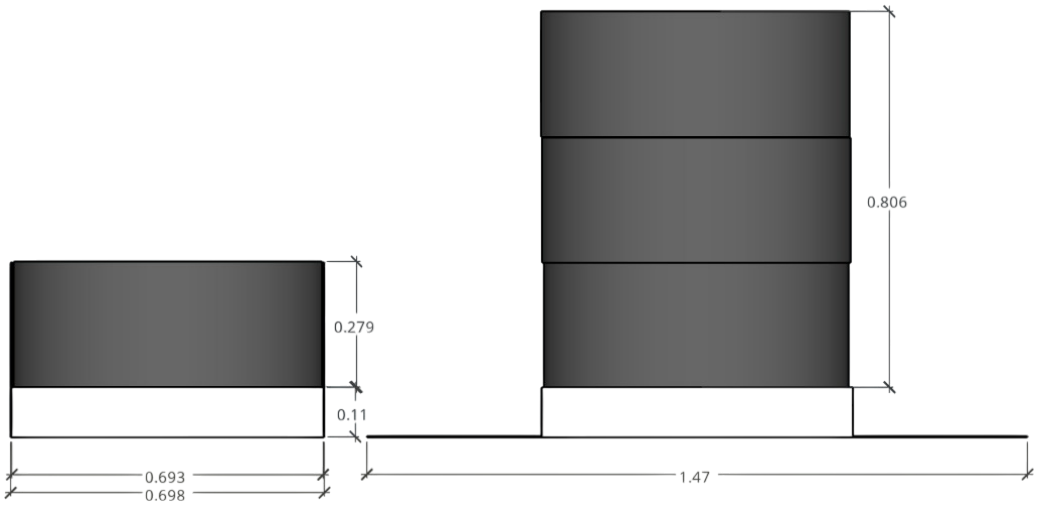

(d) DST in LEO

Figure 8.3: The four combinations of payload deployability and orbital altitude

References

[1] European Space Agency. *Copernicus Sentinel-2 shows dense plastic patches*. Image captured on 18 September 2020; processed by the National Technical University of Athens. Contains modified Copernicus Sentinel-2 data (2020). Aug. 2022. URL: https://www.esa.int/ESA_Multimedia/Images/2022/08/Copernicus_Sentinel-2_shows_dense_plastic_patches.

[2] J. Bouwmeester and J. M. Kuiper. "Enabling cost-effective high-resolution earth observation with deployable space telescopes". English. In: 2023.

[3] J. Vanhamel and J. Bouwmeester. "The design of a global oceanic plastic debris monitoring system using imaging spectroscopy onboard low-flying satellites". In: Apr. 2024, pp. 1–5. DOI: 10.1109/OCEANS51537.2024.10682315.

[4] R. Geyer, J. R. Jambeck, and K. L. Law. "Production, use, and fate of all plastics ever made". In: *Science Advances* 3.7 (2017), e1700782. DOI: 10.1126/sciadv.1700782. URL: https://www.science.org/doi/abs/10.1126/sciadv.1700782.

[5] S. Perreard et al. *Plastic overshoot day*. EA – Earth Action, Lausanne, Switzerland, 2024.

[6] S. B. Borrelle et al. "Predicted growth in plastic waste exceeds efforts to mitigate plastic pollution". In: *Science* 369.6510 (2020), pp. 1515–1518. DOI: 10.1126/science.aba3656. URL: https://www.science.org/doi/abs/10.1126/science.aba3656.

[7] D. K. A. Barnes et al. "Accumulation and fragmentation of plastic debris in global environments". In: *Philosophical Transactions of the Royal Society B: Biological Sciences* 364.1526 (2009), pp. 1985–1998. DOI: 10.1098/rstb.2008.0205. URL: https://royalsocietypublishing.org/doi/abs/10.1098/rstb.2008.0205.

[8] A. Danilov and E. Serdiukova. "Review of methods for automatic plastic detection in water areas using satellite images and machine learning". In: *Sensors* 24.16 (2024). ISSN: 1424-8220. URL: https://www.mdpi.com/1424-8220/24/16/5089.

[9] V. Martínez-Vicente et al. "Measuring marine plastic debris from space: initial assessment of observation requirements". In: *Remote Sensing* 11.20 (2019). ISSN: 2072-4292. DOI: 10.3390/rs11202443. URL: https://www.mdpi.com/2072-4292/11/20/2443.

[10] T. Irfan, A. Isobe, and H. Matsuura. "A particle tracking model approach to determine the dispersal of riverine plastic debris released into the Indian Ocean". In: *Marine Pollution Bulletin* 199 (2024), p. 115985. ISSN: 0025-326X. DOI: https://doi.org/10.1016/j.marpolbul.2023.115985. URL: https://www.sciencedirect.com/science/article/pii/S0025326X23014200.

[11] A. Cózar et al. "Proof of concept for a new sensor to monitor marine litter from space". In: *Nature Communications* 15 (2024). DOI: https://doi.org/10.1038/s41467-024-48674-7.

[12] V. Martinez-Vicente. "The need for a dedicated marine plastic litter satellite mission". In: *Nature Reviews Earth & Environment* 3 (2022). DOI: 10.1063/1.5007734. URL: https://doi.org/10.1038/s43017-022-00360-2.

[13] T. Dube and O. Mutanga. "Evaluating the utility of the medium-spatial resolution Landsat 8 multispectral sensor in quantifying aboveground biomass in uMgeni catchment, South Africa". In: *ISPRS Journal of Photogrammetry and Remote Sensing* 101 (2015), pp. 36–46. ISSN: 0924-2716. DOI: https://doi.org/10.1016/j.isprsjprs.2014.11.001. URL: https://www.sciencedirect.com/science/article/pii/S0924271614002603.

[14] S. Lavender. "Detection of Waste Plastics in the Environment: Application of Copernicus Earth Observation Data". In: *Remote Sensing* 14.19 (2022). Cited by: 13; All Open Access, Gold Open Access, Green Open Access. DOI: 10.3390/rs14194772. URL: https://www.scopus.com/inward/record.uri?eid=2-s2.0-85139972659&doi=10.3390%2frs14194772&partnerID=40&md5=f24286eeb4657c630402a9b371909304.

[15] M. M. Duarte and L. Azevedo. “Automatic detection and identification of floating marine debris using multispectral satellite imagery”. In: *IEEE Transactions on Geoscience and Remote Sensing* 61 (2023). Cited by: 14; All Open Access, Hybrid Gold Open Access. DOI: 10.1109/TGRS.2023.3283607. URL: https://www.scopus.com/inward/record.uri?eid=2-s2.0-85162613459&doi=10.1109%2fTGRS.2023.3283607&partnerID=40&md5=efee08906b3fb54842f5341a43937515.

[16] S. Sannigrahi et al. “Development of automated marine floating plastic detection system using Sentinel-2 imagery and machine learning models”. In: *Marine Pollution Bulletin* 178 (2022). Cited by: 30; All Open Access, Hybrid Gold Open Access. DOI: 10.1016/j.marpolbul.2022.113527. URL: https://www.scopus.com/inward/record.uri?eid=2-s2.0-85127312776&doi=10.1016%2fj.marpolbul.2022.113527&partnerID=40&md5=e3c73a5565475ca1062166dcc0fab489.

[17] A. Jamali and M. Mahdianpari. “A cloud-based framework for large-scale monitoring of ocean plastics using multi-spectral satellite imagery and generative adversarial network”. In: *Water (Switzerland)* 13.18 (2021). Cited by: 21; All Open Access, Gold Open Access. DOI: 10.3390/w13182553. URL: https://www.scopus.com/inward/record.uri?eid=2-s2.0-85115435905&doi=10.3390%2fw13182553&partnerID=40&md5=7aa145df5785a2f6a098be414387695c.

[18] C. Hu. “Remote detection of marine debris using Sentinel-2 imagery: A cautious note on spectral interpretations”. In: *Marine Pollution Bulletin* 183 (2022). Cited by: 19; All Open Access, Bronze Open Access. DOI: 10.1016/j.marpolbul.2022.114082. URL: https://www.scopus.com/inward/record.uri?eid=2-s2.0-85137068189&doi=10.1016%2fj.marpolbul.2022.114082&partnerID=40&md5=230175f5a599e61dbd530b02e53a8b4a.

[19] C. Hu et al. “Spectral characteristics of sea snot reflectance observed from satellites: Implications for remote sensing of marine debris”. In: *Remote Sensing of Environment* 269 (2022). Cited by: 32; All Open Access, Bronze Open Access. DOI: 10.1016/j.rse.2021.112842. URL: https://www.scopus.com/inward/record.uri?eid=2-s2.0-85121324531&doi=10.1016%2fj.rse.2021.112842&partnerID=40&md5=355bcb291959597a2be8b410571bd39a.

[20] V. Nivedita et al. “Plastic debris detection along coastal waters using Sentinel-2 satellite data and machine learning techniques”. In: *Marine Pollution Bulletin* 209 (2024). Cited by: 0. DOI: 10.1016/j.marpolbul.2024.117106. URL: https://www.scopus.com/inward/record.uri?eid=2-s2.0-85205778711&doi=10.1016%2fj.marpolbul.2024.117106&partnerID=40&md5=88f1763b6cad15528fcbc0288824c344.

[21] L. Biermann et al. “Finding plastic patches in coastal waters using optical satellite data”. In: *Scientific Reports* 10 (Apr. 2020), p. 5364. DOI: 10.1038/s41598-020-62298-z.

[22] M. Kremezi et al. “Increasing the Sentinel-2 potential for marine plastic litter monitoring through image fusion techniques”. In: *Marine Pollution Bulletin* 182 (2022), p. 113974. ISSN: 0025-326X. DOI: https://doi.org/10.1016/j.marpolbul.2022.113974. URL: https://www.sciencedirect.com/science/article/pii/S0025326X22006567.

[23] S. P. Garaba and H. M. Dierssen. “An airborne remote sensing case study of synthetic hydrocarbon detection using short wave infrared absorption features identified from marine-harvested macro- and microplastics”. In: *Remote Sensing of Environment* 205 (2018), pp. 224–235. ISSN: 0034-4257. DOI: https://doi.org/10.1016/j.rse.2017.11.023. URL: https://www.sciencedirect.com/science/article/pii/S0034425717305722.

[24] A. Kikaki et al. “Remotely sensing the source and transport of marine plastic debris in bay islands of Honduras (Caribbean Sea)”. In: *Remote Sensing* 12.11 (2020). ISSN: 2072-4292. DOI: 10.3390/rs12111727. URL: https://www.mdpi.com/2072-4292/12/11/1727.

[25] M. Kremezi et al. “Pansharpening PRISMA data for marine plastic litter detection using plastic indexes”. In: *IEEE Access* 9 (2021). Cited by: 43; All Open Access, Gold Open Access, pp. 61955–61971. DOI: 10.1109/ACCESS.2021.3073903. URL: https://www.scopus.com/inward/record.uri?eid=2-s2.0-85104611526&doi=10.1109%2fACCESS.2021.3073903&partnerID=40&md5=5f1a900e384769c5dac151edfc4f9781.

[26] K. Topouzelis et al. “Floating marine litter detection algorithms and techniques using optical remote sensing data: A review”. In: *Marine Pollution Bulletin* 170 (2021). Cited by: 71. DOI: 10.1016/j.marpolbul.2021.112675. URL: https://www.scopus.com/inward/record.uri?eid=2-s2.0-85109461919&doi=10.1016%2fj.marpolbul.2021.112675&partnerID=40&md5=0627abeea6af1db4ccf9badf1ff121fb.

[27] M. D. Simpson et al. “Monitoring of plastic islands in river environment using sentinel-1 SAR data”. In: *Remote Sensing* 14.18 (2022). Cited by: 11; All Open Access, Gold Open Access, Green Open Access. DOI: 10.3390/rs14184473. URL: https://www.scopus.com/inward/record.uri?eid=2-s2.0-85138764869&doi=10.3390%2frs14184473&partnerID=40&md5=af8f36f87a6da46673025881801e2596.

[28] N.H. Crisp et al. “The benefits of very low earth orbit for earth observation missions”. In: *Progress in Aerospace Sciences* 117 (2020). Cited by: 148; All Open Access, Green Open Access. DOI: 10.1016/j.paerosci.2020.100619. URL: https://www.scopus.com/inward/record.uri?eid=2-s2.0-85087959073&doi=10.1016%2fj.paerosci.2020.100619&partnerID=40&md5=178f4a160d22cd9349d670f46d364931.

[29] M. A. Najafabadi and I. Kazemi. “Systemic design of the very-high-resolution imaging payload of an optical remote sensing satellite for launch into the VLEO using an small launch vehicle”. In: *Heliyon* 10.6 (2024). Cited by: 1; All Open Access, Gold Open Access. DOI: 10.1016/j.heliyon.2024.e27404. URL: https://www.scopus.com/inward/record.uri?eid=2-s2.0-85188051355&doi=10.1016%2fj.heliyon.2024.e27404&partnerID=40&md5=2752de4e91e5a06386b4b1d50e527629.

[30] C. Y. Chi, Indraji Ushantha Wanigaratne, and David Dubinsky. “How low can you go: advocating very low earth orbit as the nex frontier for satellite operations”. In: *8th European Conference on Space Debris (virtual)*. Darmstadt, Germany, 2021.

[31] F. Hild et al. “Optimisation of satellite geometries in Very Low Earth Orbits for drag minimisation and lifetime extension”. In: *Acta Astronautica* 201 (2022). Cited by: 11; All Open Access, Green Open Access, pp. 340–352. DOI: 10.1016/j.actaastro.2022.09.032. URL: https://www.scopus.com/inward/record.uri?eid=2-s2.0-85138476488&doi=10.1016%2fj.actaastro.2022.09.032&partnerID=40&md5=23a8a4bf55ae5335a6dcf57488bf228b.

[32] K. Moe and M. M. Moe. “Gas–surface interactions and satellite drag coefficients”. In: *Planetary and Space Science* 53.8 (2005), pp. 793–801. ISSN: 0032-0633. DOI: https://doi.org/10.1016/j.pss.2005.03.005. URL: https://www.sciencedirect.com/science/article/pii/S0032063305000486.

[33] J. Emmert. “Thermospheric mass density: A review”. In: *Advances in Space Research* 56 (2015), pp. 773–824. DOI: 10.1016/j.asr.2015.05.038. URL: http://dx.doi.org/10.1016/j.asr.2015.05.038.

[34] Y. Jiang et al. “Aerodynamic drag analysis and reduction strategy for satellites in Very Low Earth Orbit”. In: *Aerospace Science and Technology* 132 (2023). Cited by: 14; All Open Access, Bronze Open Access. DOI: 10.1016/j.ast.2022.108077. URL: https://www.scopus.com/inward/record.uri?eid=2-s2.0-85145654423&doi=10.1016%2fj.ast.2022.108077&partnerID=40&md5=d61f5b7a17777bcfd41d7d9d3c9407eb.

[35] J. Walsh, L. Berthoud, and C. Allen. “Drag reduction through shape optimisation for satellites in Very Low Earth Orbit”. In: *Acta Astronautica* 179 (2021). Cited by: 29; All Open Access, Green Open Access, pp. 105–121. DOI: 10.1016/j.actaastro.2020.09.018. URL: https://www.scopus.com/inward/record.uri?eid=2-s2.0-85095699263&doi=10.1016%2fj.actaastro.2020.09.018&partnerID=40&md5=939d30eb14c1d1bc8f85da306a25cdcc.

[36] V. S. Aslanov and D. A. Sizov. “Attitude dynamics of spinning magnetic LEO/VLEO satellites”. In: *Aerospace* 10.2 (2023). Cited by: 2; All Open Access, Gold Open Access. DOI: 10.3390/aerospace10020192. URL: https://www.scopus.com/inward/record.uri?eid=2-s2.0-85149001348&doi=10.3390%2faerospace10020192&partnerID=40&md5=2e2e5410c79a6a5f05acf651e67c8fcc.

[37] S. Livadiotti et al. “Uncertainties and design of active aerodynamic attitude control in very low earth orbit”. In: *Journal of Guidance, Control, and Dynamics* 45.5 (2022). Cited by: 6; All Open Access, Green Open Access, pp. 859–874. DOI: 10.2514/1.G005999. URL: https://www.scopus.com/inward/record.uri?eid=2-s2.0-85129174593&doi=10.2514%2f1.G005999&partnerID=40&md5=75a2f76115dc9db0eed2ae7e8c905cb4.

[38] C. Marianowski et al. “Satellite design optimization for differential lift and drag applications”. In: *CEAS Space Journal* (2024). Cited by: 0; All Open Access, Hybrid Gold Open Access. DOI: 10.1007/s12567-024-00550-2. URL: https://www.scopus.com/inward/record.uri?eid=2-s2.0-85191058155&doi=10.1007%2fs12567-024-00550-2&partnerID=40&md5=c59daea963f3aa0f1171e58c30d5f302.

[39] N.H. Crisp et al. “System modelling of very low Earth orbit satellites for Earth observation”. In: *Acta Astronautica* 187 (2021). Cited by: 45; All Open Access, Green Open Access, pp. 475–491. DOI: 10.1016/j.actaastro.2021.07.004. URL: https://www.scopus.com/inward/record.uri?eid=2-s2.0-85109945099&doi=10.1016%2fj.actaastro.2021.07.004&partnerID=40&md5=0e305a0a998a1536d150504d4c944319.

[40] V. C. Munoz et al. “Attitude control for satellites flying in VLEO using aerodynamic surfaces”. In: *JBIS - Journal of the British Interplanetary Society* 73.3 (2020). Cited by: 8, pp. 103–112. URL: https://www.scopus.com/inward/record.uri?eid=2-s2.0-85094907464&partnerID=40&md5=988f170fb969c18fc7726fae1aabd01a.

[41] K. Watanabe et al. “Attitude control and on-orbit performance evaluation of spacecraft with variable shape function”. In: *Advances in Space Research* 72.6 (2023), pp. 2313–2323. ISSN: 0273-1177. DOI: https://doi.org/10.1016/j.asr.2023.06.002. URL: https://www.sciencedirect.com/science/article/pii/S0273117723004325.

[42] J. W. Gangestad, B. S. Hardy, and D. Hinkley. “Operations, orbit determination, and formation control of the AeroCube-4 CubeSats”. In: 2013. URL: https://api.semanticscholar.org/CorpusID:116598294.

[43] Y. Tang. *AE4ASM525 Materials for space*. Slides. 2024.

[44] B. A. Banks, S. K. Miller, and K. K. De Groh. “Low earth orbital atomic oxygen interactions with materials”. In: vol. 2. Cited by: 22; All Open Access, Green Open Access. 2004, pp. 978–996. DOI: 10.2514/6.2004-5638. URL: https://www.scopus.com/inward/record.uri?eid=2-s2.0-20344375958&doi=10.2514%2f6.2004-5638&partnerID=40&md5=a662ef6cec6280a9f4ec4a52356ae155.

[45] K. K. de Groh and B. A. Banks. “Misse-2 peace polymers erosion morphology studies”. In: 2009. URL: https://api.semanticscholar.org/CorpusID:201918387.

[46] M.S.M. Raihan and A.S.M. Harithuddin. “Feasibility study for exploiting aerodynamic drag in very low earth orbit with different flat plates configurations”. In: *Journal of Aeronautics, Astronautics and Aviation* 53.2 (2021). Cited by: 1, pp. 303–312. DOI: 10.6125/JoAAA.202106_53(2).24. URL: https://www.scopus.com/inward/record.uri?eid=2-s2.0-85104204729&doi=10.6125%2fJoAAA.202106_53%282%29.24&partnerID=40&md5=6d97be2a4963fbb2e117ab78442974b6.

[47] L. McCreary. “A satellite mission concept for high drag environments”. In: *Aerospace Science and Technology* 92 (2019). Cited by: 12, pp. 972–989. DOI: 10.1016/j.ast.2019.06.033. URL: https://www.scopus.com/inward/record.uri?eid=2-s2.0-85069577924&doi=10.1016%2fj.ast.2019.06.033&partnerID=40&md5=6908efd519eb415a1c2bf16beb05a78f.

[48] K. Xie, R. A. Martinez, and J. D. Williams. “Current–voltage characteristics of a cathodic plasma contactor with discharge chamber for application in electrodynamic tether propulsion”. In: *Journal of Physics D: Applied Physics* 47.15 (2014), pp. 1–2.

[49] H. Kuninaka and P. Molina-Morales. “Spacecraft charging due to lack of neutralization on ion thrusters”. In: *Acta Astronautica* 55.1 (2004), pp. 37–38.

[50] H. A. Cohen et al. “Sounding rocket flight of a satellite positive ion beam system”. In: *Princeton/AIAA/DGLR 14th International Electric Propulsion Conference*. 1979, pp. 4, 10.

[51] M. Cho et al. “Interaction between high voltage solar array and ion thruster plasma”. In: *Proceedings of the 23rd International Symposium on Space Technology and Science*. 2002-b-28 379. Japan Society for Aeronautical and Space Sciences. 2002, pp. 1–2.

[52] B. S. Borisov et al. “Exhaust plasma plume impacts on onboard antenna field distribution”. In: *International Electric Propulsion Conference*. IEPC-93-145. 1993, pp. 1, 3, 6.

[53] V. Cañas et al. “Attitude control for satellites flying in VLEO using aerodynamic surfaces”. In: Nov. 2019.

[54] I. Oz and Ü Yılmaz. “Design tradeoffs in full electric, hybrid and full chemical propulsion communication satellite”. In: *Sakarya University Journal of Computer and Information Sciences* 2 (Dec. 2019), pp. 124–133. DOI: 10.35377/saucis.02.03.654206.

[55] M. Leomanni et al. “Propulsion options for very low Earth orbit microsatellites”. In: *Acta Astronautica* 133 (2017), pp. 444–454. ISSN: 0094-5765. DOI: https://doi.org/10.1016/j.actaastro.2016.11.001. URL: https://www.sciencedirect.com/science/article/pii/S0094576516305197.

[56] S. H. Yeo et al. “Miniaturization perspectives of electrostatic propulsion for small spacecraft platforms”. In: *Progress in Aerospace Sciences* 126 (2021). Cited by: 24; All Open Access, Bronze Open Access. DOI: 10.1016/j.paerosci.2021.100742. URL: https://www.scopus.com/inward/record.uri?eid=2-s2.0-85111297317&doi=10.1016%2fj.paerosci.2021.100742&partnerID=40&md5=2d1272035faa35b901972c3d1695475c.

[57] C.E. Pigeon et al. “A low power cylindrical hall thruster for next generation microsatellites”. In: *Small Satellite Conference*. SSC15-P36. Space Flight Laboratory. 2015.

[58] A. Cervone et al. “Electrothermal microthruster”. In: Jan. 2022, pp. 125–149. ISBN: 9780128190371. DOI: 10.1016/B978-0-12-819037-1.00003-7.

[59] F. Romano et al. “RF helicon-based Inductive Plasma Thruster (IPT) design for an Atmosphere-Breathing Electric Propulsion system (ABEP)”. In: *Acta Astronautica* 176 (2020), pp. 476–483. ISSN: 0094-5765. DOI: https://doi.org/10.1016/j.actaastro.2020.07.008. URL: https://www.sciencedirect.com/science/article/pii/S0094576520304264.

[60] T. Huang et al. “Study and modeling of propellant ablation in coaxial ablative pulsed plasma thrusters”. In: *Acta Astronautica* 173 (2020). Cited by: 16, pp. 69–75. DOI: 10.1016/j.actaastro.2020.04.010. URL: https://www.scopus.com/inward/record.uri?eid=2-s2.0-85083303439&doi=10.1016%2fj.actaastro.2020.04.010&partnerID=40&md5=5d3bfa778ca8228c8a832c4b09f3e7ae.

[61] K. Polzin et al. “State-of-the-art and advancement paths for inductive pulsed plasma thrusters”. In: *Aerospace* 7.8 (2020). Cited by: 29; All Open Access, Gold Open Access. DOI: 10.3390/AEROSPACE7080105. URL: https://www.scopus.com/inward/record.uri?eid=2-s2.0-85089501522&doi=10.3390%2fAEROSPACE7080105&partnerID=40&md5=198e01b03cc4997290a3211c899165c0.

[62] J. Polk et al. “Development of high power lithium magnetoplasmadynamic thrusters to support human Mars exploration”. In: June 2024.

[63] P. Wu et al. “The performance of a magnetic nozzle enhanced magnetoplasmadynamic thruster”. In: *Acta Astronautica* 217 (2024), pp. 188–196. ISSN: 0094-5765. DOI: https://doi.org/10.1016/j.actaastro.2024.01.041. URL: https://www.sciencedirect.com/science/article/pii/S0094576524000493.

[64] C. Adkins et al. “Design and optimization of a high thrust density air-breathing pulsed plasma thruster array”. In: *Journal of Electric Propulsion* 3.1 (2024). Cited by: 0; All Open Access. DOI: 10.1007/s44205-024-00071-4. URL: https://www.scopus.com/inward/record.uri?eid=2-s2.0-85205402734&doi=10.1007%2fs44205-024-00071-4&partnerID=40&md5=08389e4c200eae80ac72fe108d6d4e0a.

[65] M. U. Siddiqui and C. Cretel. “Updated performance measurements and analysis of the phase four RF thruster”. In: July 2018. DOI: 10.2514/6.2018-4817.

[66] A. Shabshelowitz and A. D. Gallimore. “Performance and probe measurements of a radio-frequency plasma thruster”. In: *Journal of Propulsion and Power* 29.4 (2013), pp. 919–929. DOI: 10.2514/1.B34720. URL: https://doi.org/10.2514/1.B34720.

[67] T. Matsuoka et al. “Laboratory model development of Lissajous acceleration for electrodeless helicon plasma thruster”. In: Cited by: 2. 2012. DOI: 10.2514/6.2012-3956. URL: https://www.scopus.com/inward/record.uri?eid=2-s2.0-85087536719&doi=10.2514%2f6.2012-3956&partnerID=40&md5=9f4e7fbf1d859f54a5942313a6711565.

[68] K. Takahashi et al. “Performance improvement of a permanent magnet helicon plasma thruster”. In: *Journal of Physics D: Applied Physics* 46.35 (2013). Cited by: 55. DOI: 10.1088/0022-3727/46/35/352001. URL: https://www.scopus.com/inward/record.uri?eid=2-s2.0-84882801001&doi=10.1088%2f0022-3727%2f46%2f35%2f352001&partnerID=40&md5=63f1478903c1862aeac4d127aaba2e63.

[69] G. Herdrich et al. “System design study of a VLEO satellite platform using the IRS RF helicon-based plasma thruster”. In: *Acta Astronautica* 215 (2024). Cited by: 0, pp. 245–259. DOI: 10.1016/j.actaastro.2023.11.009. URL: https://www.scopus.com/inward/record.uri?eid=2-s2.0-85180366488&doi=10.1016%2fj.actaastro.2023.11.009&partnerID=40&md5=70c51776e3061aec83a337036c09d25f.

[70] F. Chen. “Permanent magnet helicon source for ion propulsion”. In: *Plasma Science, IEEE Transactions on* 36 (Nov. 2008), pp. 2095–2110. DOI: 10.1109/TPS.2008.2004039.

[71] T. Andreussi, E. Ferrato, and V. Giannetti. “A review of air-breathing electric propulsion: from mission studies to technology verification”. In: *Journal of Electric Propulsion* 1 (2022), p. 31. DOI: 10.1007/s44205-022-00024-9.

[72] J. Zhou et al. “A study of an air-breathing electrodeless plasma thruster discharge”. In: *Propulsion and Power Research* (2024). ISSN: 2212-540X. DOI: https://doi.org/10.1016/j.jppr.2024.10.001. URL: https://www.sciencedirect.com/science/article/pii/S2212540X24000750.

[73] F. Marchioni and M. A. Cappelli. “Extended channel Hall thruster for air-breathing electric propulsion”. In: *Journal of Applied Physics* 130.5 (2021). Cited by: 19. DOI: 10.1063/5.0048283. URL: https://www.scopus.com/inward/record.uri?eid=2-s2.0-85112351835&doi=10.1063%2f5.0048283&partnerID=40&md5=32499d7ad0a248a2f74d74b2e6c26095.

[74] P. Hu et al. “Study of multi-cusped plasma thruster applied to Air-Breathing Electric Propulsion”. In: *Vacuum* 190 (2021). Cited by: 7. DOI: 10.1016/j.vacuum.2021.110275. URL: https://www.scopus.com/inward/record.uri?eid=2-s2.0-85105268507&doi=10.1016%2fj.vacuum.2021.110275&partnerID=40&md5=3f1caec6fac914c96f2f954a05c4cdcd.

[75] Z. Wang, Y. Eun, and X. Wu. “Design and demonstration of a micro air-fed magnetoplasmadynamic thruster for small satellites”. In: *Acta Astronautica* 181 (2021), pp. 482–491. ISSN: 0094-5765. DOI: https://doi.org/10.1016/j.actaastro.2021.01.047. URL: https://www.sciencedirect.com/science/article/pii/S0094576521000576.

[76] B. Göksel and I. Mashek. “First breakthrough for future air-breathing magneto-plasma propulsion systems”. In: *Journal of Physics: Conference Series* 825 (Sept. 2016). DOI: 10.1088/1742-6596/825/1/012005.

[77] J. Wu et al. “Recent development of intake devices for atmosphere-breathing electric propulsion system”. In: *Progress in Aerospace Sciences* 133 (2022). Cited by: 21. DOI: 10.1016/j.paerosci.2022.100848. URL: https://www.scopus.com/inward/record.uri?eid=2-s2.0-85134184050&doi=10.1016%2fj.paerosci.2022.100848&partnerID=40&md5=71fdbde4c5090cacc66f9390d9cfbc4c.

[78] P. Zheng et al. “Optimization investigation of vacuum air-intake for atmosphere-breathing electric propulsion system”. In: *Proceedings of the Institution of Mechanical Engineers, Part G: Journal of Aerospace Engineering* 236.7 (2022). Cited by: 5, pp. 1253–1268. DOI: 10.1177/09544100211029829. URL: https://www.scopus.com/inward/record.uri?eid=2-s2.0-85109036793&doi=10.1177%2f09544100211029829&partnerID=40&md5=c988081d5437ad87b7810686ed69ef2d.

[79] P. Zheng et al. “Design and Optimization of vacuum Intake for Atmosphere-Breathing electric propulsion (ABEP) system”. In: *Vacuum* 195 (2022). Cited by: 18. DOI: 10.1016/j.vacuum.2021.110652. URL: https://www.scopus.com/inward/record.uri?eid=2-s2.0-85116752408&doi=10.1016%2fj.vacuum.2021.110652&partnerID=40&md5=6a88c5d9c3709f573815fb04b3912990.

[80] P. Zheng et al. “Design and numerical investigation on the intake of atmosphere-breathing electric propulsion”. In: *Acta Astronautica* 188 (2021). Cited by: 16, pp. 215–228. DOI: 10.1016/j.actaastro.2021.07.036. URL: https://www.scopus.com/inward/record.uri?eid=2-s2.0-85111301906&doi=10.1016%2fj.actaastro.2021.07.036&partnerID=40&md5=5f3e42cc115a0362c7c36f40f0f39e50.

[81] F. Romano et al. “Design of an intake and a thruster for an atmosphere-breathing electric propulsion system”. In: *CEAS Space Journal* 14.4 (2022). Cited by: 10, pp. 707–715. DOI: 10.1007/s12567-022-00452-1. URL: https://www.scopus.com/inward/record.uri?eid=2-s2.0-85130692010&doi=10.1007%2fs12567-022-00452-1&partnerID=40&md5=32a31525ef6697ec534092ef93ea6e8e.

[82] S. Andrews et al. “Cathode-less RF plasma thruster design and optimisation for an atmosphere-breathing electric propulsion (ABEP) system”. In: *Acta Astronautica* 225 (2024), pp. 833–844. ISSN: 0094-5765. DOI: https://doi.org/10.1016/j.actaastro.2024.09.041. URL: https://www.sciencedirect.com/science/article/pii/S0094576524005435.

[83] G. Moon, M. Yi, and E. Jun. “Design and operational concept of a cryogenic active intake device for atmosphere-breathing electric propulsion”. In: *Aerospace Science and Technology* 151 (2024), p. 109300. ISSN: 1270-9638. DOI: https://doi.org/10.1016/j.ast.2024.109300. URL: https://www.sciencedirect.com/science/article/pii/S1270963824004310.

[84] V. Giannetti, E. Ferrato, and T. Andreussi. “On the critical parameters for feasibility and advantage of air-breathing electric propulsion systems”. In: *Acta Astronautica* 220 (2024). Cited by: 1; All Open Access, Hybrid Gold Open Access, pp. 345–355. DOI: 10.1016/j.actaastro.2024.04.042. URL: https://www.scopus.com/inward/record.uri?eid=2-s2.0-85192293935&doi=10.1016%2fj.actaastro.2024.04.042&partnerID=40&md5=dfb1c457c1ad08759ccb49132c8bfa66.

[85] M. Tisaev et al. “Air-breathing electric propulsion: Flight envelope identification and development of control for long-term orbital stability”. In: *Acta Astronautica* 191 (2022), pp. 374–393. ISSN: 0094-5765. DOI: https://doi.org/10.1016/j.actaastro.2021.11.011. URL: https://www.sciencedirect.com/science/article/pii/S009457652100607X.

[86] F. Romano et al. “Intake design for an Atmosphere-Breathing Electric Propulsion System (ABEP)”. In: *Acta Astronautica* 187 (2021), pp. 225–235. ISSN: 0094-5765. DOI: https://doi.org/10.1016/j.actaastro.2021.06.033. URL: https://www.sciencedirect.com/science/article/pii/S0094576521003301.

[87] Y. Ko et al. “Parametric study on the flight envelope of a radio-frequency ion thruster based atmosphere-breathing electric propulsion system”. In: *Acta Astronautica* 212 (2023), pp. 198–212. ISSN: 0094-5765. DOI: https://doi.org/10.1016/j.actaastro.2023.07.043. URL: https://www.sciencedirect.com/science/article/pii/S0094576523003946.

[88] P. Crandall and R. E. Wirz. “Air-breathing electric propulsion: mission characterization and design analysis”. In: *Journal of Electric Propulsion* 1.1 (2022). Cited by: 10; All Open Access, Hybrid Gold Open Access. DOI: 10.1007/s44205-022-00009-8. URL: https://www.scopus.com/inward/record.uri?eid=2-s2.0-85167405372&doi=10.1007%2fs44205-022-00009-8&partnerID=40&md5=3edff14b5f8f1eeee8df750b4a8c668c.

[89] G. Sánchez-Arriaga, E. C. Lorenzini, and S. G. Bilén. “A review of electrodynamic tether missions: Historical trend, dimensionless parameters, and opportunities opening space markets”. In: *Acta Astronautica* 225 (2024). Cited by: 1; All Open Access, Hybrid Gold Open Access, pp. 158–168. DOI: 10.1016/j.actaastro.2024.09.002. URL: https://www.scopus.com/inward/record.uri?eid=2-s2.0-85203426041&doi=10.1016%2fj.actaastro.2024.09.002&partnerID=40&md5=a2d1926b01a6204e804346fbfc4efea3.

[90] F. Barato. “Optimal use of electric propulsion for drag compensation in very low earth orbit on satellites with deployable solar panels”. In: *Acta Astronautica* 213 (2023). Cited by: 1; All Open Access, Hybrid Gold Open Access, pp. 1–19. DOI: 10.1016/j.actaastro.2023.08.038. URL: https://www.scopus.com/inward/record.uri?eid=2-s2.0-85170828964&doi=10.1016%2fj.actaastro.2023.08.038&partnerID=40&md5=22aa73febcb8704a7725eebe8475fd68.

[91] Y. Yue et al. “Elliptical orbit design based on air-breathing electric propulsion technology in very-low earth orbit space”. In: *Aerospace* 10.10 (2023). Cited by: 2; All Open Access, Gold Open Access. DOI: 10.3390/aerospace10100899. URL: https://www.scopus.com/inward/record.uri?eid=2-s2.0-85175159254&doi=10.3390%2faerospace10100899&partnerID=40&md5=613ba058b563f7dc41e52a7a4aaee6e6.

[92] X. Zuo et al. “Maintenance strategy for elliptical orbit satellite with air-breathing electric propulsion”. In: *IEEE Transactions on Aerospace and Electronic Systems* 59.5 (2023). Cited by: 2, pp. 6863–6877. DOI: 10.1109/TAES.2023.3282611. URL: https://www.scopus.com/inward/record.uri?eid=2-s2.0-85161573082&doi=10.1109%2fTAES.2023.3282611&partnerID=40&md5=d5144de24e01ebbbb2352f48fe6a4f6d.

[93] D. G. Fearn. “Economical remote sensing from a low altitude with continuous drag compensation”. In: *Acta Astronautica* 56.5 (2005), pp. 555–572. ISSN: 0094-5765. DOI: https://doi.org/10.1016/j.actaastro.2004.09.052. URL: https://www.sciencedirect.com/science/article/pii/S0094576504003704.

[94] J. V. Llop et al. “Very low earth orbit mission concepts for earth observation: Benefits and challenges.” English. In: *Reinventing Space Conference*. Reinventing Space Conference ; Conference date: 18-11-2014 Through 20-11-2014. Nov. 2014.

[95] A. Bacon and Ben Olivier. “Skimsats: bringing down the cost of Earth Observation”. In: *Proceedings of the 12th Reinventing Space Conference*. Ed. by Scott Hatton. Cham: Springer International Publishing, 2017, pp. 1–7. ISBN: 978-3-319-34024-1.

[96] D. Di Cara et al. “RAM electric propulsion for low earth orbit operation: an ESA study”. In: Sept. 2007.

[97] K. Diamant. “A 2-stage cylindrical Hall thruster for air breathing electric propulsion”. In: *46th AIAA/ASME/SAE/ASEE Joint Propulsion Conference and Exhibit*. AIAA2010–6522. 2010. DOI: 10.2514/6.2010-6522. URL: http://dx.doi.org/10.2514/6.2010-6522.

[98] A. Shabshelowitz. “Study of RF plasma technology applied to air-breathing electric propulsion”. PhD thesis. University of Michigan, 2013.

[99] L. Pekker and M. Keidar. “Analysis of air-breathing Hall-effect thrusters”. In: *Journal of Propulsion and Power* 28.6 (2012), pp. 1399–1405.

[100] K. Fujita. “Air-intake performance estimation of air-breathing ion engines”. In: *Transactions of the Japan Society of Mechanical Engineers B* 70.700 (2004), pp. 3038–3044. URL: http://ci.nii.ac.jp/naid/110004999698/en/.

[101] H. Kuiper and D. Dolkens. “A cutting edge 6U CubeSat ADCS design for earth observation with sub-meter spatial resolution at 230–380 km altitude”. In: *CEAS Space Journal* 12.4 (2020). Cited by: 9; All Open Access, Hybrid Gold Open Access, pp. 613–621. DOI: 10.1007/s12567-020-00323-7. URL: https://www.scopus.com/inward/record.uri?eid=2-s2.0-85086710963&doi=10.1007%2fs12567-020-00323-7&partnerID=40&md5=38b42b1c6bf72a281701242c8f70f7df.

[102] *SLATS - Satellite Missions - eoPortal Directory*. Accessed: 05-12-2024. URL: https://www.eoportal.org/satellite-missions/slats#references.

[103] *SOAR - Satellite Missions - eoPortal Directory*. Accessed: 05-12-2024. URL: https://www.eoportal.org/satellite-missions/soar#background.

[104] *SOAR: Satellite for Orbital Aerodynamics Research*. Accessed: 05-12-2024. URL: https://discoverer.space/soar-satellite-for-orbital-aerodynamics-research/.

[105] E. Canuto and L. Massotti. “All-propulsion design of the drag-free and attitude control of the European satellite GOCE”. In: *Acta Astronautica* 64.2-3 (2009). Cited by: 78; All Open Access, Green Open Access, pp. 325–344. DOI: 10.1016/j.actaastro.2008.07.017. URL: https://www.scopus.com/inward/record.uri?eid=2-s2.0-56349169856&doi=10.1016%2fj.actaastro.2008.07.017&partnerID=40&md5=a69afce3819a6dc194fa6d23a27c527d.

[106] G. Sechi et al. “In-flight results from the drag-Free and attitude control of GOCE satellite”. In: *IFAC Proceedings Volumes* 44.1 (2011). 18th IFAC World Congress, pp. 733–740. ISSN: 1474-6670. DOI: https://doi.org/10.3182/20110828-6-IT-1002.02966. URL: https://www.sciencedirect.com/science/article/pii/S1474667016436980.

[107] K. Woellert et al. “Cubesats: Cost-effective science and technology platforms for emerging and developing nations”. In: *Advances in Space Research* 47.4 (2011). Cited by: 307, pp. 663–684. DOI: 10.1016/j.asr.2010.10.009. URL: https://www.scopus.com/inward/record.uri?eid=2-s2.0-79551474683&doi=10.1016%2fj.asr.2010.10.009&partnerID=40&md5=11f944fa2aadf3c67d636b9279d7992f.

[108] K. Saddul et al. “HexSats: A novel flat hexagonal nanosatellite for high-power applications”. In: *Acta Astronautica* 225 (2024), pp. 27–40. ISSN: 0094-5765. DOI: https://doi.org/10.1016/j.actaastro.2024.09.007. URL: https://www.sciencedirect.com/science/article/pii/S0094576524005034.

[109] R. Welle et al. “DiskSat: Demonstration Mission for a Two-Dimensional Satellite Architecture”. In: *Small Satellite Conference*. 2022.

[110] Y. Yang, Xia R., and Jianrong W. “Development of integrated and intelligent surveying and mapping satellite project with corresponding key technology; [□□□□□□□□□□□□□□□□□□□□□□□□]”. In: *Cehui Xuebao/Acta Geodaetica et Cartographica Sinica* 51.6 (2022). Cited by: 8, pp. 854–861. DOI: 10.11947/j.AGCS.2022.20220048. URL: https://www.scopus.com/inward/record.uri?eid=2-s2.0-85135384111&doi=10.11947%2fj.AGCS.2022.20220048&partnerID=40&md5=6d83bfb76650a363c712431b783cd52e.

[111] J. Bouwmeester et al. “Towards an innovative electrical interface standard for PocketQubes and CubeSats”. In: *Advances in Space Research* 62.12 (2018). Advances in Technologies, Missions and Applications of Small Satellites, pp. 3423–3437. ISSN: 0273-1177. DOI: https://doi.org/10.1016/j.asr.2018.03.040. URL: https://www.sciencedirect.com/science/article/pii/S0273117718302801.

[112] C.W. de Boom et al. “In-orbit experience of TNO sun sensors”. English. In: *Proceedings of the 8th International ESA Conference on Guidance, Navigation and Control Systems*. Ed. by s.n. GNC 2011 - Karlovy Vary, Czech Republic ; Conference date: 05-06-2011 Through 10-06-2011. ESA, 2011, pp. 1–17.

[113] T. T. K. Tuoi, N. Van Toan, and T. Ono. “Self-powered wireless sensing system driven by daily ambient temperature energy harvesting”. In: *Applied Energy* 311 (2022), p. 118679. ISSN: 0306-2619. DOI: https://doi.org/10.1016/j.apenergy.2022.118679. URL: https://www.sciencedirect.com/science/article/pii/S0306261922001441.

[114] L. J.; Machin and J. Bouwmeester. “Thermoelectric harvesting for an autonomous self-powered temperature sensor in small satellites”. English. In: *Proceedings of the 68th International Astronautical Congress*. TUDelft, 2017, pp. 1–17.

[115] T. Jaeger, W. Mirczak, and B. Crandall. ““Cellularized satellites - A small satellite instantiation that provides mission and space access Adaptability”. In: *SmallSat Conference*. Aug. 2016.

[116] Y. Zhang et al. “A self-reconfiguration planning strategy for cellular satellites”. In: *IEEE Access* 7 (2019). Cited by: 12; All Open Access, Gold Open Access, pp. 4516–4528. DOI: 10.1109/ACCESS.2018.2888588. URL: https://www.scopus.com/inward/record.uri?eid=2-s2.0-85058899469&doi=10.1109%2fACCESS.2018.2888588&partnerID=40&md5=3f5c774e261caa7d90710ad18fa257c6.

[117] J. Guo, J. Bouwmeester, and E. K. A. Gill. “In-orbit results of Delfi-n3Xt: Lessons learned and move forward”. In: *Acta Astronautica* 121 (2016), pp. 39–50. ISSN: 0094-5765. DOI: https://doi.org/10.1016/j.actaastro.2015.12.003. URL: https://www.sciencedirect.com/science/article/pii/S0094576515004373.

[118] J.. Bouwmeester et al. “A new approach on the physical architecture of cubesats & pocket qubes”. In: *JBIS - Journal of the British Interplanetary Society* 71.7 (2018). Cited by: 3, pp. 239–249. URL: https://www.scopus.com/inward/record.uri?eid=2-s2.0-85060660799&partnerID=40&md5=c87934e2bba8e1ca697dae1c281120f2.

[119] S. Radu et al. “Delfi-PQ: The first pocketqube of delft university of technology”. In: *IEEE Aerospace Conference*. Oct. 2018, 69th International Astronautical Congress.

[120] M. Pajusalu et al. “Design of the electrical ppower system for the ESTCube-1 satellite”. In: *Latvian Journal of Physics and Technical Sciences* 49 (July 2012), pp. 16–24. DOI: 10.2478/v10047-012-0014-4.

[121] V. Platero et al. “2-In-1 smart panels: Embedding phased array patch antennas within satellite structures”. In: *Acta Astronautica* 175 (2020), pp. 51–56. ISSN: 0094-5765. DOI: https://doi.org/10.1016/j.actaastro.2020.04.050. URL: https://www.sciencedirect.com/science/article/pii/S0094576520302654.

[122] A. Erlank and C. Bridges. “Satellite stem cells: The benefits & overheads of reliable multicellular architectures”. In: *IEEE Aerospace Conference*. Big Sky, 2017.

[123] C. Mcnutt et al. “Modular nanosatellites–(Plug-and-Play) PnP CubeSat”. In: (Jan. 2009), pp. 2009–4003.

[124] T. Shrestha et al. “Nepal’s high school 1U CubeSat MUNAL integrated bus system: Modification of the BIRDS open-source standardized bus”. In: vol. 2023-October. Cited by: 0. 2023. URL: https://www.scopus.com/inward/record.uri?eid=2-s2.0-85188008419&partnerID=40&md5=286265af3310ec812f89afa5c9c87ddd.

[125] A.R. Aslan et al. “The integration and testing of BeEagleSat”. In: July 2015. DOI: 10.13140/RG.2.1.2219.0562.

[126] Q. Wang et al. “Design of an integrated system for spaceborne SAR imaging and data transmission”. In: *Sensors* 24.19 (2024). ISSN: 1424-8220. DOI: 10.3390/s24196375. URL: https://www.mdpi.com/1424-8220/24/19/6375.

[127] D. Ivanov et al. “Electromagnetic uncoordinated control of a ChipSats swarm using magnetorquers”. In: *Acta Astronautica* 192 (2022). Cited by: 3, pp. 15–29. DOI: 10.1016/j.actaastro.2021.12.014. URL: https://www.scopus.com/inward/record.uri?eid=2-s2.0-85121223159&doi=10.1016%2fj.actaastro.2021.12.014&partnerID=40&md5=db9d17cc7f021532d77ed0b85dc4eb31.

[128] T. Abate. *Stanford and NASA Ames researchers put inexpensive chip-size satellites into orbit*. Stanford University, 2019.

[129] J. Vanhamel et al. “RF-driving of acoustic-optical tunable filters; design, realization and qualification of analog and digital modules for ESA”. In: *Microelectronics Reliability* 55.9 (2015). Proceedings of the 26th European Symposium on Reliability of Electron Devices, Failure Physics and Analysis, pp. 2103–2107. ISSN: 0026-2714. DOI: https://doi.org/10.1016/j.microrel.2015.07.034. URL: https://www.sciencedirect.com/science/article/pii/S0026271415301207.

[130] NASA. *Earth fact sheet*. Accessed: 02-03-2025. 2024. URL: https://nssdc.gsfc.nasa.gov/planetary/factsheet/earthfact.html.

[131] V. Nagy. *Design of a novel deployable baffle for a deployable space telescope*. Tech. Rep. [Online]. Available: http://resolver.tudelft.nl/uuid:2a6b175b-f254-463e-8ff4-59215e95d1c4. Delft: Delft University of Technology, 2021.

[132] F. Eshuis. “Passive thermal design of a thermal infrared telescope”. Master thesis. Delft University of Technology, 2023. URL: http://resolver.tudelft.nl/uuid:787a5034-3659-43ec-b082-d6d9d695a72c.

[133] C. W. Chen and C. R. Chen. “Comprehensive design and analysis of a RC-Ccassegrain telescope for micro-satellite mission”. In: *International Journal of Novel Research* 2: 1 (2019). Accessed: 02-03-2025. URL: https://www.innovationinfo.org/articles/IJNR/IJNR-2-112.pdf.

[134] H. Jin et al. “Optical design of a reflecting telescope for CubeSat”. In: *Journal of the Optical Society of Korea* 17.6 (2013). Accessed: 02-03-2025, pp. 533–537. URL: https://opg.optica.org/directpdfaccess/ba3c83b1-6665-4c28-97c0c140aaba2888_276792/josk-17-6-533.pdf?da=1&id=276792&seq=0&mobile=no.

[135] P. Mazzinghi. “An ultra-lightweight, large aperture, deployable telescope for advanced lidar applications”. In: 621 (May 2006), p. 15.

[136] N. Schwartz et al. “6U CubeSat deployable telescope for optical Earth observation and astronomical optical imaging”. In: *Space Telescopes and Instrumentation 2022: Optical, Infrared, and Millimeter Wave*. Ed. by Laura E. Coyle, Shuji Matsuura, and Marshall D. Perrin. Vol. 12180. Society of Photo-Optical Instrumentation Engineers (SPIE) Conference Series. Aug. 2022, 1218031, p. 1218031. DOI: 10.1117/12.2627248.

[137] H. K. Karrenberg. *Eclipse fractions for sun-synchronous orbits*. Tech. rep. Accessed: 02-03-2025. Defense Technical Information Center (DTIC), 1964. URL: https://apps.dtic.mil/sti/trecms/pdf/AD0603152.pdf.

[138] NASA. *Space solar cells improve efficiency and durability*. Accessed: 02-03-2025. 2016. URL: https://spinoff.nasa.gov/Spinoff2016/ee_5.html.

[139] N. *Fill factor in solar cells: Definition and importance*. Accessed: 02-03-2025. 2021. URL: https://sinovoltaics.com/learning-center/quality/fill-factor/.

[140] ASTM International. *ASTM E490-00a: Standard solar constant and zero air mass solar spectral irradiance tables*. Tech. rep. Accessed: 02-03-2025. ASTM International, 2000. URL: https://cdn.standards.iteh.ai/samples/7317/9d374cafe49e4190a032fd7e6a1caf61/ASTM-E490-00a.pdf.

[141] K. Cunningham, J. Carr, and B. Lewis. *MSFC electrical power systems for Cubesats*. Tech. rep. Accessed: 02-03-2025. NASA, 2018. URL: https://ntrs.nasa.gov/api/citations/20180007969/downloads/20180007969.pdf.

[142] W. C. Young and R. G. Budynas. *Roark’s formulas for stress and strain*. 7th ed. New York: McGraw-Hill, 2002.

[143] ISISPACE. *ISIS CubeSat solar panels*. Accessed: 12-05-2025. 2025. URL: https://www.isispace.nl/product/isis-cubesat-solar-panels/.

[144] D. Zhao et al. “Online estimation of satellite lithium-ion battery capacity based on approximate belief rule base and hidden Markov model”. In: *Energy* 256 (2022), p. 124632. ISSN: 0360-5442. DOI: https://doi.org/10.1016/j.energy.2022.124632. URL: https://www.sciencedirect.com/science/article/pii/S0360544222015353.

[145] V. Knap, L. Vestergaard, and D. I. Stroe. “A review of battery technology in CubeSats and small satellite solutions”. In: *Energies* 13 (Aug. 2020), p. 4097. DOI: 10.3390/en13164097.

[146] A. Cratere et al. “On-board computer for CubeSats: State-of-the-art and future trends”. In: *IEEE Access* PP (Jan. 2024), pp. 1–1. DOI: 10.1109/ACCESS.2024.3428388.

[147] intoPIX. *Pocket book about JPEG 2000*. Tech. rep. Accessed: 02-03-2025. intoPIX, 2012. URL: https://www.intopix.com/Ressources/WPs_and_Sc_Pub/intoPIX%20-%20Pocket%20book%20about%20JPEG%202000.pdf.

[148] R. Eastman, S. Warren, and C. Hahn. “Variations in cloud cover and cloud types over the ocean from surface observations, 1954-2008”. In: *Journal of Climate* 24 (Nov. 2011), pp. 5914–5934. DOI: 10.1175/2011JCLI3972.1.

[149] NASA. *State-of-the-art of small spacecraft technology*. Tech. rep. Accessed: 02-03-2025. National Aeronautics and Space Administration (NASA), 2023. URL: https://www.nasa.gov/smallsat-institute/sst-soa/.

[150] T. Nizanthi S. P. Thiagarajah. “A study on the effects of rain attenuation for an X-band satellite system over Malaysia”. In: *Progress In Electromagnetics Research B* 45 (2012), pp. 37–56. DOI: 10.2528/PIERB12083108.

[151] NASA Small Spacecraft Systems Virtual Institute. *State-of-the-art of small spacecraft technology – Communications*. Accessed: 02-03-2025. 2025. URL: https://www.nasa.gov/smallsat-institute/sst-soa/soa-communications/.

[152] European Telecommunications Standards Institute (ETSI). *ETSI EN 302 307: Digital Video Broadcasting (DVB); Second generation framing structure, channel coding and modulation systems for broadcasting, interactive services, news gathering and other broadband satellite applications*. Tech. rep. Accessed: 02-03-2025. ETSI, 2009. URL: https://www.etsi.org/deliver/etsi_en/302300_302399/302307/01.02.01_60/en_302307v010201p.pdf.

[153] EO Portal. *KSAT - Kongsberg satellite services global ground station network*. Accessed: 02-03-2025. 2020. URL: https://www.eoportal.org/other-space-activities/ksat#ksat-kongsberg-satellite-services-global-ground-station-network.

[154] J.R. Wertz, W.J. Larson, and J.J. Puschell. *Space mission engineering: The new SMAD*. Microcosm Press, 2011.

[155] Intelsat. *Satellite link budget*. Accessed: 02-03-2025. 2018. URL: https://itso.int/wp-content/uploads/2018/04/LBA-1.pdf.

[156] International Telecommunication Union (ITU). *Recommendation ITU-R P.676-11: Attenuation by atmospheric gases*. Tech. rep. Accessed: 02-03-2025. ITU, Sept. 2016. URL: https://www.itu.int/dms_pubrec/itu-r/rec/p/R-REC-P.676-11-201609-I!!PDF-E.pdf.

[157] International Telecommunication Union (ITU). *Recommendation ITU-R P.676-9: Attenuation by atmospheric gases*. Tech. rep. Accessed: 02-03-2025. International Telecommunication Union (ITU), 2012. URL: https://www.itu.int/rec/R-REC-P.676-9-201202-I/en.

[158] Code 453 NASA Near Earth Network (NEN) Project. *Near Earth Network (NEN) users' guide, Revision 4*. Tech. rep. Effective Date: March 14, 2019. Expiration Date: March 14, 2024. NASA, Mar. 2019.

[159] K. Cheung. *The role of margin in link design and optimization*. Tech. rep. Available at: Kar-Ming.Cheung@jpl.nasa.gov. Pasadena, CA, USA: Jet Propulsion Laboratory (JPL), 2015.

[160] NASA. *Attitude determination and control systems, Chapter 19.1*. Accessed: 01-15-2025. 2011. URL: https://ntrs.nasa.gov/api/citations/20110007876/downloads/20110007876.pdf.

[161] A. Black and D. Spencer. "DragSail systems for satellite deorbit and targeted reentry". In: *Journal of Space Safety Engineering* 7 (Aug. 2020). DOI: 10.1016/j.jsse.2020.07.030.

[162] European Cooperation for Space Standardization (ECSS). *ECSS-E-10-04: Space engineering – Space environment standard*. Tech. rep. Accessed: 02-03-2025. European Cooperation for Space Standardization (ECSS), 2020. URL: https://ecss.nl/standard/ecss-e-10-04c-rev-1-space-environment-15-november-2008/.

[163] K. Patankar and N. Fitz-Coy. "A hybrid cmg-rw attitude control strategy for agile small satellites". In: *Advances in the Astronautical Sciences* 150 (Jan. 2014), pp. 2057–2066.

[164] S. Barral et al. "Conceptual design of an air-breating electric propulsion system". In: *Proceedings of the 34th International Electric Propulsion Conference (IEPC-2015-271) and 30th International Symposium on Space Technology and Science (ISTS-2015-b-271)*. Presented at Joint Conference of 30th International Symposium on Space Technology and Science, 34th International Electric Propulsion Conference and 6th Nano-satellite Symposium. QuinteScience, Sitael SpA, European Space Agency. Warszawa, Poland, Ospedaletto (Pisa), Italy, Noordwijk, The Netherlands: IEPC/ISTS/Nano-satellite Symposium, July 2015.

[165] K. Lemmer. "Propulsion for CubeSats". In: *Acta Astronautica* 134 (2017), pp. 231–243. ISSN: 0094-5765. DOI: https://doi.org/10.1016/j.actaastro.2017.01.048. URL: https://www.sciencedirect.com/science/article/pii/S0094576516308840.

[166] D. O'Reilly, G. Herdrich, and D. F. Kavanagh. "Electric propulsion methods for Small satellites: A review". In: *Aerospace* 8.1 (2021). ISSN: 2226-4310. DOI: 10.3390/aerospace8010022. URL: https://www.mdpi.com/2226-4310/8/1/22.

[167] R. P. Welle. "Propellant storage considerations for electric propulsion". In: *Proceedings of the 1991 International Electric Propulsion Conference (IEPC 1991)*. The Aerospace Corporation. Los Angeles, CA 90009, 1991. URL: https://electricrocket.org/IEPC/IEPC1991-107.pdf.

[168] R. S. Sankovsky and S. R. Oleson. *HAN-Based monopropellant propulsion system with applications*. NASA Technical Memorandum 19970010493. Cleveland, Ohio 44135: NASA Lewis Research Center, 1997. URL: https://ntrs.nasa.gov/api/citations/19970010493/downloads/19970010493.pdf.

[169] M. Liu. *Special report: Monte Carlo simulation trials*. Tech. rep. Accessed: 02-03-2025. Valuation Research Corporation, 2017. URL: https://www.valuationresearch.com/wp-content/uploads/kb/SpecialReport_MonteCarloSimulationTrials.pdf.

[170] T. Schörner-Sadenius. *The Monte Carlo method: Basics and (simple) applications*. https://indico.cern.ch/event/75452/contributions/2089762/attachments/1049563/1496230/mc.pdf. GEANT4 Training Event, DESY Hamburg, 28 January 2010. 2010.

[171] ThrustMe. *NPT30-I2-1U: Smart iodine electric propulsion system*. Accessed: 22-05-2025. 2023. URL: https://www.thrustme.fr/base/stock/ProductBannerFiles/2_20231106-thrustme-npt30-i2-1u.pdf.

[172] ENPULSION. *MICRO R3: Electric propulsion system for small and medium satellites*. Accessed: 22-05-2025. 2020. URL: https://catalog.orbitaltransports.com/micro-r3/.

[173] G. C. Potrivitu et al. “A review of low-power electric propulsion research at the space propulsion centre Singapore”. In: *Aerospace* 7.6 (2020). ISSN: 2226-4310. DOI: 10.3390/aerospace7060067. URL: https://www.mdpi.com/2226-4310/7/6/67.

[174] SpaceX. *SpaceX rideshare program*. Accessed: 11-12-2024. 2025. URL: https://www.spacex.com/rideshare/.